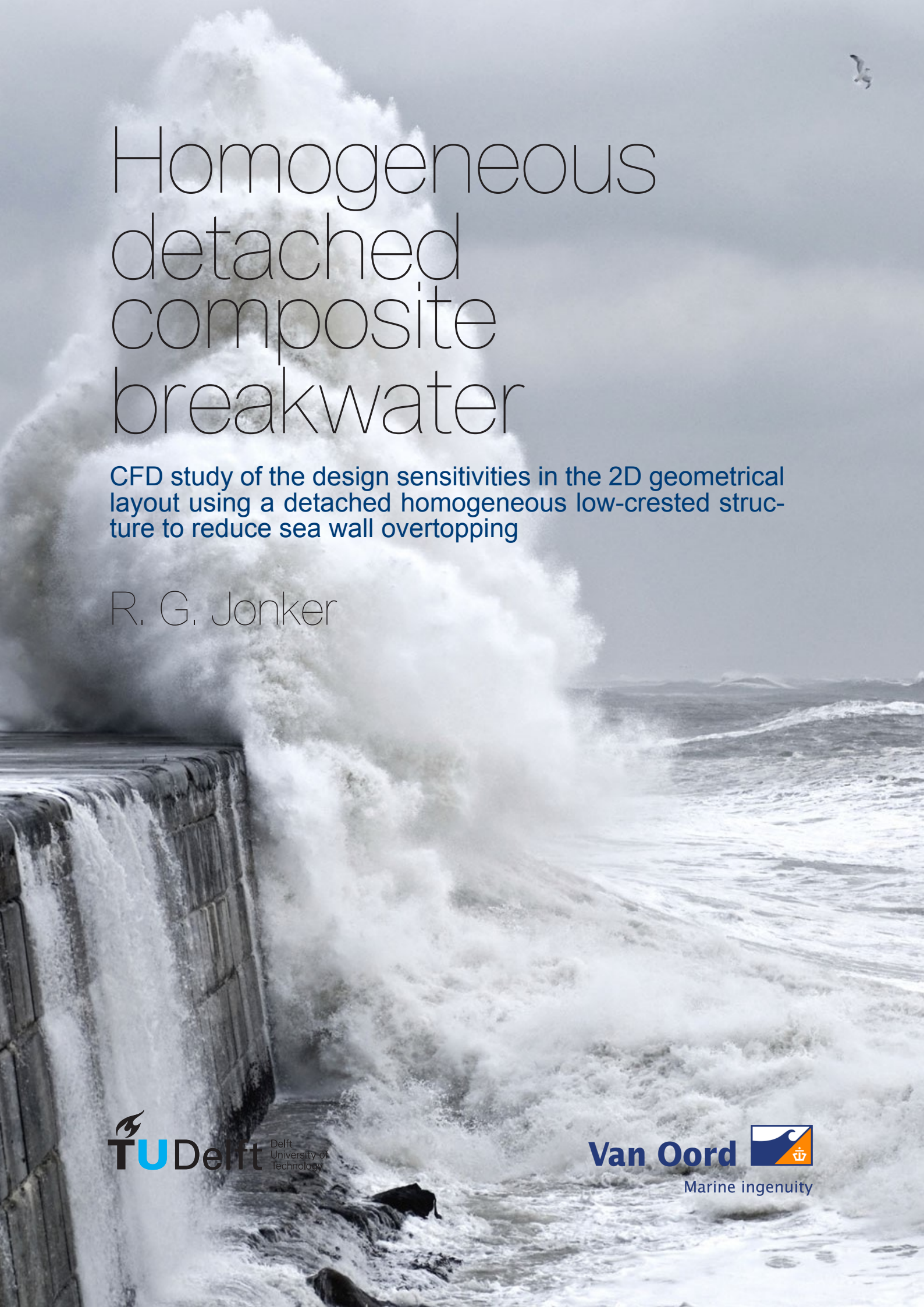

Homogeneous detached composite breakwater

CFD study of the design sensitivities in the 2D geometrical layout using a detached homogeneous low-crested structure to reduce sea wall overtopping

R. G. Jonker

TU Delft Delft University of Technology

Van Oord Marine ingenuity

Cover: credits: WSI

Homogeneous detached composite breakwater

CFD study of the design sensitivities in the 2D geometrical layout using a detached homogeneous low-crested structure to reduce sea wall overtopping

by

R. G. Jonker

in partial fulfilment of the requirements for the degree of

Master of Science
In Civil Engineering

at the Delft University of Technology,
to be defended publicly on Thursday August 27th, 2020 at 15:00 PM.

Student number:	4372123	
Thesis committee:	Dr. ir. A. Antonini,	TU Delft, chair
	Dr. ir. B. Hofland,	TU Delft
	Ir. G. M. Smith,	TU Delft, Van Oord
	Ir. A. Zoon,	Van Oord, supervisor

TU Delft

(This page is intentionally left blank)

Preface

The report that you are about to read is the result of the research that I conducted in collaboration between the dutch marine contractor Van Oord and the Delft University of Technology. This thesis work has been the final challenge in obtaining my Master of Science degree in Hydraulic Engineering at the Delft University of Technology. For the last 9 months I have been part of the Coastal Engineering section at Van Oord where I had the great opportunity to gain insight in the real world of engineering and work on my thesis.

Personally, this research project has been one of the most challenging projects that I have worked on so far. Working individually with a sophisticated numerical model turned out to be both very challenging and interesting at the same time. I can say that I learned a lot about numerical modelling, scientific research and engineering practice during the last couple of months.

I want to take this opportunity to express my gratitude to everyone who had an impact on my thesis work. First of all I would like to thank all the members of my thesis committee, Alessandro Antonini, Bas Hofland, Greg Smith and Arthur Zoon for all their time, guidance, valuable insights and feedback. It helped me a lot during the progress meetings and overall progression of my research. In special I would like to thank my Van Oord supervisor Arthur Zoon for his great support during my daily work. Always finding time whenever I needed it, being open and honest and for taking me to the Houtribdijk to show me around some great engineering work in progress. I would also like to thank Van Oord and all the people from the Coastal Engineering section for the opportunity to conduct the thesis work at their office in Rotterdam, providing the computational capacity for the simulations, guidance and great work space.

Finally I would like to thank my family and friends for their support during both my graduation as well as during the rest of my study. A special thanks go out to my parents, sisters and girlfriend for always supporting me in every possible way, keeping me motivated while working from home during the COVID-19 pandemic and providing me with encouragement, love and happiness.

I hope you enjoy your reading.

R. G. Jonker
Nijkerk, August 2020

(This page is intentionally left blank)

Summary

In this research OpenFOAM is used to model and determine the complex hydrodynamic behaviour of a Homogeneous low-crested structure (HLCS) consisting of cubipod artificial concrete elements. The validated model is used to gain insight in the design sensitivities of a two dimensional cross sectional layout to reduce sea wall overtopping.

HLCS and Low-crested structure (LCS) in general dissipate energy from the incoming wave field by wave breaking over the crest of the structure and porous flow through the structure. By energy dissipation milder wave conditions are created inside the basin between the HLCS and the sea wall. Milder wave conditions result in reduced hydrodynamic loads on the sea wall and reduced flood risk. However not only the milder wave conditions determine the amount of sea wall overtopping. Additionally wave-induced water level set-up and basin hydrodynamics (i.e. seiching and resonance) contribute to the amount of overtopping. The relative importance of these different hydrodynamic interactions on sea wall overtopping depend on the main geometrical layout parameters of the system. The main geometrical layout parameters that are analysed in this research are the crest height of the HLCS (R_c), the crest width of the HLCS (B) and the basin length between the HLCS and the sea wall (L_{pool}). These geometrical layout parameters can be used by the engineer to steer the hydrodynamic behaviour towards the most cost effective design to reduce sea wall overtopping. However, due to the complexity of physical processes involved and their interactions, theoretical analysis is cumbersome. Therefore advanced OpenFOAM Computational Fluid Dynamics (CFD) simulations are performed in this research. These simulations are used to capture the complex hydrodynamics and gain more insight in the design sensitivities of these types of hydrodynamic systems.

A coupled numerical model using both OceanWave3D and OpenFOAM has been set-up in this research. Model dimensions are based on conducted physical model experiments to assess the amount of wave transmission over HLCS as described in J. Medina et al. (2019). No raw data was available from these physical model experiments. Therefore the wave flume hydrodynamics (i.e. irregular wave characteristics) have been calibrated using a grid resolution study. In this study also simulations with varying courant numbers have been performed. Both extracted statistical wave parameters of the coupled model and a standalone OceanWave3D model have been compared. Additionally the separate output of OceanWave3D and OpenFOAM within the coupled model have been compared. Grid convergence has been found for increasing OpenFOAM grid resolution. The measured mean overtopping discharges from the OpenFOAM model are validated against Eurotop 2018 prediction guidelines. The grid which showed the most accurate results in comparison to the required computational time has been selected for the remainder of the study. This OpenFOAM grid is characterized a grid resolution of $\Delta_{x,swl} = \Delta_{y,swl} = H_s/10$.

In order to assess the hydrodynamic behaviour related to wave transmission for HLCS, the van Gent (1995) parameterization of the extended Darcy Forchheimer equation has been used to model the amount of flow resistance that is exerted on the flow by the HLCS. Based on the differences between conventional rubble mound low-crested structures and HLCS a detailed analysis on the input parameters of the van Gent (1995) parameterization (i.e. the D_{n50} , KC, n_p and the closure coefficients α and β) has been conducted. Large porosity gradients are found near the boundaries of the artificial cubipod elements. This effect has been implemented in the numerical model using two numerical layers with different porosity values resulting from the derived porosity distribution for artificial cubipod concrete elements. Additionally the effect of numerical outer layer schematization has been addressed. Both numerical additions only show to have minor effect on the modelled wave transmission behaviour (i.e. < 2% on K_t). The closure coefficients α and β have been calibrated and validated based on the conducted physical model experiments J. Medina et al. (2019). Additionally a sensitivity analysis is included which can be used for the calibration of different artificial concrete elements. The best agreement between the modelled transmission coefficient and the experimental transmission coefficient is

found for $\alpha = 500$ and $\beta = 1.0$.

A parametric study is performed using the validated OpenFOAM model including the HLCS and sea wall to describe the complex hydrodynamic interactions within the hydrodynamic system and assess the design sensitivities. For this parametric study multiple simulations on 6 parallel processors were performed with a duration of 500 waves. Each simulation took approximately 48 hours to complete.

The most important findings and implications of the parametric study are in summary:

- Wave transmission is found to be the dominant over the water level set-up, seiching and resonance inside the basin for the overtopping assessment of varying crest height and crest width of the HLCS. The most striking result for wave transmission over HLCS is that HLCS shows a constant trend in wave transmission for emergent structures (i.e. $R_c > 0$). A further increase of crest height does not result in reduced wave transmission, contrary to conventional rubble mound LCS where a further reduction is observed.
- Furthermore a large dependency is found for varying basin length. The propagation of broken waves (i.e. hydraulic bores) due to wave breaking over the crest of the HLCS result in a significant increase in mean overtopping discharge. It is observed that these hydraulic bores die out for larger basin length. Additionally low-frequency wave motion (i.e. seiching and resonance) is observed for varying basin length. However this effect is smaller compared to the dissipating bores.
- For all varying geometrical parameters a decay in the form of an exponential function of the mean overtopping discharge is found for increasing parameter value. The most influence on the overtopping reduction is found for varying crest height of the HLCS.
- By comparing the estimated overtopping discharge using the Eurotop guidelines solely based on the amount of wave transmission and the obtained overtopping discharge from the OpenFOAM model a mean underestimation of 69% is found by only using the transmission coefficient for the assessment of the amount of mean overtopping discharge. This concludes that the water level set-up cannot be neglected for overtopping assessments. Furthermore the use of advanced CFD modelling (e.g. using OpenFOAM) or physical modelling is of added value for the assessment of the amount of overtopping for these complex hydrodynamic systems due to the influence of dissipating bores, seiching and resonance inside the basin.

The ability of OpenFOAM to gain insight and to study the interactions for complex hydrodynamic systems has been demonstrated. Moreover design sensitivities of the hydrodynamic system under consideration are presented. These results can be used during early design stages for the assessment of the most cost effective design for these types of hydrodynamic systems. Additionally the sensitivity of the geometrical layout parameters can be used by the engineer to make targeted adjustments. Furthermore for comparable hydraulic boundary conditions (i.e. the same order of H_s, H_s/h, h/L_p) and the use of low-crested structures (i.e. $R_c/H_{s,i} \approx 0$) this OpenFOAM model can be used during design stages without further calibration.

Contents

List of Symbols

Latin symbols

B	Crest width of the HLCS	[m]
C	Courant number	[-]
C_{max}	Maximum prescribed courant number to OpenFOAM	[-]
D_{n50}	Nominal diameter related to the cube root of the volume of the material $D_{n50} = D_n = (M/\rho_c)^{1/3}$	[m]
e_p	Openness of the ventilated boundary condition	[%]
f_p	Peak frequency of wave spectrum	[1/s]
g	Gravitational acceleration	[m/s2]
H	Wave height, from trough to crest	[cm]
h	Water depth; water depth at the toe of the structure	[cm]
h_0	Offshore water depth	[cm]
h_b	The water depth at the moment of incipient breaking	[cm]
h_c	Structure height	[cm]
$H_{1/3}$	Significant wave height using time domain analysis, average of highest 1/3 of all waves	[cm]
$H_{s,i}$	Incoming significant wave height, $H_{s,i} = H_{1/3}$	[cm]
$H_{s,OW}$	Significant wave height resulting from the OceanWave3D output	[cm]
$H_{s,OF}$	Significant wave height resulting from the OpenFOAM output	[cm]
$H_{s,t}$	Transmitted significant wave height, $H_{s,t} = H_{1/3}$	[cm]
H_{m0}	Significant wave height calculated using spectral analysis, $H_{m0} = 4 \cdot (m_0)^{0.5}$	[cm]
$H_{m0,OW}$	Spectral wave height resulting from the OceanWave3D output	[cm]
$H_{m0,OF}$	Spectral wave height resulting from the OpenFOAM output	[cm]
H_b	Breaker wave height	[cm]
$i_{\overline{\eta},HLCS}$	Mean water level set-up gradient over the HLCS	[-]
$i_{\overline{\eta},basin}$	Mean water level set-up gradient inside the basin	[-]
K_t	Transmission coefficient, $K_t = H_{s,t}/H_{s,i}$	[-]
KC	Keulegan–Carpenter number, $KC = uT/n_p D_{n50}$	[-]
L	Wavelength, in the direction of wave propagation	[m]
$L_{m-1,0}$	Wavelength inside the basin based on spectral moment m_{-1} and m_0	[cm]
$L_{m-1,0,O}$	Offshore wavelength based on spectral moment m_{-1} and m_0, $L_{m-1,0,0} = gT^2_{m-1,0,O)}/2\pi$	[cm]
L_p	Wavelength in shallow water, based on $T_{p,i}$	[cm]
L_{pool}	Distance between the HLCS and the sea wall. L_{pool} = basin length	[cm]
m	Foreshore slope = $\tan\alpha_{foreshore}$	[-]
n_L	Scaling factor = prototype scale/model scale	[-]
n_p	Porosity	[-]
$n_{p,core}$	Core porosity	[-]
$n_{p,outer}$	Outer layer porosity	[-]
N_x	Number of grid cells in horizontal direction	[-]
N_y	Number of grid cells in vertical direction	[-]
q	Mean overtopping discharge	[l/s/m]
$q_{initial}$	Mean overtopping discharge resulting from a simulation without HLCS	[l/s/m]
R_c	Crest freeboard of the HLCS, $R_c = h_c - h$	[cm]
$R_{c,seawall}$	Crest freeboard of the sea wall	[cm]
$s_{op,O}$	Fictitious wave steepness for peak period wave, $s_{op} = 2\pi H_s/(gT^2_{p,i})$	[-]
t	Time	[s]
T_{clock}	Real time	[min]
$T_{m-1,0}$	Mean period inside the basin based on spectral moments m_0 and m_{-1}	[s]
T_p	Peak period of the wave spectra	[s]
$T_{p,i}$	Peak period of the wave spectra	[s]
$T_{simulation}$	Simulation time	[s]
T_t	Layer thickness	[cm]
u	Horizontal particle velocity	[m/s]
x	Horizontal flume coordinate	[m]
x_p	Breaker travel distance	[m]

Greek symbols

α	Laminar porous media closure coefficient	[-]
α_s	Seaward slope angle of the HLCS	[degrees]
$\alpha_{foreshore}$	Foreshore slope angle	[degrees]
β	Turbulent porous media closure coefficient	[-]
γ	Jonswap peak enhancement factor	[-]
δ	Water level set-up = $\overline{\eta}$	[cm]
Δ_t	Adopted numerical time step	[s]
Δ_x	Horizontal grid resolution	[cm]
$\Delta_{x,swl}$	Horizontal grid resolution around Still Water Level (SWL)	[cm]
$\Delta_{y,swl}$	Vertical grid resolution around SWL	[cm]
ζ_p	Head loss coefficient for the ventilated boundary condition	[-]
η	Free surface elevation	[cm]
$\overline{\eta}_{0.1}$	Mean surface elevation using a low pass filter with 0.1 frequency	[cm]
$\overline{\eta}_{seawall}$	Measured mean free surface elevation (0-680s) from a wave gauge closest to the sea wall	[cm]
ξ	Surf similarity parameter or Iribarren number, $\xi = tan\alpha/(s)^{0.5}$	[-]
ξ_{op}	Surf similarity parameter or Iribarren number for peak wave period Tp, $\xi_{op} = tan\alpha_s/(s_{op})^{0.5}$	[-]
ρ_c	The mass density of the concrete armour unit	$[kg/m^3]$

Acronyms

LCS Low-crested structure

HLCS Homogeneous low-crested structure

SWL Still Water Level

CFD Computational Fluid Dynamics

VOF Volume Of Fluid

RANS Reynolds Averaged Navier-Stokes

VARANS Volume Averaged Reynolds Averaged Navier-Stokes

JIP Joint Industry Project

1 Introduction

1.1. Context and background

Densely populated coastal areas around the world are commonly protected by vertical sea walls. Sea walls can withstand highly energetic wave environments, only need limited construction space and are good to use for recreation, leisure and sight seeing. However climate change causes a combination of rising sea levels and increasing intensity of storms. This results in severe problems to the existing coastal infrastructure and increases flood risk of the hinterland as more waves are able to overtop existing coastal structures. The increase in wave overtopping events leads to increasing risk of inundation of the hinterland. Inundation leads to possible high amounts of life and economic losses and should therefore be prevented. Flood risk reduction can be achieved by either increasing the strength of existing coastal infrastructure or reducing the direct hydrodynamic load on the structure (i.e. waves and water levels) (van den Bos & Verhagen, 2018). Nowadays the use of low-crested structures such as detached breakwaters and artificial reef structures become very common for coastal protection and hydrodynamic load reduction, sometimes also in combination with an artificial sand nourishment (Pilarczyk, 2003). A typical combination of a sea wall protected by a artificial reef, which is closely related to a HLCS is presented in figure 1.1. The assessment of the hydrodynamic behaviour and amount of overtopping reduction related to the geometrical layout of such a system is however a complex task. The hydrodynamic system that is created is dominated by wave transmission, wave-induced water level set-up and basin hydrodynamics related to reflecting wave energy (i.e. seiching and resonance). The magnitude of these various hydrodynamic interactions are again influenced by the main geometrical layout parameters of the system.

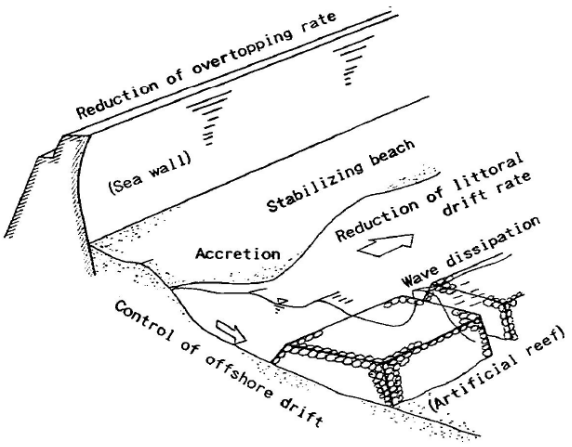

Figure 1.1: A typical combination of a sea wall protected by a LCS. Adopted from (Pilarczyk, 2003)

1.1.1. Homogeneous low-crested structures

Low-crested structures modify the wave conditions but also allow for significant wave overtopping due to their crest being around the SWL. These structures can be both emergent and submerged depending on the site specific tidal ranges and water level set-up during storm surges (Ciria et al., 2007). Like other detached coastal structures (e.g. coast parallel breakwaters and artificial reefs), these structures interact with the incoming waves and reduce transmitted energy to the lee side of the structure through energy dissipation (e.g. through wave breaking and porous resistance) and energy reflection. Detached LCS have the advantage of enhanced water circulation, reduced visual impact (e.g. for aesthetic purposes), increased biodiversity and lower material costs compared to an emergent detached structure (Ciria et al., 2007). A typical cross-section of a detached LCS with corresponding geometrical and hydraulic parameters is presented in figure 2.3.

Homogeneous low-crested structures (HLCS) are a typical form of low-crested structures made of stable pre-cast concrete elements without a core. In the absence of suitable (armour) quarry stone or in case of heavy design conditions, the only suitable alternative is the use of artificial concrete elements for these types of detached LCS. Additionally the advantages of HLCS consisting of stable pre-cast concrete elements compared to a conventional rubble mound LCS are the reduced environmental impact, the clean construction phase, the easy dismantling and re-use and increased biodiversity of marine life around the structure (J. Medina et al., 2019). Due to the porous structure of the elements a wide range of different light intensities between the individual elements is accommodated which enhances their value as multi-purpose green infrastructure according to (Odériz et al., 2018).

1.1.2. Numerical modelling of coastal structures

For the past decades, generally the initial design of complex hydrodynamic systems is made using (semi-) empirical prediction formulas for governing isolated wave structure interactions. However theoretical analysis is cumbersome due to the complexity of the physical processes that play a role in these hydrodynamic systems. Therefore physical or numerical modelling or a combination of both is necessary to define site-specific interactions between the wave climate and the HLCS and iterate towards a final design. Nowadays it is of great interest to use advanced CFD models based on the Navier Stokes equations during the design iteration phase. The use of CFD models results in achievement of most cost-effective optimization and quicker iteration during the design phases, especially since computer processing power is increasing.

In order to investigate the hydrodynamic behaviour of complex hydrodynamic coastal protection systems, detailed CFD modelling using the CFD package OpenFOAM can give very useful insights. It can help to assess design sensitivities in the geometrical layout of the system to optimise overtopping reduction (i.e. structural parameters and location of the HLCS). OpenFOAM is an advanced open-source CFD code based on the Reynolds Averaged Navier-Stokes (RANS) equations which combined with the waves2Foam toolbox shows great potential for the use of coastal engineering applications due to its ability to model complex hydrodynamics in and around coastal structures (i.e. wave breaking and porous flow). It has already been used to validate several types of permeable coastal structures, for which the reader is referred to the work of (Higuera et al., 2014a,b; Jacobsen et al., 2018, 2017, 2015; Jensen et al., 2014; Molines et al., 2019) and more. The ability of OpenFOAM to help during the different design phases is large but still more experience should be gained in the use of OpenFOAM to model all types of coastal structures and provide validated results.

1.2. Problem description

The construction of HLCS in front of a sea wall is one possible solution to reduce flood risk and stimulate the coastal environment by boosting marine life in the coastal region. However the prediction of overtopping reduction by the construction of a HLCS in front of a sea wall is not a straightforward task. There are empirical design guidelines for wave transmission over conventional rubble mound LCS, water level set-up behind conventional rubble mound LCS and overtopping discharges over sea walls. However, due to the complexity of the system, the use of separate design guidelines altogether cannot capture the complex behaviour of the hydrodynamic system. Also the geometrical layout starts to play a role which will influence the interactions itself and their mutual interactions. To understand

the complex hydrodynamics of this system and to be able to make design recommendations for the optimisation of overtopping reduction, physical- or numerical modelling is required. Due to the large potential of OpenFOAM for these types of complex hydrodynamic coastal engineering applications within the coastal engineering community and the availability of this CFD code at Van Oord this numerical model is utilized for this research. However in contrary to conventional rubble mound structures no validated porous media resistance parameters exist for the use of large artificial concrete elements in OpenFOAM.

1.3. Research objective and questions

It is the aim of this research to shed light on the use of detached HLCS consisting of cubipod artificial concrete elements in OpenFOAM by analysing the implementation of such structures in OpenFOAM and addressing the porous media resistance coefficients for the use of large artificial concrete elements. Furthermore the ability to model HLCS in OpenFOAM assists in the main objective of this thesis; to describe and quantify the effect of the most important 2D geometrical layout parameters on the hydrodynamics to asses the design sensitivities of such hydrodynamic systems (i.e. using a detached homogeneous low-crested structure) to reduce sea wall overtopping. All of this can be summarized in the following research objective:

"To verify and demonstrate the ability of OpenFOAM to capture the hydrodynamic interactions of HLCS consisting of cubipod artificial concrete elements and gain insight in the design sensitivities to optimise the two dimensional cross sectional layout using a HLCS to reduce sea wall overtopping."

Based on this research objective the following research questions are formulated:

1. What type of relevant hydrodynamic interactions play a role in a system using a HLCS consisting of cubipod artificial concrete elements and what are the main geometrical layout parameters that can be adjusted within this system to reduce sea wall overtopping?
2. How can OpenFOAM be used to model the hydrodynamic behaviour of HLCS related to wave transmission?
3. What are the design sensitivities in the cross-sectional layout of a hydrodynamic system using a HLCS consisting of cubipod artificial concrete elements to reduce sea wall overtopping and how can they be optimised?

1.4. Research methodology

In this section the research methodology is presented that has been followed to structurally answer the research question. The considered steps of the research methodology are represented by the chapters of the thesis which concludes the thesis outline as presented in figure 1.2.

- Chapter 1 presents a general introduction to the context of the research itself, the use of HLCS, numerical modelling of coastal structures and the research objective and questions.
- In chapter 2 a literature study is provided where knowledge is obtained regarding properties and structural parameters of HLCS and LCS in general. Moreover the influence of the geometrical parameters for wave transmission, wave-induced water level set-up, seiching and overtopping is discussed and well-known empirical prediction formulas are elaborated to be able to draft hypothesis regarding the hydrodynamics of the system investigated in this research.
- In chapter 3 the cubipod physical model experiments have been described that have been used to calibrate and validate the OpenFOAM model.
- Chapter 4 describes the numerical framework of a coupled OceanWave3D and OpenFOAM model that is used in this research including mathematical equations, numerical procedures and theoretical aspects.
- In chapter 5 the numerical model set-up is elaborated where the numerical flume, the used numerical grids, resolutions, system characteristics and boundary conditions are described.

- Chapter 6 describes the calibration and validation procedure of the wave flume hydrodynamics including the effect of grid- and temporal resolution on the coupling of both numerical models and an overtopping validation by comparing predicted overtopping discharges to the 2018 Eurotop manual. Additionally the effect of the ventilated boundary condition on overtopping discharges is analysed and the chapter concludes with a sensitivity analysis.
- In chapter 7 a detailed analysis is performed to the input parameters of the van Gent (1995) parameterization used by OpenFOAM to describe the porous hydrodynamic behaviour of the HLCS. The influence of structure schematization and addition of a schematized porosity distribution is analysed and the hydrodynamic behaviour of HLCS consisting of cubipod artificial concrete elements is calibrated and validated using the physical model experiments described in chapter 3. Additionally a sensitivity analysis is included which can be used to assess the calibration of hydrodynamic behaviour for structures using different artificial concrete elements.
- Chapter 8 elaborates on the design sensitivities in the geometrical layout of the hydrodynamic system that is created using a HLCS to reduce sea wall overtopping. First the model set-up is described and the adaptations of the numerical model for varying geometrical layouts are elaborated. The methods applied to extract the wave and hydrodynamic characteristics are described. Subsequently an initial parametric study is performed using practical limits of the geometrical parameters after which a more detailed analysis is provided based on the three identified main geometrical parameters. Next a practical assessment is performed by assessing the uncertainty related to solely predicting the overtopping discharge for the hydrodynamic system based on the transmitted wave height over the HLCS. Based on the obtained knowledge related to the main geometrical layout parameters, design recommendations for this hydrodynamic system are presented that can be used during design assessments of the main geometrical layout.
- In chapter 9 the results and research methodology are discussed and conclusions are drawn based on the research questions formulated in chapter 1. Additionally recommendations related to numerical modelling in OpenFOAM and recommendations for future research are presented.

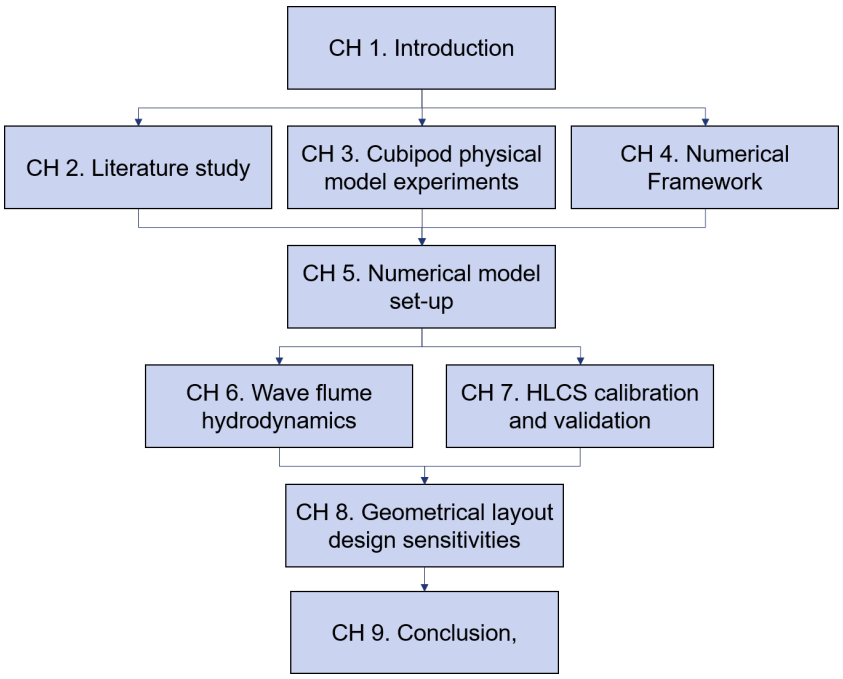

Figure 1.2: Thesis outline

2

Literature study

2.1. Introduction

This chapter discusses the concept of homogeneous low-crested structures including the geometrical and structural parameters that influence the hydrodynamic behaviour of these structures. Moreover important hydrodynamic wave structure interactions and basin hydrodynamics are elaborated and well known prediction guidelines are presented.

2.2. Homogeneous low-crested structures

According to van der Meer & Pilarczyk (1991) LCS can be divided into three categories: Dynamically stable reef breakwaters, statically stable low-crested breakwaters and statically stable submerged breakwaters. A general structural layout of each of these types of LCS is presented in figure 2.2. A reef breakwater is a homogeneous pile of stones without a filter layer or core and is allowed to reshape under design wave conditions. Statically stable low-crested structures on the other hand are stable under design storm conditions and generally consist of a rubble mound core protected by an armour layer, including possible filter layers. Due to their crest level relative to SWL, energy can pass over the crest of the structure which increases their stability. Statically stable submerged breakwaters are submerged and allow for high amounts of wave transmission due to their crest level relative to SWL. HLCS are similar to reef breakwaters but contrary to reef breakwaters form a statically stable structure due to the stability of the large units which are therefore able to withstand extreme storm wave conditions.

The HLCS consisting of cubipod artificial concrete elements was seen to enhance certain ecosystem services and facilitate marine ecosystem restoration (J. Medina et al., 2019). If used as a detached structure they protect the coastline in the same way as conventional LCS. However due to the difference in internal porous structure and use of stable concrete elements HLCS have minimized environmental impacts, a relatively clean construction phase, are re-usable and can easily be dismantled if necessary. These structures have considerable potential in the sustainable improvement of marine habitats and

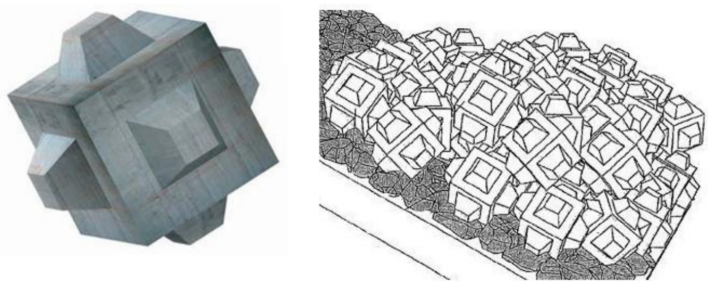

Figure 2.1: Impression of an artificial concrete cubipod element and layered placement

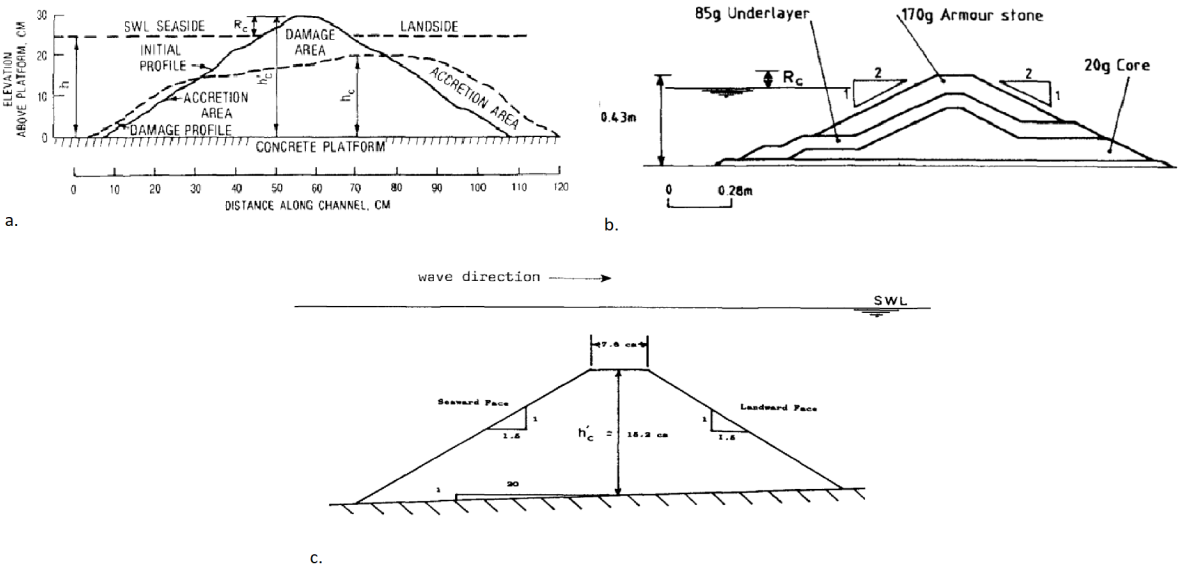

Figure 2.2: The 3 categories of low-crested structures. a. a reef type breakwater. b. a low-crested breakwater. c. a submerged breakwater. Adopted from van der Meer & Pilarczyk (1991)

coastal protection according to (Odériz et al., 2018). In figure 2.1 the cubipod artificial concrete element is presented which is used as construction material for the HLCS in this research.

2.2.1. Structural parameters

In this section various structural parameters and characteristics of HLCS and low-crested structures in general are elaborated. Additionally different methods to model these parameters and the effect hereof are examined. Moreover parameters with high influence on the hydrodynamic behaviour are outlined. Figure 2.3 shows a typical schematized cross-section of a LCS with some of the main geometrical parameters (i.e. structure height (h_c), water depth (h), freeboard (R_c) and crest width (B)).

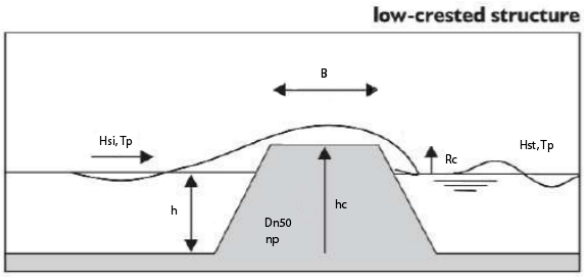

Figure 2.3: Typical cross section of a LCS including important parameters related to hydrodynamic behaviour. Adopted from (Ciria et al., 2007)

Structure crest height (h_c)

The most important parameter related to the hydrodynamic behaviour of LCS is found to be the structure freeboard (R_c) which is directly related to the structure crest height (h_c). Van der Meer & Daemen (1994) already noted that the correct definition of the crest level is crucial if the size of the armour layer is large and the crest level is close to SWL (i.e. low-crested structures). This has a large influence on the hydrodynamic behaviour for these types of structure configurations, see also section 2.3. The definition of the crest level of the structure should therefore be precisely examined.

However the precise definition of the crest level is ambiguous due to the natural roughness of the elements. This makes it not a straightforward task as described in (SBRCURnet, 2014). In order to

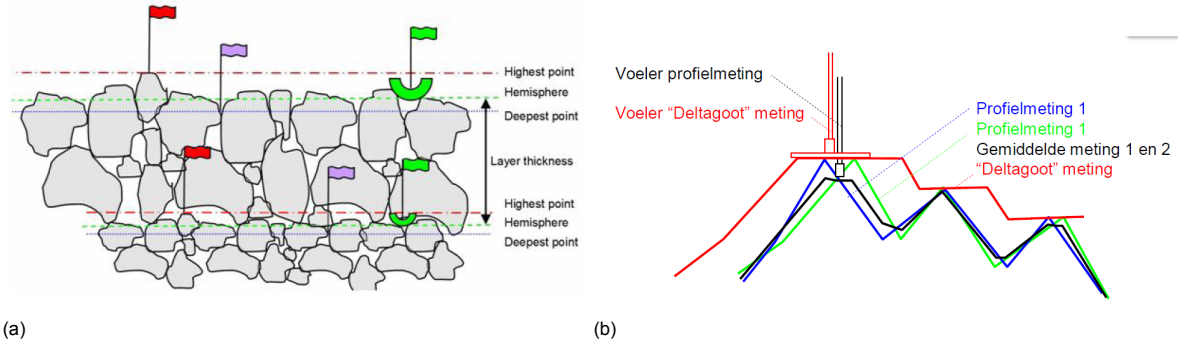

(a) (b)

Figure 2.4: a. Different reference levels and associated layer thickness dependent on the type of measurement technique used, adopted from (SBRCURnet, 2014). b. The principle of the 'Deltagoot' method and comparison to the conventional 3D profiler method, adopted from (Hofland & van Gent, 2010)

eliminate this ambiguity SBRCURnet (2014) prescribes three standard definitions for the reference level of a rubble mound layer which can be used to assess the crest level of rubble mound structures and layer thicknesses:

- The level that is measured by a 3D profiler staff with a semi spherical foot having a diameter of equal to half the nominal stone diameter of the rock grading examined.
- The level that connects to the top of the stones which follows form the survey using a plate which is sometimes larger than the stone size.
- The level which follows from the layer thickness calculated using the dumped stone mass per m^2.

Figure 2.4a shows large differences that can be obtained using different measurement techniques to access the reference level of a rubble mound layer. The HLCS examined in this research is made out of large artificial concrete cubipod elements, for which similarities can be observed to the concrete cubes used during the Maasvlakte 2 project. The method adopted during the Maasvlakte 2 project uses the concept of the highest point in the theoretical design envelope to calculate the crest height (Hofland & van Gent, 2010). Both a conventional 3D profiler and a 3D profiler with a larger diameter (e.g. the 'Deltagoot' method) are adopted and differences are reported in figure 2.4b. Based on both figures the introduced uncertainty on the assessment of the crest height for the numerical modelling of such structures is visualised.

One can imagine that the determined reference level during modelling of such structures also affects the porosity of the structure near the outer layer which is also an important input value for the model. If the modelled crest level is chosen using the highest point method the outer layer has larger porosity compared to modelling of structures where different methods are adopted. Based on this observation the relation of crest level and porosity is further analysed in the next section.

Porosity (n_p)

Porosity is the amount of empty space within the porous structure. Porosity has a large influence on the hydraulic performance of structure and is closely related to the permeability of the structure. Porosity affects the hydraulic performance of the structure because of energy dissipation occurring in the voids and ability of flow to go through the structure. This in turn affects wave reflection, wave transmission, stability, run-up and overtopping. Porosity is defined as the percentage of voids between the elements within the structure using a arbitrary control volume as presented in equation 2.1.

$$n_p = \frac{V_V}{V} \tag{2.1}$$

In equation 2.1 V_V is the volume of voids and V is the total control volume for which the porosity is derived. The porosity mainly depends on the type, grading, shape and placement method of the material. Typical values of porosity for rubble mound and concrete armour units range from 30-55%. Homogeneous low-crested structures consisting of concrete elements generally have higher porosity

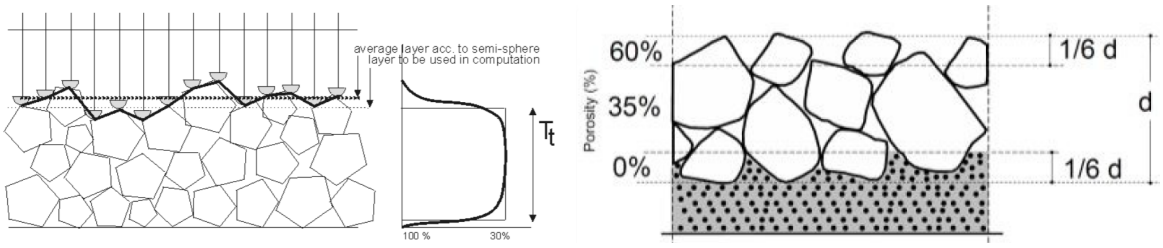

(a) (b)

Figure 2.5: a. Porosity distribution over a rubble mound layer, with indicated layer thickness (Bosma et al., 2003). b. Porosity of a rock layer on a sandy bed (SBRCURnet, 2014)

values compared to rubble mound structures due to the size of the elements and the amount of interlocking of the elements. One can can imagine that the porosity in the outer layer is not homogeneous but shows large heterogeneity as a result of boundary effects due to the variability of the elements and the random placement. This heterogeneity results in a distribution of porosity over the height of a layer. The porosity calculated using equation 2.1 is a homogeneous porosity which does not take the boundaries of the structure into account.

Numerical models only consider a homogeneous value for the porosity within the computational cells enclosed by the boundary of the surface defined by the user thus lacking knowledge on the boundary effects. Especially for large artificial elements (e.g. cubipods in this research), larger porosity gradients are found over the elements and the upper and lower surfaces of the layer also have a larger contribution to the total layer thickness (SBRCURnet, 2014). This increases the importance of the boundaries to the total porosity. In order to obtain insight in this boundary effect and the relation to the crest level a closer look at the porosity distribution is needed. For rubble mound layers this distribution has already been explored by (Bosma et al., 2003).

Porosity distribution

An example of a porosity distribution for a rubble mound layer is presented in figure 2.5a. In here the porosity reduces from 100 percent at the top of the layer to the mean porosity and then increases back to 100 percent at the bottom of the layer. In order to remove this variability most engineering manuals, like the rock manual (Ciria et al., 2007), introduce a mean porosity and layer thickness (T_t) to asses the porosity of a layer. The mean porosity is defined as the porosity of the rock layer excluding the open spaces near the upper and lower surfaces of the layer (SBRCURnet, 2014). The mean porosity transforms the actual porosity profile to a block function with a specified layer thickness related to nominal diameter of the material and the number of layers, see figure 2.5a.

The first ideas to describe this transition boundary layer is found in the area of road construction by Knieß (1977), where the porosity values in the transition of a filter layer on top of a rubble mound layer are prescribed. A different average porosity is defined for each layer including the transition layers, as presented in figure 2.5b. The outer layer was defined as 1/6 of the total layer thickness. However these values are not provided with proof and are derived for rock layers in road constructions works. The application of such a porosity model to rubble mound coastal structures has been conducted by Bosma et al. (2003). In here the thickness of the transition layers, related to the nominal diameter, and the porosity that belongs to these transition layers for both single layer and double layer (armour and filter layer) rubble mound layers are quantified. The outer armour transition layer was found to be $0.74D_{n50}$ for rubble mound layers.

2.3. Wave transmission

Wave transmission is the wave structure interaction where incoming wave energy is transmitted to the lee side of the structure where it creates transmitted waves. Energy can be transmitted by either going over the structure (i.e. overtopping) or going through the structure (i.e. porous flow). Wave transmission by energy going through the structure is enhanced when the core of the structure is very permeable and the wave period is relatively long (van den Bos & Verhagen, 2018). For emerged structures less water can overtop and wave transmission is mostly generated by energy going through the structure whereas for low crested structures the largest amount of transmitted energy comes from energy going over the structure (e.g. overtopping). Submerged structures are a special form of a low crested structures while they have a crest level below SWL and are therefore continuously overtopped.

An important concept used in the description of the wave mitigation process of HLCS is the law of conservation of energy. This law describes the balance of energy (e.g. incoming energy, reflected energy, dissipated energy and transmitted energy) over a control volume around the HLCS. In formulae form:

$$E_i = E_r + E_d + E_t \tag{2.2}$$

In which E_i is the incoming energy, E_r is the reflected energy, E_d is the dissipated energy and E_t is the transmitted energy.

According to Goda (2010), the propagation of the transmitted waves behind the structure propagates in a pattern similar to that of the incident waves, but with reduced wave heights. This results in the concept that wave transmission can be measured in terms of the transmission coefficient. For an irregular wave field the definition of the transmission coefficient is usually based on the significant wave height (H_s) or the spectral wave height (H_{m0}). In this research the significant wave height is used which results in the following transmission coefficient:

$$K_t = \frac{H_{s,t}}{H_{s,i}} \tag{2.3}$$

Because the wave height is also related to the amount of wave energy, the transmission coefficient can also be written in terms of the amount of incoming and transmitted energy (i.e. $\sqrt{\frac{E_t}{E_i}}$) (Ciria et al., 2007). Rewriting equation 2.2, the wave transmission coefficient can be reduced to $\frac{E_t}{E_i} = 1 - \frac{E_r}{E_i} - \frac{E_d}{E_i}$, which suggests that the wave transmission coefficient implicitly includes the sum of the dissipation and reflection coefficients. The limits of the wave transmission coefficient are zero for no energy transmission and one for complete energy transmission without dissipation. For low crested structures with a crest level around SWL generally transmission coefficients in the range of 0.5 are found.

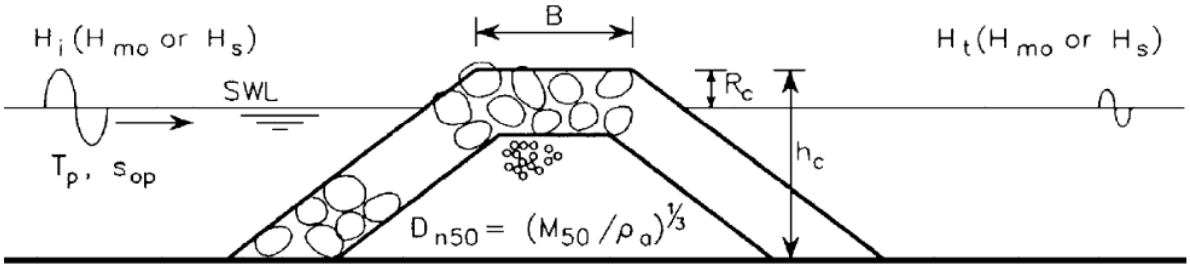

Figure 2.6: Governing wave transmission parameters. (van der Meer et al., 2005)

Various hydraulic boundary conditions and structural conditions influence the amount of transmitted wave energy. The most important parameters related to wave transmission are found to be the freeboard R_c and the crest width of the structure B. Therefore the definition of the crest level is crucial for the assessment of wave transmission. All literature studies to wave transmission for artificial concrete

elements examined in this research use a plane through the upper edge of the armour units to define the crest height, see (Hirose, N; Watanuki, A; Saito, 2002) and (Hofland & van Gent, 2010). The crest width influences the amount of wave breaking on the crest of the structure and the total resistance on the flow through the structure due to the longer flow path. In figure 2.6 the most used structural and hydraulic parameters are presented that are used in literature to describe the wave transmission phenomena.

Table 2.1 presents the most used empirical wave transmission formulas in engineering practice and their validity ranges. In this table also the wave transmission formula derived by J. Medina et al. (2019) for HLCS is presented for a 1, 3 and 5 layer cubipod HLCS. The formulas are based on the formula of D'Angremond et al. (1996) and are derived based on experimental data presented in J. Medina et al. (2019), Odériz et al. (2018). Only the data corresponding to the 5 layered cubipod HLCS is used in this research which is described in more detail in chapter 3. The most striking result from the experiments conducted by J. Medina et al. (2019) for a 5 layered cubipod HLCS is that a constant wave transmission coefficient is predicted for emergent structures where a decreasing transmission coefficient is found for conventional rubble mound structures. For a more in depth review and origin of the empirical formulas presented in table 2.1, the reader is referred to appendix A.

Table 2.1: Relevant literature regarding wave transmission

Author	Formulae	Validity range
(Van der Meer, 1990)	$K_t = 0.8$ $K_t = 0.46 + 0.3R_c/H_i$ $K_t = 0.1$	$-2.0 < R_c/H_i < -1.13$ $-1.13 < R_c/H_i < 1.2$ $1.2 < R_c/H_i < 2.0$
(Van der Meer & Daemen, 1994)	$K_t = a\frac{R_c}{D_{n50}} + b$ $a = 0.031\frac{H_{s,i}}{D_{n50}} - 0.24$ $b = -5.42s + 0.0323\frac{H_{s,i}}{D_{n50}} - 0.0017\left(\frac{B}{D_{n50}}\right)^{1.84} + 0.51$	$-2 < R_c/D_{n50} < 2$ $1 < H_{s,i}/D_{n50} < 6$ $0.01 < s_{op} < 0.05$
(D'Angremond et al., 1996)	$K_t = -0.4\frac{R_c}{H_{s,i}} + 0.64\left(\frac{B}{H_{s,i}}\right)^{-0.31}\left(1 - e^{-0.5\xi}\right)$	$-2.5 < R_c/H_{s,i} < 2.5$ $B/H_{s,i} < 10$
(Briganti et al., 2003)	$K_t = -0.35\frac{R_c}{H_{s,i}} + 0.51\left(\frac{B}{H_{s,i}}\right)^{-0.65}\left(1 - e^{-0.41\xi}\right)$	$-2.5 < R_c/H_{s,i} < 2.5$ $10 < B/H_{s,i} < 50$
(van der Meer et al., 2005)	$K_t = -0.4\frac{R_c}{H_{s,i}} + 0.64\left(\frac{B}{H_{s,i}}\right)^{-0.31}\left(1 - e^{-0.5\xi}\right)$ Linear interpolation between both formulae $K_t = -0.35\frac{R_c}{H_{s,i}} + 0.51\left(\frac{B}{H_{s,i}}\right)^{-0.65}\left(1 - e^{-0.41\xi}\right)$	$B/H_{s,i} < 8$ $8 < B/H_{s,i} < 12$ $12 > B/H_{s,i} > 50$
(Seabrook & Hall, 1998)	$K_t = 1 - \left[e^{-0.65\frac{R_c}{H_{m0,i}} - 1.09\frac{H_{m0,i}}{B}} + 0.047\frac{BR_c}{LD_{n50}} - 0.067\frac{R_c H_{m0,i}}{BD_{n50}}\right]$	$0 < BR_c/(L_p D_{n50}) < 7.08$ $5 < B/H_{m0,i} < 74.47$ $0 < R_c H_{m0,i}/BD_{n50} < 2.14$
(Buccino & Calabrese, 2007)	$K_t = \frac{1}{1.18\left(\frac{H_{s,i}}{R_c}\right)^{0.12} + 0.33\left(\frac{H_{s,i}}{R_c}\right)^{1.5} \cdot \frac{B}{\sqrt{H_{s,i}L_0}}}$ $K_t = \left[\min\left(0.74; 0.62\xi_{op}^{0.17}\right) - 0.25 \cdot \min\left(2.2; \frac{B}{\sqrt{H_{s,i}L_0}}\right)\right]^2$	$0.3 < B/H_{s,i}L_0^2 < 10.5$ $1/0.5 < R_c/H_{s,i} < 1/1.2$ $Rc/H_{s,i} = 0$
J. Medina et al. (2019)	$K_t = 0.45 - 0.3\frac{R_c}{H_{s,i}}$	1 layer cubipod HLCS $-1.47 \leq Rc/H_{si} \leq 0.00$
J. Medina et al. (2019)	$K_t = 0.60 - 0.35\frac{R_c}{H_{s,i}}$	3 layer cubipod HLCS $-0.43 \leq Rc/H_{si} \leq 0.63$
J. Medina et al. (2019)	$K_t = max[0.54; 0.54 - 0.40\frac{R_c}{H_{s,i}}]$	5 layer cubipod HLCS $-0.36 \leq Rc/H_{si} \leq 0.89$

2.3.1. The concept of breaker travel distance

The crest width (B) of the breakwater is important for the wave breaking process on the crest of the structure. Waves approaching the structure do not break instantaneously on the front slope of the structure but travel a certain distance while breaking. In the Shore Protection Manual (*Shore Protection Manual*, 1984) a method to calculate the breaker travel distance on a sloping beach is presented. The breaker travel distance is the distance from incipient breaking to the plunge of the breaking wave, see figure 2.7a for a definition sketch. In this method to calculate the breaker travel distance it is suggested that the breaker travel distance is related to the breaker wave height (H_b) and the nearshore slope of the beach (m). For low-crested structures wave breaking is initiated at the seaward slope and eventually breaks on the horizontal crest of the structure. The following formula to calculate the breaker travel distance for plunging breakers is presented by (*Shore Protection Manual*, 1984):

$$x_p = (4.0 - 9.25 \cdot m) \cdot H_b \tag{2.4}$$

In which x_p is the breaker travel distance, m is the foreshore slope and H_b is the breaker wave height which can be calculated from the graph (i.e. see figure 2.7b) using the the deep water wave height and steepness if the nearshore slope is known. If the crest width of the structure is longer than the breaker travel distance calculated using equation 2.4 it can be reasoned that almost all incoming waves will break on the crest of the structure, which can indicate an optimal crest width related to energy dissipation by wave breaking.

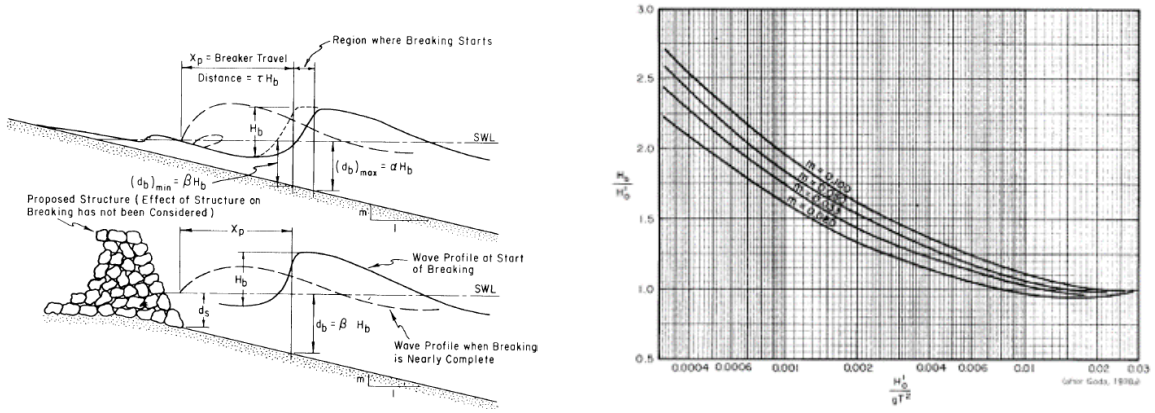

(a) (b)

Figure 2.7: a. Definition sketch of breaker height and breaker travel distance. b. Graph to calculate the breaker height depending on offshore wave characteristics. Both adopted from (*Shore Protection Manual*, 1984)

2.4. Wave-induced water level set-up

Wave-induced water level set-up at the lee side of a low-crested structure is an increase of the water-level relative to SWL. It is induced by a combination of wave momentum release due to wave breaking and the conservation of mass transport of water over the crest by overtopping and through the structure by porous flow. These processes in combination with a usually impermeable shoreline (e.g. a beach or a sea wall) result in accumulation of water at the lee side of the structure. This increase in waterlevel behind the structure induces pressure differences (hydraulic head) over the structure that result in flow. The magnitude of the flow depends on the flow resistance in the direction of the flow (Calabrese et al., 2008). For a 2D situation (i.e. a continuous alongshore LCS) water level set-up can be restored by water flowing over the crest of the LCS (usually cyclic due to waves going over the crest in opposite direction) and through the core of the LCS (which largely depends on the flow resistance of the LCS). The additional increase in water level is found to play a key role in the erosive processes of sea bed material behind LCS Calabrese et al. (2008). Moreover, the increase in SWL effectively reduces the freeboard of structures behind the LCS an therefore results in larger overtopping events for the same wave characteristics.

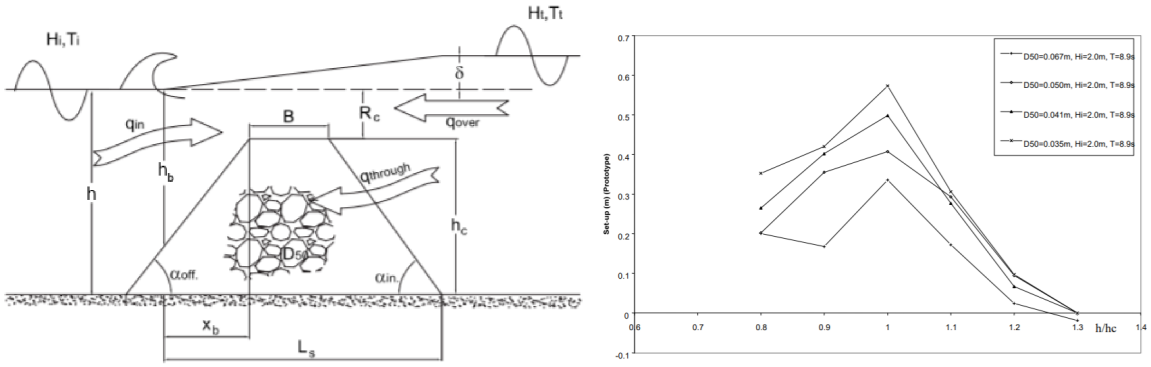

(a) (b)

Figure 2.8: a. Governing parameters for wave-induced water level set-up, adopted from (Soldini et al., 2009). b. Effect of structure crest level and nominal diameter on water level set-up. Adopted from (Loveless et al., 1998)

The most important parameter related to water level set-up is the crest freeboard (R_c) which has a large influence on the wave breaking processes on the structure and the water restoring capacity. Other important parameters are the porosity of the structure and crest width. Figure 2.8a presents the most used structural and hydraulic parameters that are used in literature studies to describe the wave-induced water level set-up phenomena. Table 2.2 presents the most used empirical wave-induced water level set-up formulas for 2DV situations in engineering practice and their validity ranges. Most empirical formulas are based on conducted physical model experiments but also theoretical approximations are included. For a more in depth review and origin of these empirical formulas, the reader is referred to appendix A.

Table 2.2: Relevant literature regarding water level set-up behind low-crested structures

Author	Formulae	Validity range
(Longuet-Higgins, 1967)	$\delta = \frac{H_i^2(1+K_R^2)k_1}{8\sinh(2k_1h_1)} - \frac{H_i^2K_t^2k_2}{8\sinh(2k_2h_2)}$	
(Diskin et al., 1970)	$\frac{\delta}{H_i} = 0.6 \cdot \exp\left[-\left(0.7 - \frac{R_c}{H_i}\right)^2\right]$	$-2.0 < R_c/H_i < 1.5$ $0.10 < h/H_i < 0.83$
(Loveless et al., 1998)	$\frac{\delta}{B} = \frac{\left(\frac{H_iL}{hT}\right)^2}{8gD_{n50}} \exp\left[-20\left(\frac{R_c}{h_c}\right)^2\right]$	
(Calabrese et al., 2003)	$\delta = \delta_{mf} + \delta_c$ $\delta_{mf} = 0.5\left(-b + (b^2 - 4c)^{0.5}\right)$ $\delta_c = \frac{\left(\frac{1}{16}H_i^2\sqrt{\frac{g}{h}}\right)^2}{400\lvert R_c\rvert^{10/3}} \cdot B + h_c\,\mathrm{ctg}(\alpha_{off})$ $b = (2h - a)$ $a = \left(1 + \frac{x_b+B}{L_s}\right)h_c - \frac{x_b}{L_s}(h_b + R_c)$ $c = -\frac{3}{16}H_i^2\left(1 - K_t^2\right)$ $h_b = h^{0.2}\left(\frac{H_i}{0.56e^{3.5\tan(\alpha_{off})}}\right)^{\frac{4}{5}}$	

Work of (Loveless et al., 1998) did not explicitly include the effect of porosity of the structure. However, they report the effect of the nominal diameter on the wave-induced water level set-up which can be used as a crude approximation of the effect of porosity. Figure 2.8b presents the effect of both

relative freeboard and nominal diameter. From this figure water level set-up is found to be maximum for crest levels around SWL and reduces for emergent and submerged structures.

2.5. Seiching

Seiches are long-period standing oscillations in an enclosed basin or in a locally isolated part of a basin (Rabinovich, 2009). These type of free surface oscillations in basins like harbours, lakes or the sloshing effect in coffee cups are directly related to the natural resonant periods of the basin and can result in enhanced overtopping near the boundaries of the system (e.g. sea wall in this research). The eigen frequencies (periods) of the seiching motion are a fundamental property of a particular basin depending on the depth and the geometry of the basin and are independent of the external forcing. The amplitude of the oscillations on the other hand strongly depend on the external forcing. Resonance occurs when the dominant frequencies of the external forcing match the eigen frequencies of the basin. Resonance influences the individual overtopping events due to an increase in temporal water level set-up by this enhanced low-frequency motion.

2.5.1. Theoretical assessment

The theory behind seiche oscillations is similar to theory related to free and forced oscillations of mechanical, electrical and acoustical systems (Rabinovich, 2009). Free oscillations occur at the natural frequency of the system when it is disturbed beyond its equilibrium. The system responds by developing a restoring force to re-establish the equilibrium. Without additional forcing, these free oscillations exponentially reduce in amplitude due to energy dissipation until equilibrium is restored. In case of periodic forced vibrations the system responds with amplitudes depending on the friction of the system and the proximity of the frequency of the forcing to the natural frequency of the system. In case the frequency of the forcing is within close proximity of one of the natural frequencies of the system, resonance can occur (Rabinovich, 2009).

In order to derive the eigen frequencies of the basin, the trigonometric function which describes a standing wave within an enclosed basin can be used. This function is valid for a closed, long and narrow non-rotating rectangular basin of length (L_{basin}) and water depth (h) and is given by Rabinovich (2009) as:

$$\zeta(x,t) = A\cos(kx)\cos(\omega t) \tag{2.5}$$

In here ζ is the free sea level elevation, A is the wave amplitude, x is the along-basin coordinate, t is time, $k = 2\pi/\lambda$, λ is the wave length, $\omega = k \cdot c$ is the angular wave frequency, $T = \lambda/c$ is the wave period, g is the gravitational acceleration and c is the long wave phase speed $c = \sqrt{gh}$. Using the no flow boundary condition at both ends of the basin ($x = 0$ and $x = L_{basin}$) results in the following wave numbers:

$$k = \frac{\pi}{L_{basin}}, \frac{2\pi}{L_{basin}}, \frac{3\pi}{L_{basin}}, ..., \frac{n \cdot \pi}{L_{basin}} \tag{2.6}$$

in which n is an integer corresponding to the modes presented in figure 2.9 for a closed basin. The fundamental mode (n=1) is anti symmetric and has a wave length equal to twice the length of the basin. Higher modes have a wave length equal to one half, one third etc. of the fundamental mode. In figure 2.9, the different resonance modes for both a fully enclosed basin and a partially enclosed (open ended) basin are presented. Using equation 2.6 and the relations for the angular frequency, the long wave speed and wave number the well known Merian's formula for the eigen periods of natural resonance modes in a rectangular closed basin of uniform depth can be derived, which is given as (Rabinovich, 2009):

$$T_n = \frac{2 \cdot L_{basin}}{n \cdot \sqrt{gh}} \tag{2.7}$$

The fundamental mode corresponding to n=0 has the largest period, and the higher frequencies (overtones) have shorter periods. All the odd modes corresponding to a closed basin are anti symmet-

ric while even modes show symmetric behaviour.

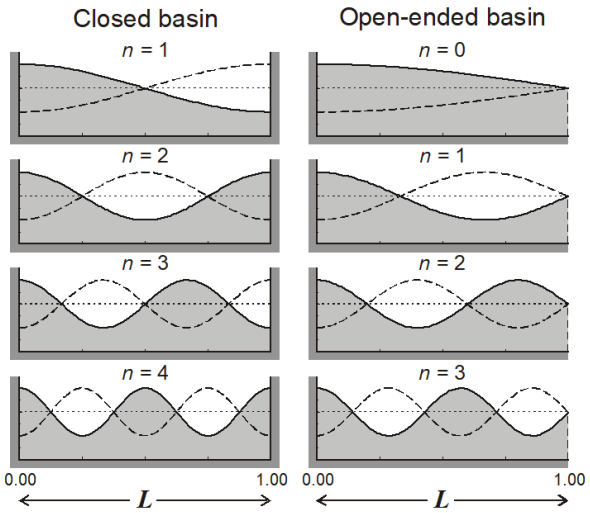

Figure 2.9: Surface profiles for the first four seiche modes in closed and open-ended rectangular basins of uniform depth, adopted from (Rabinovich, 2009)

2.6. Wave overtopping

Wave overtopping is a wave structure interaction where waves pass over the crest of the structure in the form of a continuous sheet of water, plumes or splashes. Wave overtopping is an extremely complex and non uniform process. Sea walls are often fronted by shallow water which might expose these structures to breaking waves (impulsive conditions). A distinction in calculation procedure is made for impulsive wave breaking conditions and non-impulsive conditions. On steep walls with relatively small waves in relation to the local water depth non-impulsive conditions prevail. Under these conditions the waves are not significantly influenced by the structure toe or foreshore. The overtopping waves run up and over the wall which give rise to smoothly varying loads and green water overtopping. Impulsive conditions occur when waves are relatively large in relation to the local water depth. The waves might shoal over the foreshore or toe of the structure and some waves break violently on the structure. This will cause large impulsive loads and a violent up-rushing jets of water and splashing overtopping.

Most of the time average overtopping discharges are used for the design assessment of coastal structures. The coastal structures and the drainage system of the hinterland have to be able to withstand certain amounts of overtopping without structural damage or flooding. There are several empirical formulas and neural networks developed during large scale funded projects to estimate mean overtopping discharges under varying structural and hydraulic parameters. During the Crest Level Assessment of Coastal Structure by full scale monitoring neural network prediction and Hazard analysis on permissible wave overtopping (CLASH) a database of 10532 tests from 163 independent test series on wave overtopping by means of 31 parameters was set-up (Steendam et al., 2004). The intention of this database was the use for the development of a neural network that could predict overtopping discharges at all sorts of coastal structures.

There is also a variety of empirical formula based on physical model tests to predict overtopping discharges. These empirical formulas have different ranges of applicability and use different parameters based on different hydraulic or structural conditions. The most used empirical formulas used in the engineering industry are described in the Eurotop manual (Van der Meer et al., 2018). In figure 2.10 the definition sketch is given for wave overtopping of a steep vertical wall as investigated in this research.

For vertical walls without a mound structure in front, **impulsive** conditions ($h^2/H_{m0}L_{m-1,0} < 0.23$)

prevail. The mean overtopping discharge using the mean value approach can be predicted by eq. 7.7 and 7.8 from the Eurotop Manual. These equations differ in the adopted crest freeboard of the sea wall. Equation 7.7 for from the Eurotop is given as (Van der Meer et al., 2018) :

$$\frac{q}{\sqrt{gH_{m0}^3}} = 0.011\left(\frac{H_{m0}}{hs_{m-1,0}}\right)^{0.5}\left(e^{-2.2\frac{R_c}{H_{m0}}}\right) \tag{2.8}$$

This equation is valid for $0 < R_c/H_{m0} < 1.35$. For the design overtopping rate the factor 0.011 should be added with one standard deviation which results in the factor 0.0155. For $R_c/H_{m0} > 1.35$ the mean overtopping discharge for **impulsive** conditions can be calculated using equation 7.8 of the Eurotop which is given as:

$$\frac{q}{\sqrt{gH_{m0}^3}} = 0.0014\left(\frac{H_{m0}}{hs_{m-1,0}}\right)^{0.5}\left(\frac{R_c}{H_{m0}}\right)^{-3} \tag{2.9}$$

This equation is valid for $R_c/H_{m0} > 1.35$. For the design overtopping rate the factor 0.0014 should be added with one standard deviation which results in the factor 0.0020. The use of $s_{m-1,0}$ for impulsive conditions results in more weight for the longer wave periods in the spectral domain.

On the other hand, for vertical walls under **non-impulsive** conditions ($h^2/H_{m0}L_{m-1,0} > 0.23$) the mean value approach overtopping discharge can be predicted by eq. 7.5 from the Eurotop Manual which is given as (Van der Meer et al., 2018):

$$\frac{q}{\sqrt{gH_{m0}^3}} = 0.05\left(e^{-2.78\frac{R_c}{H_{m0}}}\right) \tag{2.10}$$

This equation is valid for $0 < R_c/H_{m0} < 2.8$. For the design overtopping rate the factor 0.05 should be added with one standard deviation which results in the factor 0.062 and the factor -2.78 should be replaced with the factor -2.61.

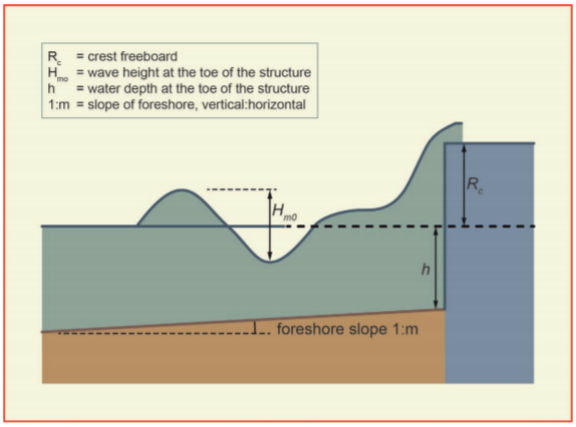

Figure 2.10: Definition sketch for assessment of overtopping at plain vertical walls (Van der Meer et al., 2018)

2.7. Conclusion

There are no integrated design formulas for the prediction of overtopping discharges using a detached structure to protect vertical coastal structures. Only prediction formulas exist for the evaluation of the effect of various separate wave structure interactions for rubble mound structures. For the use of HLCS J. Medina et al. (2019) presented a prediction formula for wave transmission over cubipod HLCS however in here only the crest freeboard is used as input parameter. The effect of crest width on wave transmission and the effect of HLCS on water level set-up behind the structure is still unknown. On the other hand more widely applicable separate prediction formulas exist for rubble mound structures. However using these separate formulas the effect of HLCS cannot be evaluated as important structural

parameters separating HLCS from conventional rubble mound structures (i.e. porosity) are missing. Some prediction formulas include porosity using the nominal diameter of the elements however the applicability using this method is questionable for the large artificial concrete elements found in the HLCS used in this research. Overall the applicability of separate design formulas to predict overtopping discharges for these types of complex hydrodynamic systems is questionable and the use of CFD simulations can be very use full. However the modelling of hydrodynamic behaviour of HLCS using large artificial concrete elements in OpenFOAM still forms a niche.

2.7.1. Hypotheses

Based on the lacking empirical prediction formulas for the prediction of overtopping discharges using HLCS in front of a sea wall hypotheses have been drafted for the different hydrodynamic characteristics eventually leading to overtopping. Hypotheses related to differences between HLCS and conventional rubble mound LCS including a core and armour layer are elaborated. Additionally the effect of the main geometrical parameters are also included.

Wave transmission

All literature studies of wave transmission that have been reported in table 2.1 are based on conventional rubble mound LCS with a core and armour layer. Compared to conventional rubble mound LCS, HLCS have a different internal geometry. Consequently the values for porosity, roughness of the elements and nominal diameter (D_{n50}) are not comparable. Increasing the porosity of the structure results in different wave breaking behaviour on the crest according to Hattori & Sakai (1994). The amount of energy dissipation by wave breaking increases for larger crest width as continuous wave breaking is expected over the crest which in turn reduces the amount of transmitted energy. Furthermore as noted by (Buccino & Calabrese, 2007), a higher porosity results in enhanced energy transmission through the structure which increases the amount of wave transmission. Concluding, for HLCS compared to conventional LCS more wave transmission is expected by both differences in wave breaking and porous flow.

For increasing crest width, the amount of wave transmission is expected to reduce which also holds for increasing crest height of the HLCS. The combined effect of enhanced wave breaking on the crest of the structure and the increased resistance of the flow through the porous structure results in more energy dissipation. More energy dissipation leads to less wave transmission. For increasing freeboard of the structure a reduction in energy going over the structure is expected which reduces the amount of wave transmission by overtopping. Moreover, increasing the crest height of the structure results in more energy going through the structure. Additionally maintaining the same structure slope also increases the cross-sectional area of the structure for increasing crest height which increases the resistance of the flow that goes through the structure. The exact effect of the trade off between the enhanced dissipation by porous flow or the reduced dissipation by wave breaking is not known. For differences in basin length a constant wave transmission is expected because no changes are made to the HLCS itself resulting in no differences in the dissipation processes.

Wave-induced water level set-up

The effect of using HLCS compared to conventional LCS is that the wave-induced water level set-up is expected to reduce. The amount of wave-induced water level set-up depends on the amount of wave momentum that is released by wave breaking and the restoration capacities of the excess water at the lee side of the LCS. Important parameters are the freeboard of the LCS and the porous ability of the LCS to restore the water level set-up by water flowing trough the structure. Following observations by (Hattori & Sakai, 1994), increased porosity reduces the wave-induced water level set-up because less wave breaking is expected due to the shift in location of incipient breaking. Secondly, increased porosity is expected to have better water level restoring capacity (higher permeability) and therefore reduces the wave-induced water level set-up Calabrese et al. (2008); Zanuttigh et al. (2008).

For increasing crest width the amount of water level set-up is expected to increase due to the increase of wave breaking on the crest of the structure which results in more momentum release and

thus more water level set-up within the basin. Also increasing the crest width increases the resistance of back flow through the structure which also results in more water level set-up. Additionally for increasing crest height of the structure the water level set-up is expected to increase due to enhanced wave breaking on the slope of the structure but more importantly a reduced cross section available for back flow. However according to Loveless et al. (1998) the water level set-up is largest for zero freeboard of the structure. For crest height larger than SWL less water overtops the structure which reduces the set-up. For varying basin length the mean water level set-up is expected to be lower for larger basin length. Due to the available storage volume inside the basin a reducing speed at which the set-up increases is expected which reduces the mean water level set-up. This however also depends on the structural characteristics of the HLCS which determine the restoring abilities.

Overtopping

Ultimately an increase/decrease of expected overtopping discharges results from the combined effect of all hydrodynamic characteristics. Wave transmission, water level set-up and additional basin hydrodynamic (e.g. seiching and resonance) within the basin can result more overtopping.

For an increase in crest width less wave transmission yet a higher water level set-up is expected. For an increase in structure height an optimum is expected between the amount of wave transmission and the water level set-up. The wave transmission is expected to reduce for larger crest height whereas the mean water level set-up is expected to have an optimum for a crest height around SWL. It is expected that the reduction in wave transmission weighs more than the increase in water level set-up. Therefore less overtopping for increasing crest width is expected and less overtopping for increasing crest height is expected. The effect of the basin length is expected to be small due to the homogeneous water level-setup behind the HLCS. Moreover wave transmission is also almost independent on the basin length for constant water depth due to the small resistance of the sea bed which affects the transmitted waves. Only for wave breaking within the basin (e.g. for wave breaking on a perched beach), a reduction of overtopping is expected. However, if the eigen frequencies of the basin coincide with the forcing frequency of the waves, resonance of seiching behaviour can start to play a role (see chapter 2.5). It is expected that resonance of seiching behaviour considerably increases the expected overtopping discharges.

(This page is intentionally left blank)

3

Cubipod physical model experiments

3.1. Introduction

The numerical model set-up used in this research is based on the performed 2D physical model experiments described in J. Medina et al. (2019); Odériz et al. (2018). The scale of the conducted experiments is 1/37.5 (i.e. $n_L = 37.5$). In this section the performed physical model experiments at Instituto de Ingenieria of the Universidad Nacional Autónoma de México (II-UNAM) in Mexico are introduced. The physical wave flume set-up is explained and the used hydrodynamic- and cubipod characteristics are elaborated. Three types of structures were examined, 1, 3 and 5 layers of cubipods. This chapter mainly focuses on the experiments conducted for the 5 layer cubipod HLCS used for the calibration and validation of the OpenFOAM model.

3.2. Experimental set-up

The wave flume at II-UNAM is 29 m long, 0.4 m wide and 0.59 m deep. During the physical model experiments 20 minute long irregular wave trains (JONSWAP spectrum with a peak enhancement factor $\gamma = 3.3$) were generated. A piston-type wave generation system equipped with a dynamic wave absorption system is used. Each HLCS that has been tested was placed on a $0.1m$ elevated horizontal platform with a foreshore slope of 2% (i.e. $m = 0.02$). A total of 8 wave gauges were installed in the flume measuring the free surface elevation at a frequency of $100Hz$. Of these 8 wave gauges, three wave gauges were placed in front of the HLCS to measure the wave reflection and three wave gauges were placed behind the HLCS to measure the wave transmission. Also one wave gauge was placed just behind the wave paddle to measure the generated waves and one wave gauge on top of the crest of the HLCS. A passive absorption gravel beach was placed at the end of the flume to prevent wave reflection interference. The used cubipod units have a mass density ρ_c of $2280kg/m^3$ and a nominal diameter D_{n50} of $4.35cm$.

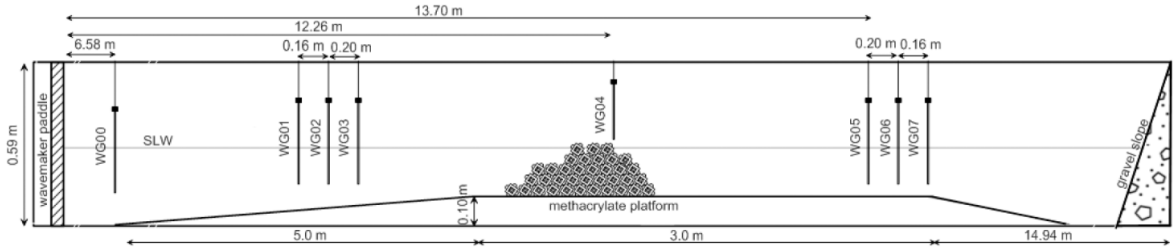

Figure 3.1: Longitudinal cross-section of wave flume used for the cubipod experiments, adopted from Odériz et al. (2018)

From a top-view, the cubipods were placed in a triangular grid configuration as presented in figure 3.2b. The positioning of the cubipod grid is described based on the mean distance between subsequent cubipods measured in D_{n50}. The mean distances between F-lines and C-lines are $1.27D_{n50}$ and

$1.58D_{n50}$ respectively. From side view the 5 layered structure has lines of $11, 9, 7, 5$ and 3 cubipods per layer, also presented in figure 3.1.

3.3. Experimental characteristics

The range of tested hydraulic and structural boundary conditions are significant wave heights ($H_{s,i}$) in the range of 4.50-11.60cm, a spectral peak period ($T_{p,i}$) ranging from 1.27-1.91s and a structure freeboard (R_c) ranging from -1.0 - 4.0cm. The structure freeboard is defined as the distance from the water level to the crest of the structure. A positive freeboard resulting in an emergent structure and negative freeboard in an submerged structure respectively. Figure 3.2a presents the obtained wave transmission results from the experiments compared to the estimation of the transmission coefficient using the formula derived by D'Angremond et al. (1996) for conventional rubble mound structures. For 1 and 3 layer cubipod structures a reduction in wave transmission trend is observed for increasing structure height. The 5 layer cubipod structure however predicts a constant wave transmission coefficient for emergent structures. Wave transmission coefficients found for those experiments show a wave transmission coefficient independent of the crest freeboard for $R_c > 0$.

Extracted wave transmission coefficients reported in J. Medina et al. (2019) are used to calibrate the OpenFOAM model based on statistical validation. From figure 3.2a the measured transmission coefficients corresponding to the experiments for a 5 layer cubipod HLCS are extracted using a data extracting algorithm. From these transmission coefficients the transmitted wave height is calculated using $K_t = H_{s,t}/H_{s,i}$. Table 3.1 presents the conducted experiments for the 5 layer cubipod HLCS and the complementary extracted wave transmission coefficients.

Table 3.1: Experimental characteristics of structure B with corresponding extracted wave transmission coefficients

Test ID	$H_{s,i}[cm]$	$T_{p,i}[s]$	$R_c[cm]$	$R_c/H_{s,i}$	$K_{t,extracted}$	$H_{s,t}[cm]$
B5bLH	4.50	1.27	4.00	0.89	0.58	2.60
B5bLM	5.00	1.27	3.00	0.60	0.53	2.60
B5bLL	4.90	1.27	1.00	0.20	0.60	2.90
B5bMH	9.80	1.63	4.00	0.41	0.58	5.70
B5bMM	9.90	1.71	1.00	0.10	0.47	4.70
B5bML	10.30	1.71	-1.00	-0.10	0.53	5.50
B5bHH	10.40	1.91	4.00	0.39	0.48	5.00
B5bHM	10.30	1.91	1.00	0.10	0.55	5.70
B5bHL	11.60	1.91	-1.00	-0.09	0.60	7.00

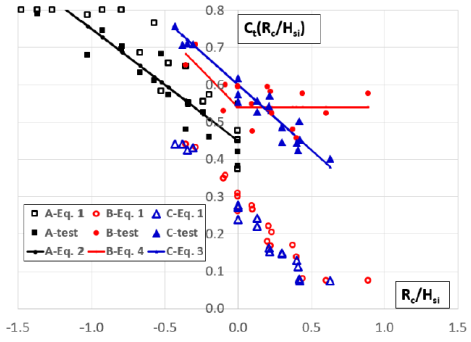

(a)

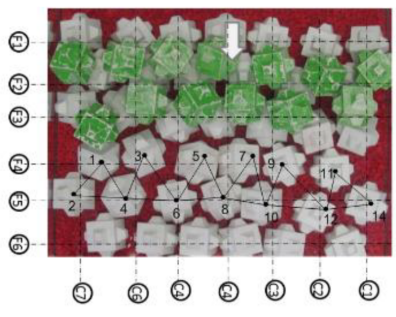

(b)

Figure 3.2: a. Measured coefficient of transmission Ct (full symbols) of the 1 layer cubipod structure (black), 3 layer cubipod structure (blue) and 5 layer cubipod structure (red) compared with estimated Ct from D'Angremond et al. (1996) valid for conventional LCS (open symbols) and the newly derived transmission formula by J. Medina et al. (2019) for cubipod HLCS (solid lines). b. Forward triangular-type placement grid for the cubipod HLCS. The white arrow indicated the direction of the incoming waves. Adopted from Odériz et al. (2018)

4 Numerical model

4.1. Introduction

The use of CFD for engineering applications is of great interest as physical modelling is expensive and can be time consuming. By simulating a wave flume on a computer, geometrical shapes can be easily adapted and detailed information can be extracted at every location in the numerical grid which can stimulate and accelerate different design iterations. This section describes the basic principles (i.e. mathematical equations, theoretical principles, numerical methods) of CFD modelling using Open source Field Operation And Manipulation (OpenFOAM) and various other software additions used in this research including the coupling with OceanWave3D. First the numerical framework is addressed in which the various OpenFOAM software packages (i.e. additions) are discussed as well as the advantage of coupling with OceanWave3D. Additionally the hydrodynamic equations (i.e. the RANS and Volume Averaged Reynolds Averaged Navier-Stokes (VARANS) equations), the implementation of porous structures using the extended Darcy-Forchheimer equation, handling turbulence, the Volume Of Fluid (VOF) method to track the free water surface, the generation and absorption of free surface water waves and the ability to extract wave forces and overtopping volumes in OpenFOAM are discussed.

4.2. Numerical framework

The numerical framework that is used in this research is composed of various packages (i.e. additions) of OpenFOAM which is coupled to OceanWave3D and results in an advanced numerical framework able to solve complex coastal wave structure interactions while being numerically attractive.

The core of the used numerical framework is the OpenFOAM toolbox (foam-extend 3.1), which is an open-source CFD C++ library provided by a general public license (GNU). The OpenFOAM toolbox contains a method for solving two-phase free surface Newtonian fluids using the RANS equations coupled with a VOF method. With this method OpenFOAM can track magnitudes of pressures and velocities in any point of the grid and is therefore able to model overturning and breaking waves. OpenFOAM first suffered from the inability to accurately generate and absorb free surface waves. This problem has been resolved in Jacobsen et al. (2012) in which the plug-in waves2Foam toolbox was developed. This toolbox allows the generation and absorption of free surface water waves using wave relaxation zones. Consequently this opened up the possibility to use these relaxation zones for coupling of different wave generation models (e.g. OceanWave3D) to OpenFOAM, increasing numerical efficiency. Additionally to use OpenFOAM for coastal engineering applications the ability of OpenFOAM to model the interaction of free surface waves with permeable coastal structures was implemented by (Jensen et al., 2014), who transformed the RANS equations in the waves2Foam toolbox. The transformation was achieved by volume averaging the momentum equation and solving the additional resistance terms using an extended Darcy-Forchheimer equation.

All these additions (e.g. waves2foam, coupling to OceanWave3D, permeable interactions) to the core OpenFOAM toolbox allow the coastal engineering community to use detailed CFD to model

the coastal zone environment. Additionally several non open source Joint Industry Project (JIP) improvements (i.e. tools and processing utilities) developed during the JIP CoastalFOAM program, are compiled with the wave2Foam toolbox. The JIP CoastalFOAM is a collaboration between Van Oord, Boskalis, Royal HaskoningDHV and Deltares. The ambition of this JIP is to validate and expand the use of OpenFOAM as a coastal engineering design tool. The additional JIP improvements for example are related to improvements of the numerical schematization of structures and the implementation of a method to extract wave forces under impulsive conditions, referred to as the ventilated boundary condition. A lot of progress has been made over the last years in validating and improving OpenFOAM as a design tool. OpenFOAM, in combination with the waves2Foam toolbox, has already been validated for the ability to model free surface water waves and their interactions with permeable coastal structures on wave overtopping, wave reflection, wave damping, wave forces, and sediment transport in open granular filters. For more information on these topics the reader is referred to research work described in (Higuera et al., 2014a,b; Jacobsen et al., 2018, 2017, 2015; Jensen et al., 2014) and more.

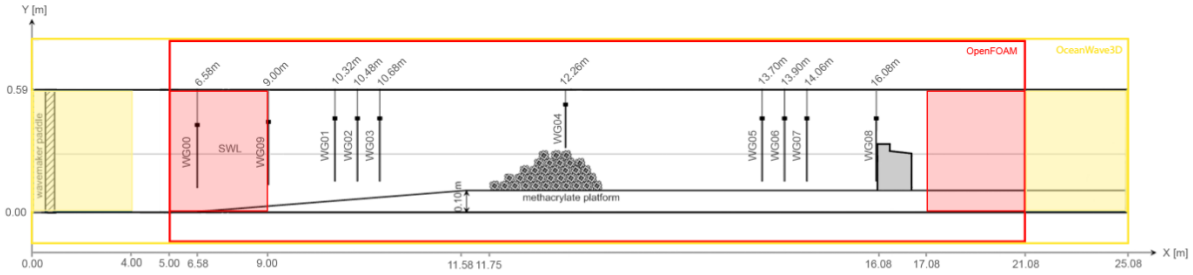

Figure 4.1: Numerical flume layout with nested OpenFOAM domain within the OceanWave3D domain

4.2.1. Coupling with OceanWave3D

In this research the waves are generated by OceanWave3D and applied at the OpenFOAM inlet relaxation zone as boundary condition. This results in numerical flume where a OpenFOAM domain is nested within a larger OceanWave3D domain, visualised in figure 4.1. The main reason of using OceanWave3D is that this creates a more numerically attractive solution by the different numerical methods that both models use.

OceanWave3D is developed by Engsig-Karup et al. (2009) in Denmark and is a wave transformation model based on potential wave theory. It can compute fully nonlinear three-dimensional water waves under validity of the potential flow theory (see section A.4.1) and is therefore not able to model wave overturning, wave breaking and porous flow interaction. However, potential flow solvers are orders of magnitude faster than Navier-Stokes/VOF solvers like OpenFOAM (Paulsen et al., 2014) which combined with the the introduction of the wave relaxation zones in the waves2foam toolbox opened up possibility to achieve a more computational efficient solution by using a coupled OceanWave3D/OpenFOAM approach. If OpenFOAM is used along the entire domain from the wave paddle to the structure the computational time is very large. Therefore it is computationally interesting to model the offshore waves from the paddle to the vicinity of the coastal structure using OceanWave3D where the potential flow assumption is valid and couple OceanWave3D to the OpenFOAM model which then describes the complex wave breaking and wave structure interactions around the coastal structure(s).

The coupling between OceanWave3D and OpenFOAM is implemented in the waves2Foam toolbox using the relaxation zones technique described by Paulsen et al. (2014). For the mathematics and details behind the coupling the reader is referred to section 4.6. For more detailed information on the use of OceanWave3D and the mathematical equations behind OceanWave3D to generate, transform and absorb free surface water waves the reader is referred to (Engsig-Karup et al., 2009).

4.3. Reynolds-averaged Navier Stokes equations

In OpenFOAM version foam-extend-3.1 the RANS equations are implemented for the hydrodynamic computations of flow velocities and pressures for two-phase flow. These equations are based on the Reynolds averaging process which decomposes the time series of turbulent fluctuations into a mean parameter value and a random fluctuation. The flow velocity and pressure are separated in a time averaged component and a turbulent component which in equations is presented by $u = \bar{u} + u'$ and $p = \bar{p} + p'$. This procedure however introduces additional terms (i.e. Reynolds stresses) in the momentum equation which have to be dealt with. This can be done by a turbulence model of choice (e.g. $k-\epsilon$, $k-\omega$, RNG). The RANS equations are used for CFD computations in OpenFOAM because solving the short turbulent fluctuations comes at a very high computational cost and this detailed information on turbulent fluctuations is not important for most engineering purposes.

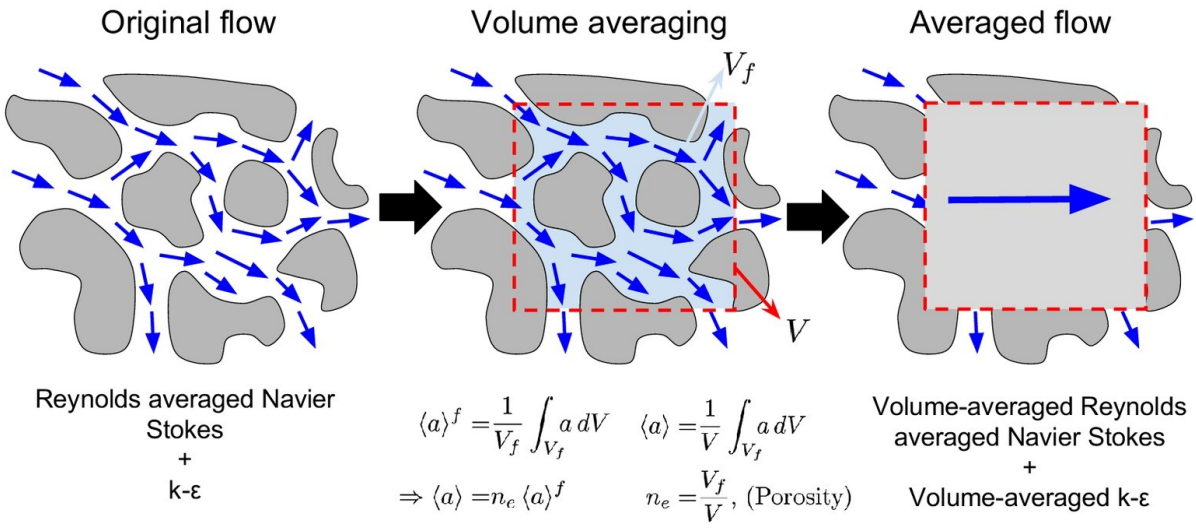

Figure 4.2: Volume averaging method, adopted from Losada et al. (2016)

The RANS equations do not allow to solve the hydrodynamics (i.e. flow velocities and pressures) inside porous structures. For coastal engineers the interaction of porous structures with the hydrodynamics is of great interest for the design of coastal structures (e.g. breakwaters, scour protection and permeable sea bottoms). The most intuitive way to solve flow through a porous material is the microscopic approach in which each element of the porous structure is individually assessed. This technique however requires advanced techniques to determine the actual geometry of the porous structure and this level of detail also comes at a high computational costs. This microscopic approach is not practical for coastal engineering applications, and a macroscopic approach seems more functional since the bulk parameters of the structure are of greater interest for coastal engineers Losada et al. (2016). A macroscopic approach based on a description of bulk parameters is introduced by (Jensen et al., 2014) in the so called VARANS equations. The VARANS equations consider the porous media to be continuous and characterized by its macroscopic properties instead of a detailed description of the complex internal geometry Losada et al. (2016). Volume averaging of the RANS equations result in replacing the velocity in the filter velocity, which describes the average direction and magnitude of the velocity in the control volume of the porous structure, visualised in figure 4.2. However these adaptations to the momentum equation result in additional resistance terms which are solved using the extended Darcy-Forchheimer equations, described in section 4.4.

The VARANS equations have been validated for various coastal structures and their applications by (Jacobsen et al., 2015), (van Gent, 1995) and others. The VARANS equations as presented by (Jensen et al., 2014) are given in equation 4.1 and 4.2 as:

$$\left(1 + c_p\right)\frac{\partial}{\partial t}\frac{\rho \mathbf{u}}{n_p} + \frac{1}{n_p}\nabla\frac{\rho}{n_p}\mathbf{u}\,\mathbf{u}^T = -\nabla \mathrm{p}^* + \mathbf{g}\cdot\mathbf{x}\nabla\rho + \frac{1}{n_p}\nabla\cdot\mu\nabla\mathbf{u} - \mathbf{F}_p \tag{4.1}$$

$$\nabla \cdot \mathbf{u} = 0 \tag{4.2}$$

Where C_m is the added mass coefficient, t is time, ρ is the density of the fluid, **u** is the vector of the filter velocity in cartesian coordinates, n_p the porosity, $\nabla = (\partial/\partial x, \partial/\partial y, \partial/\partial z)$ is the differential operator, $p* = p - \rho \mathbf{gx}$ is the excess pressure, p is the total pressure, **g** is the vector of acceleration due to gravity, $x = (x, y, z)$ is the Cartesian coordinate vector, μ is the dynamic viscosity and $\mathbf{F}_p$ represents the flow resistance due to the interaction with the porous structure. In the next section (section 4.4) the resistance term $\mathbf{F}_p$ is elaborated.

4.4. Flow resistance

The resistance term introduced by the VARANS equations for the interaction of flow with the porous structure needs to be quantified and parameterized in order to become practical. This is done in this research using the parameterization of van Gent (1995). However first the theoretical principles behind flow through porous structures are explained.

Porous structures are permeable structures that allow flows induced by waves and currents to pass through. The flow that flows trough a porous structure experiences friction from the interaction with the solids inside the porous structure. This interaction is quantified using empirical formulas that describe the friction of the flow depending on various hydraulic and structural parameters and empirical coefficients. Therefore the success of the modelling largely depends on the used empirical formulas and empirical coefficients (Losada et al., 2016). The classical formulation used in modelling practice is known as the extended Darcy-Forchheimer equation which uses a combination of inertial and drag forces for non-stationary flow conditions to describe a hydraulic gradient that can be used to assess the amount of friction. The extended Darcy-Forchheimer equation is presented in equation 4.3:

$$I = a_p u^d + b_p u^d \mid u^d \mid + c_p \frac{\partial u^d}{\partial t} \tag{4.3}$$

In which I is the hydraulic gradient and a_p, b_p and c_p are empirical coefficients related to the porous flow conditions. The first two terms represent the drag forces and the last term represents the inertia force of the flow. The drag force is subdivided in a linear component to account for the viscous forces and a nonlinear component to account for turbulent fluctuations. For very low Reynolds numbers, the linear component dominates and the nonlinear component does not influence the total flow resistance. The opposite is the case for high Reynolds numbers, which is most common for the interaction of waves with porous coastal structures.

In van Gent (1995) a parameterization for a_p and b_p has been derived based on the extended Darcy-Forchheimer equation. In here the hydraulic gradient, as presented in equation 4.3, is used to describe the flow resistance term ($\mathbf{F}_p$) in the VARANS equations (i.e. in equation 4.1. This parameterization is the most extended and used parameterization found in coastal engineering applications and is therefore also adopted in this research. The flow resistance term as adopted in the momentum equation is given as:

$$\mathbf{F}_p = a_p \rho \mathbf{u} + b_p \rho \|\mathbf{u}\|_2 \mathbf{u} \tag{4.4}$$

In here a_p and b_p are drag force resistance coefficients which according to the parameterization by van Gent (1995) are given as:

$$a_p = \alpha \frac{\left(1 - n_p\right)^2}{n_p^3} \cdot \frac{\mu}{\rho D_{n50}^2} \tag{4.5}$$

$$b_p = \beta \left(1 + \frac{7.5}{\mathrm{KC}}\right) \cdot \frac{1 - n_p}{n_p^3} \frac{1}{D_{n50}} \tag{4.6}$$

Where D_{n50} is nominal diameter of the porous layer, n_p is the porosity of the porous layer, KC is the Keulegan-Carpenter number and α and β are closure coefficients. In agreement with the originally derived parametrization of van Gent (1995) the nominal diameter D_{n50} is used in contrary to the D_{50}

adopted by Jensen et al. (2014).

The α and β are the empirical porous media drag coefficients used in equation 4.5 and 4.6. The α and β coefficients depend not only on the material properties like grading, shape, aspect ratio and orientation but also on the flow regime within the porous structure. The determination of α and β is traditionally done based on one of three approaches:

1. Based on a best fit using experimental data from laboratory experiments.
2. Based on analytical considerations.
3. Using calibration based on numerical computations.

Originally van Gent (1995) derived these values using laboratory experiments as $\alpha = 1000$ and $\beta = 1.1$, and reported ranges of $0 < \alpha < 2780$ and $0.36 < \beta < 1.33$ to account for different material properties. However, there is no predictive methodology to determine α and β coefficients in advance for various material properties, and flow regimes so calibration has to be performed as was noticed by (del Jesus et al., 2012). This results in a large range of α and β values found in literature, based on various approaches, structure and material types and flow conditions. Also not one combination of α and β exist but multiple different combinations of α and β can be used resulting in similar behaviour (Jensen et al., 2014). In Losada et al. (2016) a detailed summary of all proposed literature values of α and β is presented. However, the authors note that more study should be conducted on how the shape and nature (natural rocks or artificial armour units) affect the drag forces and therefore the closure coefficients.

The KC number describes the relative importance of drag and inertia forces on a object under oscillatory flow. It is included by van Gent (1995) to account for the effect of oscillatory flow (i.e. cyclic wave action) on the flow boundary layers and small eddies that are formed and continuously destroyed on the interface of the flow with the porous structure. This destruction requires an extra amount of momentum which is larger if the flow is inertia dominated related to the turbulence term. This is inversely proportional to the KC number which is therefore introduced in the parametrization of (van Gent, 1995). The KC number is defined as:

$$KC = \frac{u_m T}{n_p D_{n50}} \tag{4.7}$$

In which u_m is the maximum velocity and T is the characteristic wave period. The KC number is hard to estimate because under irregular wave action it is highly dynamic both in space and in time (Jacobsen et al., 2015). The maximum velocity varies in time and because of the rapid damping of the wave energy through the porous structure the KC number should also be spatially varying. In other words, the KC number should preferably have a temporal an spatial distribution depending on the changing cyclic hydrodynamics. In this research a simplified method is adopted following the approach described in (Jacobsen et al., 2015). The KC number at the toe of the structure is calculated by taking the maximum orbital velocity based on linear wave theory as an approximation of the velocity in the top part of the filter.

$$KC = \frac{H_{m0}}{2} \sqrt{\frac{g}{h}} \frac{1.1 T_{m-1,0}}{D_{n50}} \tag{4.8}$$

Finally the parameterization of van Gent (1995) describes the inertial force, the third term of equation 4.3 (c_p), by adding an added mass term on the momentum equation (see equation 4.1) which is given as:

$$c_p = \gamma_p \frac{1 - n_p}{n_p} \tag{4.9}$$

In which γ_p is an empirical coefficient which value is often taken as 0.34. Jacobsen et al. (2015) analysed the sensitivity of this value by setting it to zero and practically no difference was observed. In line with most numerical studies the originally derived coefficient of 0.34 is adopted in this research.

4.4.1. Turbulence

Wave breaking and turbulent flow through porous media are sources of turbulence which,if necessary, can be modelled using additional turbulence models. Including a turbulence model results in shorter time steps and higher mesh resolutions which will reduce numerical efficiency. However, it is argued by Jensen et al. (2014) and Jacobsen et al. (2015) that for many engineering applications, with little wave breaking, the implementation of additional turbulence closure models is not necessary because the expected amount of turbulence does not influence the bulk hydrodynamics (free surface elevations, wave reflection, overtopping) and thus create no added value.

Jensen et al. (2014) argues that the turbulence generated inside the porous media can best be modelled via the resistance coefficients in the Darcy-Forchheimer equation without a separate turbulence model. This is a valid method if the actual turbulence levels inside the porous media are of minor interest (Jensen et al., 2014). The Darcy-Forchheimer equation is in fact a closure model for handling porous media resistance forces which cannot be resolved directly in the model. Therefore the effect of turbulence can be included in this closure model without affecting the bulk hydrodynamics. The porous media closure coefficients α and β should be defined/altered as such that these turbulence influences are integrated within the coefficients. However if the applied α and β are obtained from physical measurements, the resistance terms already include all dissipative effects among which also turbulence (Jensen et al., 2014). If an additional turbulence model would be applied the dissipative turbulent effects are overestimated by the numerical model (Jacobsen et al., 2015). Therefore re-calibration of the α and β is needed. Overall re-calibration of α and β is highly recommended due to the uncertainties related to site specific conditions and the wide range of values found for these closure parameters (see section 4.4).

4.5. Tracking of free surface

OpenFOAM solves two-phase free surface Newtonian fluids (i.e. water and air) using the VOF method which is necessary to track the highly non-linear interface between both fluids. Other types of free surface tracking methods adopted by other types of models (e.g. potential wave theory) are not applicable for overturning and wave breaking processes that OpenFOAM is able to solve using the VOF method.

The VOF method tracks the free surface based on an indicator field F. The nature of the VOF method is that the interface is not explicitly computed but that it emerges from the indicator field which takes a value between 0 and 1 for each computational cell. If the indicator field (F) has a value of 1 the computational cell is completely filled with water, if the indicator field has a value of 0 it is completely filled with air and also arbitrary values between 0 and 1 are found if the computational cell is partly filled with fluid (Jacobsen, 2017). The temporal behaviour of the indicator field is calculated using an advection algorithm for multi-phase fluids which is used to describe the relative volume fraction of the two-phases (i.e. water and air) in each computational cell per time step. OpenFOAM by default uses an explicit advection algorithm called MULES (Multidimensional Universal Limiter with Explicit Solution) to asses the advection of the indicator field.

(Jensen et al., 2014) adapted the original transport equation of the indicator field in OpenFOAM to correctly account for permeable structures by adding the $1/n_p$ term (see equation 4.10). This factor consequently limits the amount of fluid in a computational cell to the available porous volume within the porous structure and thereby ensures mass conservation. The transport equation of the indicator field that is introduced by Jensen et al. (2014) is given as:

$$\frac{\delta F}{\delta t} + \frac{1}{n_p}[\nabla \cdot \mathbf{u}F + \nabla \cdot \mathbf{u}_r(1-F)F] = 0 \tag{4.10}$$

In which F is the indicator field which is defined as the volume ratio of water to air per computational cell and $1/n_p$ is the factor included by Jensen et al. (2014) to ensure mass conservation for fluid motion through permeable structures. In order to keep a sharp interface using the indicator field a relative velocity u_r is introduced which artificially compresses the solution at the interface. For more detailed information the reader is referred to (Berberović et al., 2009).

The indicator field (F) is used to compute the spatial variation of fluid properties (e.g. density and viscosity) per computational cell in which the computational cell is either air, water or a mixture of both. The spatial variation of for instance density and viscosity can be calculated using the indicator field function, see equation 4.11.

$$\rho = F\rho_1 + (1-F)\rho_0 \qquad \mu = F\mu_1 + (1-F)\mu_0 \tag{4.11}$$

The sub-indices 1 and 0 in these equations refer to water and air respectively. These obtained densities and viscosities per computational cell are used in the VARANS equations to calculate subsequent time steps which are then used to re-evaluate the indicator function for which the process starts all over again. The higher the spatial resolution around the SWL the more accurately the VOF method is able to assess the correct surface elevation.

4.6. Generation and absorption of free surface waves

OpenFOAM uses wave relaxation zones to generate and absorb free surface water waves which is made possible by the waves2Foam toolbox Jacobsen et al. (2012). The advantage of using relaxation zones is that it behaves like an active sponge which removes (spurious) wave reflections within the numerical simulation, as well as that it takes care of compensation of the inward stokes drift preventing water accumulation within the numerical flume.

In this research irregular fully non-linear free surface water waves are generated by the external wave generation model OceanWave3D. Details on the reasons why OceanWave3D is used as wave generation model can be found in section 4.2.1. The generated and transformed waves within the OceanWave3D domain are transferred to the OpenFOAM domain using a coupling relaxation zone at a location in the vicinity of the structure where potential wave theory is still valid. The relaxation zone technique updates the velocity field and the water volume fraction (i.e. indicator field) at each time step in the coupling zone based on a weighting method between a set target solution and the numerical solution of the indicator field and velocity field within the OpenFOAM domain (see equation 4.12 and 4.13). The target solution can for instance be given by a potential flow solver, a fluctuating linear superposition signal based on a target wave spectra (i.e. wave generation by the waves2Foam toolbox) or by a constant value (i.e. outlet relaxation zone).

The indicator field F and velocity field $\mathbf{u}$ within the relaxation zone are updated at each time step replacing them by the ϕ in equation 4.12 and using a weighing function (Jacobsen, 2017). Three different methods to calculate the specified weighting χ are implemented in the waves2Foam package. The default is the exponential weight (equation 4.13 but also the free polynomial weight and the third order polynomial weight can be used. In equation 4.12 the ϕ is used to calculate both the indicator field F as well as the velocity field $\mathbf{u}$. Both equations are solved to correct the indicator- and velocity field prior to the pressure-velocity coupling. Because OceanWave3D does not model two-phase fluids, the target solution of the air phase is simply set to zero while the solution is independent of this parameter according to (Paulsen et al., 2014).

$$\phi = \chi\phi_{\text{computed}} + (1-\chi)\phi_{\text{target}} \tag{4.12}$$

$$\chi(\zeta) = 1 - \frac{\exp(\zeta^{\omega_R}) - 1}{\exp(1) - 1} \tag{4.13}$$

In which ω_R is a shape factor which is by default 3.5, χ is the weighting factor applied in equation 4.12 and ζ is a local coordinate which is zero at the end of the relaxation zone where only the computed values are present and 1 at the end of the relaxation zone where only the target solution is present Jacobsen (2017). Based on the weighing between the target solution and the computed numerical solution a gradual adaptation (i.e. coupling of information) is created from the potential flow solution (OceanWave3D) to the Navier-Stokes/VOF solution (OpenFOAM).

4.7. Measuring overtopping and wave forces

In the following sections the ability of OpenFOAM in combination with the waves2Foam plug in to capture overtopping volumes is described and the ventilated boundary addition is elaborated.

4.7.1. Measuring overtopping

The amount of overtopping water at a structure can be measured using the waves2Foam toolbox by defining an overtopping face which covers multiple cell faces and calculates the amount of water going through the face (Jacobsen, 2017). The overtopping has to be measured in run-time (i.e. at every time step) as the process of overtopping is very rapid and large fluctuations are found in time. Three types of fluxes are available during the simulation:

ϕ= The flux of fluid across a face $[m^3/s]$
ϕ_ρ= The flux of fluid across a face multiplied with the density of the fluid $[kg/s]$
ϕ_F= The flux of fluid across a face multiplied with the indicator function F $[m^3/s]$

The combination of ϕ and ϕ_F would be perfect for the evaluation of the flux of water across a face. However this is not possible as ϕ_F is not available at the time when the function is evaluated. The flux of water across a face is therefore estimated by the use of ϕ and ϕ_ρ (Jacobsen, 2017):

$$\phi_F = \frac{\phi_\rho - \rho_{F=0}\phi}{\rho_{F=1} - \rho_{F=0}} \tag{4.14}$$

It should be noted that ϕ and ϕ_ρ are not based on the same volume flux at the time of evaluating ϕ_F and therefore only an estimation is possible. Assuming that the fluid is water when $F = 1$, the overtopping discharge q over a set of faces f can now be calculated as (Jacobsen, 2017):

$$\mathbf{q} = \sum_{f \in \mathrm{f}} \phi_{F,f} \frac{\mathbf{s}_f}{\|\mathbf{S}_f\|_2} \tag{4.15}$$

In which $\mathbf{q}[m^3/s]$ is the overtopping volume flux and $\mathbf{S}_f$ is the non-unit normal vector to the face. ϕ_F is positive in the direction of the normal vector and negative in the opposite direction. The combination of both will give the directional overtopping.

4.7.2. Measuring wave forces

OpenFOAM is able to measure the generated pressures and translate these into forces. OpenFOAM is a two-phase model in which both air- and water flow are described. During wave impact in closed cavities, air will mix and become entrapped in the water. It was observed that this air entrapment resulted in much larger force predictions compared to situations where air was able to escape and re-enter (Jacobsen et al., 2018, 2015). An approach where small mesh tubes were installed in the boundary was found to be computationally not attractive as high velocities were observed in the tube which restricts the time step. The proposed solution for this problem is developed by Jacobsen et al. (2018) and uses a ventilated boundary condition. This method allows for air ventilation while enforcing a pre-defined head loss characteristic without restricting the time step of the simulation. For the pressure drop over the structural element a classical head loss relations ship is used. For the full derivation of the ventilated boundary condition the reader is referred to (Jacobsen et al., 2018). The final boundary condition for the ventilated boundary condition reads:

$$\frac{\rho}{2}\frac{\xi_p}{e_p^2}u\perp AD, f\nabla b\perp pb* + pb* = p^*_{ref} + \frac{\rho}{2}\frac{\xi_p}{e_p^2}u\perp u\perp* \tag{4.16}$$

The openness and the head loss coefficient can be adjusted for calibration purposes.(Jacobsen et al., 2018) validated that an openness of 3% and a head loss coefficient of 1.5 correctly reproduced the force prediction for a crown wall on top of a rubble mound breakwater.

5

Numerical model set-up

5.1. Introduction

The geometrical scale of the numerical experiments is $n_L = 37.5$. All values presented in this report relate to model scale, unless stated otherwise. First the numerical wave flume layout is discussed after which both numerical grids will be presented and the boundary conditions and measurement devices within the numerical model are explained. For more detailed information (i.e. considerations, observations, choices) related to the numerical flume layout dimensions and both numerical grid resolutions the reader is referred to appendix B.

5.2. Numerical wave flume layout

The numerical wave flume used in this research is composed of a nested OpenFOAM model within a larger Oceanwave3D model, see figure 5.1. The numerical wave flume starts at $x = 0m$ and ends at $x = 25.08m$. The height of the numerical flume is $0.59m$. The use of both OceanWave3D and OpenFOAM increases numerical efficiency of the numerical framework as previously elaborated in section 4.2.1. Both OpenFOAM and OceanWave3D use relaxation zones to generate, couple and absorb free surface waves. Details on the generation, coupling and absorption of waves can be found in chapter 4.2.1 and section 4.6. Both numerical models run side by side and information can be extracted from both models at any point within the numerical flume.

A platform is used to create the bottom slope which starts at $x = 6.58m$, is $0.1m$ high and has a foreshore slope of 2% (i.e. $m = 0.02$) in correspondence with the physical model experiments. In yellow and red both the OceanWave3D and OpenFOAM relaxation zones are presented respectively. According to Paulsen et al. (2014) there is a dependence on the location of the relaxation zone and the solution in the vicinity of the structure. Once the interaction between the incoming waves and reflected waves can be neglected the inner domain can be truncated according to (Paulsen et al., 2014). This is done using relaxation length based on the peak wave length (L_p) calculated using linear wave theory. Waves are generated at $x = 0m$ (i.e. the OceanWave3D wave generation zone) and travel in positive x direction. At $x = 5m$ information on free surface elevation is coupled from OceanWave3D to the OpenFOAM domain where also the HLCS and sea wall are implemented. OpenFOAM models the wave interaction with the HLCS and sea wall from which the data is extracted. At $x = 17m$ the waves within OpenFOAM are absorbed using the outlet relaxation zone and at $x = 21m$ also the waves within OceanWave3D are absorbed using the outlet relaxation zone based on pressure damping.

5.2.1. Measurement devices

In order to extract wave characteristics within the numerical flume 9 wave gauges have been manually placed, see figure 5.1 for the positions of these wave gauges. These wave gauges correspond to the exact location of the wave gauges that have been used in the physical model experiments described in chapter 3. Additionally, 81 wave gauges have been placed with increments of 0.1m starting at x=17.0. These wave gauges are referred to as bulk wave gauges and are used for the parametric study.

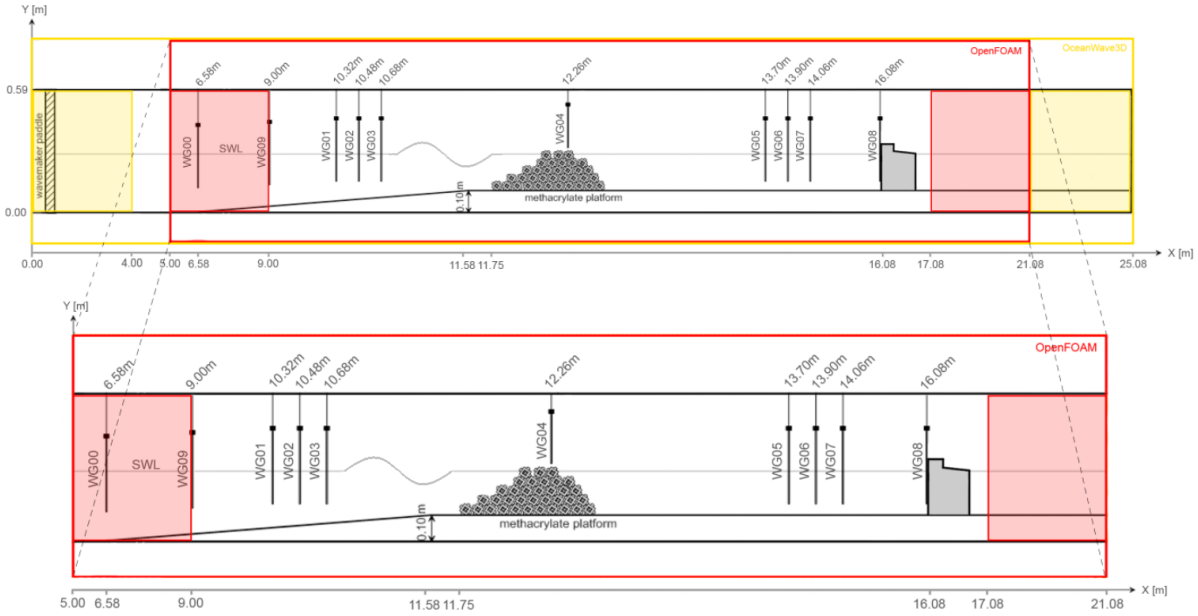

Figure 5.1: Numerical flume layout including the OceanWave3D domain and the OpenFOAM domain (not to scale)

5.3. Grid design

The computational grid is the foundation of a numerical model. The computational grid should be designed as such that physical processes are well described and realistic results are obtained in areas of interest. Moreover, the grid should be designed to have the most efficient relation between computational efficiency and accuracy/level of detail. For both numerical models used in this research, OceanWave3D and OpenFOAM, the design of the numerical grid is described. Additionally the implementation of the sea wall is elaborated. The implementation of the HLCS is separately treated and can be found in section 7.3.

5.3.1. OceanWave3D

OceanWave3D uses a structured cartesian finite difference grid in horizontal direction, determined by a grid size Δx. In vertical direction also a finite differences grid is used prescribed by a user selected number of layers. Based on a preliminary Oceanwave3D study and recommendations by Paulsen et al. (2014) 10 numerical layers have been used with vertical stretching near the free surface to increase accuracy near regions of interest. Moreover it was found that the horizontal resolution is normative for the performance of OceanWave3D, especially for expected high levels of non-linear wave behaviour. Therefore the grid has been designed using 40 grid cells per peak wave length (L_p) for the smallest expected wave length during all numerical experiments.

5.3.2. OpenFOAM

In order to generate and refine the OpenFOAM numerical grid the blockMesh and snappyHexMesh utility are used in this research. The use of orthogonal grid cells with an aspect ratio of 1 ($\Delta x = \Delta y$) where the free surface is expected is recommended. This is found to have significant effect on the wave propagation performance of OpenFOAM as described in (ITTC, 2011; Jacobsen et al., 2012; Roenby et al., 2017). A mesh structure of rectangular grid cells has been designed over the complete numerical domain using blockMesh. Moreover, refinements were applied using snappyHexMesh to regions of interest and regions where larger gradients were expected in order to achieve affordable computational costs without losing accuracy in these regions. The regions of interest that were selected were those near the free surface, near the HLCS and near the sea wall. Near regions of interest grid cells were resized up to 1/4 of the original size, see figure 5.2 for the applied refinements. The grid cells that coincide with the prescribed dimensions of the sea wall are removed using snappyHexMesh. A sea wall with a freeboard of 0.06m is implemented. Moreover an overtopping face on top of the sea wall and a front face are applied to measure the overtopping volumes and wave forces respectively. The

implementation of the HLCS is separately treated in section 7.3.

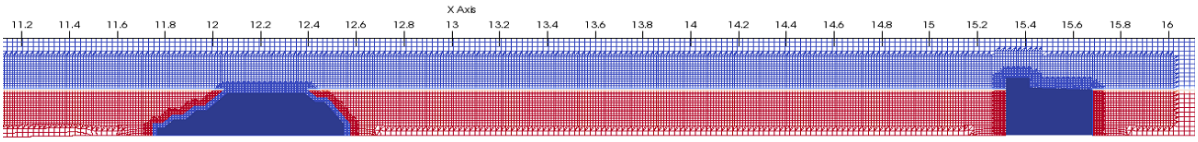

Figure 5.2: Part of the used OpenFOAM numerical grid with refinements near the regions of interest. In red and blue the cells which only contain water or air respectively are visualised. Additionally the sea wall and HLCS are presented.

Grid resolution

For the calibration of the numerical model (i.e. the grid resolution study) the grid resolutions presented in table 5.1 are used. These resolutions follow from analysed literature sources and other research related to numerical modelling of coastal structures in OpenFOAM. It was found that the number of grid points per significant wave height was normative. The hydrodynamics (i.e. wave overtopping, wave transmission and water level set-up) of the system are mostly governed by the larger and longer waves. These waves should be prescribed well by the numerical model. However also the smaller waves should be correctly captured by the numerical model. To achieve both accurate results and a computationally efficient numerical simulation the significant wave height is used instead of the maximum wave height. All the 4 presented grid resolutions in table 5.1 are used for the calibration of the wave flume hydrodynamics which can be found in chapter 7.4.

Table 5.1: Investigated grid resolutions and dimensionless characteristics

Grid ID	N_x	N_y	$\#ofcells[-]$	$\Delta_{x,swl} = \Delta_{y,swl}[m]$	$\frac{H_s}{\Delta_{y,swl}}$	$\frac{L_p}{\Delta_{x,swl}}$
501	1462	54	111771	0.0055	20	418
502	731	27	27982	0.011	10	209
504	512	19	13721	0.016	7	148
503	366	14	7290	0.022	5	105

5.4. Temporal resolution

Numerical models can use explicit or implicit time integration methods to calculate the state of system in time for a given grid design and resolution. Explicit time integration schemes can directly calculate the state of the system at following time steps using the previous time step. Implicit time integration schemes on the other hand find solutions by solving equations that include both the current and the later state(s) of the system. These type of time integration schemes do not have stability requirements but can become computationally very expensive. Explicit time integration methods are in general faster than implicit time integration methods but require stability requirements to prevent the solution to become unstable. Both OceanWave3D and OpenFOAM use an explicit time integration method. In order to obtain a stable solution for an explicit time integration numerical scheme the CFL condition is used which is further explained in the next section (i.e. section 5.4.1).

5.4.1. CFL condition

The CFL (Courant, Friedrichs and Lewy) condition is a necessary condition for the convergence of a finite difference scheme to a (non)linear hyperbolic partial differential equation (Zijlema, 2015). This means that in order for the numerical scheme to approach the exact solution of the physical equations the CFL condition should be met. This limits the time step that can be used to solve the methematical system. If the CFL condition is not met the solution of the numerical model can become unstable and eventually blow up to infinity. The CFL condition can be explained using the concept of domain of dependence. The numerical domain of dependence must contain the analytical domain of dependence (Zijlema, 2015). This means that information must not travel faster than one computational cell per time step. For a one dimensional numerical model the CFL condition takes the following form:

$$| \sigma | \equiv \frac{| u | \cdot \Delta t}{\Delta x} \leq C \tag{5.1}$$

5.4.2. OceanWave3D and OpenFOAM

The limiting time step for OceanWave3D used in this research is based on the CFL condition with a max courant of 0.8 based on the expected velocity within the maximum wave height during the simulations which results in a time step of 0.01s. It was found that once OceanWave3D is coupled to OpenFOAM, OpenFOAM adjusts the time step of Oceanwave3D as well due to the coupling of both models. However it was found that due to the higher courant restriction of OpenFOAM this did not jeopardize the numerical stability of OceanWave3D.

The temporal resolution in OpenFOAM is based on the limiting max courant number (σ) which is prescribed by the user of the model and has a default value of 0.35. OpenFOAM, in contrary to OceanWave3D uses an adaptive time stepping method which aims to increase the time step up to the limiting time step for every time step of the simulation in such a way that the time step corresponds to the maximum prescribed courant number. This adjustment method is based on computational efficiency while maintaining numerical stability. However also very low flow velocities can be present in the flume (e.g. during the start of the simulation) resulting in nonphysically very large time steps which is prevented by setting a maximum time step restriction of 0.001s. The max courant number has a large influence on the total computational time (i.e. numerical efficiency) and is therefore analysed in more depth. Larsen et al. (2019) studied the interFOAM solver and concludes that in order to increase the accuracy of the numerical prediction it is computationally more efficient to reduce the maximum courant number in stead of increasing the resolution of the grid. Moreover, Roenby et al. (2017) studies 2D wave propagation for the interFOAM solver and concluded that a maximum courant number of 0.1-0.2 shows good results regarding wave propagation. Additionally a numerical trick is analysed which uses additional iterations around the interface of water and air in order to allow for a larger limiting time step without compromising the numerical stability. The effect of different combinations of courant number and grid resolution on the numerical prediction of OpenFOAM have been analysed in section 7.4 for the wave flume hydrodynamic calibration.

5.5. Boundary conditions

In this section the applied boundary conditions are elaborated that have been used for the calibration and validation of the wave flume hydrodynamics as well as for the analysis of the geometrical layout of the system. The applied boundary conditions are reported in table 5.2. Irregular wave trains of 500 waves are generated and absorbed in relaxation zones, which form the inlet and outlet boundary condition in horizontal direction. The use of 500 waves is appropriate for overtopping simulations according to recommendations by (Romano et al., 2015). In vertical direction the wave flume is restricted by the bottom of the flume on which a slip boundary condition is applied and the top of the flume an atmospheric boundary condition is applied. For the atmospheric boundary condition water and air can flow out but only air can enter the flume which can result in water losses if the height of the flume is not adequately chosen related to the computational efficiency. The sea wall is implemented using the slip boundary condition. On the front face of the sea wall the ventilated boundary condition is applied to measure the wave forces. The boundary conditions prescribed for the HLCS are elaborated in more detail in chapter 7, the reported values in table 5.2 are the validated values which are described in more detail in chapter 8.

For the parametric study, hydraulic boundary conditions resulting in severe overtopping (i.e. a prototype overtopping ≈300 l/s/m) are applied for which the HLCS remains stable (i.e. no movement of cubipod elements). The Hudson stability condition is used combined with a KD value of 12, which is valid for truck stability of a single cubipod armour layer (J. R. Medina et al., 2010). For multiple layers of cubipod even higher KD values are found due to the stabilizing effect of interlocking layers. A resulting limiting significant wave height of $13cm$ is obtained. The generated hydraulic boundary conditions have a significant wave height of $11.24cm$ near the HLCS and therefore the HLCS is assumed to be stable during the simulations thus resulting in a physically sound numerical prediction for a stable HLCS.

Table 5.2: Applied boundary conditions and system characteristics to the OpenFOAM model

	Input	Symbol	Value	Unit
Hydraulic	Spectral type		Jonswap	
	Peak enhancement factor	γ	3.3	[-]
	Water depth in basin	h	23	[cm]
	Offshore boundary wave height	H_s	11	[cm]
	Offshore boundary peak period	T_p	1.63	[s]
	Offshore boundary wave steepness	s_{op}	0.027	[-]
	Peak wave length in basin	L_p	230	[cm]
	Number of waves		500	[-]
Front face sea wall	Openness	e_p	3	[%]
	Head loss coefficient	ξ_p	1.5	[-]
HLCS	Alpha	α	500	[-]
	Beta	β	1.0	[-]
	Core porosity	$n_{p,core}$	50	[%]
	Armour porosity	$n_{p,outer}$	75.2	[%]
	Keulegan–Carpenter number	KC	13.15	[-]
	Nominal diameter	D_{n50}	4.35	[cm]
System	Simulation duration		680	[s]
	Turbulence model		Laminar	[-]
	Solver		InterFOAM	[-]
	Number of cores		6	[-]

(This page is intentionally left blank)

6

Calibration and validation of wave flume hydrodynamics

6.1. Introduction

In this chapter the calibration and validation of wave flume hydrodynamics is elaborated. First the calibration and validation procedure is described after which the statistical methods adopted to perform the calibration and validation are described. Subsequently the use and performance of a wave reflection procedure is described which is used to derive the transmitted wave characteristics. Using a grid resolution study including also varying courant numbers, the coupling between both numerical models OceanWave3D and OpenFOAM is described on two locations in the flume (i.e. directly at the end of the coupling zone and at a location further in the wave flume). Subsequently the predicted overtopping discharges by OpenFOAM are compared to empirical prediction guidelines and conclusions are drawn. Furthermore the effect of the ventilated boundary condition on the predicted overtopping by OpenFOAM is analysed an a sensitivity analysis is included.

6.2. Calibration and validation procedure

Generally numerical studies present a calibration and validation procedure based on a surface elevation record or other data extracted from a physical model experiments by mimicking the same hydraulic and structural boundary conditions. For these types of validation raw data on surface level elevation, overtopping volumes, pressures or a steering paddle input signal is needed. However no such raw data was available to the author. Therefore a more general approach has been followed to calibrate and validate the coupled numerical model to be used to analyse the design sensitivities related to the main geometrical layout parameters, which has been divided in two phases. The first one is the calibration and validation of wave flume hydrodynamics, elaborated in this chapter (i.e. chapter 6). Where wave flume hydrodynamics of the coupled numerical model are calibrated using a grid resolution study including variability in courant number. Subsequently the adopted grids and courant numbers are validated on wave overtopping by comparing the extracted overtopping data to the Eurotop 2018 prediction guideline for vertical structures. The second phase is the calibration and validation of the hydrodynamic behaviour of the HLCS which has been elaborated in chapter 7. For this calibration and validation a combination of significant wave height H_s and peak period T_p from a wave reflection procedure at a wave gauge in front of the structure, behind the structure and the corresponding structural dimensions of the HLCS are used to statistically compare the wave transmission behaviour.

The calibration and validation of wave flume hydrodynamics within the numerical model (this chapter) is conducted following three steps. The first two steps are used for the calibration of the numerical model and the third step is a validation step. The first two steps are conducted in an empty flume without a sea wall (i.e. where only the platform representing the beach slope is included) and for the third step the sea wall is implemented within the numerical model. The calibration and validation steps are listed below:

1. An analysis is performed to the direct coupling between both models on raw surface elevation signals at the end of the coupling zone for different grid resolutions and courant numbers, see section 6.3.1.

2. An analysis is performed to the wave propagation ability of OpenFOAM after the coupling zone, see section 6.3.2. In here the surface elevation signals and statistical parameters are compared between the output of a standalone OceanWave3D model (i.e. the reference output) and the outputs of the coupled OceanWave3D-OpenFOAM model (i.e. the OceanWave3D output and the OpenFOAM output of the coupled model) for varying grid resolutions and courant numbers. The aim of this calibration phase is to have matching output (i.e. surface elevation signals and statistical wave parameters between both coupled outputs and the reference output) at a location within the validity range of both OceanWave3D and OpenFOAM to gain confidence in the calibrated coupled numerical frame work.

3. An analysis is performed to the effect of different grid resolutions, courant numbers and the use of different ventilated boundary condition parameters on the predicted overtopping by the coupled OpenFOAM model, see section 6.4. A wave reflection analysis based on the work of Zelt et al. (1993) is conducted to extract the incoming and reflected surface elevation signals. Additionally the predicted overtopping discharges by OpenFOAM are validated with empirical design guidelines presented in the Eurotop 2018 Van der Meer et al. (2018).

6.2.1. Signal comparison methodologies

In order to access the goodness of the calibration several methodologies are adopted in order to compare the surface elevation signals and statistical parameters. These methodologies are elaborated in the following subsections. First two methodologies for comparison of surface elevation signals are elaborated and subsequently two methodologies for the extraction of statistical wave parameters from surface elevation time signals are described. Additionally the use of the wave reflection procedure by Zelt et al. (1993) and the related uncertainties are presented.

Pearson Correlation Coefficient

For the goodness of fit between extracted surface elevation signals the Pearson Correlation Coefficient (PCC) is used in this research. This method describes the correlation between two random time signals using the co-variance between the two signals and the standard deviations of both signals. If the PCC value is equal to 1, both signals are fully correlated and if the PCC value is equal to 0, both signals are fully uncorrelated. The PCC value can be calculated using:

$$PCC = \frac{Cov(X_1, X_2)}{\sigma_{X_1} \cdot \sigma_{X_2}} \tag{6.1}$$

In which Cov is the co-variance between the two time signals and σ is the standard deviation of the separate time signals.

Root Mean Squared Error

Additionally, the root mean squared error (RMSE) is used in this research to compare surface elevation signals. The RMSE is a statistical parameter which like the PCC can be used to quantify the magnitude of the error between two signals. If the RMSE is equal to 0, there is no difference between both signals thus implying that both signals are identical. The RMSE can be calculated using:

$$RMSE = \sqrt{\frac{\sum_{i=1}^{N} (\hat{y}_i - y_i)^2}{N}} \tag{6.2}$$

In which $\hat{y}_i$ is the predicted value, y_i is the observed value and N is the number of observations within the signal. The RMSE is used for the grid resolution study where the predicted value is set to the output OpenFOAM value (i.e. surface elevation signal) and the observed value is the output OceanWave3D value of the coupled model. Additionally the RMSE is used for validation of the wave transmission over the HLCS where the predicted value is the transmission coefficient modelled by OpenFOAM and the observed value is the transmission coefficient observed during the physical model tests.

Significant wave height

In order to compute the significant wave height using wave by wave analysis a zero down crossing analysis to distinguish individual waves has been carried out on the coupled model output of a surface level elevation signal. The minimum and maximum surface elevation within each wave was identified and the difference between the two were taken as individual wave heights. The highest 1/3 of wave heights were collected and averaged to obtain the significant wave height (H_s)). A sample plot of the procedure for a certain wave field is presented in figure 6.1.

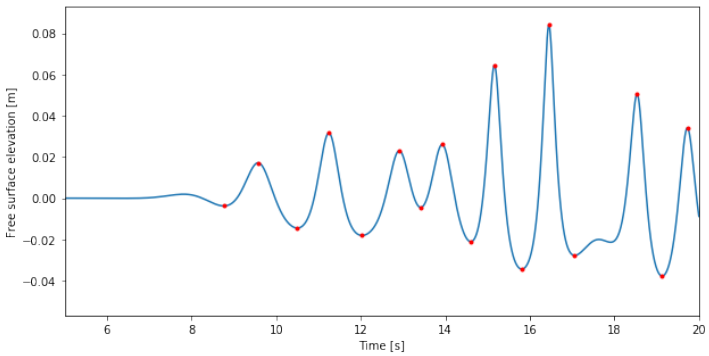

Figure 6.1: A sample of the minimum-maximum analysis used in this investigation. The red dots represent the maximum and minimum surface elevations as detected by the used algorithm, while the blue curve represents the original surface elevation time series.

Spectral wave height

The surface elevation time series that are extracted from the coupled numerical model are characterized by a variance density spectrum ($E(f)$). This spectrum describes the distribution of energy over the various frequencies within the time series. The characteristic statistical wave parameters of the spectrum can be described using spectral moments (m_n) which can be described using equation 6.3 following Bosboom & Stive (2015):

$$m_n = \int_0^\infty f^n E(f) df \quad for \quad n = ..., -3, -2, -1, 0, 1, 2, 3, ... \tag{6.3}$$

Next to the visualisation of the energetically dominant frequencies within the time series various characteristic average wave parameters can be obtained from the spectral moments. Some examples are the peak spectral period (T_p), which is the period where most spectral energy is contained, the mean period ($T_{m-1,0} = m_{-1}/m_0$) and the spectral significant wave height ($H_{m0} = 4 \cdot (m_0)^{0.5}$).

Reflection procedure

When waves interact with a structure, part of the wave energy is reflected back offshore. The reflected wave energy interferes with the incoming wave energy which creates a standing wave pattern depending on the amount of energy within the incoming and reflecting waves. For this research a highly reflecting vertical sea wall is used as shore ward boundary. In order to be able to compare the OpenFOAM overtopping data with design guidelines presented in the Eurotop 2018 manual the incoming wave field is extracted from the total wave field (i.e. into an incoming and reflected wave field). During this research, the incoming wave field and reflected wave field are separated using the multiple wave gauges procedure as described in Zelt et al. (1993). This procedure is based on linear wave theory and uses Fourier analysis to separate the incoming and reflected surface level elevation signals. According to Zelt et al. (1993), the accuracy of the wave reflection separation increases when using more wave gauges, especially for broad band wave spectra. Although a broad band spectra is expected for wave transmission over LCS only three wave gauges are used to separate the incoming and reflected waves corresponding to the same method adopted during the physical model experiments described in section 3.

Preferably, when comparing to the case without a structure in the flume, the exact same surface level elevation distribution is produced by the reflection procedure. However, the wave reflection procedure is based on linear wave theory. The waves in the numerical model behave highly nonlinear due to the slope within the flume and eventually also after wave breaking over the HLCS. Therefore high levels of non linearity are found within the transmitted waves. Consequently the exact surface level elevation cannot be produced by using a wave reflection procedure. This does not imply that the wave reflection procedure cannot be used. Namely, the higher order non linearities that are found in the wave field shift the surface level elevation towards higher peaks and lower troughs. It is observed that the wave reflection procedure is not able to reproduce the steep non linear peaks of the wave and the low troughs, even when using very high Fourier frequencies. However, both the additional non linearities in the wave crest and the wave troughs can cancel out to give the same wave height during wave analysis. The uncertainties related to using a wave reflection procedure have been elaborated in section 6.6.2.

A wave reflection procedure requires a range of frequencies that should be resolved by the procedure. From spectral analysis it is concluded that almost no energy is present for frequencies higher than 2.5 Hz and lower than 0.1 Hz. Therefore this range of frequencies is adopted for the reflection procedure during this study.

6.3. Coupling OceanWave3D and OpenFOAM

As previously described while explaining the calibration and validation procedure (in section 6.2) the calibration of the wave flume hydrodynamics is performed using a grid resolution study including varying courant numbers. Both the coupling between OceanWave3D and OpenFOAM at the end of the coupling zone (i.e. using direct surface elevation comparison, elaborated in section 6.3.1) and the wave propagation ability (i.e. using statistical comparison between wave parameters, elaborated in section 6.3.2) are described. For both these analysis the relative calculation time (i.e. $T_{clock}/T_{simulation}$) is presented based on the simulation duration while using 1 processor to make a relative comparison between the accuracy of the coupling and the computation effort required.

6.3.1. Coupling at the end of the coupling zone

The first step in the calibration procedure is based on a raw comparison of the surface elevation signals at the end of the coupling zone as outputted by OceanWave3D and OpenFOAM from the coupled model. The coupling in raw surface elevation signal is compared using the Pearson Correlation Coefficient (PCC) and the Root Mean Square error (RMSE) between both signals at the end of the coupling zone (i.e. at wave gauge 9, see figure 5.1). The results for different grid resolutions and courant numbers on the PCC and RMSE are presented in table 6.1. For run BC502A both the outputted surface elevation signal of OceanWave3D and OpenFOAM within the coupled model as well as the corresponding wave spectra are presented in figure 6.2.

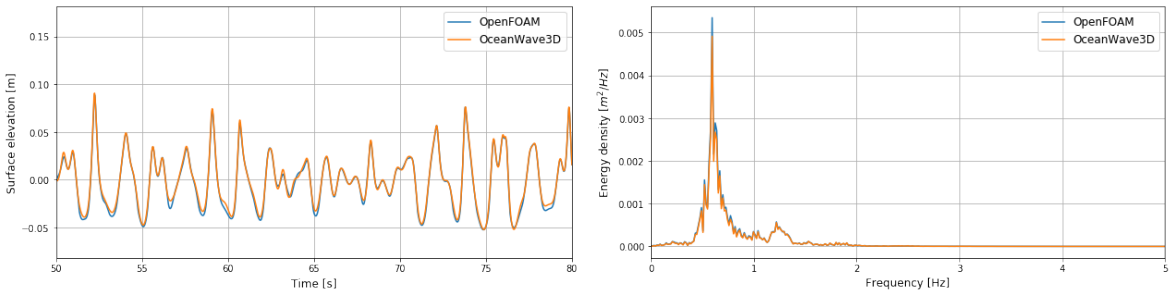

(a) Time series comparison

(b) Energy density spectral comparison

Figure 6.2: Time and frequency domain comparison of surface elevation signals of OpenFOAM and Oceanwave3D for the coupled model at wave gauge 9 corresponding to run BC502A.

Table 6.1: Comparison output of OceanWave3D and OpenFOAM from the coupled model at the end of the coupling zone (i.e. at wave gauge 9) in order of reducing grid resolution

Run ID	Wave type	Grid ID	C_{max} [-]	$RMSE$ [cm]	PCC [-]	$\frac{T_{clock}}{T_{simulation}}$ [min/s]
BC501	Irregular	501	0.35	0.2792	0.9951	82.0
BC501A	Irregular	501	0.10	0.2612	0.9961	178.0
BC501B	Irregular	501	0.50	0.2711	0.9956	76.0
BC502	Irregular	502	0.10	0.2804	0.9968	17.5
BC502A	Irregular	502	0.20	0.2784	0.9968	10.3
BC504	Irregular	504	0.10	0.3739	0.9965	5.6
BC503	Irregular	503	0.10	0.3777	0.9953	2.7
BC503A	Irregular	503	0.20	0.3523	0.9958	1.6

Analysis and conclusion

All grid resolutions perform well for the coupled model at the end of the coupling zone. The relative simulation time (i.e. $T_{clock}/T_{simulation}$) reduce considerably for coarser grid resolution whereas on the other hand the RMSE only slightly increases for coarser grid resolution. Therefore it is concluded that the coupling between OceanWave3D and OpenFOAM is correctly set-up and that the coupling at the end of the coupling zone does not play a role while determining the grid resolution of the numerical model. More valuable is the wave propagation, which is elaborated in the next section (i.e. section 6.3.2).

6.3.2. Wave propagation

The surface elevation distribution computed by the coupled model (i.e. OceanWave3D and OpenFOAM together) is compared with the standalone OceanWave3D model at a wave gauge where both models are in their range of validity. Using the breaking limit presented in figure A.4 and the maximum observed wave height in the time series, it is expected that the highest waves break between wave gauge 2 and 3. Therefore wave propagation is compared at wave gauge 2 in order to evaluate the ability to model the correct wave propagation for different mesh sizes and courant numbers. This wave gauge corresponds to a wave gauge at a water depth of 0.252 m, see figure 5.1.

OceanWave3D uses a 4th order numerical method, which produces higher accuracy for the same resolution compared to OpenFOAM. In order to obtain a grid independent solution a OceanWave3D standalone run is used as target solution. In table 6.2 both the standalone Oceanwave3D (i.e. run id OCW3D) and the coupled OceanWave3D with different grid resolutions and temporal resolutions of OpenFOAM (i.e. BC50-) are presented. The 3 groups of simulations are sorted from highest to lowest grid resolution. In this table the used grid, the adopted courant number, the outputted significant wave height of the coupled model (i.e. both the OceanWave3D output and the OpenFOAM output of the coupled model), the outputted spectral wave heights of the coupled model are presented. In the 9th column the difference in percent between the OceanWave3D output of the coupled model and the standalone OceanWave3D run is presented and in the 10th column the difference in percent between the OceanWave3D and OpenFOAM output of the coupled model is presented. Both values from these columns are used to determine the best grid for this numerical study based on the convergence between the outputs of the coupled model as well as the convergence towards the target OceanWave3D solution. Additionally the relative computation times are presented which are also used as a criteria for the grid decision.

Please note that due to the enormous computational costs, runs BC501x have been cancelled after 230s (160 waves). This should be taken into account when comparing the statistical wave parameters presented in table 6.2. The spectral and significant wave height of this grid namely shows higher values, a difference of 4.9% is observed for $H_{s,OW}$ compared to the standalone OceanWave3D simulation. However, this is most likely due to the larger ratio of higher waves in this part of the time series. For completeness of this hypothesis the effect of the use of the shorter time series (0-230 s) from grid 501x

is analysed for all grid resolutions. Using a time series of (0-230 s) for both grid 501x and 502x results in a difference of only 0.2% which confirms that the significant differences of grid 501 are caused by use of the shorter time series. Moreover, the 501x grid resolution is rejected from further analysis because computational times are too large and not feasible for the intended uses. These runs can however be used to compare the relative effect of courant number on the computation time and accuracy. For reducing courant numbers the difference between the coupled model output (i.e. OceanWave3D output and OpenFOAM output of the coupled model) reduces whereas the computation time increases considerably.

Table 6.2: Wave characteristics analysis at wave gauge 2, water depth = 0.252 m. The runs are sorted from high to low resolution per group

Run ID	Wave type	Grid ID	C_{max} [-]	$H_{s,OW}$ [cm]	$H_{s,OF}$ [cm]	$H_{m0,OW}$ [cm]	$H_{m0,OF}$ [cm]	$\Delta H_{s,OW}$ [%]	$\Delta H_{s,OF,OW}$ [%]	$\frac{T_{clock}}{T_{simulation}}$ [min/s]
OCW3D	Irregular	-	-	11.18	-	10.43	-	-	-	0.1
BC501A	Irregular	501	0.10	11.73	11.74	10.93	11.08	+4.9	+0.1	178.0
BC502	Irregular	502	0.10	11.25	11.36	10.56	10.77	+0.6	+1.0	17.5
BC504	Irregular	504	0.10	11.12	11.40	10.49	10.82	-0.5	+2.5	5.6
BC503	Irregular	503	0.10	11.09	11.49	10.48	10.92	-0.8	+3.6	2.7
BC501	Irregular	501	0.35	11.71	11.76	10.91	10.76	+4.7	+0.4	82.0
BC501B	Irregular	501	0.50	11.72	11.53	10.95	10.67	+4.8	-1.6	57.0
BC502A	Irregular	502	0.20	11.15	11.26	10.48	10.56	-0.3	+1.0	10.3
BC503A	Irregular	503	0.20	11.07	11.45	10.47	10.72	-1.0	+3.4	1.6

Analysis and conclusion

Effect of the interaction between both numerical models is observed. A standalone run of OceanWave3D shows the non-influenced OceanWave3D model for comparison, which is independent on the OpenFOAM resolution and therefore included in figure 6.3 as a horizontal line. OceanWave3D uses a high-order numerical method compared to OpenFOAM and therefore OpenFOAM needs significantly more resolution for equivalently accurate results compared to OceanWave3D. OceanWave3D shows very high accuracy in the input of the coupling but this accuracy is found to be degraded by the lack of resolution in OpenFOAM to produce equivalent results further in the numerical domain.

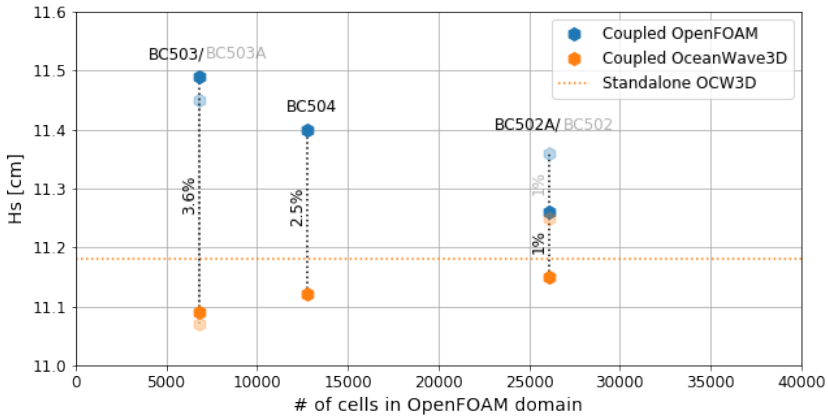

Figure 6.3: Grid convergence analysis for different grid resolutions

Some observation from table 6.2 and figure 6.3 are presented below:

- By increasing the spatial resolution of OpenFOAM higher agreement is found between the spectral and significant wave height of both models as well as higher agreement between the coupled and standalone OceanWave3D output (i.e. convergence).

- For grid 502 and 501 a reduction in courant number does not show an increase towards the target solution, whereas grid 503 shows a convergence towards the target solution for lower courant numbers.
- The coupled model OceanWave3D output shows an under-estimation of the spectral wave height compared to the standalone model for every grid resolution. However, an increase towards the target solution is found for increasing OpenFOAM grid resolution. This can be a result of the smaller time steps of the coupled model due to courant number restrictions of the OpenFOAM model which determines the subsequent time steps of the coupled model, which shows better results in capturing the steep peaks.
- The ratio of $\frac{H_s}{H_{m0}}$ approaches values higher than one, which corresponds to values found in literature for (steep) shoaling waves according to chapter 4.2.4.5 of the Rock manual (Ciria et al., 2007).
- A numerical trick to obtain the same wave characteristics yet decrease the computational costs has been performed by adjusting the number of alpha cycles which has been described in the appendix in section B.4.3. This run (i.e. run BC501B) shows a reduction of 68 % of computational time compared to run BC501A. However, 3.7% is lost on the spectral wave height in OpenFOAM. The reduced computation time is not considered to outweigh the loss in H_{m0}. Additionally in section 6.4 it is shown that 14% is lost on the predicted overtopping discharge. This is not considered to outweigh the increase in computation time and this numerical trick is rejected from further analysis. The implications of this numerical trick on the porous flow behaviour is unknown as this grid and resolution combination are not studied any further.

Based on analysis of figure 6.3 it is observed that for increasing grid resolution the difference between the output of the coupled model reduces as well as that convergence towards the target solution is found. Run BC502A approaches to the target solution with only 0.3% difference between the output of the OceanWave3D of the coupled model compared to the standalone OceanWave3D run. Furthermore run BC502A only shows a difference between the coupled model output of 1%. For this run the coupling at wave gauge 2 in surface elevation and spectral analysis is presented in figure 6.4, which shows an almost perfect match.

Generally it is observed that both increasing resolution and decreasing the courant number convergence is found toward the target solution. The effect of decreasing the courant number on the correlation with the target solution reduces for increasing OpenFOAM resolution. Therefore for high spatial resolutions (+- 20 cells per significant wave height) the use of the default courant number is recommended in order to have reasonable computational costs for this numerical model setup. For lower spatial resolutions (less than 10 cells per significant wave height) the use of lower courant numbers is recommended to increase the accuracy of the coupled model. These conclusions are drawn based on this model set-up however it is likely that these conclusions also hold for other similar model set-ups. For this research 10 grid cells per significant wave height with a courant number of 0.2 have shown to give the best results for wave propagation (i.e. corresponding to run BC502A).

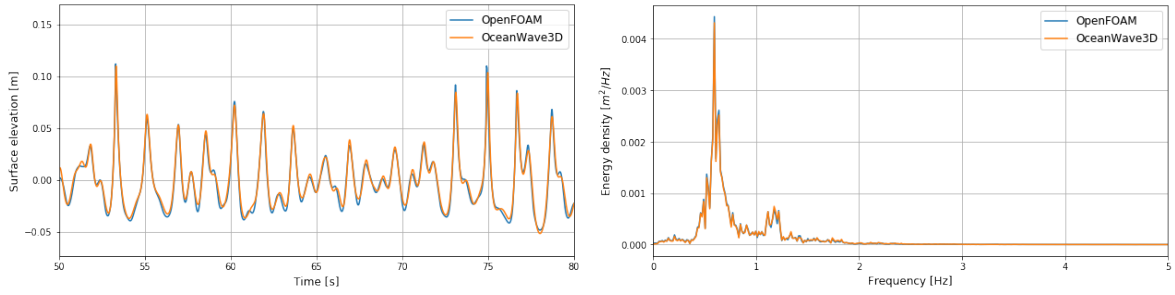

(a) Time series comparison

(b) Energy density spectral comparison

Figure 6.4: Time and frequency domain comparison of surface elevation BC502A OpenFOAM and Oceanwave3D at wave gauge 3

6.4. Overtopping comparison and validation

In this section the various potential grid designs are compared, and the selected grid is validated based on the predicted overtopping discharges against data from a large European funded overtopping project CLASH and Eurotop 2018 prediction guidelines. Moreover the effect of the ventilated boundary condition is analysed. In order to compare predicted overtopping discharges to the Eurotop design guideline, the incoming wave field has to be separated from the reflected wave field. The separation of the incoming and reflected waves is performed by the 3 gauge method described in Zelt et al. (1993), which has been elaborated in section 6.2.1.

First various simulations with different grid resolutions and courant numbers are compared. Table 6.3 presents the performed overtopping simulations for the various grid dimensions in descending order. The adopted courant numbers are presented in the fourth column and predicted mean overtopping discharges are presented in the fifth column. Additionally, the prototype overtopping values are presented which have been calculated using Froude scaling. According to Froude scaling prototype overtopping can be calculated using the specific discharge scale factor $n_L^{1.5}$. Lastly, relative computation times are presented as a ratio of the number of minutes it takes to compute 1 second of simulation.

Table 6.3: Investigated grid resolutions and dimensionless characteristics, $R_{c,seawall} = 6cm$

Run ID	Grid ID	Wave type	C_{max} [-]	q_{model} [l/m/s]	$q_{prototype}$ [l/m/s]	$\frac{T_{clock}}{T_{simulation}}$ [min/s]
SW502	502	Irregular	0.1	1.32	302	21.1
SW502B	502	Irregular	0.2	1.28	298	15.1
SW502A	502	Irregular	0.5 (5 sub-cycles)	1.11	256	5.8
SW504	504	Irregular	0.1	1.28	294	8.3
SW503	503	Irregular	0.1	1.25	286	3.7

One can observe that on average OpenFOAM predicts higher mean overtopping discharges for increasing grid resolution. This effect is probably related to numerical artefacts (i.e. truncation errors and numerical diffusion) which are related to the size of the grid cells near the overtopping face that are used to calculate the amount of overtopping. Comparing the effect of differences on mean overtopping discharges for varying grid resolution it can be observed that when using sufficiently energetic wave conditions the relative effect of grid resolution on the predicted mean overtopping discharge is small. However the increase in computation time comparing grid 502 for a courant number of 0.2 and 0.1 shows that the additional gain in mean overtopping discharge for lower courant number does not outweigh the increase in computation time. Additionally the trick using 5 sub-cycles is not able to predict the overtopping discharge in line with the other simulations, and under predicts the mean overtopping discharge compared to the other simulations.

Looking at figure 6.5b, a large overtopping event is presented which shows the correct shape of an overtopping event. Additionally a visual inspection of this large overtopping event from the simulation is presented in figure 6.5c where a lot of spray is observed.

6.4.1. Validation

In this section the selected grid (i.e. grid 502 with a maximum courant number of 0.2) is validated by comparing the predicted overtopping discharges against data from a large European funded overtopping project CLASH and Eurotop 2018 prediction guidelines for **impulsive** overtopping conditions (i.e. equation 2.8 and 2.9). Figure 6.6 presents simulations with grid 502 and a courant number of 0.2 for different crest freeboard of the sea wall in order to validate the overtopping prediction for different crest freeboard and gain confidence in the numerical framework. Also predicted overtopping discharges are presented using comparable grid resolution yet a longer wave flume (i.e. where waves start in deep water but with the same hydraulic boundary conditions, elaborated in appendix D, see figure D.1). High agreement is found between the CLASH database and the predicted mean overtopping discharges by OpenFOAM while all data points predicted by OpenFOAM lie close towards the prediction guideline and between all CLASH database data points.

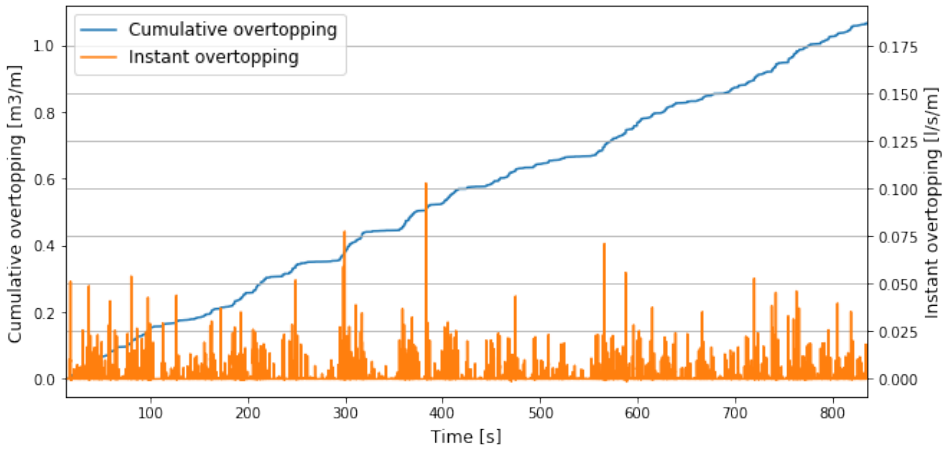

(a)

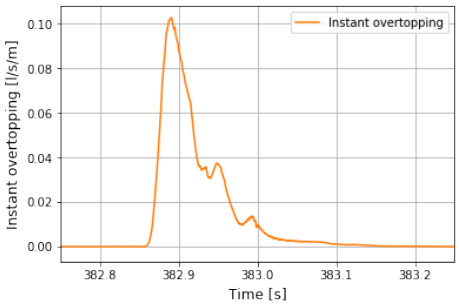

(b)

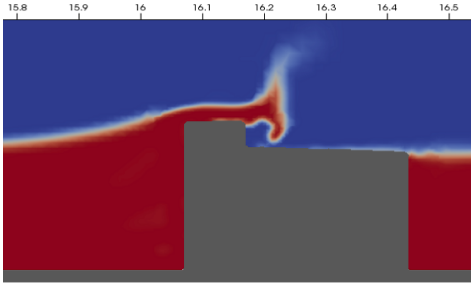

(c)

Figure 6.5: Overtopping analysis for run ID SW502B. a: Cumulative and instant overtopping discharges. b: Instant overtopping at the largest wave overtopping event t=382 s. c: Visual overtopping for the largest wave overtopping event t=382 s.

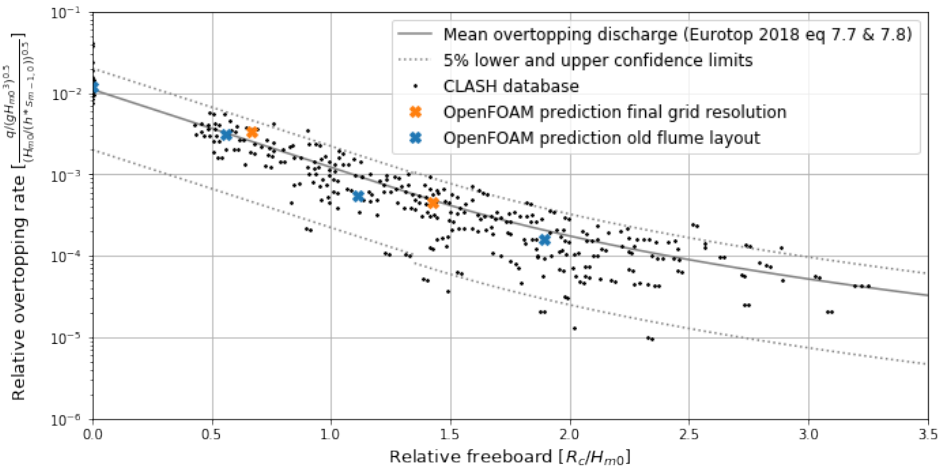

Figure 6.6: Comparison between the CLASH database, the Eurotop 2018 empirical prediction formula (i.e. equation 2.8 and 2.9) and the numerical OpenFOAM prediction using grid 502. Data adopted from Van der Meer et al. (2018)

6.4.2. Effect of ventilated boundary condition on overtopping

The ventilated boundary condition is implemented by Jacobsen et al. (2018) to validate wave force predictions by OpenFOAM. It implements the effect of air entrapment on the calculation of wave forces on a crest wall element. The ventilated boundary condition makes use of a head loss coefficient (ξ_p) and a degree of openness (e_p). For more detailed information on the use of the ventilated boundary condition the reader is referred to section 4.7.2. Not only the wave force prediction is affected by the

implementation of the ventilated boundary condition while it is found that this boundary condition also affects overtopping discharges. The effect of the openness of the ventilated boundary condition on the measured overtopping discharge is found to be significant, differences of 42.7% on mean overtopping discharges are reported in Moretto (2020). In here the same model set-up as used by Jacobsen et al. (2018) was adopted. In Jacobsen et al. (2018) an openness ranging from 0-6 % was adopted and it was concluded that 3% openness performed best for the validation of the wave forces on a crest element. Moretto (2020) found that a lower degree of openness of 0.5 %, results in a 42.7 % higher overtopping discharge compared to a degree of openness of 3%.

In order to quantify the effect of the ventilated boundary condition on overtopping discharges it has been analysed by adapting the openness of the boundary condition on the front face of the sea wall and replacing it by a default No slip boundary condition. Table 6.4 shows the different boundary conditions on the front face of the sea wall and their corresponding effect on the mean overtopping discharge for grid design 502 with a courant number of 0.2. Moreover a temporal comparison is presented in figure 6.7 for the different boundary conditions.

Table 6.4: Different boundary conditions on the front face of the sea wall and the effect on the measured mean overtopping discharge of the sea wall

Run ID	Alpha	U	P	e_p [%]	ξ_p	q_{model} [l/m/s]
	Zero gradient	PressureInletOutletVelocity	Ventilated	3.0	1.5	1.296
	Zero gradient	PressureInletOutletVelocity	Ventilated	0.5	1.5	1.378
	Zero gradient	No Slip	Zero gradient	-	-	1.409

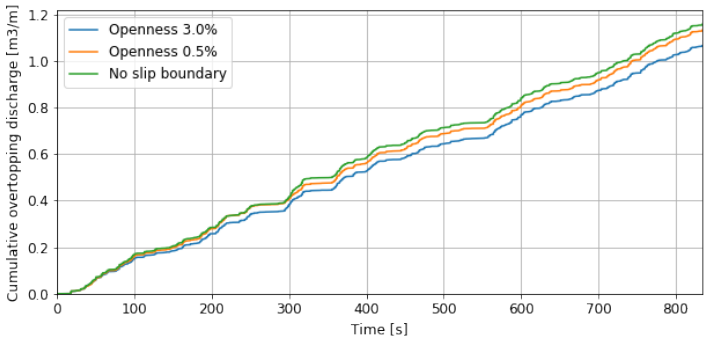

Figure 6.7: Cumulative overtopping discharges for different front face sea wall boundary conditions. 2 Different openness of the ventilated boundary condition and a no slip boundary condition and the effect on the overtopping discharge

Based on table 6.4 and figure 6.7 it is concluded that the effect of the ventilated boundary condition on the overtopping discharges is present but much less pronounced compared to the crest wall case. By reducing the default openness of 3% (blue line) to 0.5% (orange line) an increase of overtopping discharge of 6.3% is found. And by removing the ventilated boundary condition and replacing it by a no slip boundary (green line) an increase of overtopping discharge of 8.7 % is found. This can be explained by the fact that a lower degree of openness results in a ”less permeable” structure. Less air is drained by the front face of the structure which increases the pressure near the front face and therefore increases the water flux in upward direction. This results in higher volumes of water near the crest of the structure and consequently more overtopping.

The differences between the crest wall case and this research are probably due to the impulsiveness of the impacting waves on the structure and the amount of air entrapment that corresponds to the type of impacting wave. The overtopping in this research is mainly related to pulsating wave overtopping which has less air entrapment compared to the more violent impacting waves present for the crest wall case. The crest wall is mainly loaded by impulsive waves due to the initialisation of breaking on the

front slope of the breakwater resulting in more air entrapment during wave impact on the crest wall and thus more effect of the ventilated boundary condition. This effect increases for larger waves in the spectrum which also affect the overtopping discharge the most and therefore shows more effect of the ventilated boundary condition on overtopping discharges. It is therefore recommended to make the degree of openness for the ventilated boundary conditions related to the amount of impulsiveness of the incoming waves. In case more violent wave structure interaction is expected more effort should be included in the correct calibration of the wave forces and overtopping discharges. For less violent wave structure interaction the default model settings can be adopted but also calibration is recommended if data is available. For this research no data on overtopping discharges or wave forces is available and therefore the default openness of 3% is applied at the front face of the sea wall.

6.5. Conclusion

Based on the different steps that have been conducted to calibrate and validate the wave flume hydrodynamics, it is concluded that grid design 502 is the most suitable grid for this research and is therefore selected for the remainder of this study. This grid has a grid resolution of $\Delta x = \Delta y = 0.011m$ (10 grid cells per significant wave height) combined with a maximum courant number of 0.2. It shows the best convergence towards the target resolution in comparison to the required computational time at a location after the coupling zone further in the numerical flume. Moreover the difference between the computed statistical wave parameters of the OceanWave3D output and OpenFOAM output only showed a difference of 1%, which is accepted for the intended uses. Moreover grid 502 with courant number of 0.2 has been validated against the CLASH database and the Eurotop 2018 design guideline and showed high agreement on the predicted mean overtopping discharge.

6.6. Sensitivity analysis

An effect of the interaction between OceanWave3D and OpenFOAM on the output significant wave height was found in section 6.3.2. A standalone OceanWave3D model is used as a target solution for the grid study and because the horizontal resolution of OceanWave3D is found to be normative for the correct coupling between OceanWave3D and OpenFOAM a the sensitivity analysis to the horizontal resolution of the standalone OceanWave3D output is conducted. Furthermore the sensitivity of the adopted wave gauges for the wave reflection procedure is analysed because this procedure is used for the remainder of this study during the parametric study.

6.6.1. Oceanwave3D standalone wave generation

Two additional standalone OceanWave3D simulation have been performed, which are presented in table 6.5. Here different grid resolution of the OceanWave3D standalone model have been varied, while maintaining the same courant number (i.e. manually adjusting the adopted time step to have matching courant number). The extracted significant wave height at wave gauge 3 and the relative computation time has been reported.

Table 6.5: Sensitivity horizontal resolution OceanWave3D at wave gauge 2

# points per wavelength based on L_p	H_s [cm]	$\frac{T_{clock}}{T_{simulation}}$ [min/s]
20	10.79	0.03
40	11.18	0.13
165	11.78	14.8

Comparing the significant wave height with the relative computation time it is observed that 40 grid cells per wave length based on T_p results in the best ratio of accuracy vs computation time. The extracted significant wave height increases for increasing grid resolution, however this increase in computation time is not considered to outweigh the increase in significant wave height.

6.6.2. Wave reflection procedure

This section is used to describe the uncertainties related to using a wave reflection procedure on the statistical wave parameters. During this study often surface elevation signals from wave gauges 5,6 and 7 (see figure 5.1) have been used to separate the incoming and reflected wave field. First the related uncertainties to the use of a wave reflection procedure are described by comparing statistical wave parameters and surface elevation signals at the same location of a run with sea wall (i.e. using the reflection procedure) and a run without sea wall (i.e. no reflection procedure necessary).

Figure 6.8 presents a time series comparison of a run without sea wall and a run with sea wall where the wave reflection procedure has been used to find the incoming surface elevation. A mean under prediction of 4 % is found while comparing statistical wave parameters, which is related to the non linearity within the wave field. The wave reflection procedure is found to be sensitive to the output wave gauge related to the used wave gauges for the procedure and for the use of a highly nonlinear wave field. However, the wave reflection procedure can be used for separating the incoming and reflected wave field but uncertainties related to the procedure should be taken into account. Additionally as explained the wave reflection procedure is more accurate for more linear waves. During the remainder of this research the reflection procedure is used between the HLCS and the sea wall, where waves have been broken on the HLCS resulting in a wider wave spectra. The uncertainties related to using a wave reflection procedure should be taken into consideration.

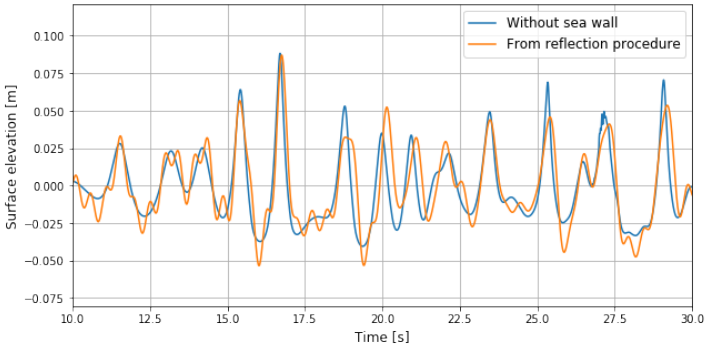

Figure 6.8: Time series comparison of a run without sea wall at wave gauge 7 and the extracted incoming free surface using the reflection analysis of a run with sea wall at wave gauge 7

7

Calibration and validation of HLCS hydrodynamic behaviour

7.1. Introduction

The HLCS is implemented in the numerical flume by applying the porous media concept. The water that flows trough the HLCS experiences resistance which results in energy dissipation. In contrast to assessing the resistance of the individual elements, the porous media concept uses layers with spatially averaged values in order to describe the flow resistance. In this research the flow resistance is described using the van Gent (1995) parameterization to describe the resistance term in the VARANS equations used by OpenFOAM. For more detailed information on the modelling of flow resistance the reader is referred to chapter 4.3 and 4.4. First the modelling of flow resistance for HLCS is addressed and the input parameters of the van Gent (1995) parameterization are analysed. Secondly the numerical structure schematization is explained and different types of schematization are analysed. After that the closure parameters α and β are calibrated and validated using physical model data described in section 3. Moreover the sensitivity of the porous media resistance parameters on the hydrodynamic behaviour of HLCS is analysed and quantified for educational purposes and for the ability to properly adopt different porous media resistance parameters for different structure types, structural elements or placement grids in the future.

7.2. Modelling flow resistance for HLCS

The van Gent (1995) parameterization calculates the flow resistance based on the grading of the elements (D_{n50}), the flow regime related to the size of the elements (KC), the porosity (n_p), and the closure parameters α and β. In order to describe and model the hydrodynamic behaviour of HLCS knowledge on the background of these parameters is necessary. Therefore differences between HLCS using cubipod artificial concrete elements and conventional LCS are analysed.

7.2.1. Nominal diameter D_{n50}

For this research the nominal diameter (D_{n50}) is constant based on the use of artificial concrete elements (i.e. $D_{n50} = D_n = (M/\rho_c)^{1/3}$. Contrary to rubble mound structures, production of concrete elements is conducted in factory conditions with adequate quality control. This results in a very narrow (i.e. an almost constant) grading which results in the ability to adopt a constant D_{n50} with high certainty.

7.2.2. Keulegan-Carpenter number KC

For this research, in contrary to research by Jacobsen et al. (2018), the KC is adopted in the numerical model. Its value, depending on the incoming wave characteristics, is taken as constant over the structure. The KC number is related to the formation and development of the flow boundary layer and eddies during interaction between oscillatory flow and structural elements. The formation of the flow boundary layer and eddies is a time dependent process which also depends on the shape of the el-

ement under oscillatory flow. Due to the sharp corners of the concrete elements, it can be reasoned that in the outer layer of the structure immediate flow separation takes place without the formation of the flow boundary layer. Thus resulting in no energy related to the destruction of the flow boundary layer and therefore no need of adding the KC number in the parameterization of the outer layer flow resistance. On the other hand, the oscillatory velocity magnitude reduces further towards the core of the structure which therefore increases the effect of the flow boundary layer on energy dissipation for the core of the structure. This effect especially increases for wider structures. Moreover, part of this effect of immediate flow separation is implicitly included in the description of the KC number, while this term takes the period of the oscillation and the nominal diameter into account. For a KC number in the range of 13.15 (as calculated using equation 4.7 for the governing boundary conditions) vortex shedding takes place and the flow is predominantly turbulent and drag force related (i.e. large KC numbers). Therefore it is decided to include the effect of the KC while modelling the flow resistance for HLCS. Additionally a sensitivity analysis is included in section 7.4.4 which is used to quantify the effect of the KC number on the predicted wave transmission.

7.2.3. Porosity n_p

The porosity of a structure consisting of artificial concrete elements largely depends on the placement grid of the elements and the elements shape and size. Furthermore, as described in section 2.2.1, the porosity of cubipod HLCS is not constant over the structure height (h_s) and shows large high levels of heterogeneity and large gradients near the boundaries, which has also been noticed by Pardo et al. (2014). These porosity gradients near the boundaries can have a large influence on the hydrodynamic behaviour of HLCS, especially for structures with their crest level close to SWL. Therefore the porosity distribution for artificial concrete unit armour layers is addressed and analysed in more detail in section 7.2.3. The derived porosity distribution is used to construct a schematized porosity profile using 2 numerical layers. These two layers have been implemented with different porosity values in the numerical model corresponding to the derived porosity distribution. However, first the core porosity is analysed and quantified for the HLCS used in this research (in section 7.2.3). Subsequently, a numerical approach is performed to obtain a porosity distribution of a randomly placed cubipod armour layer in section 7.2.3. This porosity distribution in combination with the derived core porosity are used to determine a schematized porosity profile with corresponding layer thickness and outer layer porosity value corresponding to the HLCS used in this research.

Core porosity

According to the cubipod manual (J. R. Medina & Gómez-Martín, 2016), cubipods arrange themselves in random orientations and with homogeneous porosity. This characteristic is used to derive a mean porosity for the core of the HLCS. Two methods to calculate the core porosity are described.

The first method calculates the theoretical mean porosity using the placement grid of the cubipods and equation 7.1 which is based on figure 7.1a.

$$n_p = 1 - \left[\frac{D_{n50}}{a} \cdot \frac{D_{n50}}{b}\right] \tag{7.1}$$

According to (J. Medina et al., 2019) a placement grid with $a/D_{n50} = 1.58$ and $b/D_{n50} = 1.27$ is recommended for a HLCS consisting of cubipods. Moreover, this placement grid has also been adopted during the physical model experiments described in section 3. Using these grid characteristics a theoretical mean porosity of 50% is derived. However, equation 7.1 is a theoretical equation which is derived for conventional cubipod armour units on a slope and the verification for homogeneous structures on a flat bed is still missing.

The second method uses the actual volumes of the cubipods during the physical model test and the total volume of the schematized structure to derive a mean porosity of the structure porosity (i.e. using equation 2.1). Details on the used schematization can be found in section 7.3. From this method a mean porosity of the core layer of 55% is obtained.

The second method uses the outer contour of the structure to derive the mean porosity including the highly porous outer layer, which increases the predicted mean porosity using this method. Also near

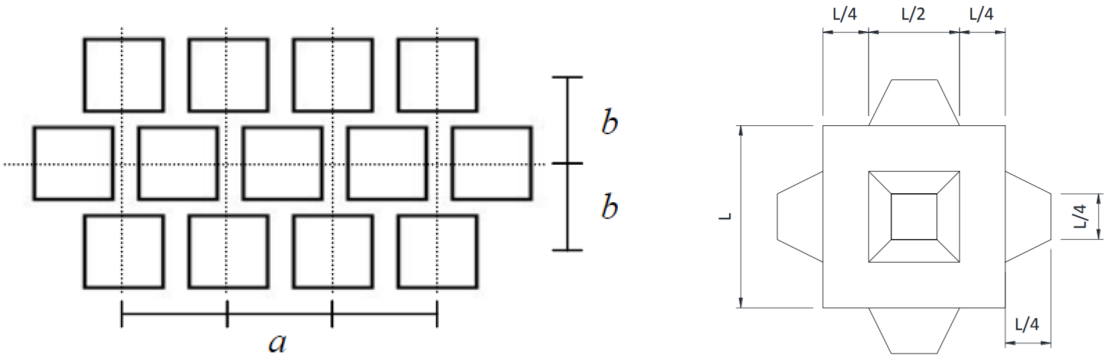

(a) (b)

Figure 7.1: a. Placement grid perpendicular to the slope used for randomly placed cubipod armour units (J. R. Medina et al., 2010) b. Cubipod unit dimensions

the boundaries of the flume in cross-sectional view there are larger gradients which have not been accounted for using this method and which increase the calculated core porosity. For these reasons it is reasonable to assume that the mean porosity of 50% is representative for the core of the HLCS which corresponds to the derived core porosity using the first method (i.e. equation 7.1). Furthermore, in order to quantify the uncertainty related to the decision of core porosity for numerical modelling a sensitivity analysis is conducted which is presented in section 7.4.4.

Porosity distribution

As previously addressed (i.e. in section 2.2.1 and 7.2.3) large gradients and high heterogeneity are found near the boundaries of HLCS. In order to capture these gradients and obtain knowledge on the effect of these gradients a porosity distribution has been derived for randomly placed cubipod layers. 9 different orientations, which represents complete random placement of cubipod armour units are analysed. The dimensions of the analysed cubipod for the assessment of the porosity distribution can be derived from figure 7.1b with $L = 1.0$. The cross sectional area intersecting the cubipod for 15 layers with increments of 0.1 m are calculated. From these cross sectional areas a solidity curve can be constructed which for each cubipod orientation is presented in figure 7.2. The 9 orientations are derived based on a 22.5 degree rotation in plane and a 22.5 degree rotation out of plane of the cubipod unit. This results in a description of all possible orientations with 22.5 degree increments. It should be noted that orientation 2, 3 and 6 are the same as orientation 4, 7 and 8 due to the symmetry of the cubipod unit.

From these solidity curves and the placement grid of the HLCS ($a/D_{n50} = 1.58$ and $b/D_{n50} = 1.27$) a mean (i.e. over all 9 orientations) porosity curve of 1 layer of randomly placed cubipod can be obtained, which is presented in figure 7.3. As expected, large porosity gradients are found over the vertical, especially near the boundaries. In order to derive the mean porosity over a layer of cubipods it should be noted that the porosity profile as presented in figure 7.3 is a porosity profile over a cubipod element with $L = 1.0$ which corresponds to a $D_{n50} = 1.06m$. Because of interlocking between subsequent and layering cubipod units the cubipod manual (J. R. Medina & Gómez-Martín, 2016) prescribes to calculate the mean porosity not based on the height of the cubipod unit but based on a layer thickness of 1 D_{n50}. This results in a mean porosity of 66% and 51% respectively as shown in figure 7.3. The found 51% shows good resemblance with the porosity calculated using the theoretical equation 7.1 (i.e. method 1 with a mean porosity of 50%) and the porosity derived while using the actual number of cubipod units used in the physical model experiment (i.e. method 2 with a mean porosity of 55 %) which gives confidence in validity of the used approach.

In order to use this porosity distribution and implement 2 separate layers with different average porosity values within the numerical model special focus is put on the transitions of the outer cubipod layer during the schematization. The porosity schematization that has been adopted is elaborated in section 7.2.3.

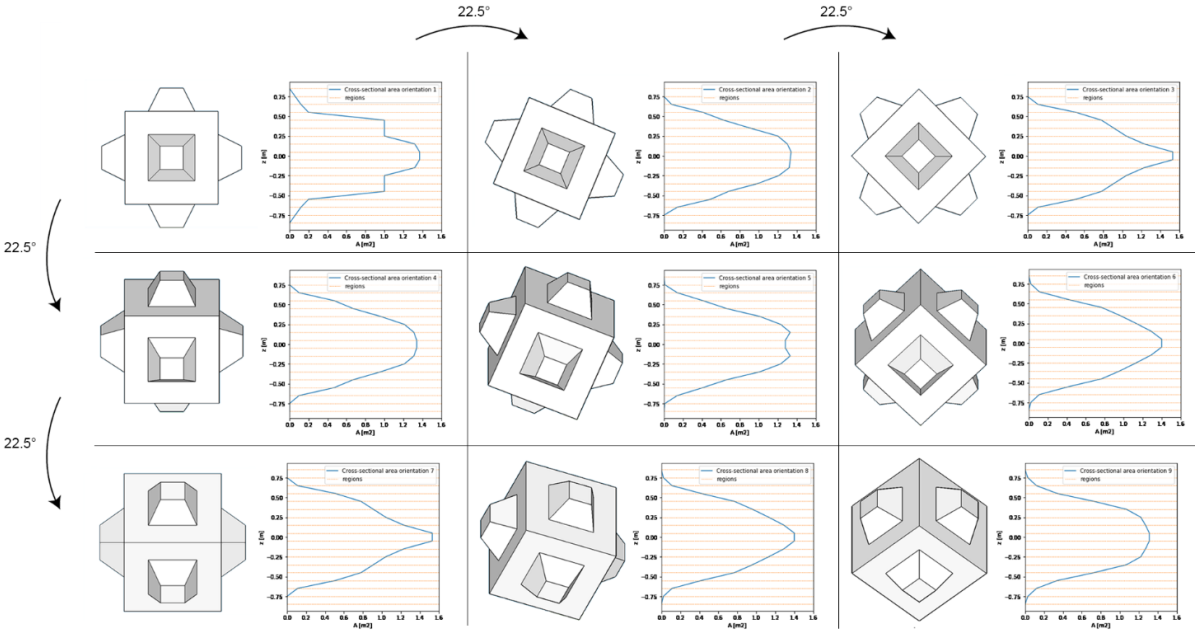

Figure 7.2: Analysed cubipod orientations with 22.5 degree increments, including the corresponding solidity curves

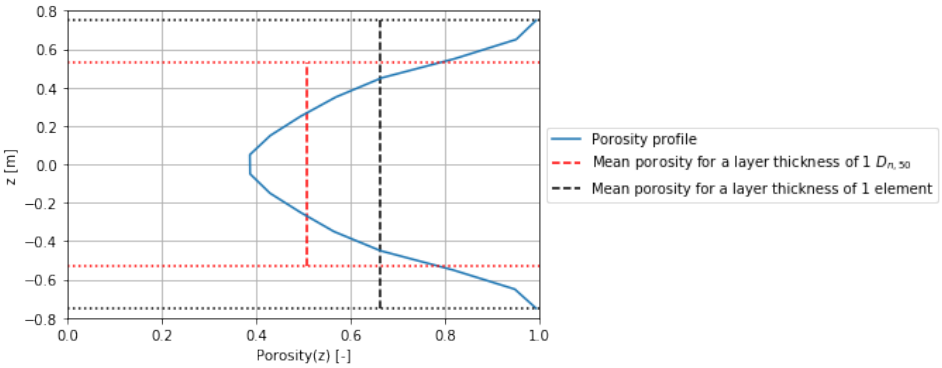

Figure 7.3: Mean porosity distribution of a 1 layer randomly placed cubipod armour with layer formation (a/dn=1.58, b/dn=1.27)

Porosity schematization

Following the derived porosity distribution presented in figure 7.3 the outer part of the structure is separately implemented in the numerical model to give a more detailed representation of the gradients near the boundary. Only two layers have been adopted to describe this porosity profile for the reason that it is not necessary to implement the exact porosity profile using small layer increments while using bulk calibration coefficients with high uncertainty (i.e. α and β). The additional level of detail for implementing multiple layers with smaller increments does not outweigh the automatic loss of detail by calibration of the porous media coefficients. Moreover this is not practical to implement because the implementation is limited to the grid resolution of the numerical grid and a minimum of 3 grid cells per numerical layer is prescribed.

The thickness of the derived outer layer follows from the intersection of the theoretical core porosity value and the porosity distribution, see figure 7.4. The adopted core porosity of 50% is adopted following reasons described in section 7.2.3. The mean porosity of the outer layer is derived by taking the mean value of the porosity within the thickness of the outer layer. This mean porosity (i.e. 75.2 %), is prescribed to the outer layer corresponding with a layer thickness of $0.42D_{n50}$ (i.e. 1.8 cm).

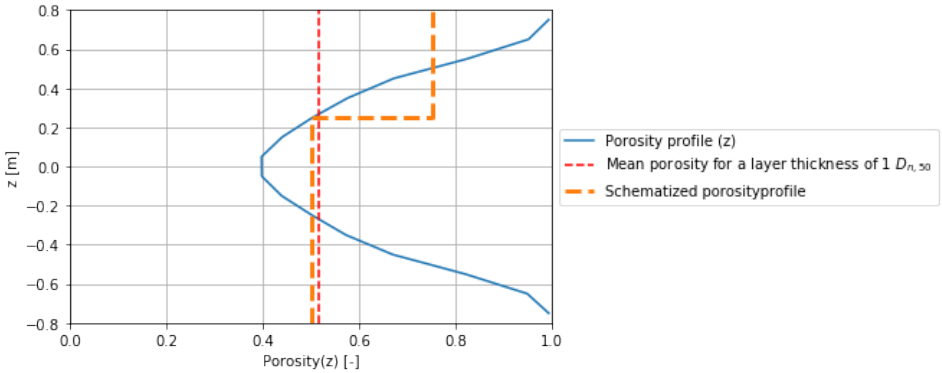

Figure 7.4: Schematized porosity distribution a 1 layer randomly placed cubipod armour with layer formation (a/Dn50=1.58, b/Dn50=1.27). The outer layer has a layer thickness of 0.42 D_{n50} and a porosity of 75.2 % while the core has a porosity of 50%

7.2.4. Closure coefficients α and β

The parameterization of van Gent (1995) uses two bulk closure coefficients (i.e. α and β). As previously noted in section 4.4, there is a large range of α and β values reported in literature and there is no predictive methodology to determine these coefficients in advance, thus calibration is necessary.

Originally van Gent (1995) derived the α and β values to be 1000 and 1.1 respectively based on experimental results under oscillatory flow for rubble mound structures. Based on differences in shape, grading and orientation van Gent (1995) reported ranges of $0 < \alpha < 2780$ and $0.36 < \beta < 1.33$ to account for differences in material properties. In Losada et al. (2016) a detailed overview of all the various reported values for α and β reported in various scientific works is presented. It is identified that the use of a turbulence model influences the reported α and β coefficients. Moreover, the type of model (i.e. experimental experiments or numerical) that is used to derive the reported α and β value affects the coefficients. In this research no additional turbulence model is adopted, therefore the α and β are expected to be larger compared to studies in which a turbulence model is included because all turbulence is now included within these parameters as described in section 4.4.1. On the other hand, α and β values reported in literature measured using physical model tests are expected to be larger compared to numerical values due to numerical diffusion which artificially reduces the energy of the flow within numerical models. With this in mind, various reported literature coefficients for α and β are presented and the backgrounds are analysed.

First of all research of Burcharth & Andersen (1995) suggests a theoretical range of α and β for rock based on empirical relations of $90 < \alpha < 15.000$ and $0.47 < \beta < 11$. These values show large differences in ranges of α and β for the shape, roundness, packing, grading and irregularity of the rocks. For more irregular randomly placed rocks with small grading ($d_{85}/d_{15} \approx 1.3$-$1.4$), α and β values in the range of $980 < \alpha < 2.100$ and $2.4 < \beta < 3$ are reported.

Lara et al. (2011) suggested a set of mathematical formula, presented by equation 7.2, to calculate α and β depending on the porous material properties (i.e. nominal diameter and porosity). This mathematical relationship finds its roots in simplified empirical formulations for permeability and the non linear drag force coefficient and is presented as:

$$\alpha = 4409.22 D_{50}^{0.43} \quad and \quad \beta = 12.27 \cdot \frac{n_p^3}{(1-n_p)^{1.5}} D_{50}^{-0.1075} \tag{7.2}$$

On the other hand various authors (del Jesus et al., 2012; Higuera et al., 2014a; Jensen et al., 2014; Lara et al., 2012) used numerical calibration to determine the α and β coefficients. In del Jesus et al. (2012) a porous dam of crushed rock with a porosity of 0.49 is investigated. In this research a separate turbulence model was included and α and β values were varied ranging from $5000 < \alpha < 20.000$ and $1 < \beta < 6$. The largest correlation with physical model experiments (i.e. the calibration procedure) was found for $\alpha = 2500$ and $\beta = 3.0$.

In Higuera et al. (2014a) also a separate turbulence model was included in the model and α and β values were calibrated for regular waves interacting with a 2D rubble mound breakwater. In this research the α was kept constant (at a value of 2000) and β values were varied for the different layers of the breakwater. The β values in the core and outer armour layer were calibrated as 1.0 and 3.0 respectively. This seems logical as turbulent flow is more dominating in the outer armour layer thus resulting in more turbulent dissipation in the outer layer compared to the core layer. Furthermore, in here also a full three dimensional vertical porous structure was investigated (also investigated in Lara et al. (2012)) and values of $\alpha = 20.000$ and $\beta = 1.5$ were calibrated.

Concluding, all the aforementioned research shows large variability in reported values and is therefore very case specific. This makes applicability of these parameters to other cases with different hydrodynamic conditions questionable. In (Jensen et al., 2014) more effort was put in the visualisation of the complete parameter space of α and β for different flow regimes. Various combinations of α and β were investigated for different types of flow regimes. In this research flow through a porous dam was investigated for three types of flow regime and errors using different α and β values between the numerical and experimental results were reported. In order to determine the type of flow regime Jensen et al. (2014) used the concept of pore Reynolds number. The pore Reynolds number is given as:

$$Re_p = \frac{\langle \bar{u} \rangle D_{n50}}{n_p \nu} \tag{7.3}$$

In which $\langle \bar{u} \rangle$ is the averaged flow velocity per time step per control volume (computational cell) and ν is the kinematic viscosity. Jensen et al. (2014) describes 3 types of flow regime: a Forchheimer flow regime for $10 < Re_p < 150$, a transitional regime for $150 < Re_p < 300$ and a fully turbulent flow regime for $Re_p > 300$. In this research α values were ranging from 0 to 3000 and β values were ranging from 0.5 to 4.0 for the three types of flow regime with a pore Reynolds number of 62 for laminar flow up to a pore Reynolds numbers of 2750 for fully turbulent flow. In this research no separate turbulence model is included, therefore all turbulence is included in the closure coefficients. Figure 7.5 describes the error found for combinations of α and β for the three different flow regimes compared to the experimental results. In here, regions of combinations of α and β can be observed which result in the same error. This indicates that not only one pair of α and β are correct but multiple combinations exist that result in the same hydrodynamic behaviour. The final coefficients, which performed best for all flow regimes, were identified as $\alpha = 500$ and $\beta = 2.0$, but flow regime specific values can be extracted from figure 7.5. For porous flow trough artificial concrete elements very large pore Reynolds numbers $Re_p >> 300$ are expected.

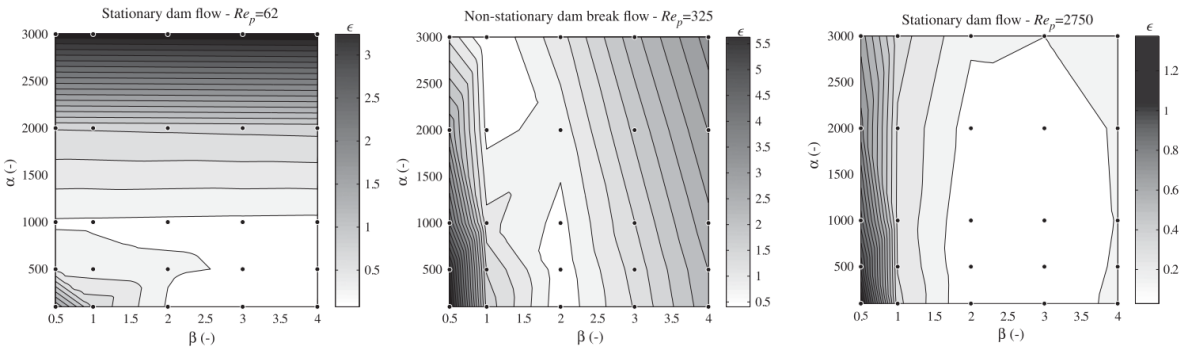

Figure 7.5: Contours of the error between simulated and experimental surface elevation for the three flow regimes, adopted from Jensen et al. (2014)

The KC number was shown to be important by van Gent (1995). However, (Jacobsen et al., 2018) eliminated the KC from the parametrization of van Gent (1995) by setting the KC value to 10.000. In this research the effect of KC is included but also a run with a KC value of 10.000 is performed to visualize the sensitivity of this parameter.

Concluding, as previously stated, the aforementioned literature studies are all based on rubble mound structures. Therefore in the next section (i.e. section 7.2.4) hypothesis are formulated on the

closure coefficients for the applicability of a structure consisting of artificial concrete elements. Because Jensen et al. (2014) noticed only a small dependency of α on fully turbulent flows, see also figure 7.5, the parameter space will mostly be based on variations in β.

Hypothesis
It was observed that the α and β depend on both the flow regime and the material properties. The flow regimes mostly dominates the relative magnitude of α compared to β. Preliminary analysis on the effect of α and β show that α is dominating for laminar flow regimes and β is dominating for turbulent flow regimes. The flow regime can be determined by calculating the pore Reynolds number as reported in Jensen et al. (2014). For artificial concrete elements the pore Reynolds number under design wave conditions is always found to be in the order of $1 \cdot 10^5$, therefore corresponding to a fully turbulent flow regime according to Jensen et al. (2014). For a fully turbulent flow regime Jensen et al. (2014); Losada et al. (2016) reported relatively large effect of the β coefficient which seems logical as this term describes the nonlinear drag which has a larger contribution for more turbulent flow regimes. Additionally it is expected that for artificial concrete elements lower α and β values should be used because less energy is dissipated from the flow, as can be seen in figure 3.2a.

7.3. Numerical structure schematization

The large size of the artificial concrete elements results in a stepped outer contour (i.e. taking the individual elements into account resulting in a stepped wise slope) compared to a smooth slope for rubble mound structures. This opens up different techniques to schematize the HLCS in OpenFOAM from which are analysed in this section to verify the importance of the schematization compared to conventional rubble mound structures. Furthermore the addition of the two layer schematization following from the porosity distribution (described in section 7.2.3) is analysed here.

Two types of schematization of the HLCS are addressed. Main geometrical dimensions are adopted from direct measurements of the cubipod HLCS that has been used during the physical model tests. Dimensions were provided by Odériz et al. (2018) which corresponded to a crest width of 0.11m, structure height of 0.23m and structure base width of 0.59m. The structure height has been determined by averaging obtained crest heights from individual experiments using the reported water level inside the basin and freeboard of the structure. In line with the literature related to wave transmission (i.e. provided in section 2.2.1) the crest height in this research has been determined based on a plane through the upper edge of the cubipod unit (see figure 7.6a and 7.7). The front slope of the HLCS (H/V = 1.5) was kept constant during all simulations.

The first schematization does not take the individual elements into account but schematises the structure using two measured corner points at the base and two measured corner points at the crest and intersect these points to form a polynomial (i.e. presented in figure 7.6). The theoretically derived porosity of 0.5 (derived using equation 7.1) is homogeneously adopted over the structure. The second schematization follows the individual elements to derive the outer contour (i.e. presented in figure 7.7). Additionally the porosity distribution schematization presented in 7.2.3 is adopted in the model. The outer layer has a thickness of $0.42D_{n50}$ and is implemented using 3 grid cells (i.e. equal to 0.016m) which corresponds to approximately $0.38D_{n50}$. However the oblique layers have slightly more width resulting in a mean thickness of the outer layer of $0.42D_{n50}$ which corresponds to the theoretically derived value.

7.3.1. Analysis

In table 7.1 the characteristics of the performed simulations to investigate both types of schematization are shown. The first two runs (i.e. 001A, 002A) differ in the adopted schematization shape with the same homogeneous porosity (50%) over the structure. The third run (i.e. 002B has the porous outer layer included). No sea wall is included for these simulations and therefore no reflection procedure has to be applied. In order to obtain the incoming significant wave height, a model run without HLCS has been performed from which this quantity is obtained.

Following results from simulations 001A and 002A, a difference of less than 1% on the wave transmission coefficient is reported for the different outer contour schematization. The effect of including

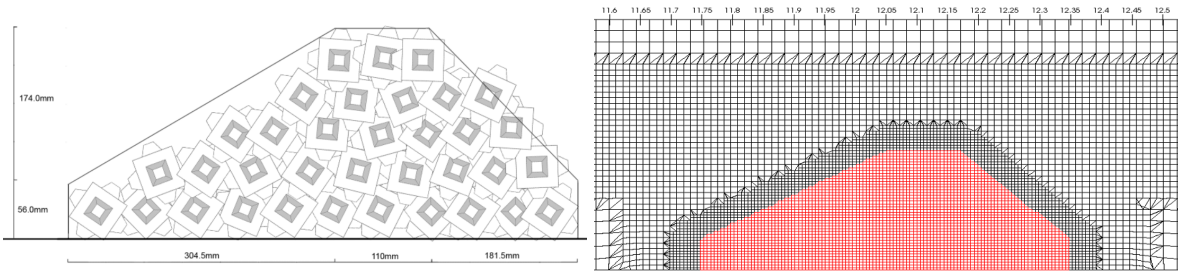

(a) (b)

Figure 7.6: Structure schematization 1: a. Contour design b. Grid around the HLCS, in red the structure

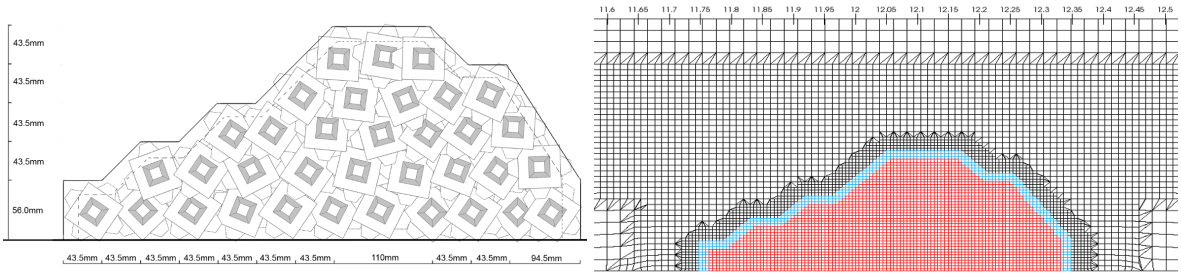

(a) (b)

Figure 7.7: Structure schematization 2: a. Contour design b. Grid around the HLCS, in red the core, in blue the outer armour layer with higher porosity.

the porous outer layer following the derived porosity distribution is also found to be lower than initially expected, a reduction of 2% is reported on the extracted wave transmission coefficient.

From figure 7.8 the difference in wave breaking on the crest of the HLCS is presented. Due to the stepped schematization wave breaking is initialised on the steeper parts of the steps. More wave breaking on the seaward slope of the structure results in more wave interaction with the structure which results in higher dissipation (Zanuttigh & van der Meer, 2008). Using knowledge from equation 2.2, more energy dissipation result in less energy transmission thus a lower transmission coefficient. However according to the reported transmission coefficients in table 7.1, only minor effect is reported on the transmitted significant wave height and transmission coefficient corresponding to the different runs.

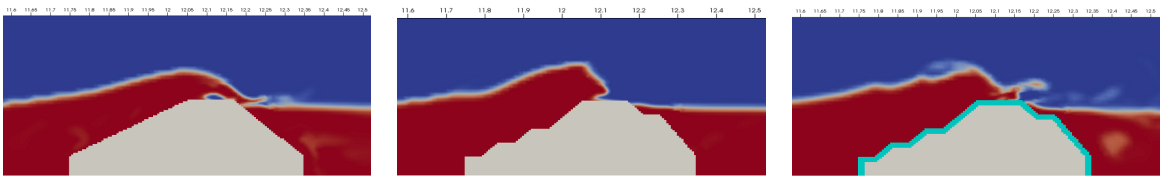

(a) (b) (c)

Figure 7.8: Wave breaking on the sea ward slope effect for the different runs reported in table 7.1 at a large wave event, t=216 s. a. Test ID 001A. b: Test ID 002A. c: Test ID 002B

The addition of the porous outer layer only shows to have a minor effect (2% reduction) on the extracted wave transmission coefficient. Additionally to only analysing the wave transmission coefficient, which does not reveal much detail of the hydrodynamics, also the surface level elevation and wave spectra are analysed. Figure 7.9 shows a more in depth review, where surface elevation and wave spectra are analysed and compared to the incident wave spectra. Both schematizations (001A, 002A) result in similar behaviour regarding surface elevation levels. However, the wave spectra shows less energy in the transmitted spectrum for structure schematization 2 around the peak frequency. More-

Table 7.1: Transmission coefficient comparison for both structure schematizations and the addition of the porosity distribution, using wave gauge 2 and 6 for the incident and transmitted wave characteristics

Test ID	schematization	$H_{s,i}[cm]$	$T_{p,i}[s]$	$R_c[cm]$	α	β	KC	$n_{p,outer}[\%]$	$H_{s,t}[cm]$	$K_t[-]$
001A	1	10.19	1.71	1.0	1000	1.1	10.000	-	5.11	0.50
002A	2	10.19	1.71	1.0	1000	1.1	10.000	50	5.14	0.50
002B	2	10.19	1.71	1.0	1000	1.1	10.000	75.2	5.03	0.49

over, it is found that the secondary non-linear peak in the incident spectra completely disappeared in the transmitted wave spectra for both structure schematizations. The peak period did not shift which is in line with observations made by (van der Meer et al., 2005).

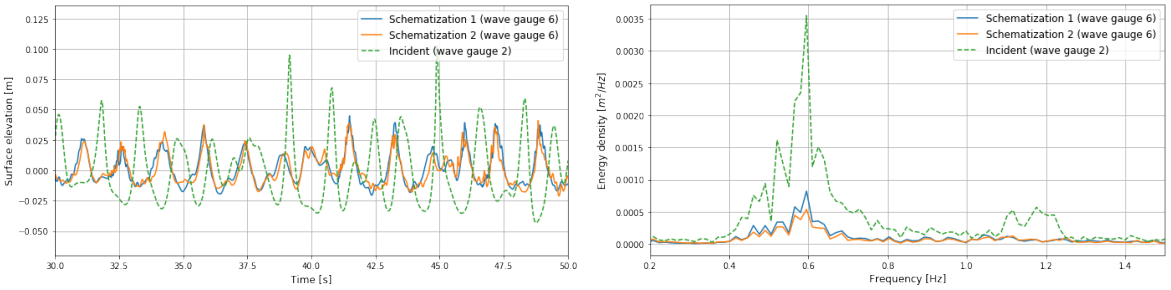

(a) (b)

Figure 7.9: a. Surface elevation comparison for both structure schematizations (001A, 001B) b. Wave spectra comparison for both structure schematizations

7.3.2. Conclusion

The difference between both numerical schematizations and the addition of the porous outer layer result in different wave breaking on the seaward slope of the structure. However only minor effect on wave transmission behaviour is found. A difference on wave transmission coefficient between both schematizations of less than 1% is reported. The addition of the porous outer layer, following the porosity distribution for large concrete armour units, only showed a reduction of 2%. However, due to the higher level of detail of structure schematization 2 it is decided to proceed with this schematization for the remainder of the research. This schematization includes a differentiation in the porous behaviour of the outer layer and core and describes the stepped outer contour for HLCS in a more realistic way.

The addition of a more accurate representation of the porosity distribution did not show to have a large effect on wave transmission behaviour for the bulk hydrodynamic parameter wave transmission coefficient. However for different types of structures (i.e. composite breakwaters) or combinations of structures (i.e. crest wall element on porous breakwater) the effect of including the porosity distribution can give important insight. Especially for more detailed types of data (i.e. force predictions and overtopping) more research is needed to the effect of including the porosity distribution within OpenFOAM. However the additional costs of obtaining detailed information on the porous structure should be in line with the expected gain in results for practical use because only limited effect is reported in this research. The method adopted in this research can be used as foundation to assess the effect of the porosity distribution more thoroughly.

7.4. Calibration

In this chapter the closure coefficients of the parametrization of van Gent (1995) are calibrated to predict the correct hydrodynamic behaviour related to wave transmission over a HLCS consisting of cubipod artificial concrete elements.

7.4.1. Calibration case

The calibration case should be as close as possible to the intended uses of the model. These are to investigate the geometrical layout of the hydrodynamic system using a HLCS to reduce sea wall overtopping for a constant set of hydraulic boundary conditions. Section 2.3 describes the relative importance of overtopping and porous flow on wave transmission. Both are dominated by the crest freeboard of the structure. This research aims to describe the porous behaviour of HLCS with a crest freeboard around zero. Therefore case B5bMM (see table 3.1 with corresponding $H_{s,i} = 9.90cm$, $T_{p,i} = 1.71s$ and $R_c = 1.00cm$, $K_t = 0.47$) is used as calibration case.

Because the hydraulic boundary conditions during the physical model tests are unknown, hydraulic boundary conditions belonging to measured wave characteristics from case B5bMM at wave gauge 2 (see figure 5.1) are prescribed to the model. Running these hydraulic boundary conditions without the structure in the flume results in wave characteristics at wave gauge 2 of $H_s = 10.19cm$ which is 3% higher due to the shoaling of the waves. However during these experiments the mentioned wave characteristics were obtained using a wave reflection procedure. This produces an under prediction of 4% on the significant wave height as described in section 6.6.2. From the combination of the uncertainty in wave height due to the wave reflection analysis, the additional shoaling and the fact that the transmission coefficient is used for comparison (which includes both the transmitted and incoming waves, both affected by the differences in hydraulic boundary conditions and thus almost negligible) it is assumed that this does not compromise the calibration results.

7.4.2. Calibration runs and analysis

Based on literature values for rubble mound structures and hypothesis for HLCS described in section 7.2.4 the runs presented in table 7.2 have been performed. The values adopted for the core numerical layer and the outer layer are separately presented. The same KC value is prescribed for both the core layer and the outer armour layer. The outer layer is very porous and thin, it is therefore likely that the same velocity magnitude is found for the core layer. As explained in section 7.2.4 β is dominant for the turbulent flow regime. Therefore only two values of α have been performed, whereas almost no effect is predicted for variable α values on the results. From figure 7.10 this minor effect of differences in α is confirmed where almost vertical contour lines are found.

Table 7.2: Test characteristics belonging to multiple sets of dimensionless porous media closure coefficients (i.e. α and β) used for the calibration

	Armour				**Core**						
Case	α [-]	β [-]	KC [-]	n_p [%]	α [-]	β [-]	KC [-]	n_p [%]	$H_{s,t}[cm]$	$H_{m0,t}[cm]$	$K_t[-]$
Jacobsen et al. (2018)	1000	1.1	10.000	75.2	1000	1.1	10.000	50	5.03	4.79	0.49
van Gent (1995)	1000	1.1	13.15	75.2	1000	1.1	13.15	50	4.76	4.63	0.47
Lara et al. (2011)	1145	59	13.15	75.2	1145	6.1	13.15	50	3.75	3.77	0.37
Jensen et al. (2014)	500	2.0	13.15	75.2	500	2.0	13.15	50	4.65	4.52	0.46
	500	0.2	13.15	75.2	500	0.2	13.15	50	5.19	4.92	0.51
	500	0.5	13.15	75.2	500	0.5	13.15	50	5.18	4.89	0.51
	500	1.0	13.15	75.2	500	1.0	13.15	50	4.81	4.63	0.47
	500	6.0	13.15	75.2	500	6.0	13.15	50	4.29	4.16	0.42
	2500	0.2	13.15	75.2	2500	0.2	13.15	50	5.19	4.91	0.51
	2500	0.5	13.15	75.2	2500	0.5	13.15	50	5.18	4.87	0.51
	2500	1.0	13.15	75.2	2500	1.0	13.15	50	4.77	4.67	0.47
	2500	6.0	13.15	75.2	2500	6.0	13.15	50	4.37	4.21	0.43

It is noted that in agreement with observations by Jensen et al. (2014) different combinations of α and β result in the wave transmission coefficient. Therefore additional requirements/measurements are needed to determine the correct details of hydrodynamic behaviour if necessary (i.e. measurements of flow velocity inside and outside the breakwater, amount of overtopping water over the crest of the structure, amount of wave reflection etc.).

In order to visualise the parameter range of different values of α and β, figure 7.10 is presented. This figure shows the absolute error (i.e. absolute difference between the measured experimental transmission coefficient of case B5bMM ($K_t = 0.47$) and the predicted transmission coefficient by OpenFOAM) for different values of α and β corresponding to the reported simulations in table 7.2 with a KC of 13.15.

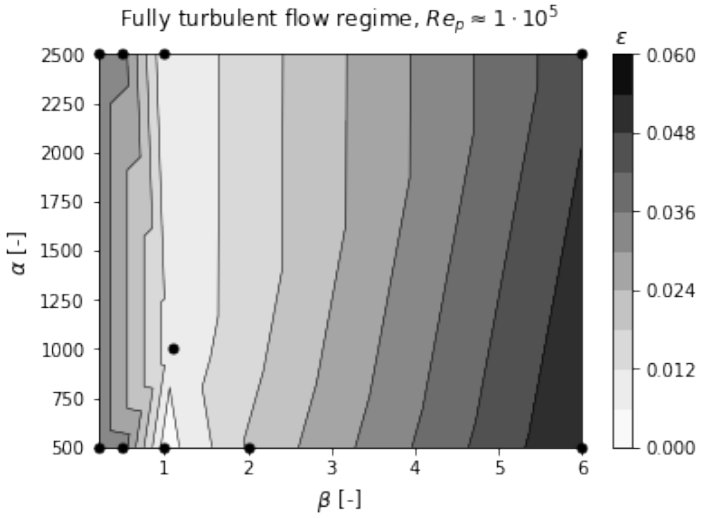

Figure 7.10: Contours of the error between simulated and experimental transmission coefficient

The highest agreement with the calibration case B5bMM is found for a combination of α and β of $\alpha = 500$ and $\beta = 1.0$ which results in an error of the wave transmission coefficient with only an uncertainty of only 0.7%.

7.4.3. Discussion

It has been observed that at one point the further reduction of β does not have a result on the transmission coefficient. Moreover, for further reduction of β the results become theoretically questionable. The theoretical range of α and β as derived by (Burcharth & Andersen, 1995) for rubble mound porous media prescribes β values with a minimum of 0.47. Due to the applicability of these ranges for other types of porous media, concrete elements in this research, slight differences in these ranges can be observed. However, in this research β has been reduced up to 0.2 which indicates that it might become theoretically invalid even for these types of elements and in that case it is only used as a fitting parameter without a physical meaning which should be prevented.

For the calibration of the porous media resistance parameters hydraulic boundary conditions similar to case B5bMM have been implemented. Based on calibration of α and β with constant n_p, KC and D_{n50} it has been found that OpenFOAM is able to predict the transmission coefficient within 0.7% for the calibration case. However this does not imply that all other simulations can also be predicted within this range of error. Especially since the spread in transmission coefficients reported in J. Medina et al. (2019) is very large, as presented in figure 3.2a. Based on knowledge obtained from the calibration of α and β this spread in data most likely cannot only be explained by only adopting α and β as discussed above. It is therefore required to obtain insight in the effect of the other porous media resistance parameters (i.e. n_p, KC and D_{n50}). A sensitivity analysis is performed in section 7.4.4 to gain insight in the sensitivity of n_p and KC on the wave transmission coefficient. Additionally a critical review is needed on the model set-up and the post processing methods adopted during the physical model experiments

and the numerical experiments in this research to make a quantitative comparison.

Critical review of physical model experiments

In this section a bullet point review is presented based on knowledge obtained from analysing the physical model experiments described in section 3 and the effect of the adopted methods on the wave transmission coefficient. The physical model experiments show a large spread in obtained results which cannot only be explained by the physical processes involved but also depend on the measurements techniques and the post processing tools.

- In the physical model experiments a wave reflection analysis is used to extract incoming wave characteristics at wave gauge 2. However due to the bottom slope and restricted water depth, highly nonlinear waves are observed in the wave flume. As described in section 6.6.2 the wave reflection procedure is not able to recognize these non linearities which introduces uncertainty on the results. In this research separate simulations, with and without the HLCS for the different hydraulic boundary conditions, are performed which results in the fact that no wave reflection procedure is necessary for the calibration of the porous media resistance parameters, which affects the uncertainty.

- The hydraulic boundary conditions adopted for the physical model experiments reported in section 3 were not available. Therefore the physical model wave characteristics extracted at wave gauge 2 are adopted as hydraulic boundary conditions for the OpenFOAM numerical experiments, also described in section 7.4.1. This results in the fact that the extracted wave characteristics at wave gauge 2 in the numerical model do not coincide with the extracted wave characteristics at wave gauge 2 for the physical model experiments, a mean difference of 3% on the significant wave height at wave gauge 2 is established.

- For several hydraulic boundary conditions wave breaking is observed on the sea bed slope between wave gauge 2, where the incoming wave characteristics are extracted and the HLCS. The wave breaking in front of the HLCS results in additional energy loss which is not related to interaction with the HLCS yet is accounted for in the experimentally derived transmission coefficient. This additional energy loss results in lower measured transmission coefficients.

7.4.4. Sensitivity analysis

It was found that a decrease of the α and β as the only two calibration coefficients only affect the transmission behavior to a certain extent. In order to obtain higher transmission coefficients, which are achieved by lowering the α and β, physical limits of these parameters come into play. Moreover the spread in the range of data from the physical model experiments cannot only be explained by changing the α and β. In order to access the most important parameters also the effect and sensitivity of other parameters in the parametrization of van Gent (1995) are analysed and the effect on wave transmission is reported.

Porosity (n_p)

As described in chapter 7.2.3 the porosity of HLCS shows large heterogeneity near the boundaries of the structure. Moreover, porosity is one of the most important physical parameters that distinguish a conventional rubble mound structure with a core from a HLCS consisting of large concrete elements. Therefore, a lot of effort has been put into the correct representation of the porosity within the numerical model (i.e. elaborated in section 7.2.3). The core porosity is calculated using three methods (see section 7.2.3) which result in values of 50, 51, 55 % respectively. For the calibration case a core porosity of 50% is adopted and in order to get a better understanding in the sensitivity and the effect of the core porosity on the wave transmission behavior the core porosity has been varied 5% from the base prediction (50%) which results in additional runs with a core porosity of 45% and 55% respectively. The porosity of the outer layer is kept constant at the value derived in chapter 7.2.3 at a value of 75.2 %. The effect of porosity is also important for the prediction of wave transmission behavior related to other types of artificial concrete elements or different placement characteristics with corresponding core porosity and the sensitivity is therefore very interesting.

Table 7.3: Sensitivity of the core porosity on wave transmission behavior. Calibrated values of $\alpha = 500$, $\beta = 1.0$ and $KC = 13.15$ are used.

Case	α [-]	β [-]	KC	$n_{p,core}$ [%]	$n_{p,armour}$ [%]	$H_{s,t}[cm]$	$H_{m0,t}[cm]$	$K_t[-]$
	500	1.0	13.15	45	75.2	4.59	4.42	0.45
	500	1.0	13.15	50	75.2	4.81	4.63	0.47
	500	1.0	13.15	55	75.2	5.19	4.96	0.51

Increasing the core porosity with 5% results in in a 9% increase in wave transmission coefficient. For a 5% decrease of the core porosity a 4% decrease in wave transmission coefficient is observed. Based on these observations it can be concluded that the core porosity of the structure has a large influence on the wave transmission behaviour and should be very accurately assessed for hydrodynamic calculations, for instance following the method described in section 7.2.3. Moreover the wave transmission coefficient shows more sensitivity to an increase in core porosity compared to a decrease in core porosity which comes into play for more porous concrete elements or different placement grids.

KC parameter

As shown earlier in table 7.2 by comparing the Jacobsen et al. (2018) with the van Gent (1995) run, the effect of including the KC number in the flow resistance parametrization can be seen. The KC number is related to the formation and development of the flow boundary layer and eddies during interaction between oscillatory flow and structural elements. By including the KC number in the parametrization the numerical model calculates more flow resistance and thus more energy dissipation within the porous structure. This results in less energy reflection and transmission to the lee side of the structure. The physical meaning of including the KC number in the parameterization is described in section 7.2.2.

A run for which the KC number is practically eliminated from the parametrization by setting it to 10.000 and using the calibrated $\alpha = 500$ and $\beta = 1.0$ results in only a 2% difference in transmission coefficient presented in table 7.4.

Table 7.4: Sensitivity of including the KC number in the parametrization of van Gent (1995)

Case	α [-]	β [-]	KC	$n_{p,core}$ [%]	$n_{p,armour}$ [%]	$H_{s,t}[cm]$	$H_{m0,t}[cm]$	$K_t[-]$
	500	1.0	13.15	50	75.2	4.81	4.63	0.47
	500	1.0	10.000	50	75.2	4.98	4.77	0.49

7.4.5. Conclusion

The combination of a higher core porosity and a highly turbulent flow regime throughout the entire structure for HLCS result in more wave transmission compared to conventional rubble mound LCS. Compared to the proposed calibration coefficients by Jensen et al. (2014) for rubble mound structures it has been found that for HLCS lower values should be prescribed. This results in less energy dissipation trough the porous structure. The corresponding porous media resistance coefficients that should be prescribed to the van Gent (1995) parametrization in OpenFOAM are: $\alpha = 500$ and $\beta = 1.0$ while including the KC number. The largest sensitivity of the other input parameters was found to be the core porosity of the structure (n_p) which underlines the importance of correct representation of the porosity. It is decided to continue the validation of the wave transmission behavior with the calibrated porous media resistance coefficients. However taking into account the uncertainties that belong to the calibration case and the overall spread in physical model data that might affect the spread during validation.

7.5. Validation

Validation of the hydrodynamic behavior of the HLCS is performed using extracted wave transmission coefficients from physical model experiments as described in chapter 3. During these physical model experiments the water level and wave conditions at the offshore boundary were varied instead of changing the structural parameters of the HLCS (i.e. instead of removing or adding a layer of cubipods). For different hydraulic boundary conditions both a model run without the HLCS and with the HLCS have been performed to eliminate the need of a wave reflection procedure, in line with the calibration methodology. The calibrated porous media resistance parameters $\alpha = 500$ and $\beta = 1.0$ have been adopted combined with a core porosity $n_{p,core} = 50\%$, outer layer porosity $n_{p,outer} = 75.2\%$, a nominal diameter D_{n50} of $4.35cm$ and a KC value of 13.15 based on linear wave theory.

7.5.1. Validation and analysis

For the validation experimental results from chapter 3 in the full range of the investigated hydraulic and structural boundary conditions have been used. Validation run B5bLL is used to validate the porous media resistance coefficients for milder wave conditions with the same structure freeboard. Validation runs B5bML and B5bHH have been used to validate the hydrodynamic behaviour for different structure freeboard. Table 7.5 reports the extracted wave characteristics from OpenFOAM at wave gauge 2, which are compared to the OpenFOAM wave characteristics at wave gauge 6 to derive a transmission coefficient $K_{t,OpenFOAM}$. The transmission coefficient extracted from the physical model experiments is also presented as $K_{t,extracted}$

Table 7.5: Wave transmission validation offshore boundary conditions and structure freeboard with corresponding transmission coefficients for $\alpha = 500$, $\beta = 1.0$, $KC = 13.15$, $n_{p,core} = 50\%$ and $n_{p,armour} = 75.2\%$

Test ID	$H_{s,i}[cm]$	$T_{p,i}[s]$	$R_c[cm]$	$R_c/H_{s,i}$	$H_{s,t}[cm]$	$K_{t,extracted}$	$K_{t,OpenFOAM}$
Calibration	10.19	1.71	1.0	0.10	4.81	0.47	0.47
B5bLL	4.40	1.27	1.0	0.23	2.49	0.60	0.57
B5bML	10.40	1.71	-1.0	-0.10	5.53	0.53	0.53
B5bHH	10.48	1.91	4.0	0.38	4.31	0.48	0.41
B5bHM	10.30	1.91	1.0	0.10	5.28	0.55	0.51

Figure 7.12a presents the measured and estimated transmission coefficients for the validation cases. In this figure also the calibration run has been plotted however this run is not used to calculate the RMSE of the validation procedure. The validation of the wave transmission coefficient provided a RMSE value of 0.0427. The calibrated porous media resistance parameters provided good results, but for every case underestimated the extracted transmission coefficient from the physical model experiments. The KC and porosity have not been calibrated but a sensitivity analysis has been adopted to map the effect of porosity and KC on the wave transmission coefficient as described in section 7.4.4.

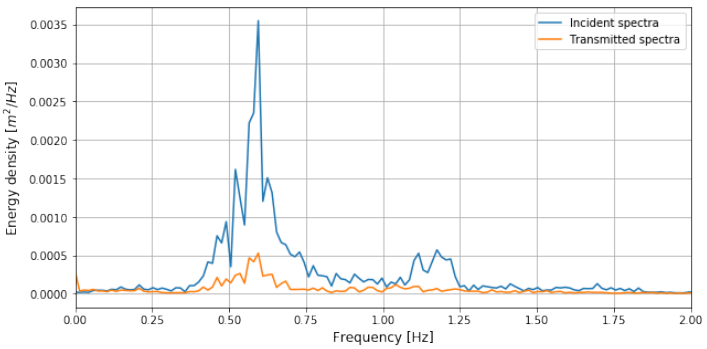

Figure 7.11: Wave spectra change due to interaction with the HLCS

From the validation runs it can be observed that OpenFOAM predicts the most accurate results with a crest level around SWL. This makes sense because the numerical model is calibrated for crest levels around SWL. Overall it is observed that OpenFOAM under predicts the wave transmission behaviour for all performed numerical experiments with a mean under prediction of 6.6%. The most difference between the modelled and extracted transmission coefficient is found for positive crest free boards (i.e. 14.7%), for submerged structures also differences are observed (i.e. 6.7%). Around the SWL OpenFOAM predicts wave transmission behaviour with the least amount of uncertainty (i.e. within 2.6% of the measured data).

A solution to reduce the underestimation of OpenFOAM is to reduce the calibration coefficients α and β but mostly the β as this is the dominant parameter for the turbulent flow regime around HLCS. It is argued based on the validation predictions that β can be lowered to 0.5 to obtain the most accurate results because lowering β results in approximately 8% higher transmission coefficient according to the calibration test runs (table 7.2). However the α and β should remain within the theoretical limits derived for these parameters to present a physically sound numerical prediction. Moreover this will also influence the validation of cases with a crest level close to SWL which are now well described and forms the most interesting case for the remainder of this research where the crest level is close to SWL. Depending on the intended uses of the numerical model calibration coefficients α and β should be adjusted as such that for the given freeboard the correct physical processes are included in the numerical prediction.

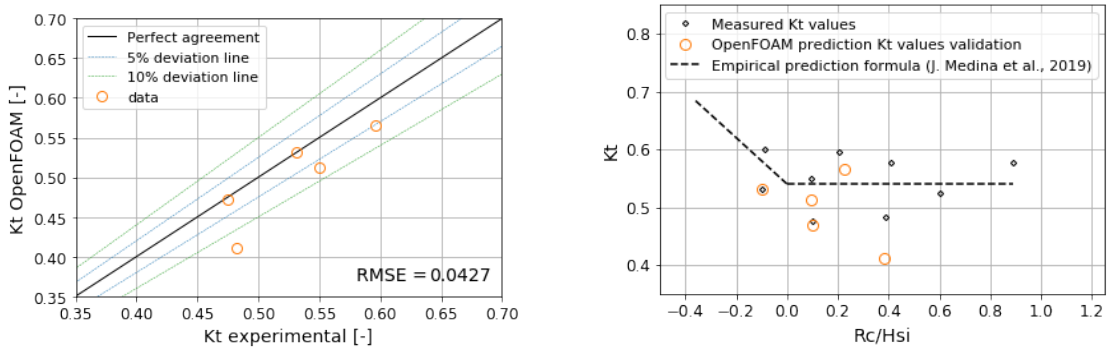

(a) (b)

Figure 7.12: Validation of OpenFOAM to predict wave transmission behind HLCS

7.5.2. Conclusion

OpenFOAM is validated to predict the correct wave transmission behaviour for HLCS using the calibrated porous media resistance parameters described in chapter 7.4. The ranges of applicability that have been validated are: $-0.10 < R_c/H_{s,i} < 0.38$. Preferably more validation runs should have been performed for more extreme cases (i.e. higher/lower crest free boards, differences in crest width) to gain more confidence in the range of applicability of the numerical model. However, for this validation new physical model experiments should be performed as there is no data available for more extreme cases. Overall it is observed that OpenFOAM under predicts the wave transmission behaviour for all performed numerical experiments with a mean under prediction of 6.6%. The most difference between the modelled and extracted transmission coefficient is found for positive crest free boards (i.e. -14.7%), for submerged structures also differences are observed (i.e. -6.7%). Around the SWL OpenFOAM predicts wave transmission behaviour with the least amount of uncertainty (i.e. within -2.6% of the measured data). This underlines the effect of using the numerical model inside or outside the validated ranges, which brings higher levels of uncertainty that should be taken into account by the user of the model.

Considering all the variability and uncertainty regarding the exact mimicking of the physical model experiment and the uncertainties of the physical model experiments itself combined with the intentions of the numerical model the underestimation of OpenFOAM is found to be acceptable for the intended

uses of the numerical model. It is therefore decided to continue with these validated porous media resistance parameters. However the overall underestimation should be taken into account for further analysis using these parameters. Additionally for different model set-ups of hydrodynamic behaviour for HLCS the porous media resistance parameters need to be re-calibrated by the user of the model. This can be done using knowledge from the sensitivity analysis on the different porous media resistance parameters (n_p and KC) which is included in section 6.6.

8

Analysis of geometrical layout and design considerations

8.1. Introduction

During previous chapters the OpenFOAM model is calibrated and validated to correctly describe the hydrodynamics around a HLCS consisting of cubipod artificial elements. The validated model is used in this chapter to extent the limits of current knowledge and present the most interesting design considerations for a HLCS to reduce sea wall overtopping. One set of hydraulic boundary conditions are applied for the parametric study. All boundary conditions can be found in table 5.2. The effect of the main geometrical layout parameters, crest width (B), freeboard ($R_c = h_c - h$) and distance between the HLCS and sea wall (L_{pool}) are analysed. These geometrical layout parameters are made dimensionless to the incoming wave characteristics (i.e. $B/H_{s,i}$, $R_c/H_{s,i}$ and L_{pool}/L_p). The wave transmission coefficient (K_t), mean water level set-up near the sea wall ($\overline{\eta}_{seawall}$), cumulative mean overtopping discharge (q), hydraulic gradients over the HLCS ($i_{\overline{\eta},HLCS}$) and basin ($i_{\overline{\eta},basin}$) and temporal variations in water level set-up and overtopping are analysed.

First the model set-up is described and the adopted numerical grid changes for varying geometrical layout parameters are elaborated. Next the adopted methods to extract the hydrodynamic characteristics from the model are described. Additionally an initial parametric sensitivity study is conducted based on a bandwidth of the most practical layout configurations described in appendix C. This analysis is used to obtain initial insight in the behaviour of the system and find interesting phenomena that need more attention. Subsequently, the three main geometrical layout parameters are independently analysed using the extracted hydrodynamic characteristics. The effect of geometrical layout on the hydrodynamic characteristics are analysed and compared to literature values and hypotheses. Furthermore a comparison is made between the predicted overtopping by OpenFOAM and the Eurotop guideline by only taking the transmitted waves into account (i.e. no water level set-up and low frequency basin hydrodynamics) to verify the added value of OpenFOAM compared to quick assessments.

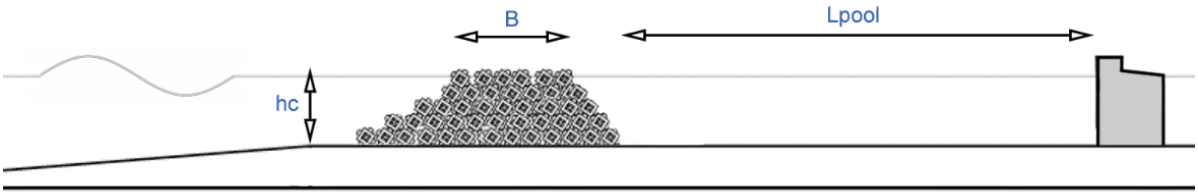

Figure 8.1: Outline of the parametric study, indicated in the figure are the parameters that have been investigated

Figure 8.1 presents the parameters that are investigated during this parametric study. In section 8.2.2 the changes to the parameters from figure 8.1 and the corresponding changes to the numerical grid are described.

8.2. Model set-up

In this section the adopted hydraulic boundary conditions, the grid adaptions to changes in geometrical layout and the methods used to extract data from the model are elaborated.

8.2.1. Hydraulic boundary conditions

Hydraulic boundary conditions resulting in severe overtopping (i.e. more than 50-200 l/s/m at prototype scale, corresponding to structural damage at a non paved revetment sea wall (Ciria et al., 2007)) are prescribed at the inlet boundary. The adopted boundary conditions can be found in table 5.2 combined with a sea wall freeboard of 6 cm. By selecting hydraulic boundary conditions corresponding to severe overtopping, the effect of numerical finite precision, truncation errors and other numerical artifacts are minimized compared to the bulk characteristics. Using these boundary conditions a base overtopping of $q_{initial} = 1.28$ l/s/m is predicted by OpenFOAM (simulation SW502B) which corresponds to a prototype overtopping discharge of 294 l/s/m.

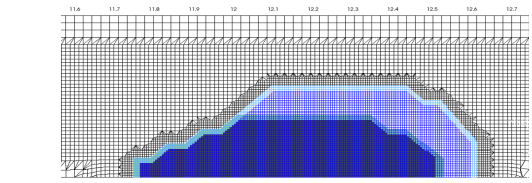

(a) $-0.4 < R_c/H_{si} < 0.4$

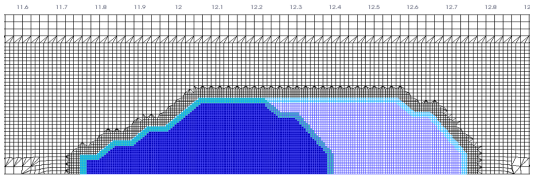

(b) $1.5 < B/H_{si} < 4.5$

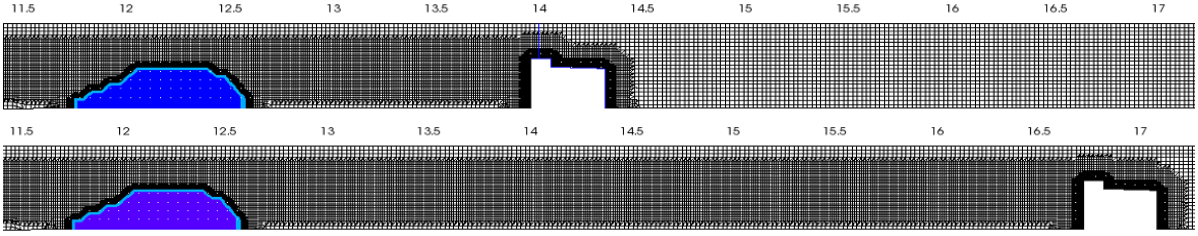

(c) $0.33 < L_{pool}/L_{m-1,0} < 1.0$

Figure 8.2: Varying procedure for varying a: crest height b: crest width c: basin length

8.2.2. Geometrical layout adaptation

Here the adaptation of the geometrical layout and the corresponding effect on the numerical grid is described. The OpenFOAM model is adopted as such that only the effect of one geometrical parameter is varied (i.e. the crest width (B), freeboard ($R_c = h_c - h$) and basin length (L_{pool})) whereas the other parameters are kept constant. Additionally the water level is kept constant to have constant wave characteristics within the flume independent of the geometrical layout. The adaptations to the numerical model are presented in figure 8.2. For varying basin length the HLCS remains at the same location and the sea wall is moved in land ward direction. For varying crest width the crest width of the HLCS is increased in land ward direction, while also moving the sea wall in land ward direction to have a constant basin length. The crest height of the structure is varied by increasing or decreasing the crest height with 1 layer of cubipods while also widening the structure to have a constant crest width. Additionally also a movement of the sea wall is required to have a constant basin length. The adopted procedure for changing geometrical parameters is described in more detail in appendix C.

8.2.3. Data extraction

In this section the various methods used to extract hydrodynamic characteristics are described. These characteristics are used to analyse the hydrodynamics of the system in relation to the changes in geometrical layout.

Wave transmission coefficient (K_t)

The transmission coefficient is defined as the ratio between the significant wave height in the lee of the structure (the transmitted significant wave height) and the significant wave height in front of the structure (the incoming significant wave height). Due to the highly reflecting sea wall, the wave field inside the basin is composed of left and right going waves. For the definition of the transmission coefficient only the right going waves should be considered (i.e. the transmitted significant wave height over the structure). In order to obtain the transmitted significant wave height, a wave reflection procedure is applied (see section 6.2.1 and 6.6.2 for more information on the applied reflection procedure).

For the parametric study wave gauge 5,6 and 7 (see figure 5.1) are used to perform the wave reflection procedure with output at wave gauge 6. The transmitted significant and spectral wave heights are extracted from transmitted surface elevation signals over the full simulation period (i.e. 0-680s). The geometrical layout and corresponding model set-up is slightly different for each simulation (see section 8.2.2) which makes it is not always possible to use wave gauges 5,6 and 7 to extract the transmitted wave characteristics. In that case the bulk wave gauges at $x = 13.0m$, $13.2m$, and $13.5m$ are used for the wave reflection procedure with output at $x = 13.2m$. There is no observed effect of using these different wave gauges to extract the transmission coefficient whereas the same transmission coefficient is found using both methods.

Mean water level set-up ($\overline{\eta}_{seawall}$)

The mean water level set-up near the sea wall is important for overtopping predictions because this increase of mean water level artificially reduces the crest freeboard of the sea wall. Water level set-up is a consequence of wave momentum release due to wave breaking and the conservation of mass transport of water over the crest. In section 2.4, this phenomena is described in more detail. Consequently smaller waves are able to overtop the sea wall during events of higher water levels. This results in larger individual overtopping volumes and a higher mean overtopping discharge.

The mean water level set-up is extracted from the model using one of the bulk wave gauges (with 0.1 m increments) within the numerical flume that is closest to the sea wall. Due to differences in geometrical layout for different simulation runs, a different wave gauge (i.e. each time the one closest to the sea wall) is used for the extraction of the mean water level set-up. No re-circulation system is implemented in the model thus resulting in gradual filling of the basin during the simulation which is compensated by a return flow over and through the HLCS resulting in hydraulic gradients within the basin. Large spatial variations of the mean water level set-up were observed. These spatial variations are elaborated in the next section.

Spatial distribution of mean water level set-up within the basin ($i_{\overline{\eta},HLCS}$ and $i_{\overline{\eta},basin}$)

It was found that the mean water level set-up is not constant over the basin length. The extracted mean water levels are dependent on the location within the flume where they are extracted. The slopes in water level that is formed over the HLCS and within the basin are a result of mass conservation within the basin and friction over the structure. At the start of the simulations the water level along the flume is equal to SWL. Once waves start interacting with the HLCS (i.e. the breaking of waves on the LCS resulting in wave-induced water level set-up and water mass flowing through the HLCS), the basin is filled with additional water. Depending on the amount of storage volume inside the basin the water levels inside the basin gradually increase. Mass conservation results in a flow of water over and through the HLCS back offshore (i.e. a return flow due to mass conservation). The amount of flow over and through and thus the ability of the HLCS to restore the water level depends on the geometrical layout of the HLCS. A dynamic equilibrium is formed between the amount of incoming water, the hydraulic gradient over the HLCS and the hydraulic gradient inside the basin.

In order to obtain insight in this spatial distribution of the mean water levels within the basin for different geometrical layout parameters the mean water level for all bulk wave gauges are plotted for the corresponding simulations. In here, three important locations are presented and highlighted which are the start of the HLCS, the end of the HLCS and the location of the sea wall. Using mean water levels from these three locations, the mean hydraulic gradient over the HLCS and inside the basin are

extracted. The depth averaged flow velocities that are found corresponding to the gradients in the basin are in the order of 0.63 - 2.4 m/s using the Chézy formula ($u = C\sqrt{hi}$) with a Chézy constant C=50 and a hydraulic radius equal to the water depth at SWL (i.e. h = 0.23 m). These types of flow velocities are found to be physically sound and in line with the expectations.

Temporal variations in water level set-up within the basin

It has been found that the interaction between wave groups of slightly different periods result in wave group formation which creates a pulsating effect of the water level inside the basin. Generally wave groups have a period of 6-8 times the period of the underlying waves that generate the wave group. More details regarding wave groups can be found in section A.4.3. Additionally seiching effects inside the basin create water motion on larger time scales. In order to obtain insight in the correlation between the temporal water level set-up due to these low frequency waves and the observed overtopping events the temporal behaviour of the mean water level resulting from a wave gauge closest to the sea wall is included. The temporal behaviour has been obtained using a low-pass filter which aims at capturing the temporal water level set-up with a 0.1 frequency, corresponding to incoming wave groups of $6 \cdot T_p \approx 10s$.

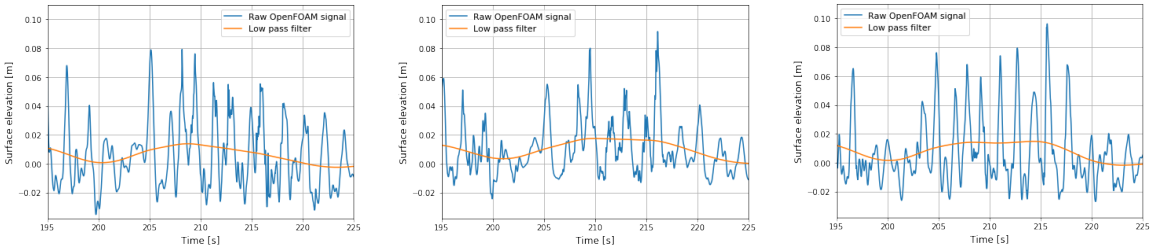

(a) $R_c/H_{s,i} = 0.0$ (b) $B/H_{s,i} = 4.5$ (c) $L_{pool}/L_p = 1.0$

Figure 8.3: The applied low pass filter including the raw surface level elevation near the sea wall for a: $R_c/H_{s,i} = 0.0$. b: $B/H_{s,i} = 4.5$. c: $L_{pool}/L_p = 1.0$

Overtopping discharge (q)

The overtopping discharge is determined using an overtopping face in OpenFOAM. This face reports the amount of water passing through it for every time step of the simulation. See section 4.7.1 for more detailed information the measurement technique to extract the amount of water passing through a computational cell in OpenFOAM. These individual overtopping volumes are added for the total simulation period (i.e. 0-680 s) resulting in a cumulative overtopping curve. By dividing the cumulative overtopping volume by the total simulation duration (i.e 680 s) a mean overtopping discharge is obtained.

8.3. Initial sensitivity study

An initial sensitivity study is performed to study the effect of the independent geometrical layout parameters on the hydrodynamics inside the basin and the predicted overtopping discharge. The outcome of the initial sensitivity analysis is used to visualise the most important design parameters and forms the foundation for the remainder of the parametric study. For the adopted boundary conditions the reader is referred to table 5.2. The water depth inside the basin is 23 cm and the incoming significant wave height is characterized by $H_{s,i} = 11.24cm$. Initially a simulation is performed for $R_c/H_{s,i} = 0$, $B/H_{s,i} = 3.0$ and $L_{pool}/L_p = 1.2$ (also referred to as the base case in table C.2). Next, the crest height, crest width and basin length are independently varied with 19%, 50% and 50% to the base case respectively as described in section 8.2.2. These variabilities correspond to the ranges $-0.4 < R_c/H_{s,i} < 0.4$, $1.5 < B/H_{s,i} < 4.5$ and $0.6 < L_{pool}/L_p < 1.8$. For considerations related to this chosen bandwidth the reader is referred to appendix C. Percentile increase or decrease between the obtained output (i.e. $\overline{\eta}_{seawall}$, K_t and q) compared to the base case are reported in table 8.1. This table is divided in three parts, each representing one of the main geometrical layout parameters.

Using this knowledge, is can be concluded that high levels of non-linearity between the parameters are observed without a straightforward trend. Furthermore no relation is observed between the extracted wave transmission coefficient and water level set-up to to predict the mean overtopping discharge for this range of geometrical parameters. The geometrical parameter with the largest effect on predicted overtopping discharge is found to be the crest height of the HLCS. For a varying crest

Table 8.1: Sensitivity study of the effect of changes in geometrical layout on the hydrodynamic output generated by OpenFOAM. The first columns representing changes in structure height, crest width and basin length respectively.

h_c	Initial	Unit	- [%]	+ [%]	B	Initial	Unit	- [%]	+[%]	L_{pool}	Initial	Unit	- [%]	+ [%]
h_c	23	cm	-19	+19	B	33	cm	-50	+50	L_{pool}	277	cm	-50	+50
$\overline{\eta}_{seawall}$	0.47	cm	-10	0	$\overline{\eta}_{seawall}$	0.47	cm	+9	+30	$\overline{\eta}_{seawall}$	0.47	cm	+2	+28
K_t	0.37	-	+43	+8	K_t	0.37	-	+27	-19	K_t	0.37	-	0	0
q	0.15	l/s/m	+198	-46	q	0.15	l/s/m	+86	-63	q	0.15	l/s/m	+102	-50

height of -19 % (i.e. resulting in an submerged structure) a 198% increase in overtopping discharge is reported, while varying +19% (i.e. resulting in an emergent structure) only a reduction of 46% is reported. The mean water level set-up near the sea wall shows to be the least sensitive to changes in geometrical layout. Additional analysis is needed to obtain more insight in the design sensitivities. In the following sections more detailed analysis is performed related to the main geometrical parameters including additional simulations.

8.4. Effect of crest freeboard R_c

Table 8.2 presents the performed simulations by changing the crest height of the HLCS. In here, simulation averaged (i.e. over the full simulation period 0-680 s) hydrodynamic characteristics are reported as described in section 8.2.3.

Table 8.2: Table with parametric test runs related to the relative freeboard of the HLCS and the effect on wave transmission, water level set-up, hydraulic gradients and overtopping.

Test ID	H_{si} [cm]	$R_c/H_{s,i}$ [-]	$B/H_{s,i}$ [-]	L_{pool}/L_p [-]	K_t [-]	$\overline{\eta}_{seawall}[cm]$	$i_{\overline{\eta},HLCS} \cdot 10^{-3}$[-]	$i_{\overline{\eta},basin} \cdot 10^{-3}$[-]	$q[l/s/m]$	$q/q_{initial}[-]$
Rch-0.4	11.24	-0.4	3.0	1.2	0.53	0.42	-0.66	3.19	0.45	0.35
Base	11.24	0.0	3.0	1.2	0.37	0.47	1.39	3.23	0.15	0.12
Rch+0.4	11.24	0.4	3.0	1.2	0.40	0.47	2.48	2.54	0.08	0.06
Rch+0.8	11.24	0.8	3.0	1.2	0.44	0.34	1.84	2.49	0.10	0.08

The data presented in table 8.2 is also visually presented in figure 8.4. In figure 8.4a the wave transmission coefficient and mean overtopping discharge corresponding to different crest height of the HLCS are presented. Additionally figure 8.4b presents the mean water level set-up near the sea wall and mean overtopping discharge for different crest height of the HLCS.

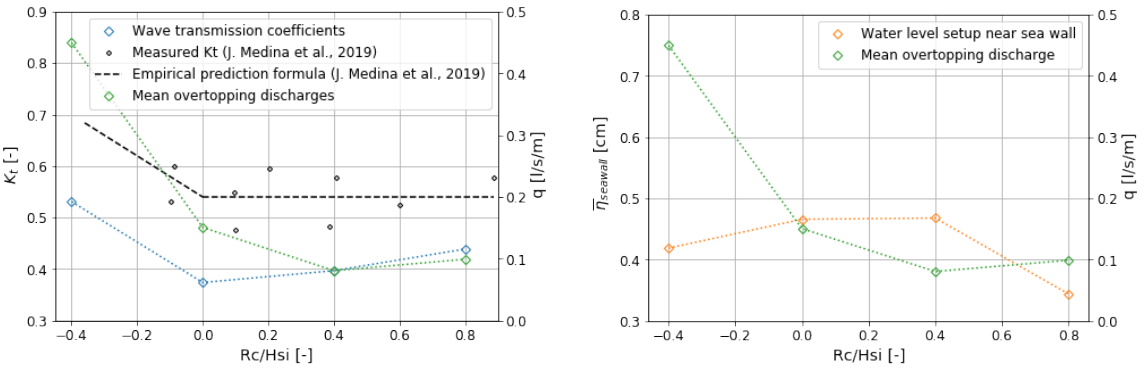

(a) (b)

Figure 8.4: a. Effect of relative crest height for $B/H_{s,i}$ = 3.0 and L_{pool}/L_p = 1.2 on a. wave transmission coefficient and the predicted overtopping discharge and b. Water level set-up and overtopping discharge

For increasing crest height a decay in the form of an exponential function of the mean overtopping discharge is found, see figure 8.4a. This behaviour in overtopping reduction is closely related to the trend observed for wave transmission for different crest height. The wave transmission trend for HLCS,

see figure 8.4a reveals a slight increase of wave transmission for emergent structures (i.e. $R_c \geq 0$). This is a counter intuitive finding that reveals the difference in hydrodynamic behaviour between HLCS and conventional rubble mound structures. For conventional rubble mound structures a continued reduction in transmission coefficient is found for $R_c \geq 0$ in contrary to the trend observed for HLCS. Consequently this behaviour for $R_c \geq 0$ is now studied in more detail.

8.4.1. Wave transmission trend for $R_c \geq 0$

The results in wave transmission behaviour are compared to the transmission coefficients found by J. Medina et al. (2019). In figure 8.4a the black dotted line and blue dotted line are compared and a striking resemblance in shape is found. J. Medina et al. (2019) predicts a constant transmission coefficient for emergent structures of a 5 layer-cubipod HLCS. The trend in transmission behaviour for increasing crest on the other hand is parallel to the trend observed by J. Medina et al. (2019) for HLCS. This is due to the fact that the HLCS used by J. Medina et al. (2019) has a smaller crest width (i.e. $B/H_{s,i} = 1$) compared to the data obtained from the OpenFOAM model (i.e. $B/H_{s,i} = 3$). This results in a different magnitude of wave transmission coefficient (i.e. a parallel trend with higher K_t values).

The constant transmission behaviour for emergent structures can be explained considering the porous structure of HLCS in relation to wave breaking and porous flow. Wave energy transmission is a result of the amount of energy dissipation by wave breaking on the crest of the structure and the amount of dissipation by porous flow. As explained in section 7.2.3 the porosity of HLCS is higher compared to conventional rubble mound structures. Energy is better able to be transported through the larger pores of the HLCS compared to conventional rubble mound structures. This increases the amount of wave transmission by porous flow. Additionally the wave breaking process is affected by the large porosity. Due to the fact that more water can enter the porous structure of the incoming wave, the wave slightly sinks into the structure. Therefore the shoaling of the wave is affected and the wave experiences a slight delay in wave breaking (due to the higher porosity). This results in less energy dissipation on the crest of the structure according to Hattori & Sakai (1994). Additionally for emergent structures wave energy is mostly going through the porous structure. This could result in more breaking wave energy penetrating in the structure and going through the HLCS instead of getting dissipated by turbulence on the slope of the structure. According to this hypothesis the amount of energy dissipation by wave breaking on the crest of the structure is then reduced. This results in an increase of the amount of energy that can be transmitted. Both the effects of energy dissipation by porous flow and wave breaking result in explanations for the higher wave transmission of HLCS compared to conventional rubble mound structures.

The fact that in this research a slight increase in transmission coefficient for emergent HLCS is found in contrary to the constant trend observed by J. Medina et al. (2019) is probably related to the uncertainties related to the accuracy of the measurements (i.e. the uncertainty related to the adopted wave reflection procedure and measurement duration). The exact trend, slightly increasing or constant for emergent structures, cannot clearly be defined while this research only provides 2 data points for emergent structures with increasing trend and are in the data range of the data found by J. Medina et al. (2019). Therefore most likely a constant trend is found for emergent HLCS.

8.4.2. Water level set-up

The mean water level set-up near the sea wall, see figure 8.4b shows an increase with increasing freeboard until the maximum, found around zero freeboard, after which the mean water level set-up reduces (i.e. for emergent structures). This trend in mean water level set-up shows resemblance to observations made by Loveless et al. (1998) where also the highest mean water level set-up is predicted with crest levels around SWL, see figure 2.8b.

Looking at the spatial distribution of the mean water level inside the wave flume presented in figure 8.5, a varying positive gradient in water level set-up within the basin is observed for different crest freeboard. The depth averaged flow velocities corresponding to these basin gradients are in the range of 1.2 - 1.35 m/s. The hydraulic gradient within the basin corresponds to the observed trend for the mean water level near the sea wall where the largest gradient is predicted for zero freeboard and

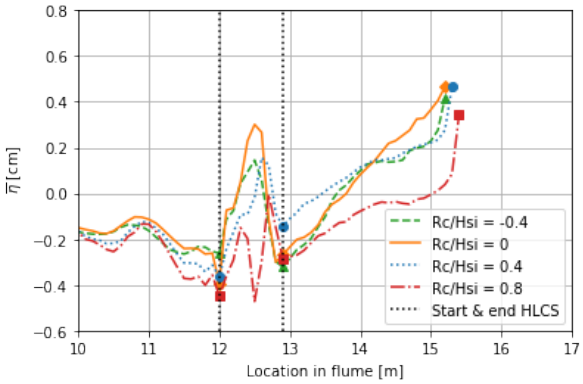

Figure 8.5: Spatial distribution of mean water level inside the flume for varying crest freeboard

decreasing for emergent and submerged structures. In front of the HLCS, the standing wave pattern resulting from wave reflection of the HLCS is visible.

8.4.3. Temporal variations

The temporal variation of the mean water level near the sea wall in relation to the measured overtopping events is presented in figure 8.6. The method to obtain the temporal water level set-up is explained in section 8.2.3. The maximum difference in temporal water level set-up around the largest overtopping event (i.e. t=220 s) is in the order of 1.5 cm for the range of performed simulations.

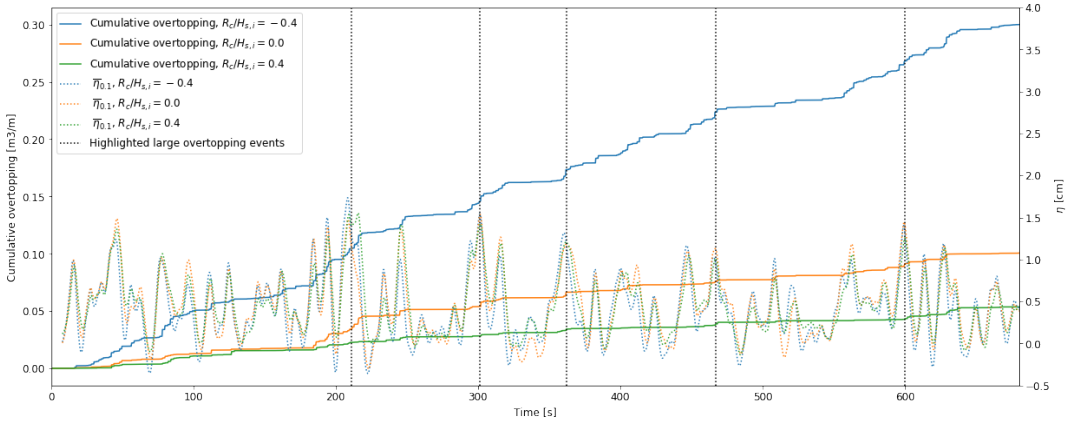

Figure 8.6: Effect of relative crest width on overtopping volumes and temporal water level set-up

From figure 8.6 the same trend in temporal behaviour of the mean water level for different crest freeboard is observed. Correlation between high mean water levels near the sea wall and observed overtopping events is found by plotting vertical lines in figure 8.6. Furthermore, the amount of individual overtopping events are constant for $R_c/H_{s,i} \geq 0.0$ whereas the volume per overtopping event differentiates the two curves, especially for the larger overtopping events (like the ones around t=220 s). For submerged structures more individual overtopping events are found combined with higher individual overtopping volumes for the same events which result in a higher mean overtopping discharge.

8.4.4. Change in spectral shape

The wave transmission coefficient only contains hydrodynamic information on the wave heights behind the HLCS. However for several other hydrodynamic computations (e.g. wave overtopping, wave run-up and morphodynamic behaviour) not only information on the wave heights is necessary but also on the wave period. Information about the wave period can be found in the wave spectrum, which is consequently analysed. Van Der Meer et al. (2000) noticed that the interaction between waves and LCS results in spectral changes. These spectral changes are mostly caused by wave breaking where

wave breaking processes may generate one or more transmitted waves at the lee side of the structure and energy dissipation through the structure combined resulting in a spectral energy shift towards the higher frequencies.

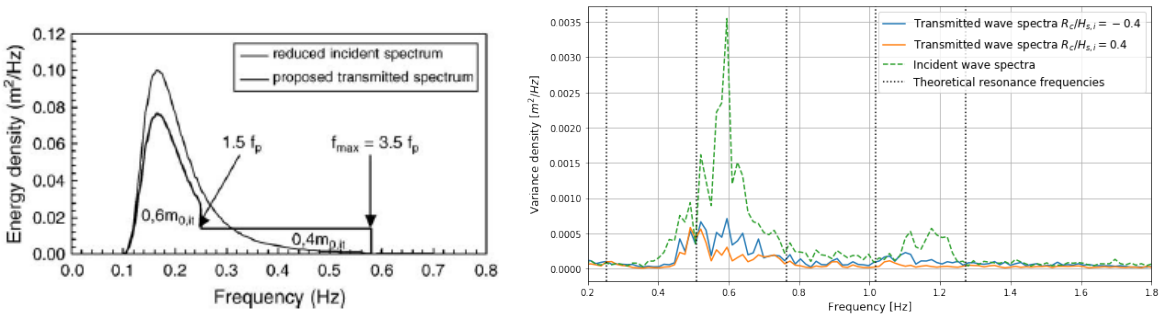

(a) (b)

Figure 8.7: a. Model of the transmitted wave spectra for submerged structures, adopted from (Van Der Meer et al., 2000) b. Effect of relative crest height on extracted transmitted spectra from OpenFOAM at wave gauge 6 for different crest height.

In order to quantify this shift in energy spectra, (Van Der Meer et al., 2000) proposed a simple model for submerged rubble mound structures (see figure 8.7a). In this model it was stated that 60 % of the transmitted energy is present in the area $< 1.5f_p$ and 40 % of the transmitted energy is evenly spread between $1.5f_p$ and $3.5f_p$. Work of van der Meer et al. (2005) reanalysed the boundaries of this simple model and including data of the DELOS project. It was found that for submerged rubble mound structures 66 percent of transmitted wave energy is in the area $< 1.5f_p$ and 34 percent of the energy is evenly spread between $1.5f_p$ and $3.2f_p$. However for emergent structures much less energy goes to the higher frequencies and fmax may become close to 2.0 which is also noticed by Briganti et al. (2003).

In this research spectral changes corresponding to HLCS for different crest freeboard ranging from submerged structures to emergent structure are presented in figure 8.7b. Relatively speaking, the most energy is lost near the peak frequency and less towards the higher frequencies. No energy is present on frequencies higher than $2 \cdot f_p$ for the emergent structure which is in line with observations made by Briganti et al. (2003). However the comparison with the theoretical model of Van Der Meer et al. (2000) is not striking. The differences are probably related to the differences between conventional rubble mound structures and HLCS, also related to the constant wave transmission behaviour found for emergent structures. The additional energy on the higher frequencies cannot only be explained by the wave breaking processes. The incident spectra already contains energy on the higher frequencies due to high amount of non linear behaviour which shifts energy to the higher frequencies due to shoaling on the front beach slope. Comparing the wave spectra for emergent structures to submerged structures it is observed that most energy difference is found near the peak frequency where more energy is dissipated for emergent structures. The energy near the lower frequencies do not seems to be affected by the crest freeboard of the HLCS whereas almost no differences in energy are observed near the lower frequencies. These frequencies are less affected by the interaction with the HLCS, which is in line with observations by van den Bos & Verhagen (2018).

8.4.5. Conclusions

The overtopping discharge decreases exponentially for increasing crest height of the HLCS. The trend is overtopping discharge is dominated by the wave transmission trend. The most striking observation of the wave transmission trend is that for structures with $R_c \leq 0$ a slight increase in wave transmission coefficient is observed. This trend shows high resemblance to the wave transmission trend observed by J. Medina et al. (2019) for HLCS (see figure 8.4a) which predicts a constant wave transmission coefficient for $R_c \geq 0$. The largest mean water level set-up near the sea wall is observed for zero freeboard of the HLCS and reduces for submerged and emergent structures. This trend is in resemblance to observations made by Loveless et al. (1998).

8.5. Effect of crest width B

In this section the effect of the crest width of the HLCS on the predicted overtopping discharges is investigated. All OpenFOAM simulations that have been performed to investigate the effect of the crest width are presented in table 8.3. The data presented in table 8.3 is also visually presented in figure 8.8. In figure 8.8a the wave transmission coefficient and mean overtopping discharge corresponding to different crest height of the HLCS are presented. Additionally figure 8.8b presents the mean water level set-up near the sea wall and mean overtopping discharge for different crest width of the HLCS.

Table 8.3: Table with parametric test runs related to the relative crest width of the HLCS and the effect on water level set-up, wave transmission and overtopping.

Test ID	H_{si} [cm]	$R_c/H_{s,i}$ [-]	$B/H_{s,i}$ [-]	L_{pool}/L_p [-]	K_t [-]	$\overline{\eta}_{seawall}[cm]$	$i_{\overline{\eta},HLCS} \cdot 10^{-3}$[-]	$i_{\overline{\eta},basin} \cdot 10^{-3}$[-]	$q[l/s/m]$	$q/q_{initial}[-]$
Rcw1.5	11.24	0.00	1.5	1.2	0.47	0.51	0.63	3.32	0.2799	0.22
Base	11.24	0.00	3.0	1.2	0.37	0.47	1.39	3.23	0.1508	0.12
Rcw4.5	11.24	0.00	4.5	1.2	0.30	0.56	2.56	3.08	0.0555	0.04
Rcw10.0	11.24	0.00	10.0	1.2	0.18	0.55	2.66	2.17	0.0098	0.01
Rcw15.0	11.24	0.00	15.0	1.2	0.13	0.56	3.52	0.77	0.0033	0.00

For increasing crest width a decay in the form of an exponential function of the mean overtopping discharge is found. This reduction shows the same trend compared to the observed wave transmission coefficient for increasing crest width, see figure 8.8a.

8.5.1. Wave transmission trend

Wave transmission is a result of two dissipation mechanisms, the first one being wave breaking on the crest of the structure resulting in turbulent flow and energy dissipation. The second one is energy dissipation by porous flow. The relative contribution of both main dissipation processes affects the amount of dissipated energy which reflects also in the amount of wave transmission. The reduction in wave transmission coefficient is mostly related to the enhanced wave breaking on the crest of the HLCS for smaller crest width and the enhanced porous flow resistance for larger crest width.

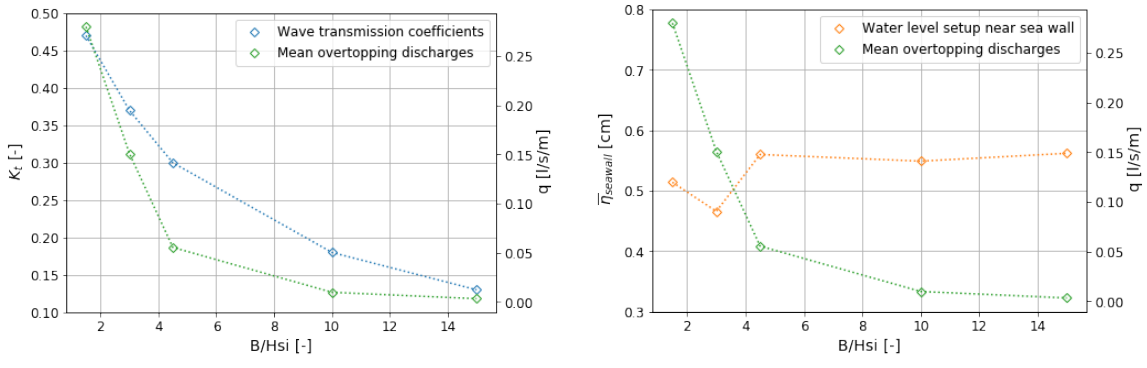

(a) (b)

Figure 8.8: Effect of crest width for $R_c/H_{s,i} = 0.0$ and $L_{pool}/L_p = 1.2$ for a. wave transmission coefficient and the predicted overtopping discharge and b. Water level set-up and the predicted overtopping discharge

Wave breaking on the crest of the HLCS

Wave breaking processes on the HLCS for different crest widths are presented in figure 8.9. In here a large wave breaking event (i.e. $H \approx H_{1\%}$) is visualised at t=211 s for different crest width of the structure. For a relative crest width of 1.5 it is observed that the tongue of the breaking wave has its impact behind the HLCS which results in more energy transmission and less energy dissipation by wave structure interaction. For a relative crest width of 4.5 continuous wave breaking on the crest of the HLCS is observed which results in high levels of energy dissipation thus resulting in lower wave transmission.

The wave tongue hits the crest first halfway the crest and continuous to break until the lee side of the HLCS is reached. For a relative crest width of 3.0 also wave breaking on the crest is observed, however no continuous wave breaking is observed due to the length of the crest for this large wave breaking event. For larger crest width (i.e. $B/H_{s,i} > 4.5$) a gradual decrease in effectiveness of wider structures related to wave transmission is observed which is partly related to the effect that all (even the largest) waves break on the crest of the structure. It has been found that this crest width corresponding to the most effective crest width related to energy dissipation by wave breaking can be estimated using the concept of breaker travel distance. This concept is further elaborated in section 2.3.1. For the given hydraulic boundary conditions (using m=0.02, and H_s) crest width values of $B/H_{s,i} = 4.4$ is found. This value corresponds well with the point of largest curvature in figure 8.9. Wave transmission behaviour keeps reducing but flattens for larger crest width thus underlining the relevance of this concept. Additionally to wave transmission, wave dissipation resulting from porous flow is important which becomes more relevant for wider crest width. For wider structures, water going through the structure encounters more friction (i.e. dissipation of energy) which results in more energy dissipation by porous flow.

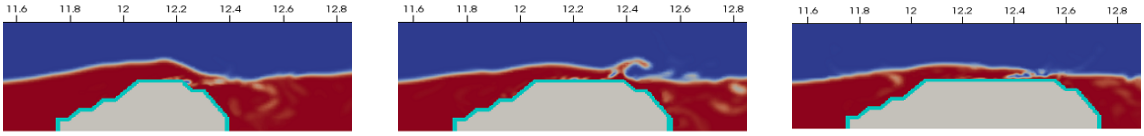

(a) $B/H_{s,i} = 1.5$ (b) $B/H_{s,i} = 3.0$ (c) $B/H_{s,i} = 4.5$

Figure 8.9: Hydrodynamic interaction HLCS and sea wall at t=220s for a relative crest width ($B/H_{s,i}$) of a: 1.5. b:3.0. c:4.5

8.5.2. Water level set-up

Based on the additional momentum release through enhanced wave breaking on the crest of the structure an increase in the mean water level set-up near the sea wall was expected for increasing crest width. The variability in water level set-up near the sea wall is not very large compared to the observed gradients and no conclusive trend can be observed for this parameter. The fact that no conclusive trend is observed can be related to the absolute distance between the measuring wave gauge and the sea wall. This is more elaborated in the discussion in section 9.1.2. Moreover the observed trend in water level set-up does not show a relation to the observed trend in overtopping discharge, which is dominated by the wave transmission trend.

The spatial distribution of the mean water level inside the flume, presented in figure 8.10, reveals an increase of hydraulic gradient over the HLCS for increasing crest width. Additionally a decrease of hydraulic gradient inside the basin is found for increasing crest width. The three locations used to obtain these hydraulic gradients are presented in the figure for varying crest width. For all simulations the same start of the HLCS is visualised. The end of the HLCS is different per simulation. A dynamic equilibrium seems to form inside the basin where the largest water level set-up near the sea wall is found for the largest crest width. The depth average velocity corresponding to the hydraulic gradients inside the basin range between 0.67 - 1.38 m/s. The contribution of both large differences in hydraulic gradient show minimal effect on the mean water level near the sea wall. The standing wave pattern in front of the HLCS related to wave reflection is clearly visible in figure 8.10.

8.5.3. Temporal variations

The mean water level set-up near the sea wall did not present a conclusive trend related to the overtopping reduction, therefore a closer look on the temporal variations in water level near the sea wall is presented in figure 8.11. The maximum difference in water level set-up around the largest overtopping event (i.e. t=220 s) is in the order of 2.2 cm. It can be observed that the water level set-up during the simulation corresponding to large overtopping events is largest for the largest crest width, which could not be observed looking at the mean water level set-up only. The ability to restore the water level to SWL within the basin is determined by the restoring capabilities of the HLCS. For wider crest width the porous flow through the structure experiences more friction and consequently the the amount of back flow through the HLCS is reduced Calabrese et al. (2008). This results in a observed higher water

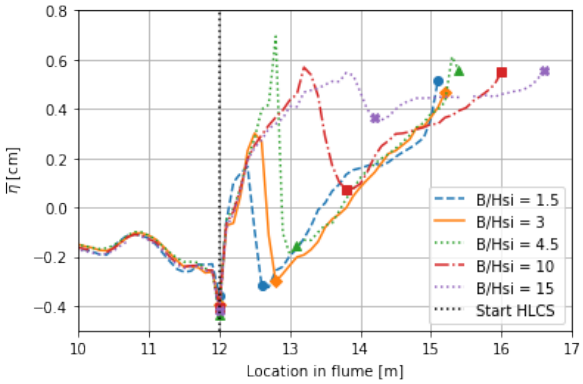

Figure 8.10: Spatial distribution of mean water level inside the flume for varying crest width

level set-up for wider crest width. However the increase in the mean overtopping discharge seems mostly determined by wave transmission. The wave transmission reduces for larger crest width which results in a reduced number of overtopping events during the simulation, as well as lower individual overtopping volumes per event resulting in lower mean overtopping discharges.

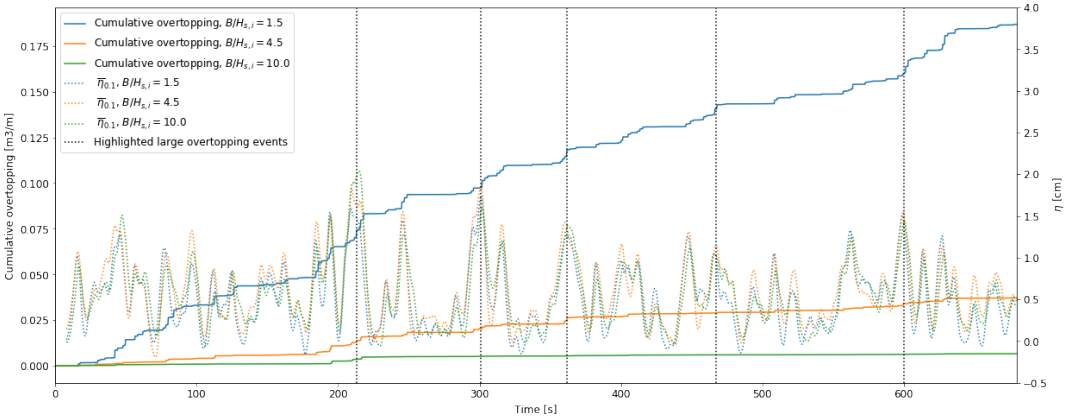

Figure 8.11: Effect of relative crest width on overtopping volumes and temporal water level set-up

8.5.4. Comparison with van der Meer et al. (2005) guideline

The effect of the crest width on the hydraulic performance of HLCS has not been analysed yet. Part of this research aims to improve the understanding of wave transmission over HLCS. This has been done by comparing the extracted OpenFOAM transmission coefficient with the empirical prediction guideline of van der Meer et al. (2005) for conventional LCS as presented in table 2.1. This guideline is used because it uses a very extensive data base including a wide range of simulations with a large spread in different crest width for conventional rubble mound LCS.

The empirical prediction guideline of van der Meer et al. (2005) presented by 8.1 and 8.2 is a result of 2337 tests over 7 different data sets (including the DELOS data base especially focusing on the effect of crest width) using both conventional rubble mound rock structures as well as tetrapod and accropode armour layers in combination with a rubble mound core under non-breaking, breaking and broken waves. The effect of crest height included in this guideline (i.e. the $R_c/H_{s,i}$ term) is removed by performing simulations with zero freeboard (i.e. see the runs reported in table 8.3) and setting the freeboard to zero in the van der Meer et al. (2005) prediction guideline . In figure 8.12, the wave transmission coefficients resulting from OpenFOAM are plotted as blue dots, including a trend line through these points. Additionally the data points that have been used by van der Meer et al. (2005) to derive equations 8.1 and 8.2 for zero freeboard have been plotted including the prediction itself.

$$K_t = -0.4\frac{R_c}{H_{s,i}} + 0.64\left(\frac{B}{H_{s,i}}\right)^{-0.31}\left(1-e^{-0.5\xi}\right) \quad valid\ \ for \quad B/H_{s,i} < 8 \tag{8.1}$$

$$K_t = -0.35\frac{R_c}{H_{s,i}} + 0.51\left(\frac{B}{H_{s,i}}\right)^{-0.65}\left(1-e^{-0.41\xi}\right) \quad valid\ \ for \quad 12 > B/H_{s,i} > 50 \tag{8.2}$$

From figure 8.12 it can be observed that the same trend in wave transmission behaviour is observed comparing the effect of crest width on wave transmission for HLCS and conventional LCS. Especially in the range where wave breaking is the dominant dissipation mechanism (i.e. $B/H_{s,i} < 4.5$, as mentioned in previously in this section) the results fit very well with the data for conventional LCS. For wider structures (i.e. $B/H_{s,i} > 4.5$) the data corresponding to HLCS are disposed towards the upper edge of the underlying data used by van der Meer et al. (2005). This data of conventional LCS corresponds to low $H_{s,i}/D_{n50}$ (i.e. larger rubble mound elements, related to HLCS which in this research has a $H_{s,i}/D_{n50}$ of 2.5). The data is slightly on the upper edge of the cloud due to the increase of the effect of porous flow on wave transmission which increases for wider HLCS. On the other hand the results are well within the bandwidth of the scatter in data for conventional LCS. Therefore it can be concluded that the van der Meer et al. (2005) equations, equation 8.1 and 8.2, can be used to assess the amount of wave transmission for HLCS.

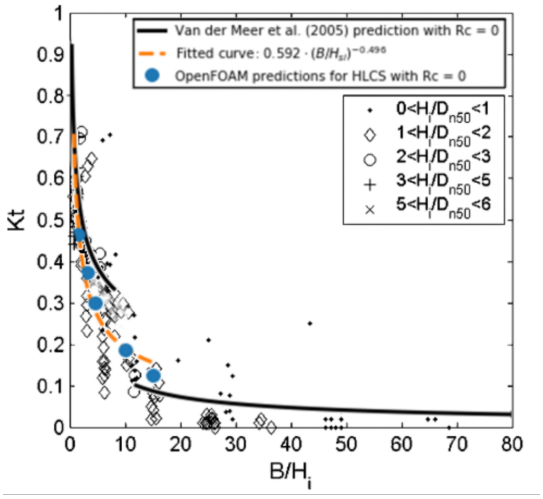

Figure 8.12: OpenFOAM predictions for the effect of crest width for HLCS, including a fitted prediction guideline compared with the empirical prediction guideline van der Meer et al. (2005), adopted from van der Meer et al. (2005)

8.5.5. Conclusions

The overtopping discharge decreases exponentially for increasing crest width of the HLCS. This trend in overtopping reduction is dominated by the wave transmission trend. The behaviour of the water levels inside the basin have shown to be of minor importance compared to the dominating effect of wave transmission.

The reduction is wave transmission for wider crest width is governed by additional wave breaking on the crest and increase of porous resistance for wider crests. Wave breaking processes are dominant for smaller crest widths and for increasing crest width porous flow interaction becomes more dominant. The shifting point between a wave breaking dominant regime and a porous flow dominant regime can be approximated using the concept of breaker travel distance. The reduction in wave transmission behaviour for wider crests is also observed if results are compared to the empirical prediction guideline of van der Meer et al. (2005) for conventional LCS. The data for HLCS fit well with this formula. Moreover the data for HLCS is within the bandwidth of scatter of the underlying data used by van der Meer et al. (2005) for conventional rubble mound structures. Therefore it is concluded that this formula can be used for first assessment of the effect of crest width for HLCS.

8.6. Effect of basin length L_{pool}

In this section the effect of basin length on basin hydrodynamics and the predicted overtopping discharge is analysed. All performed OpenFOAM simulations for this analysis are presented in table 8.4. The data presented in table 8.4 is also visually presented in figure 8.13. In figure 8.13a the wave transmission coefficient and mean overtopping discharge corresponding to different crest height of the HLCS are presented. Additionally figure 8.13b presents the mean water level set-up near the sea wall

and mean overtopping discharge for different basin length.

Table 8.4: Table with parametric test runs related to the pool length of the HLCS to the sea wall and the effect on water level set-up, wave transmission and overtopping.

Test ID	H_{si} [cm]	$R_c/H_{s,i}$ [-]	$B/H_{s,i}$ [-]	L_{pool}/L_p [-]	K_t [-]	$\overline{\eta}_{seawall}[cm]$	$i_{\overline{\eta},HLCS} \cdot 10^{-3}$[-]	$i_{\overline{\eta},basin} \cdot 10^{-3}$[-]	$q[l/s/m]$	$q/q_{initial}[-]$
Seichn1	11.24	0.0	3.0	0.5	0.41	0.38	2.97	10.32	0.53	0.41
Rpl0.33	11.24	0.0	3.0	0.6	0.37	0.48	1.72	6.86	0.30	0.24
Seichn2	11.24	0.0	3.0	1.0	0.41	0.50	1.61	4.31	0.21	0.17
Base	11.24	0.0	3.0	1.2	0.37	0.47	1.39	3.23	0.15	0.12
Rpl1.00	11.24	0.0	3.0	1.8	0.37	0.65	1.75	2.40	0.08	0.06

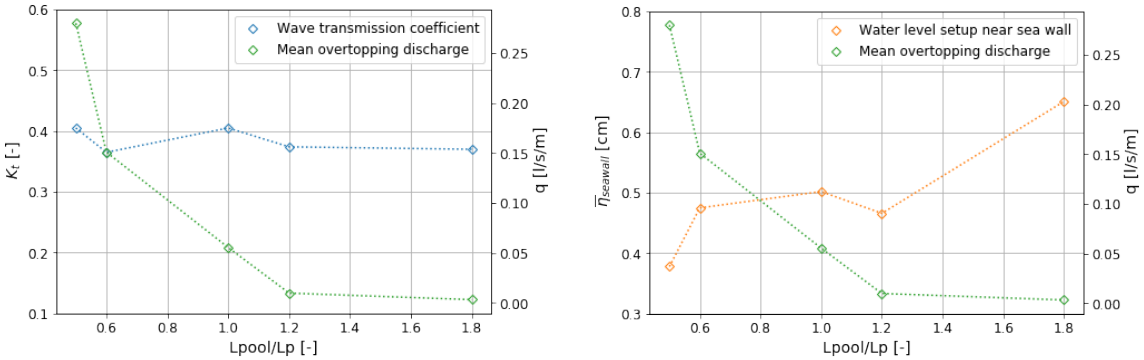

(a) (b)

Figure 8.13: Effect of relative pool length for $R_c/H_{s,i} = 0.0$ and $B/H_{s,i} = 3.0$ for a. wave transmission coefficient and the predicted overtopping discharge and b. Water level set-up and the predicted overtopping discharge

The wave transmission coefficient shows a constant trend with respect to the basin length, see figure 8.13a (because no changes are made to the structure itself). Additionally the mean water level set-up near the sea wall increases for larger basin length, see figure 8.13b. Based on the constant wave transmission and increasing water levels an increasing overtopping discharge is expected for larger basin length. However in contrary a decay in the form of an exponential function of the mean overtopping discharge is found for increasing basin length.

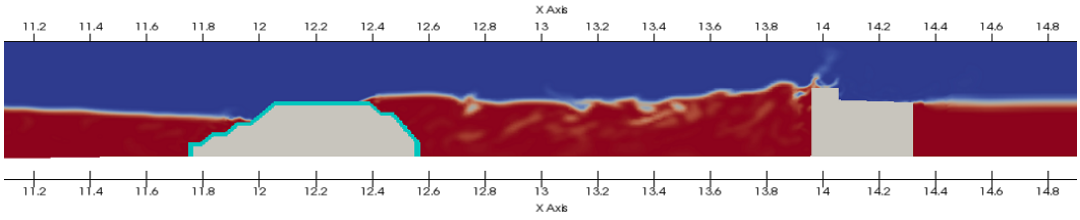

Figure 8.14: Impression of broken wave propagation resulting in a violent wave overtopping event for $L_{pool}/L_p = 0.6$

It is observed by visual inspection of the simulations that breaking waves over the HLCS travel over the free surface and result in violent wave overtopping at the sea wall. The travelling bores result in large overtopping events. In figure 8.14 the interaction of the travelling bores and the sea wall are presented for $L_{pool}/L_p = 0.6$. The effect of the travelling bores dies out for larger basin length. This effect of the initiation of travelling bores is expected to be largest for structures with $R_c \geq 0$. For emergent structures more energy goes through the HLCS reducing the appearance of a bore, in contrary to submerged structures.

Additionally to the travelling bores there is less storage volume inside the basin for smaller basin length. This results in a quicker increase of the water level inside the basin. Due to the quicker increase

in water level, smaller waves travelling at the front of the wave group are able to overtop. For larger basin length these waves cannot cause overtopping water due to the lower water levels. The quicker increase and reduction of water levels inside the flume for smaller basin length does not seem to influence the mean water levels inside the flume near the sea wall which show lower values compared to larger basin length.

8.6.1. Water level set-up

Looking at the spatial distribution of the mean water level inside the flume a positive gradient is observed which increases considerably for shorter basin length. The depth average velocities corresponding to these basin gradients range between 1.17 - 2.44 m/s. The gradient is related to the amount of storage volume that is available within the basin. For shorter basin length there is less storage volume inside the basin and a larger gradient is needed for mass conservation of water. The same hydraulic gradient over the HLCS is observed for different basin length resulting from the same adopted structure characteristics in combination with constant hydraulic boundary conditions. The resulting mean water level near the sea wall shows an increasing trend for increasing basin length, in contrary to the reduction in overtopping discharge for larger basin length. At the left the standing wave pattern in front of the HLCS is observed whereas only minor effect of a standing wave pattern is observed within the basin.

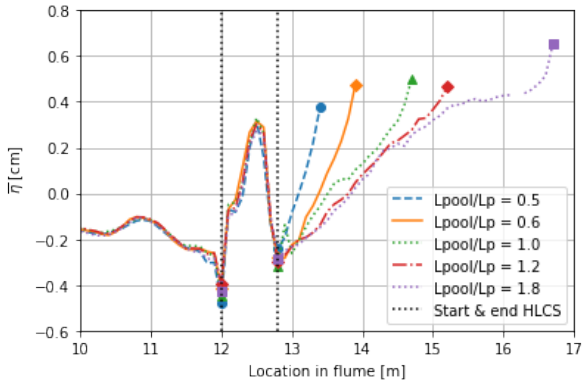

Figure 8.15: Spatial distribution of mean water level inside the flume for varying basin length

8.6.2. Temporal variations

In figure 8.16, the temporal water level set-up near the sea wall is included and presented next to the cumulative overtopping curves for various interesting basin lengths. From figure 8.16 it can be observed that the temporal peaks in low frequency water level set-up coincide with the largest predicted individual overtopping events looking at the highlighted peaks. This strengthens the hypothesis of the effect of entering wave groups resulting in low-frequency wave motion on the increase in predicted overtopping volumes. This pulsating effect of the water level set-up near the sea wall results in an increasing numbers of smaller overtopping waves in this interval which eventually increases the mean overtopping discharge. The maximum difference in water level set-up around the largest overtopping event (i.e. t=220 s) is in the order of 2.4 cm.

It was expected that for basin lengths corresponding to theoretical resonance periods (e.g. $L_{pool}/L_p = 1.0$) possible resonance and seiching would be observed. However this cannot be linked to the peaks in temporal variations of water level set-up resulting from figure 8.16. In order to understand the role of seiching and resonant behaviour on the hydrodynamics a closer look on seiching is presented in the next section (section 8.6.3).

8.6.3. Seiching

The construction of a HLCS in front of a sea wall can be considered as a locally isolated basin. Back and forth wave reflection between the HLCS and sea wall creates a standing wave pattern (i.e. seiching). This can result in resonant behaviour if the natural frequency of the forcing is equal to the eigen

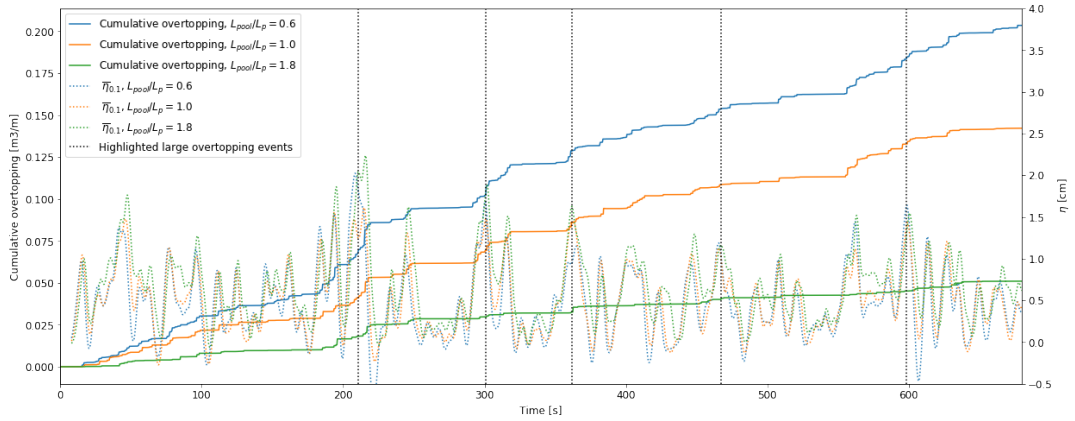

Figure 8.16: Effect of relative pool length on overtopping volumes and temporal water level set-up.

frequency of the basin. In this case, the low frequency motions starts to interfere with itself increasing the energy of the motion. The enhancement of these low-frequency waves result in enhanced sloshing of the basin which can result in an increase in predicted overtopping discharge due to the temporal behaviour of water level set-up near the boundaries of the basin. One moment in time the water level near the sea wall is higher compared to another moment where the water level is lower. On average this results in an increase of mean overtopping discharge where relatively more water is able to overtop for higher water levels compared to the lower overtopping for lower water levels.

The type of standing wave pattern depends on whether the basin can be considered as a closed basin or an open ended basin. The hydrodynamic system investigated in this research can be considered as a partly closed basin. Due to the permeability of the HLCS energy is able to escape over and through the HLCS. Additionally due to sea wall overtopping energy is also able to escape from the basin at the right boundary resulting in a partly closed basin. The origin of seiches and the theoretical assessment of the standing wave pattern related to a closed or open ended basin is discussed in detail in chapter 2.5.

In order to assess the effect of seiching within the basin, several simulations have been performed with different basin length. Raw wave spectra near the sea wall (i.e. from the bulk wave gauge closest to the sea wall) have been compared for different basin length. Additionally the theoretical resonance frequencies for a **closed** basin have been calculated using equation 2.7. In this equation the shallow water wave speed is used by default. However the incoming wave characteristics behave as transitional water waves, therefore this wave speed is adopted to calculate the theoretical resonance frequencies. Figure 8.17 presents the incoming wave spectra, the raw wave spectra near the sea wall and the first 5 theoretical resonance modes.

A match is found between the theoretically calculated resonance frequencies for a closed basin and the energy peaks of the modelled wave spectra, indicating the closed basin behaviour of this hydrodynamic system. It is observed from figure 8.17 that for each basin length there is an energy shift from the peak frequency to all theoretical resonance frequencies lower than the peak frequency of the incoming waves. The largest amount of energy shifts towards the theoretical frequency closest to the peak frequency. Theoretical resonance frequencies higher than the peak frequency are not excited by the system. For the larger basin lengths this results in more modes that are excited (i.e. all modes corresponding to resonance frequencies lower than the incoming peak frequency). Additionally for basin lengths equal to theoretical resonance frequencies (i.e. $L_{pool}/L_p = 0.5, 1.0$) enhanced energy is observed near the peak frequency and no energy is transported to other theoretical resonance frequencies. Moreover for these basin lengths higher total energy within the wave spectra is observed compared to basin lengths close to these resonance basin lengths which indicates that resonance plays a role. This effect reduces for basin lengths further away from the theoretical resonance frequency. The largest effect of resonance on the amount of energy within the system is observed for basin length

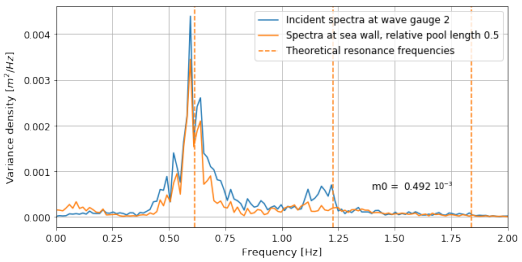

(a) $L_{pool}/L_p = 0.5$

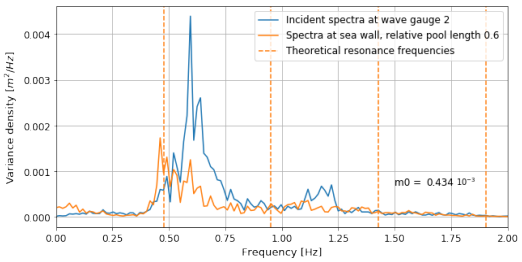

(b) $L_{pool}/L_p = 0.6$

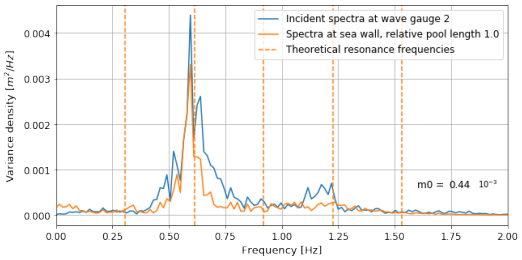

(c) $L_{pool}/L_p = 1.0$

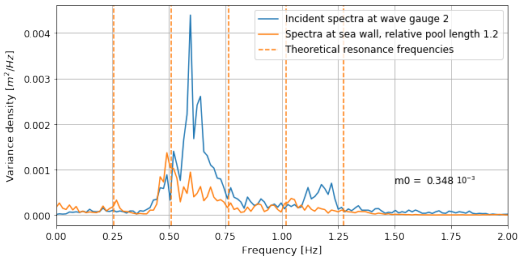

(d) $L_{pool}/L_p = 1.2$

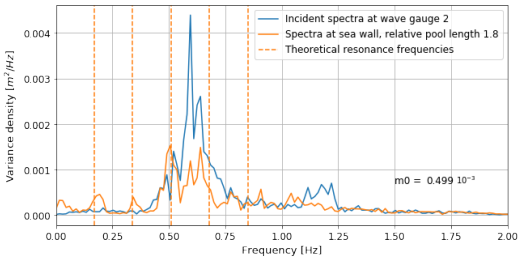

(e) $L_{pool}/L_p = 1.8$

Figure 8.17: Wave spectra at sea wall corresponding to a basin length (L_{pool}/L_p) of a: 0.5. b: 0.6. c: 1.0. d: 1.2. e: 1.8.

equal to the first mode (i.e. n=1) compared to basin lengths equal to higher order theoretical resonance modes (i.e. n=2). This can be observed by comparing the $m0$ for both basin lengths from figure 8.17a and 8.17c. However these results should be taken with care due to the distance between the bulk wave gauge (used for the raw wave spectra) and the sea wall, also elaborated in the discussion section (i.e. section 9.1.2. The standing wave pattern in front of the sea wall influences the extracted surface elevation signal depending on the distance from the sea wall to the wave gauge. This is also the reason why figure 8.17e shows a higher amount of energy within the signal. This wave gauge is very close to the sea wall compared to the other gauges, increasing the standing wave effect on the signal.

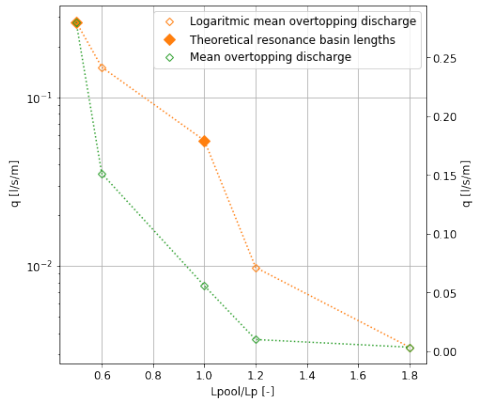

Figure 8.18: The effect of resonance on the overtopping trend

The effect of possible resonance on the overtopping behaviour is visualised in figure 8.18 where the exponential behaviour in overtopping discharge is presented for varying basin length. The simulations with basin length equal to the theoretical resonance basin lengths are highlighted and the mean overtopping discharge is presented on a logarithmic scale. It can be observed that for basin length equal to theoretical resonance basin length, a larger mean overtopping discharge is observed compared to the default exponential behaviour. This does indicate that resonance plays a role. However this effect is not very pronounced and does not result in a significant increase in overtopping.

Effect of crest height on seiching energy distribution

Resonance is observed within the basin enclosed by the HLCS and the sea wall. The ability of escaping wave energy from the basin changes for increasing and reducing structure height, and the effect of this trapping of energy is investigated here. Figure 8.19a presents the wave spectra for a basin length $L_{pool}/L_p = 1.0$ and $L_{pool}/L_p = 1.2$ for different structure heights (i.e. $R_c/H_{s,i}$ of -0.4 and 0.4). It can be observed that the total amount of energy within the spectra is higher for a submerged structure compared to an emergent structure which is related to the higher wave transmission for submerged structures by energy going over the HLCS. However, looking at the peaks corresponding to the resonance frequencies no effect of enhanced energy trapping within the basin for higher crest freeboard is observed. This can be related to the permeability of the HLCS, because also energy can escape by a return flow through the structure. The amount of energy within the spectra near the peak theoretical resonance frequency is the same for different crest freeboard. Additionally the other resonating modes are not activated for $L_{pool}/L_p = 1.0$ and only a slight shift towards the lower resonating frequencies is observed for $L_{pool}/L_p = 1.2$ which is in line with observations made in section 8.6.3. For additional analysis on the change in spectral shape for submerged structures compared to emergent structures where only the transmitted wave spectra are analysed the reader is referred to section 8.4.4.

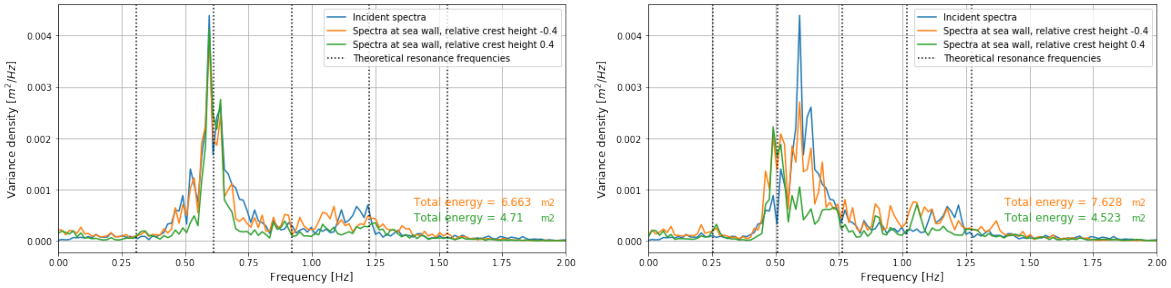

(a) $L_{pool}/L_p = 1.0$ (b) $L_{pool}/L_p = 1.2$

Figure 8.19: Effect of crest height on wave spectra near sea wall for a basin length (L_{pool}/L_p) of a: 1.0. b:1.2

8.6.4. Conclusion

The overtopping discharge decreases exponentially for increasing basin length. The overtopping reduction for increasing basin length is dominated by broken wave propagation (travelling bore) and a quicker increase of water level inside the basin for smaller basin length. Because shorter basins have less storage capacity, the water level increases faster during filling of the basin. Higher initial water levels cause more smaller waves to overtop and increase the overtopping discharge. Additionally the broken wave propagation (i.e. travelling of bores) result in violent wave overtopping of the sea wall and partly green water overtopping increasing the mean overtopping discharge significantly. These highly turbulent conditions die out in space and thus have less effect for larger basin length.

For all basin lengths energy shifts towards theoretical resonance frequencies of the basin. The hydrodynamic system behaves like a closed basin because high resemblance to the theoretical resonance frequencies corresponding to a closed basin is observed. Only resonance modes with a lower frequency than the incoming peak frequency are activated inside the basin. By plotting the overtopping discharge on a logarithmic scale the outlier near a theoretical resonance basin length is observed. However this effect on overtopping is smaller than the effect of the dissipating bores for larger basin length.

8.7. Overtopping prediction solely based on wave transmission

In the previous sections of chapter 8 detailed hydrodynamic analysis is performed to be able to shed light on the design sensitivities of the geometrical layout on the hydrodynamics inside the basin and the predicted overtopping discharge. In this section a more practical approach is presented for the prediction of sea wall overtopping for this hydrodynamic system. Based on the analysis of the geometrical layout for different crest height and crest width, a relation between the observed trend for the wave transmission coefficient and the predicted overtopping discharge was found. The dominating trend of wave transmission on the overtopping reduction results in the hypothesis to perform a quick assessment (i.e. within a limited time span without the need of a CFD model) to predict the mean overtopping discharge solely based on the wave transmission coefficient over the HLCS. No effect of water level set-up and additional basin hydrodynamics is included which were found to be less dominant compared to wave transmission. The uncertainties using this crude simplification, where wave transmission coefficients are extracted from OpenFOAM and used to predict the overtopping discharge solely based on this coefficient, are analysed here. It is assumed that in the near future wave transmission coefficients can be derived based on empirical relations for HLCS, however such empirical relations are not available at the moment and extracted wave transmission coefficients from OpenFOAM are used.

For the prediction of the theoretical overtopping discharge the **non-impulsive** mean value overtopping discharge presented in the Eurotop 2018 (i.e. Eurotop equation 7.5, presented in equation 2.10) is used. This formula is valid for non-impulsive overtopping conditions (i.e. $h^2/(H_{m0} \cdot L_{m-1,0} > 0.23)$ Van der Meer et al. (2018), which prevail for all simulations where the HLCS is included.

Table 8.5: Predicted mean overtopping discharge using equation 2.10 compared to predicted overtopping discharge using OpenFOAM for a sea wall freeboard of 0.06m.

Test ID	$H_{m0,t}$ [cm]	$q_{Eurotop}$ [l/s/m]	$q_{OpenFOAM}$ [l/s/m]	Test ID	$H_{m0,t}$ [cm]	$q_{Eurotop}$ [l/s/m]	$q_{OpenFOAM}$ [l/s/m]
Rcw1.5	5.80	0.1223	0.2799	Rch+0.4	4.90	0.0566	0.0808
Base	4.73	0.0475	0.1508	Seichn2Rc+0.4	5.33	0.0844	0.1754
Rcw4.5	4.20	0.0254	0.0555	Rch+0.8	5.45	0.0941	0.0993
Rcw10.0	2.64	0.0021	0.0098	Seichn1	4.93	0.0582	0.5271
Rcw15.0	1.62	0.0001	0.0033	Rpl0.33	4.53	0.0379	0.3043
Rch-0.4	6.63	0.2160	0.4495	Seichn2	5.10	0.0687	0.2129
Seichn2Rc-0.4	6.25	0.1694	0.4484	Rpl1.00	5.13	0.0515	0.0766

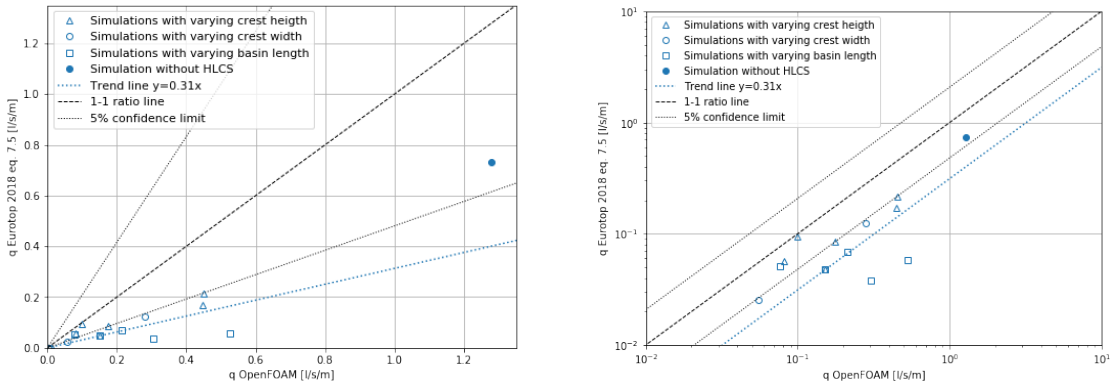

(a) Linear scale

(b) Logarithmic scale

Figure 8.20: Predicted mean overtopping discharge using equation 2.10 compared to predicted overtopping discharge using OpenFOAM for a sea wall freeboard of 0.06m on varying axis scale

In table 8.5 the transmitted spectral wave height in combination with the calculated mean overtopping discharge using equation 2.10 and the predicted mean overtopping discharge by OpenFOAM are presented for all geometrical layout simulations. Furthermore, all these data points are visualised in

figure 8.20 including the predicted and measured mean overtopping discharge of a simulation without HLCS. Additionally the 5% confidence limits (2 standard deviations) are presented. From figure 8.20 it can be deduced that the mean overtopping discharges predicted using Eurotop 2018 underestimate the measured overtopping discharges from OpenFOAM. On average the overtopping discharge is underestimated by 69%. The Eurotop mean value approach also underestimates the mean overtopping discharge for the simulation without HLCS with 28%. This underestimation however is within the 5% confidence limit prescribed by the Eurotop for equation 2.10 and within the underlying data from which the prediction guideline is derived, see also figure 6.6 for $R_c/H_{m,0} = 0.65$.

For the difference between the measured and predicted mean overtopping discharge several reasons are reported:

- The effect of water level set-up on the increase in overtopping discharge is not included using this method, in contrary to the OpenFOAM predictions where this is included.

- Additional hydrodynamics related to the differences in basin length (i.e. low frequency wave motion, or broken wave propagation) are not included using this method. These effects have a significant influence on the measured overtopping discharge (see figure 8.13a). Only changes in structure dimensions result in different wave transmission. Therefore for only varying the basin length a horizontal trend in figure 8.20 is observed which increases the uncertainty of the prediction.

From this analysis is can be concluded that the geometrical layout of such hydrodynamic systems plays an important role in the overtopping assessment. By only assessing the amount of wave transmission a mean underestimation of 69% is found. Especially the differences in measured overtopping discharges for varying basin length highly increase the uncertainty of this method. In the range where the basin length shows considerable influence on the amount of overtopping (i.e. for $L_{pool}/L_p < 1.2$, see figure 8.13) large uncertainties are found. The broken wave propagation and low frequency wave motion the effect hereof on the predicted overtopping depend both on the type of wave breaking (related to the freeboard of the HLCS) and the amount of green water overtopping by overflowing (related to the broken wave propagation and low frequency wave motion, both related to the freeboard of the sea wall). For basin length $L_{pool}/L_p > 1.2$ (i.e. constant overtopping behaviour for increasing basin length) or if the effect of basin length is known on before hand this simplification can be used in practice. However this effect is most of the time not known on beforehand and hard to examine as there are no design guidelines that take the basin length effect into account. The exact exponential reduction in overtopping discharge varies per geometrical layout and for different structural dimensions of the HLCS. OpenFOAM or physical modelling can in that case improve the understanding of the system and is advised to assess the overtopping for these types of complicated system without introducing high levels of uncertainty.

8.8. Design recommendations

Based on the obtained design sensitivities, here design recommendations related to the geometrical parameters are presented. For all geometrical layout parameters an exponential decrease for increasing geometrical parameter is found. Figure 8.21 presents the amount of wave transmission and measured overtopping discharge for varying geometrical layout parameters. Here design considerations are presented based on the maximum effectiveness (i.e. where the largest gradient in overtopping curve is found) of the independent geometrical parameters related to overtopping reduction. For smaller values of the recommended parameters a considerable increase in overtopping is obtained. On the other hand for larger values it is most likely that the construction costs start to outweigh the additional decrease in overtopping. However, in the end it is up to the engineer to design the most cost-effective layout depending on the site specific (boundary) conditions, the overtopping requirement and additional requirements.

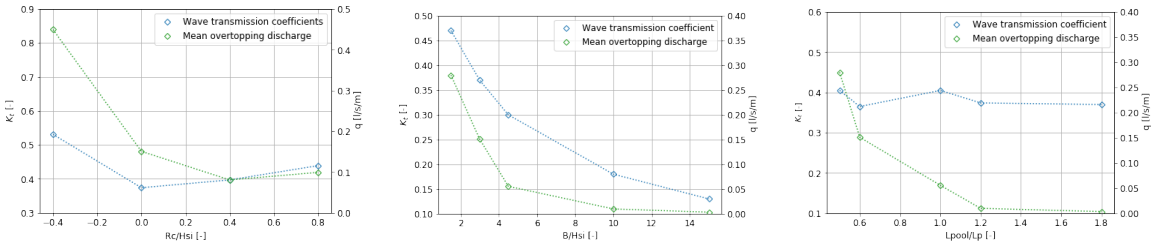

(a) Varying crest height (b) Varying crest width (c) Varying basin length

Figure 8.21: Effect of varying the main geometrical layout parameters on the wave transmission and overtopping prediction

Following figure 8.21, is can be observed that the largest curvature in the overtopping discharge can be obtained for the following layout parameter values:

- $R_c/H_{s,i} \approx 0$
- $B/H_{s,i} \approx 4.5$
- $L_{pool}/L_p \approx 1.2$

It is found that for $R_c \approx 0$ a local minimum in expected wave transmission is found. Combined with the results found by J. Medina et al. (2019) (i.e. a constant wave transmission coefficient for $R_c \geq 0$) the largest curvature in overtopping reduction is found for this range. Therefore a HLCS width a freeboard ≈ 0 is recommended. Additionally for larger crest height the construction costs increase as well as the visual hindrance. Visual hindrance is often a requirement and reason to construct a LCS in the first place.

It has been found that the largest curvature in overtopping reduction shows large resemblance to the largest curvature in wave transmission. The crest width corresponding to this largest curvature is a crest width equal to a crest width where the amount of energy dissipation by wave breaking is maximized. It has been demonstrated that for this research this crest width can be approximated using the concept of breaker travel distance, see section 8.5.1. It is expected that this concept also holds for different incoming wave characteristics and other site dependent boundary conditions. Therefore a crest width calculated using this concept is recommended to optimise the crest width.

The basin length is found to be an important factor, especially for smaller basin length. Most dominantly for $L_{pool}/L_p < 1.2$ wave breaking over the HLCS results in the propagation of bores and violent wave overtopping, see section 8.6. This results in a severe increase of individual overtopping volumes and mean overtopping discharge. Therefore a basin length of $L_{pool}/L_p \approx 1.2$ is recommended. On the other hand for very steep beach slopes is can become economically more feasible to reduce the basin length and increase the crest height or crest width of the structure to reduce the overtopping. Additionally sometimes a LCS is combined with the construction of an artificial beach, which also plays a role in the decision of the basin length.

9

Discussion, conclusions and recommendations

9.1. Discussion

This section provides a discussion on the adopted research methods and the interpretation of the research results. Additionally the applicability and confidence of the created OpenFOAM model are discussed.

9.1.1. Wave flume hydrodynamics

The numerical grid is the most important factor determining the ability of the numerical model to present valid results. Generally, numerical studies present a grid resolution study to calibrate the wave flume hydrodynamics (i.e. surface elevation signals, pressures, flow velocities, overtopping discharges) based on raw data obtained from physical model experiments. However, for this study only statistical wave parameters were available from physical model tests related to wave transmission over HLCS consisting of artificial cubipod elements. If only statistical wave parameters are of importance no raw data is necessary but statistical calibration can be used. The model reliability while using a statistical calibration increases for longer simulation duration because of the validity of statistical data for longer duration. If however event specific data is required, like for instance individual large wave overtopping events and corresponding pressures in the HLCS, raw data of the specific event is required to validate the numerical behaviour. For statistical output parameters of the numerical model statistical calibration is sufficient for a statistically valid simulation duration.

The statistical grid resolution study has been performed in an empty flume based by comparing the output of the coupled model with each other (both the coupled OceanWave3D output and the coupled OpenFOAM output) and with a standalone OceanWave3D model which was taken as reference case. In comparison to raw data, the standalone OceanWave3D run also includes uncertainty whereas this is also a numerical model that depends on the numerical grid. The OceanWave3D resolution sensitivity analysis (i.e. section 6.6.1) shows this uncertainty. However when comparing runs with large simulation duration, this uncertainty is expected to vanish. The transmission coefficient is used for the calibration of the HLCS which divides two statistical wave characteristics (i.e. $H_{s,i}$ and $H_{s,t}$) that include both the same uncertainty. This thus eliminates the uncertainty from the transmission coefficient based on statistical calibration.

9.1.2. Geometrical layout adaptation

In order to assess the different geometrical layouts, the OpenFOAM numerical grid is adopted (i.e. increasing/decreasing the structure height, shortening/widening the crest width, or increasing/decreasing the basin length) without adjusting the wave gauges within the numerical model. Therefore resulting in different relative locations within the basin where wave characteristics and water levels are extracted. The water level set-up within the basin is found not to be constant over the basin length. Therefore the

exact location where the water level near the sea wall is extracted is important for the correct description of the mean water level set-up and energy within the wave spectra near the sea wall. However, in this research wave gauges are placed with 0.1m increments within the numerical flume and the wave gauge closest to the sea wall is used to determine the water level set-up near the sea wall. Therefore different distances between the wave gauge and the sea wall within 0.1 m are adopted for the definition of the mean water level set-up near the sea wall which results in uncertainties related to the reported values. Because the raw surface elevation signal is used the standing wave pattern influences the measured mean water level set-up with a magnitude depending on the distance between the wave gauge and the sea. Additionally a hydraulic gradient within the basin is found which therefore also affects the mean water level set-up within the basin. Preferably a constant distance between the wave gauge where the mean water level set-up is extracted and the sea wall is used for each different simulation which was not the case during this research and might have affected these results of measured mean water level set-up near the sea wall. If the results have been linearly extrapolated to the exact location of the sea wall an uncertainty on the mean water level set-up near the sea wall in the order of 0-0.1 cm are found.

9.1.3. Applied porous media resistance parameters

In this research extracted wave transmission coefficients from physical model experiments are used to calibrate the hydrodynamic behaviour of the HLCS. This is a valid method to calibrate the porous media resistance coefficients if a statistically valid number of waves is modelled. It is however found that multiple combinations of α and β result in the same wave transmission coefficient. Therefore the use of multiple selection criteria can be needed if very detailed hydrodynamics are of interest or if the maximum or minimum hydrodynamic quantities are required (e.g. maximum pressures inside the layers). These quantities are required to determine the stability of the cubipod elements which not yet can be modelled in OpenFOAM. The use of different hydrodynamic parameters like, the amount of energy dissipation, wave reflection, flow velocities and pressures result in more accurate, case specific predictions of α and β from which more detailed information can be obtained with higher certainty.

The hydrodynamic behaviour related to wave transmission over HLCS has been calibrated based on a case which is most representative for the parametric study performed in section 8. All geometrical dimensions that have influential differences from the calibration case introduces uncertainties regarding the predicted hydrodynamic behaviour. The adopted parameter ranges for varying crest width of the HLCS are quite severe out of range of the validation case of the porous media resistance parameters for the HLCS. Any influential differences between the validation and the adopted range results in uncertainty on the validity of the results. For the comparison with the van der Meer et al. (2005) transmission guideline for differences in crest width $B/H_{s,i}$ values up to 15 have been simulated whereas the validation is based on a case with a crest width of $B/H_{s,i} = 1.0$. These results have more uncertainty and the designer should be aware of this. It is however assumed that the trend observed from the data points for HLCS is correct and that comparable results to conventional LCS can be found. For slim structures, where wave breaking is dominant, the formula can be trusted. For wider structures, where porous flow becomes more dominant a slight bias towards higher transmission coefficients is found and more uncertainty is introduced. However for first assessment the formula for conventional rubble mound structures seems to provide well enough results that can be trusted. Consequently more validation of the adopted porous media resistance parameters for wider crest width is highly advisable to reduce this uncertainty and validate the results for this range of geometrical parameters.

The adopted porous media resistance parameters have been validated in section 7.5. However an overall underestimation of the transmission coefficient for these porous media resistance parameters has been identified (i.e. a mean underestimation of 6.6%). This underestimation of the wave transmission coefficient in the validation is translated to less wave energy within the basin thus eventually reducing the observed overtopping discharges. For lower overtopping discharges it is numerically more difficult to predict the correct overtopping discharges due to the larger influence of numerical artefacts like finite precision and truncation errors on the results which could be taken away by validation with physical model experiments.

9.1.4. Turbulence

In this research no separate turbulence model is included to account for additional turbulent dissipation outside of the structure. The procedure that is described by Jensen et al. (2014) to account for turbulence outside the structure without adding a separate turbulence model is adopted in this research where all turbulence is included in the closure coefficients α and β of the porous structure. Calibration of these parameters is therefore necessary to describe the correct amount of energy dissipation from the flow to coincide with physical model data (Losada et al., 2016). Whereas the turbulence by wave breaking over the structure is included in the porous media resistance parameters, the effect of turbulence on the predicted overtopping discharge remains unknown. Impulsive wave overtopping is observed for the case without HLCS in the flume and the effect of the turbulence related to impulsive wave overtopping is not accounted for by the model thus introducing uncertainties related to the predicted overtopping volumes. However this effect is assumed to be minor and because the relative effect between the numerical simulations is assessed in this research, this uncertainty can almost be neglected.

9.1.5. 3D effects

This research is based on a 2D schematization of a hydrodynamic system. However, LCS are generally constructed as a row of smaller LCS along the coast introducing a third dimension. Three dimensional effects can play an important role, especially for the wave-induced water level set-up, as noted by Calabrese et al. (2008); Zanuttigh et al. (2008). In a three dimensional set-up the water level set-up is reduced due to water flowing back offshore through gaps in subsequent LCS. Due to the two dimensional nature of this model this effect is not included. These three dimensional effects have an effect on the mean water level set-up near the seawall as well as the gradients observed within the basin. Based on the results from the performed simulations the expected effect hereof is however assumed to be low. The mean water level set-up is found not to play a dominant role in the overtopping prediction. The additional computational time is expected not to outweigh the addition of including 3D water level set-up effects. Only in case of very low sea wall freeboard, the relative importance of water level set-up becomes more dominant for the freeboard of the structure.

9.1.6. Comparison with solely using the wave transmission coefficient

The applied method for the comparison between the OpenFOAM results and the theoretical design guideline using the Eurotop resulted in an average under estimation of 69%. The amount of wave transmission has been adopted from the OpenFOAM model whereas currently no wave transmission formulas exist for the combined effect of crest width and crest height of the HLCS. In the near future these types of formulas for HLCS are expected to be derived for which this analysis can be redone. The Eurotop prediction is solely based on the amount of wave transmission over the HLCS without taking the additional water level set-up into account. Water level set-up guidelines are available for conventional rubble mound structures with a core and not for HLCS which are therefore not adopted. It is however expected that by including the water level set-up in stead of using SWL, the under prediction is reduced and better comparison with the Eurotop is found. It should be noted that the Eurotop prediction guideline does not include the effect of basin length which was found to be a dominant factor for the smaller basin length. Therefore it is expected that the Eurotop can be used, but that the effect of basin length should then be known on beforehand. This is however a complex task for which no design guidelines exist. This concludes the added value of OpenFOAM, which is able to include all the hydrodynamic effects.

9.1.7. Applicability and limits of the current model

The numerical model that is created in this research can be applied with confidence to obtain real design overtopping predictions. The OpenFOAM model that has been set-up is able to model wave breaking over the HLCS, the porous flow through the HLCS, waves propagation inside the basin with corresponding water levels, low-frequency wave motion (i.e. seiching and resonance) and the overtopping over the sea wall. However one should be able to know the limitations of the current model and the ranges that are expected to yield reliable results.

500 irregular waves using a Jonswap spectra have been modelled, which according to Romano et al. (2015) provide a statistical valid number of waves to assess the mean overtopping discharge cor-

rectly. The coupling between both models depend on the applied numerical grid. The numerical grid is designed using the expected wave characteristics based on H_s and T_p. Therefore influential differences in wave characteristics result in an increase of uncertainty. Larger waves can be modelled using the adopted grid, however for smaller waves the accuracy reduces quickly. Additionally the amount of non-linearity is important for the correct description of the hydrodynamics. Therefore an increase in foreshore slope, or a reduction in water levels is important for the OceanWave3D grid and the coupling ability of the numerical model. One can increase the foreshore slope but the resolution of both models, especially the OceanWave3D model should be increased. The influence of the ventilated boundary condition is also found to be present. However, using the default values as presented in this research (see section 6.4.2), it has been shown that the OpenFOAM model can predict the mean overtopping discharges in the range of the design value approach presented in the Eurotop 2018 manual.

It is assumed that real design values can be obtained for the following ranges of geometrical layout parameters under comparable hydraulic boundary conditions:

- $-0.4 \leq R_c/H_{si} \leq 0.8$
- $1.0 \leq B/H_{si} \leq 15$

The structural dimensions of the HLCS form the most uncertainty, which is related to the uncertainty that is found for the calibrated and validated porous media resistance parameters. Especially for structures where the freeboard significantly deviates from the previously mentioned range $R_c/H_{si} \approx 0$ high uncertainty is expected. Furthermore it is assumed that the location of the HLCS relative to the sea wall can be chosen arbitrarily without increasing the uncertainty of the prediction. It is expected that this OpenFOAM model can also be applied to study the hydrodynamic system using a conventional rubble mound LCS with $R_c/H_{si} \approx 0$. However, porous media resistance parameters should be adjusted accordingly. For varying geometrical layouts that deviated considerably from the reported ranges it is advised to perform new physical model tests to validate the adjusted OpenFOAM model.

9.2. Conclusions

This section provides the main conclusions to the research questions. The main research objective was:

"To verify and demonstrate the ability of OpenFOAM to capture the hydrodynamic interactions for HLCS consisting of cubipod artificial concrete elements and gain insight in the design sensitivities to optimise the two dimensional cross sectional layout using a HLCS to reduce sea wall overtopping most effectively"

Based on this research objective the following research questions were formulated:

1. What type of relevant hydrodynamic interactions play a role in a system using a HLCS consisting of cubipod artificial concrete elements and what are the main geometrical layout parameters that can be adjusted within this system to reduce sea wall overtopping?
2. How can OpenFOAM be used to model the hydrodynamic behaviour of HLCS related to wave transmission?
3. What are the design sensitivities in the cross-sectional layout of a hydrodynamic system using a HLCS consisting of cubipod artificial concrete elements to reduce sea wall overtopping and how can they be optimised?

First the different research questions are answered after which the main conclusion is drawn based on the research objective.

1. Relevant hydrodynamic interactions and the main geometrical layout parameters

- The most relevant hydrodynamic interactions are: wave transmission over the HLCS, the additional water level set-up inside the basin (both mean and temporal behaviour as well as the spatial distribution over the basin), reflecting wave energy resulting in seiching and resonance inside the basin, broken wave propagation inside the basin and the overtopping over the sea wall. The amount of wave transmission is determined by wave breaking on the crest of the HLCS and the amount of porous flow resistance by flow through the HLCS. These mechanisms are affected and determined by the internal geometry (i.e. the porous structure) and the main geometrical parameters of the HLCS.
- The main geometrical layout parameters that are distinguished for the hydrodynamic system are:
  1. The crest freeboard R_c
  2. The crest width B
  3. The basin length L_{pool}

  These main geometrical layout parameters all affect the hydrodynamic characteristics inside the system that combined lead to an overtopping event.

2. Ability of OpenFOAM to model wave transmission hydrodynamic behaviour for HLCS

- HLCS consisting of large artificial concrete elements have a different internal geometry compared to conventional rubble mound LCS. OpenFOAM is able to model the hydrodynamic behaviour of porous structures using the van Gent (1995) parameterization of the extended Darcy Forchheimer equation as implemented in the VARANS equations. The internal differences in the porous structure for HLCS are mostly reflected in the porosity n_p and the closure coefficients α and β.
- Large porosity gradients are found near the boundaries of the HLCS due to the size and shape of the artificial concrete elements. In order to implement these porosity gradients a porosity distribution is derived. Different numerical layers are implemented in OpenFOAM resulting from a schematization of the porosity distribution (see section 7.2.3). Additionally two different outer contour schematizations are adopted and analysed (see section 7.3). The effect of implementing multiple numerical layers with different porosity values and the exact outer contour schematization is limited (i.e. less than 2% difference on K_t).

- The best agreement between the modelled transmission coefficient and the experimental transmission coefficient is found for $\alpha = 500$ and $\beta = 1.0$ in combination with a constant $D_{n50} = 4.35cm$, KC number based on linear wave theory at the toe of the structure (i.e. $KC = 13.15$) and two numerical layers with a core and outer layer porosity of 50 and 75.2 % respectively. This combination of porous media resistance coefficients is unique for cubipod HLCS in the applied placement grid. Case specific calibration is needed for different placement grids or using different concrete elements.

3. Geometrical layout design sensitivities

The main geometrical parameters in the geometrical cross-section are the crest freeboard R_c of the HLCS, the crest width of the HLCS (B) and the distance between the HLCS and the sea wall (L_{pool}). The main conclusions are presented here. For additional conclusions the reader is referred to the separate conclusion sections for varying geometrical parameters (i.e. section 8.4.5, 8.5.5 and 8.6.4).

- Wave transmission is found to be dominant over the water level set-up, seiching and resonance inside the basin for the overtopping assessment of varying crest height and crest width of the HLCS. The most striking result for wave transmission over HLCS is that HLCS shows a constant trend in wave transmission for emergent structures (i.e. $R_c > 0$). A further increase of crest height does not result in reduced wave transmission, contrary to conventional rubble mound LCS where a further reduction is observed.

- Furthermore a large dependency is found for varying basin length. The propagation of broken waves (i.e. hydraulic bores) due to wave breaking over the crest of the HLCS have a large contribution to the mean overtopping discharge. It is observed that these hydraulic bores die out for larger basin length. Additionally low-frequency wave motion (i.e. seiching and resonance) is observed for varying basin length. However this effect is smaller compared to the dissipating bores.

- For all varying geometrical parameters a decay in the form of an exponential function of the mean overtopping discharge is found for increasing parameter value. The most influence on the overtopping reduction is found for varying crest height of the HLCS.

- By comparing the estimated overtopping discharge using the Eurotop guidelines solely based on the amount of wave transmission and the obtained overtopping discharge from the OpenFOAM model a mean underestimation of 69% is found by only using the transmission coefficient for the assessment of the amount of mean overtopping discharge. This concludes that the water level set-up cannot be neglected for overtopping assessments. Furthermore the use of advanced CFD modelling (e.g. using OpenFOAM) or physical modelling is of added value for the assessment of the amount of overtopping for these complex hydrodynamic systems due to the influence of dissipating bores, seiching and resonance inside the basin.

- Finally it is demonstrated that the OpenFOAM model is capable of addressing the design sensitivities related to the main geometrical layout parameters. These design sensitivities can subsequently be used to provide design recommendations and optimise the reduction of sea wall overtopping most effectively.

Main conclusion

This research has demonstrated that OpenFOAM has high potential for the coastal engineering community to gain insight in complex hydrodynamics. It is able to capture the complex hydrodynamics that play a role in the use of a detached HLCS to reduce sea wall overtopping. The OpenFOAM model that has been set-up is able to model wave breaking over the HLCS, the porous flow through the HLCS, wave propagation inside the basin, wave induced water level set-up, hydraulic bore dissipation, low-frequency wave motion (i.e. seiching and resonance) and the overtopping over the sea wall. The most important design sensitivities in geometrical layout are highlighted and analysed which can be used during assessment, design and optimisation of such hydrodynamic systems. For comparable hydraulic boundary conditions (i.e. the same order of H_s, H_s/h, h/L_p) and the use of low-crested structures (i.e. $R_c/H_{s,i} \approx 0$) this OpenFOAM model can be used without further calibration.

9.3. Recommendations

In this section the recommendations are presented which have been divided in two sections. The first section is related to numerical model recommendations related to the use of OceanWave3D and OpenFOAM. The second section prescribes recommendations for future research to this topic related to the discussions provided in section 9.1.

9.3.1. Numerical modelling recommendations

1. It was found that the horizontal resolution of OceanWave3D has the most influence on the correct coupling between both numerical models, especially for highly non-linear waves. The proposed value based on this study (i.e. 40 grid cells per normative wave length based on Tp) is way higher compared to the initially recommended value by the JIP program which recommended more than 10 grid cells per wave length for the OceanWave3D grid. This recommendation by the JIP program is based on limited non-linear waves within the numerical flume, and therefore is not able to capture the steep peaks of the waves. For the OceanWave3D grid only minor effect of the vertical grid resolution is observed but vertical stretching is recommended to increase resolution near the SWL.

2. Based on the constructed OpenFOAM mesh in this research it is recommended to have orthogonal cells near the free surface, including mesh refinements near the free surface to capture the non-linearity of the waves better. Moreover is is recommended to base the grid resolution on the number of cells per wave height, because this proofed normative compared to the recommendations related to the number of grid cells per wave length. However the amount of non linearity also plays a role here which requirement is leading is model set-up specific. Additionally it is recommended to perform mesh refinements near regions of interest and where large gradients are expected. Based on the calibration procedure followed in this research a grid with grid resolution of 10 grid cells per normative (i.e. significant) wave height is selected. However this value is also case specific and overall values between 10-20 grid cells per normative wave height are recommended depending on the calibration and the agreement with physical model data.

3. Step 1 of the calibration and validation procedure for the wave flume hydrodynamics compares the raw surface elevation signals within the flume at the end of the coupling zone. However, all grid resolutions showed high correlation and this step did not show to be an addition to the grid consideration and is therefore not recommended for future research however it is included in this report for this study.

4. It is recommended to perform case specific calibration for the hydrodynamic behaviour of HLCS and use β values in the range of 0.5-1.5, whereas the α value can be kept constant at $\alpha = 500$ because the influence of α is small and this reduces the calibration effort. Moreover, the addition of the porous outer layer is found to have limited effect on the reported transmission coefficient and therefore is not needed in case wave transmission for HLCS is addressed, but for different applications of the model this effect is unknown.

5. During the parametric study conducted in this research it was found that for the comparison of the mean water level set-up near the sea wall the location is important for the assessment. In this research bulk wave gauges have been installed every 0.1 m within the flume. This can result in a bias during comparison of the output of these wave gauges, whereas not the same distance between the used wave gauge and the sea wall is found. It is therefore recommended to use wave gauges that follow the changes in numerical grid (i.e. to place wave gauges near important locations and move them accordingly to the changes in the numerical grid).

9.3.2. Recommendations for future research

In this sections the recommendations for future research are presented, divided by recommendations for the hydrodynamic behaviour of HLCS and recommendations for the hydrodynamic system.

HLCS

1. Additional analysis on the hydrodynamic behaviour of the HLCS is insight-full for a better understanding of the use of HLCS, and the modelling of the hydrodynamic behaviour. In this research

only the hydrodynamic behaviour related to wave transmission is addressed for varying crest height and crest width of the HLCS but the effect of dissipation within the structure and wave reflection are not quantified. Additionally the effect of other structural parameters like the slope of the HLCS on the hydrodynamic behaviour can give use full additional insights.

2. The calibrated porous media coefficients are calibrated and validated for only one crest width and a small range of different crest height. It is highly advisable to perform validation of the porous media resistance parameters for larger ranges of crest height. Additionally it is highly recommended to conduct physical model experiments for different crest width for HLCS which can be used to validate the numerical model for a larger range of input parameters. The validation for larger ranges of geometrical parameters of the HLCS result in a better description of the modelling ability and uncertainty related to the adopted porous media resistance parameters.

Hydrodynamic system

1. In this research the changes in geometrical parameters are treated predominantly independently (i.e. only varying one parameter per simulation). This results in the insight of predominantly isolated geometrical parameters. It is however recommended to investigate the dependency of the geometrical parameters, whereas it is likely that this can give additional insight that can be used for design considerations. Additionally this research focuses on only one hydraulic boundary condition. It is recommended to analyse the effect of different wave characteristics corresponding to different sea states (i.e. wind wave climate and swell climate) and their effect on the systems behaviour.

2. It is recommended to do more research to the distance of the HLCS to the sea wall. Using a crest freeboard of 0, a large dependency of basin length was found. However it is expected that this dependency varies for different crest freeboard. The considerable increase in overtopping discharge was related to broken wave propagation which depend on the type of wave breaking on the structure and thus are affected by the crest freeboard. Therefore it is interesting to perform overtopping simulations for different basin length including both submerged and emergent structures.

3. During this research a large dependency of the geometrical layout parameters on the spatial distribution of mean water level within the system (i.e. the observed hydraulic gradient over the HLCS and within the basin) is observed. The quantitative effect of this gradient on the predicted overtopping discharge is not analysed in this research due to time constraints but might result in valuable knowledge. Especially the observed increasing gradient for smaller basin length might be an additional cause of the increase in overtopping found for smaller basin length.

4. Included in the OpenFOAM model used for this research is a description of wave forces on the sea wall. Especially for different basin length violent overtopping is expected for smaller basin length due to broken wave propagation. This is expected to have significant influence on the predicted wave forces on the sea wall which affect the life span of the sea wall structure. Lots of old sea walls are damaged over the world due to wave forces which can be prevented by the use of a LCS according to Roenby et al. (2017). Data is available from the front face of the sea wall based on conducted model runs in this research which are extracted using the ventilated boundary condition with (epsilon=1.5, openness= 3%).

5. This research focused on the use of a HLCS to reduce overtopping. However it is recommended to analyse the design sensitivities in geometrical layout while using a conventional rubble mound LCS to assess the effect of using a less porous structure on the hydrodynamics inside the basin and the predicted overtopping discharge.

Bibliography

Bellotti, G. (2004, jun). A simplified model of rip currents systems around discontinuous submerged barriers. *Coastal Engineering*, *51*(4), 323–335. doi: 10.1016/j.coastaleng.2004.04.001

Berberović, E., Van Hinsberg, N. P., Jakirlić, S., Roisman, I. V., & Tropea, C. (2009). Drop impact onto a liquid layer of finite thickness: Dynamics of the cavity evolution. *Physical Review E - Statistical, Nonlinear, and Soft Matter Physics*. doi: 10.1103/PhysRevE.79.036306

Bosboom, J., & Stive, M. J. (2015). *Coastal Dynamics 1* (Version 0. ed.).

Bosma, C., Jan Verhagen, H., D'Angremond, K., & Sint Nicolaas, W. (2003). VOID POROSITY MEASUREMENTS in COASTAL STRUCTURES. In *Proceedings of the coastal engineering conference.* doi: 10.1142/9789812791306_0119

Briganti, R., Van Meer, J. D., Buccino, M., & Calabrese, M. (2003). Wave transmission behind low-crested structures. In *Coastal structures 2003 - proceedings of the conference* (pp. 580–592). doi: 10.1061/40733(147)48

Buccino, M., & Calabrese, M. (2007). Conceptual Approach for Prediction of Wave Transmission at Low-Crested Breakwaters. *Journal of Waterway, Port, Coastal and Ocean Engineering*, *133*(3), 213–224. doi: 10.1061/ASCE0733-950X2007133:3213

Burcharth, H. F., & Andersen, O. K. (1995). On the one-dimensional steady and unsteady porous flow equations. *Coastal Engineering*. doi: 10.1016/0378-3839(94)00025-S

Calabrese, M., Vicinanza, D., & Buccino, M. (2003). 2D Wave Set Up behind Low Crested and Submerged Breakwaters. In *Proceedings of the international offshore and polar engineering conference.*

Calabrese, M., Vicinanza, D., & Buccino, M. (2008, jul). 2D Wave setup behind submerged breakwaters. *Ocean Engineering*, *35*(10), 1015–1028. doi: 10.1016/j.oceaneng.2008.03.005

Ciria, Cur, & Cetmef. (2007). *The Rock Manual. The use of rock in hydraulic engineering.*

Dalrymple, R., & Dean, R. (1971). "Discussion of 'Piling-up behind low and submerged permeable breakwaters' by Diskin et al.". *J. Mar. Res.Wtrwy., Harb. and Coast. Engrg. Div.*, *97*(2), 423–427.

D'Angremond, K., Van Der Meer, J. W., & De Jong, R. J. (1996). Wave transmission at low-crested structures. In *Proceedings of the coastal engineering conference.* doi: 10.1061/9780784402429.187

del Jesus, M., Lara, J. L., & Losada, I. J. (2012). Three-dimensional interaction of waves and porous coastal structures. Part I: Numerical model formulation. *Coastal Engineering*, *64*, 57–72. Retrieved from http://dx.doi.org/10.1016/j.coastaleng.2012.01.008 doi: 10.1016/j.coastaleng.2012.01.008

Diskin, M., Vajda, M., & Amir, I. (1970). Piling-Up behind Low and Submerged Permeable Breakwaters. *Journal of the Waterways, Harbors and Coastal Engineering Division*.

Engsig-Karup, A. P., Bingham, H. B., & Lindberg, O. (2009). An efficient flexible-order model for 3D nonlinear water waves. *Journal of Computational Physics*. doi: 10.1016/j.jcp.2008.11.028

Goda, Y. (2010). Random seas and design of maritime structures. In *Advanced series on ocean engineering.*

Hattori, M., & Sakai, H. (1994). Wave Breaking Over Permeable Submerged Breakwaters. *Coastal Engineering*, *24*. doi: 10.1061/9780784400890.081

Higuera, P., Lara, J. L., & Losada, I. J. (2014a). Three-dimensional interaction of waves and porous coastal structures using OpenFOAM®. Part I: Formulation and validation. *Coastal Engineering*, *83*, 243–258. Retrieved from http://dx.doi.org/10.1016/j.coastaleng.2013.08.010 doi: 10.1016/j.coastaleng.2013.08.010

Higuera, P., Lara, J. L., & Losada, I. J. (2014b). Three-dimensional interaction of waves and porous coastal structures using OpenFOAM®. Part II: Application. *Coastal Engineering*. doi: 10.1016/j.coastaleng.2013.09.002

Hirose, N; Watanuki, A; Saito, M. (2002). New type units for artificial reef development of ecofriendly artificial reefs and the effectiveness thereof. *Proceedings of the Coastal Engineering Conference*, *30*.

Hofland, B., & van Gent, M. R. (2010). *Maasvlakte 2: Harde Zeewering, Stenig Duin + Blokkendam* (Tech. Rep.). Deltares.

Holthuijsen, L. H. (2007). *Waves in oceanic and coastal waters*. doi: 10.1017/CBO9780511618536

ITTC. (2011). *ITTC-Recommended Procedures and Guidelines: Practical Guidelines for Ship CFD Applications* (Tech. Rep.).

Jacobsen, N. G. (2017). *DRAFT WAVES2FOAM MANUAL* (Tech. Rep.). Retrieved from https://www.researchgate.net/publication/319160515{_}waves2Foam{_}Manual

Jacobsen, N. G., Fuhrman, D. R., & Fredsøe, J. (2012, nov). A wave generation toolbox for the open-source CFD library: OpenFoam®. *International Journal for Numerical Methods in Fluids*, *70*(9), 1073–1088. doi: 10.1002/fld.2726

Jacobsen, N. G., van Gent, M. R., Capel, A., & Borsboom, M. (2018, dec). Numerical prediction of integrated wave loads on crest walls on top of rubble mound structures. *Coastal Engineering*, *142*, 110–124. doi: 10.1016/j.coastaleng.2018.10.004

Jacobsen, N. G., van Gent, M. R., & Fredsøe, J. (2017, feb). Numerical modelling of the erosion and deposition of sand inside a filter layer. *Coastal Engineering*, *120*, 47–63. doi: 10.1016/j.coastaleng.2016.09.003

Jacobsen, N. G., van Gent, M. R., & Wolters, G. (2015, aug). Numerical analysis of the interaction of irregular waves with two dimensional permeable coastal structures. *Coastal Engineering*, *102*, 13–29. doi: 10.1016/j.coastaleng.2015.05.004

Jensen, B., Jacobsen, N. G., & Christensen, E. D. (2014, feb). Investigations on the porous media equations and resistance coefficients for coastal structures. *Coastal Engineering*, *84*, 56–72. doi: 10.1016/j.coastaleng.2013.11.004

Knieß, H. (1977). Bemessung von Schüttstein-Deckwerken im Verkehswasserbau; Teil 1: lose Steinschüttungen.

Kudumula, S. R., & Mutukuru, M. R. G. (2013). Experimental Studies on Low Crested Rubble Mound, Semicircular Breakwaters and Vertical Wall System. *The International Journal of Ocean and Climate Systems*, *4*(3), 213–226. doi: 10.1260/1759-3131.4.3.213

Lara, J. L., del Jesus, M., & Losada, I. J. (2012). Three-dimensional interaction of waves and porous coastal structures. Part II: Experimental validation. *Coastal Engineering*, *64*, 26–46. Retrieved from http://dx.doi.org/10.1016/j.coastaleng.2012.01.009 doi: 10.1016/j.coastaleng.2012.01.009

Lara, J. L., Losada, I. J., Maza, M., & Guanche, R. (2011). Breaking solitary wave evolution over a porous underwater step. *Coastal Engineering*. doi: 10.1016/j.coastaleng.2011.05.008

Larsen, B. E., Fuhrman, D. R., & Roenby, J. (2019). Performance of interFoam on the simulation of progressive waves. *Coastal Engineering Journal*. doi: 10.1080/21664250.2019.1609713

Longuet-Higgins, M. (1967). On the wave induced difference in mean sea level between two sides of a submerged breakwater. *J. Mar. Res.*, *25*(2), 148–152.

Losada, I. J., Lara, J. L., & del Jesus, M. (2016). Modeling the interaction of water waves with porous coastal structures. *Journal of Waterway, Port, Coastal and Ocean Engineering*. doi: 10.1061/(ASCE)WW.1943-5460.0000361

Loveless, J. H., Debski, D., & Macleod, A. B. (1998). Sea level set-up behind detached breakwaters. , 1665–1678.

Medina, J., Gómez-Martín, M. E., Mares-Nasarre, P., Odériz, I., Mendoza, E., & Silva, R. (2019). Hydraulic Performance of Homogeneous Low-Crested Structures. In *Coastal structures 2019.* doi: 10.18451/978-3-939230-64-9

Medina, J. R., & Gómez-Martín, M. E. (2016). *Cubipod Manual 2016*. Valencia. Retrieved from http://hdl.handle.net/10251/72310

Medina, J. R., Gómez-Martín, M. E., & Corredor, A. (2010). Influence of armor unit placement on armor porosity and hydraulic stability. *Proceedings of the Coastal Engineering Conference*, 1–12. doi: 10.9753/icce.v32.structures.41

Molines, J., Bayon, A., Gómez-Martín, M. E., & Medina, J. R. (2019). Influence of Parapets on Wave Overtopping on Mound Breakwaters with Crown Walls. *Sustainability*. doi: 10.3390/su11247109

Moretto, M. (2020). *An efficient numerical approach to model wave overtopping of rubble mound breakwaters* (Unpublished doctoral dissertation). TU Delft.

Odériz, I., Mendoza, E., Silva, R., & Medina, J. R. (2018). Stability and Hydraulic performance of a Homogeneous Cubipod Low-crested Mound Breakwater. In *7th international conference on the application of physical modelling in coastal and port engineering and science* (p. 8). Santander.

Pardo, V., Herrera, M. P., Molines, J., & Medina, J. R. (2014). Placement test, porosity, and randomness of cube and Cubipod armor layers. *Journal of Waterway, Port, Coastal and Ocean Engineering*. doi: 10.1061/(ASCE)WW.1943-5460.0000245

Paulsen, B. T., Bredmose, H., & Bingham, H. B. (2014, apr). An efficient domain decomposition strategy for wave loads on surface piercing circular cylinders. *Coastal Engineering*, *86*, 57–76. doi: 10.1016/j.coastaleng.2014.01.006

Pilarczyk, K. W. (2003). Design of low-crested (submerged) structures – an overview –. *6th Intern. Conf. on Coastal and Port Engineering in Developing Countries*.

Rabinovich, A. B. (2009). Seiches and harbor oscillations. In *Handbook of coastal and ocean engineering.* doi: 10.1142/9789812819307_0009

Reddy, M. G., & Neelamani, S. (2005). Hydrodynamic studies on vertical seawall defenced by low-crested breakwater. *Ocean Engineering*, *32*(5-6), 747–764. doi: 10.1016/j.oceaneng.2004.07.008

Roenby, J., Larsen, B. E., Bredmose, H., & Jasak, H. (2017). A new volume-of-fluid method in openfoam. In *7th international conference on computational methods in marine engineering, marine 2017.*

Romano, A., Bellotti, G., Briganti, R., & Franco, L. (2015). Uncertainties in the physical modelling of the wave overtopping over a rubble mound breakwater: The role of the seeding number and of the test duration. *Coastal Engineering*. doi: 10.1016/j.coastaleng.2015.05.005

SBRCURnet. (2014). *Construction and Survey Accuracies for the execution of rockworks.*

Seabrook, S. R., & Hall, K. R. (1998). Wave transmission at submerged rubblemound breakwaters. *Proceedings of the Coastal Engineering Conference*. doi: 10.1061/9780784404119.150

Shore Protection Manual. (1984). doi: 10.5962/bhl.title.47830

Soldini, L., Lorenzoni, C., Brocchini, M., Mancinelli, A., & Cappietti, L. (2009). Modeling of the wave setup inshore of an array of submerged breakwaters. *Journal of Waterway, Port, Coastal and Ocean Engineering*, *135*(2), 38–51. doi: 10.1061/(ASCE)0733-950X(2009)135:2(38)

Steendam, G. J., van der Meer, J. W., Verhaeghe, H., Besley, P., Franco, L., & van Gent, M. R. (2004). The international database on wave overtopping. (April 2005). doi: 10.1142/9789812701916

Van der Meer, J. (1990). *Data on wave transmission due to overtopping* (Tech. Rep.). Delft Hydraulics.

Van der Meer, J., Allsop, N., Bruce, T., De Rouck, J., Kortenhaus, A., Pullen, T., … Zanuttigh, B. (2018). EurOtop. Retrieved from www.overtopping-manual.com

Van der Meer, J., & Daemen, I. (1994). Stability and Wave transmission at Low-Crested Rubble-Mound Structures. *Journal of Waterway, Port, Coastal and Ocean Engineering*, *120*(1).

Van Der Meer, J. W., Regeling, E., & De Waal, J. P. (2000). Wave transmission: Spectral changes and its effects on run-up and overtopping. In *Coastal engineering 2000 - proceedings of the 27th international conference on coastal engineering, icce 2000.* doi: 10.1061/40549(276)168

van den Bos, J., & Verhagen, H. (2018). Breakwater Design - Lecture Notes CIE5308.

van der Meer, J. W., Briganti, R., Zanuttigh, B., & Wang, B. (2005, nov). Wave transmission and reflection at low-crested structures: Design formulae, oblique wave attack and spectral change. *Coastal Engineering*, *52*(10-11), 915–929. doi: 10.1016/j.coastaleng.2005.09.005

van der Meer, J. W., & Pilarczyk, K. W. (1991). Stability of low-crested and reef breakwaters. In *Proceedings of the coastal engineering conference.* doi: 10.1061/9780872627765.105

van Gent, M. R. (1995). Porous flow through rubble-mound material. *Journal of Waterway, Port, Coastal and Ocean Engineering*, *121*(3), 176–181. doi: 10.1061/(ASCE)0733-950X(1995)121:3(176)

Wamsley, T. V., & Ahrens, J. P. (2003). Computation of wave transmission coefficients at detached breakwaters for shoreline response modeling. In *Coastal structures 2003 - proceedings of the conference.* doi: 10.1061/40733(147)49

Zanuttigh, B., Martinelli, L., & Lamberti, A. (2008, jun). Wave overtopping and piling-up at permeable low crested structures. *Coastal Engineering*, *55*(6), 484–498. doi: 10.1016/j.coastaleng.2008.01.004

Zanuttigh, B., & van der Meer, J. W. (2008). Wave reflection from coastal structures in design conditions. *Coastal Engineering*. doi: 10.1016/j.coastaleng.2008.02.009

Zelt, J. A., Skjelbreia, J. E., & Wave Technologies. (1993). Estimating incident and reflected wave fields using an arbitrary number of wave gages. In *Proceedings of the coastal engineering conference.* doi: 10.1061/9780872629332.058

Zijlema, M. (2015). *Computational Modelling of Flow and Transport* (Tech. Rep.).

A

Relevant literature research

This appendix presents a more in depth review and the origin of the relevant literature research regarding the various wave structure interactions. First the wave transmission is addressed. Secondly the wave-induced water level setup is addressed after which wave reflection is addressed. Additionally general literature related to water waves and wave breaking is presented.

A.1. Wave transmission

Various studies in the past have tried to come up with prediction formulas for the wave transmission coefficient over LCS. From hydraulic laboratory tests empirical formulae have been formulated based on the most important structural parameters. Empirical formulae are based on a set of experimental studies and therefore always have their limitations based on laboratory conditions and the range of input variables used. The most relevant studies on wave transmission are treated. Based on the method used in (Buccino & Calabrese, 2007) an irregular wave field can be included in the predictions by taking the significant wave height as the regular wave height if the theoretical formulae is derived for regular wave conditions.

(Van der Meer, 1990) was the first one to propose a simple prediction formulae where K_t linearly depends on the relative freeboard made dimensionless by the incoming wave height Rc/H_i:

$$\begin{array}{lll} K_t = 0.8 & \text{for} & -2.0 < R_c/H_i < -1.13 \\ K_t = 0.46 + 0.3R_c/H_i & \text{for} & -1.13 < R_c/H_i < 1.2 \\ K_t = 0.1 & \text{for} & 1.2 < R_c/H_i < 2.0 \end{array} \tag{A.1}$$

Later his formulation was combined with work from Daemen and the transmission coefficient was made dimensionless with the nominal diameter of the armour layer to take the permeability of the structure into account. Also the effect of wave steepness was included. This formulation reduced a lot of scatter in the laboratory measurements and also did not take the crest width into account. The formulation by Van der Meer & Daemen (1994) is presented as:

$$K_t = a\frac{R_c}{D_{n50}} + b \tag{A.2}$$

In which:

$$a = 0.031\frac{H_{s,i}}{D_{n50}} - 0.24$$

$$b = -5.42s + 0.0323\frac{H_{s,i}}{D_{n50}} - 0.0017\left(\frac{B}{D_{n50}}\right)^{1.84} + 0.51 \tag{A.3}$$

$$s_{op} = \frac{H_{s,i}}{L_0} = 2\pi H_s/(gT_p)^2$$

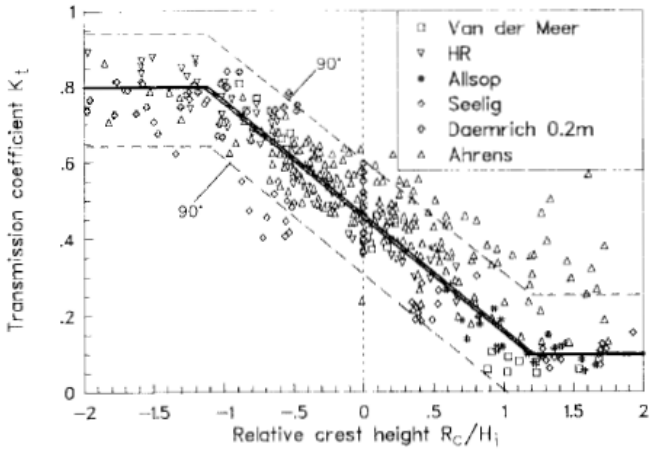

Figure A.1: Wave transmission vs relative crest height: Performance of transmission data for linear equation. (Van der Meer & Daemen, 1994)

In this formula the K_t values are bounded between $0.075 < K_t < 0.75$. This formula is valid for $1 < H_i/D_{n50} < 6$ and $0.01 < s_{op} < 0.05$.

D'Angremond et al. (1996) included the crest width in a new empirical design formulae for relatively narrow crests. In this study also some tests with tetrapods and accropodes were included to come up with transmission design formulas for both rubble mound structures and impermeable structures. The transmission is made dimensionless by the incoming wave height. D'Angremond et al. (1996) presented the following transmission formula:

$$K_t = -0.4\frac{R_c}{H_{s,i}} + 0.64\left(\frac{B}{H_{s,i}}\right)^{-0.31}\left(1 - e^{-0.5\xi}\right) \tag{A.4}$$

The factor 0.64 should be used for rubble mound structures and concrete elements. For impermeable structures the factor 0.8 should be used instead of 0.64. In this formula the K_t values are bounded between $0.075 < K_t < 0.8$. This formula is valid for $-2.5 < R_c/H_{s,i} < 2.5$ and $B/H_{s,i} < 10$.

The work by (Van der Meer & Daemen, 1994) and (D'Angremond et al., 1996) was the starting point for a large European funded project DELOS (Environmental Design of Low Crested Coastal Defence Structures). Based on the gathered data from the DELOS project (Briganti et al., 2003) revised the formula of d'Angremond to include wide crests:

$$K_t = -0.35\frac{R_c}{H_{s,i}} + 0.51\left(\frac{B}{H_{s,i}}\right)^{-0.65}\left(1 - e^{-0.41\xi}\right) \tag{A.5}$$

In this formula the K_t values are bounded between $0.05 < K_t < 0.006B/H_{s,i} + 0.93$. The effect of the crest width on the wave transmission is assumed to be linear as can be observed from figure A.2.

This formula is introduced for very wide crests and is valid for $B/H_{s,i} > 10$ and $-2.5 < R_c/H_{s,i} < 2.5$ and has been validated up to $B/H_{s,i} = 50$. It should be noted that the use of these two formulae introduce a discontinuity at the boundary $B/H_{s,i} = 10$.

(van der Meer et al., 2005) concluded that this new relation derived in (Briganti et al., 2003) was valid for $B/H_{s,i} > 12$. For $B/H_{s,i} < 8$ the formulation by (D'Angremond et al., 1996) is still valid and linear interpolation is needed for $8 < B/H_{s,i} < 12$. This took away the discontinuity introduced by Briganti et al. (2003).

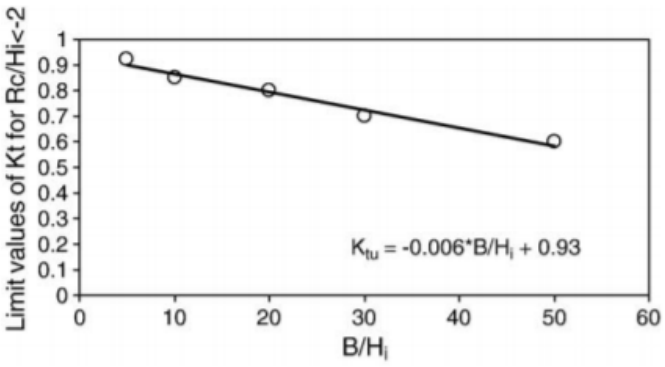

Figure A.2: Upperlimit for very wide crests, linear relationship (van der Meer et al., 2005)

$$K_t = -0.4\frac{R_c}{H_{s,i}} + 0.64\left(\frac{B}{H_{s,i}}\right)^{-0.31}\left(1-e^{-0.5\xi}\right) \quad \text{for} \quad B/H_{s,i} < 8$$
$$K_t = -0.35\frac{R_c}{H_{s,i}} + 0.51\left(\frac{B}{H_{s,i}}\right)^{-0.65}\left(1-e^{-0.41\xi}\right) \quad \text{for} \quad B/H_{s,i} > 12 \tag{A.6}$$

(van der Meer et al., 2005) also included the angle of wave attack in the empirical formulae. They concluded that for rubble mound structures the wave angle attack has no effect on the transmission coefficient and that the transmitted wave angle is approximately 80% of the incident wave angle.

For impermeable structures (van der Meer et al., 2005) presented a transmission relation for oblique incident waves. In here it must be noted that for impermeable structures the effect of the crest width is not taken into account as no energy dissipation is expected by roughness and porosity of the structure.

$$K_t = \left(-0.3\frac{R_c}{H_{s,i}} + 0.75\left[1-\mathrm{e}^{-0.5\xi}\right]\right)\cos^{2/3}\beta \tag{A.7}$$

In this formula the K_t values are bounded between $0.075 < K_t < 0.8$. This formula is valid for $0.01 < s < 0.03$, $1 < B/H_{s,i} < 4$ and $0 < \beta < 70$ degrees.

Also some studies have been performed on submerged rubble mound breakwaters only. (Seabrook & Hall, 1998) studied submerged rubble mound structures for a large range of relative freeboard and relative crest width making it a very widely applicable study. They concluded that the effect of breakwater slope on the wave transmission was relatively unimportant. The most effect was found for increasing breakwater width and increasing freeboard.

$$K_t = 1 - \left[e^{-0.65\frac{R_c}{H_{m0,i}} - 1.09\frac{H_{m0,i}}{B}} + 0.047\frac{BR_c}{LD_{n50}} - 0.067\frac{R_c H_{m0,i}}{BD_{n50}}\right] \tag{A.8}$$

This formula is valid for $5 < B/H_{m0,i} < 74.47$, $0 < BR_c/LD_{n50} < 7.08$ and $0 < R_c H_{m0,i}/BD_{n50} < 2.14$.

(Hirose, N; Watanuki, A; Saito, 2002) also studied submerged rubble mound structures only with a newly developed Aquareef armour unit for a wide range of relative crest width. Structures armoured with Aquareef units show higher limiting values of K_t compared to other structures. Moreover these limiting values are found for relatively high values of $R_c/H_{s,i}$. The larger limiting values are probably due to the high permeability of the concrete armour layer. For high $R_c/H_{s,i}$ values the crest is emerged above the waterline and most of the energy transmission is related to transmission through the breakwater. Higher permeability result in less energy dissipation through the breakwater and therefore for higher limiting values.

Wamsley & Ahrens (2003) were the first ones to propose a transmission formula based on a sum of two separate contributions, one for energy transmitted through the structure and one for energy

transmitted over the structure. Based on this approach (Buccino & Calabrese, 2007) tried to calculate the wave transmission of low crested breakwaters by taking the main energy transmitting components into account using theoretical solutions rather than experimental deduced equations. Simple analytical expressions for wave breaking, porous flow and overtopping were used to predict wave transmission for low crested breakwaters and regular waves. For low-crested breakwaters the wave breaking on top of the breakwater is the main energy transfer component which has been elaborated using a dissipation rate depending on the analogy of the movement of a hydraulic jump. (Buccino & Calabrese, 2007) presented the following prediction formula:

$$K_t = \frac{1}{1.18\left(\frac{H_{s,i}}{R_c}\right)^{0.12} + 0.33\left(\frac{H_{s,i}}{R_c}\right)^{1.5} \cdot \frac{B}{\sqrt{H_{s,i}L_0}}} \tag{A.9}$$

Valid for $1/0.5 < R_c/H_{s,i} < 1/1.2$ and for zero relative submergence $Rc/H_{s,i} = 0$ the transmission can be predicted by:

$$K_t = \left[\min\left(0.74; 0.62\xi_{op}^{0.17}\right) - 0.25 \cdot \min\left(2.2; \frac{B}{\sqrt{H_{s,i}L_0}}\right)\right]^2 \tag{A.10}$$

Both formulas are valid for $0.3 < B/H_{s,i}L_0^2 < 10.5$ and $1 < \xi_{op} < 8$.

For relatively long waves $s_{op} < 0.01$ an increase in dissipation is expected according to (Buccino & Calabrese, 2007). The factor 0.33 in the prediction formula has to be adapted for long waves to $0.33 + 47(0.01 - s_{op}$. This method has been checked for validity up to $s_{op} = 0.002$.

The most important parameters are the relative crest width, the relative freeboard of the structure and the Iribarren parameter which determines the type of wave breaking on the structure. (Buccino & Calabrese, 2007) concluded that the outliers in predicted transmission coefficient were probably due to porosity effects of the used structure and frictional effects of the armour layer. These outliers spread both in the upper and lower part of the cloud of data which indicates no systematic overestimates or under predictions. The authors explain the over predictions in several studies due to the use of a lower structure porosity. The R^2 value of the prediction method is slightly greater than 95 percent and the standard error is less than 0.05.

A.2. Water level set-up

The relevant studies on water level set-up are presented. First the 2DV models are explained and elaborated on the used principles and governing parameters. Then 3D analytical models are shortly mentioned but those will not be elaborated.

Longuet-Higgins (1967) was the first one to develop an analytical solution to predict the amount of water level set-up behind low crested structures. The difference in mean water level was calculated using a second order stokes wave theory based on small amplitude waves and irrational flow, which excludes any energy loss by either wave breaking or porous flow. The proposed formula by Longuet-Higgins (1967) reads:

$$\delta' = \frac{H_i^2\left(1 + K_R^2\right)k_1}{8\sinh\left(2k_1h_1\right)} - \frac{H_i^2K_t^2k_2}{8\sinh\left(2k_2h_2\right)} \tag{A.11}$$

It is worth noticing that the formulae derived by Longuet-Higgins (1967) gives insight in the effect of the wave reflection and transmission coefficients on the water level set-up. The higher the wave reflection the more water level set-up is predicted. Additionally more wave transmission reduces the water level set-up.

Diskin et al. (1970) created an empirical formula based on the results of 2DV flume experiments. The proposed formula only depends on the freeboard and the incident wave height. The water level

set-up follows a Gaussian curve from which the maximum set-up can be found for $R_c/H_i = 0.7$. The proposed formula reads:

$$\frac{\delta}{H_i} = 0.6 \cdot \exp\left[-\left(0.7 - \frac{R_c}{H_i}\right)^2\right] \tag{A.12}$$

This formula is valid for $-2.0 < R_c/H_i < 1.5$ and $0.10 < h/H_i < 0.83$.

Dalrymple & Dean (1971) criticised the work by Diskin et al. (1970) in a public note. According to Dalrymple & Dean (1971) the scatter in for formula of Diskin et al. (1970) resulted from fact that no wave transmission or reflection coefficients had been included. The explicit role of these quantities was already pointed out by Longuet-Higgins (1967). Furthermore they proposed a predictive procedure that the setup is partly forced by the release of momentum flux due to wave breaking and partly by the flux of water mass over the crest of the structure (continuity set-up). This effect was introduced as experimental results of only wave momentum release were underestimating the amount of water level set-up. The proposed water level set-up is calculated using superposition of both fluxes:

$$\delta = \delta_{mf} + \delta_c \tag{A.13}$$

(Loveless et al., 1998) proposed a simple formula for permeable breakwaters based on the idea that the onshore mass and momentum flux had to be compensated by the offshore mass and momentum flux. They conducted an experimental model test for both regular and irregular waves and tried to include 3D effect by using a pump to recirculate the piled up water in the flume at a rate of 1-2 m3/s/m. It was found that the largest set-up occurs at zero freeboard and increases for increased crest width. The effect of permeability of the structure is included in the use of the D_{n50}. The fact that the set-up increases for wider crest widths is probably due to the enhanced breaking and release of wave momentum which increases the set-up. For low-crested crests the flux of water over the crest has a cyclic character which alternately is directed inshore and offshore depending on the incoming wave period. They proposed the following prediction formula for regular waves:

$$\frac{\delta}{B} = \frac{\left(\frac{H_i L}{hT}\right)^2}{8gD_{n50}} \exp\left[-20\left(\frac{R_c}{h_c}\right)^2\right] \tag{A.14}$$

For application of this formula for irregular waves, the authors found that the average wave height should be used in stead of the significant wave height. The results of this formula generate much smaller values of set-up compared to the model described by Diskin et al. (1970). This result is probably related to the use of different materials with large differences in permeability. This underlines the effect of permeability of the structure on the water level set-up which is important for low-crested breakwaters consisting of artificial elements. The dimensionless water level set-up is significantly affected by the rock size i.e. the porosity. The observed average non-dimensional set-up is $\delta/H_i = 0.3$.

Calabrese et al. (2003) used the same line of reasoning as Dalrymple & Dean (1971) and Loveless et al. (1998) by calculating the 2D wave breaking induced water level set-up on the basis of a conceptual model. They based their method on impermeable low-crested structures and random waves. The effect of water flowing trough the structure and thereby compensating the water level set-up is not taken into account in this model. This method will therefore over predict the water level set-up. The model is obtained by applying the momentum equation over a control volume surrounding the low-crested breakwater. The water level set-up is determined by the distance of the point of incipient breaking to the inshore toe. The final wave momentum induced set-up derived by (Calabrese et al., 2003) is:

$$\delta_{mf} = 0.5\left(-b + (b^2 - 4c)^{0.5}\right) \tag{A.15}$$

In which:

$$b = (2d - a)$$
$$a = \left(\left(1 + \frac{x_b + B}{L_s}\right)h_c - \frac{x_b}{L_s}(d_b + R_c)\right)$$
$$c = -\frac{3}{16}H_{eni}^2\left(1 - K_t^2\right)$$

x_b and L_s can be calculated from geometrical formulas once the depth at breaking is known. The effect of the transmission is included in the water level set-up formulas indicating the interdependence of water level set-up and wave transmission. For low-crested breakwaters is can be assumed that wave breaking occurs at the crest of the structure therefore $x_b = 0$. The depth at breaking can be predicted by the criterion of Kamphuis which is given as (Calabrese et al., 2003):

$$d_b = d^{0.2}\left(\frac{H_{m0i}}{0.56e^{3.5\tan\left(\alpha_{off}\right)}}\right)^{\frac{4}{5}} \tag{A.16}$$

The continuity set-up is calculated using the Gauckler-Strickler resistance law for a uniform return flow and can be interpreted as an additional specific hydraulic thrust which is required to counteract the shear stresses induced by the return current over the crest of the structure:

$$\delta_c = \frac{\left(\frac{1}{8}H_{eni}^2\sqrt{\frac{g}{d}}\right)^2}{f^2\left|R_c\right|^{10/3}} \cdot \left(B + h_c\,\mathrm{ctg}\left(\alpha_{off}\right)\right) \tag{A.17}$$

In which f is the friction of the armour layer which is taken as 20 corresponding to the conducted experimental results. For all definitions of the parameters and more information the reader is referred to (Calabrese et al., 2003).

There are also several authors who took the 3D character of a low-crested breakwater system into account. (Bellotti, 2004) presents for instance an analytical prediction method of water level set-up for a full 3D situation with rip current formation. This model is based on the full description of horizontal circulation around a low-crested breakwater system. The difference with the previously described models is that onshore flux of water mass is not only balanced by undertow, but also through the rip-channel system.

(Zanuttigh et al., 2008) presents a 2D and 3D model for both emerged and submerged structures based on a pumping curve. This model assumes that depth limited wave breaking occurs at the seaward slope of the structure which might not always be the case. Also the precise knowledge on the effect of structure permeability can improve the predictions (Zanuttigh et al., 2008).

(Calabrese et al., 2008) adapted the equations for water level set-up from the model introduced by (Calabrese et al., 2003) as this model was never sufficiently expounded according to the authors. The same model is used but different expressions are elaborated. Several adaptations can be found in the calculation of the continuity set-up, the depth of incipient breaking and the effect of wave reflection on the momentum release flux. According to (Calabrese et al., 2008) increased porosity results in increased permeability which reduces the amount of wave-induced water level set-up. This can be explained based on the increased section available for the back flow of water which therefore reduces the transport velocities and therefore also the shear stresses that the structure exerts on the water. This will make the transport of water through the structure more easy and therefore make the structure better able to restore the water level.

A.3. Wave reflection

Wave reflection is the wave structure interaction where wave energy is reflected from interaction with a structure. Rubble mound structures will generally reflect significantly less wave energy compared to smooth structures due to energy dissipation during the interaction of the waves with the structure (Ciria et al., 2007). Reflecting wave energy interacts again with the incoming waves which can create a standing wave pattern. Wave reflection can be evaluated using the reflection coefficient which is defined as the ratio of the reflected wave height and the incoming wave height:

$$K_r = \frac{H_r}{H_i} \tag{A.18}$$

For an irregular wave field the definition of the reflection coefficient is usually based on the significant wave height (H_s) or the spectral wave height (H_{m0}). Table A.1 presents the most used empirical reflec-

tion formulas in engineering practice for low-crested structures and their limitations. These formulas are subsequently elaborated in more detail later in this section.

Table A.1: Relevant literature regarding wave reflection

Author	Formulae	Applicability
(Ciria et al., 2007)	$K_r = 0.14\xi_{op}^{0.73}$	$\xi_{op} < 10$
(van der Meer et al., 2005)	$K_r = f_r \cdot 0.071P^{-0.82}\cot(\alpha)^{-0.62}s_{op}^{-0.46}$	$\xi_{op} < 10$
	$f_r = 0.2\ R_c/H_i + 0.9$	$R_c/H_i < 0.5$
	$f_r = 1$	$R_c/H_i \geq 0.5$
(Zanuttigh & van der Meer, 2008)	$K_r = \tanh\left(a\xi_0^b\right)\cdot\left(0.67 + 0.37\frac{R_c}{H_i}\right)$	$-1 \leq R_c/H_i \leq 0.5$
	$a = 0.167\left(1 - \exp\left(-3.2\gamma_f\right)\right)$	
	$b = 1.49\left(\gamma_f - 0.38\right)^2 + 0.86$	

According to (Ciria et al., 2007) The wave energy that is reflected of a structure only depends on the relative steepness of the incoming wave field compared to the structure slope.

$$K_r = 0.14\xi_{op}^{0.73} \tag{A.19}$$

Which is valid for $\xi_{op} < 10$.

A more elaborated formula for rubble mound structures including the permeability and a different relative effect of the incoming wave steepness and the steepness of the slope is found by van der Meer et al. (2005):

$$K_r = 0.071P^{-0.82}\cot(\alpha)^{-0.62}s_{op}^{-0.46} \tag{A.20}$$

In which also the notional permeability of the slope P is taken into account and the slope angle has a larger influence relative to the wave steepness. According to van der Meer et al. (2005) the influence of the slope angle will reduce if the structured is submerged. According to van der Meer et al. (2005) and Zanuttigh & van der Meer (2008) the relative crest height R_c/H_i has the main influence on the reflection coefficient which reduces for more submerged structures and that there is no influence of crest width on the reflection as the waves only reflect on the seaward slope.

The effect of the relative crest height R_c/H_i can be implemented in A.19 and A.20 by means of a reduction factor f_r (van der Meer et al., 2005):

$$\begin{aligned} f_r &= 0.2\ R_c/H_i + 0.9 \qquad for\ \ R_c/H_i < 0.5 \\ f_r &= 1 \qquad\qquad\qquad for\ \ R_c/H_i \geq 0.5 \end{aligned} \tag{A.21}$$

During the European research program CLASH, a new reflection formula has been developed for smooth and rough slopes. This formula includes the most important parameter, the relative freeboard R_c/H_i as has been determined before.

Consequently the only difference is found that a roughness value γ_f is included which is determined by the type of slope material.

$$\begin{aligned} K_r &= \tanh\left(a\xi_0^b\right)\cdot\left(0.67 + 0.37\frac{R_c}{H_i}\right) \\ a &= 0.167\left(1 - \exp\left(-3.2\gamma_f\right)\right) \\ b &= 1.49\left(\gamma_f - 0.38\right)^2 + 0.86 \end{aligned} \tag{A.22}$$

This formula is valid for $-1 \leq R_c/H_i \leq 0.5$. The values of a and b differ for various materials and different concrete elements as they have different roughness values γ_f. One layer cubes and flat

cubes give greater reflection than all the other armour units, in general the reflection increases with larger armour roughness (Zanuttigh & van der Meer, 2008).

A.3.1. Standing waves

(Reddy & Neelamani, 2005) investigated the effect of relative height (height of breakwater over sea ward water depth) on the wave force prediction at a vertical sea wall defenced by a low-crested breakwater. According to Reddy & Neelamani (2005) the relative height of the breakwater, h_c/h, is associated with the formation of standing waves and resonant conditions which generates oscillatory behaviour of force ratios at the sea wall. They found that the basin length had minor influence on the force prediction. Only for a basin length where waves would break on the low-crested structure resulting in wave jets and then hit the wall increased the force prediction.

However the frequency of the transmitted waves is equal to the natural frequency of the pool resonance can occur which will increase wave amplitudes inside the pool. Resonance is a phenomena which depends on the natural frequency of the system, the frequency of the forcing and the damping ability of the system. If the natural frequency of the pool between the low-crested breakwater and the vertical sea wall is more than the frequency of the transmitted wave, the pool will not experience resonance (Kudumula & Mutukuru, 2013). This will also hold if the natural frequency of the system is lower than the frequency of the system. If the forcing frequency is equal or a multiple of the to the natural frequency of the system the system starts to show resonance. The amplitude of the system will increase and overtopping rates will increase considerably. The friction of the system, determines the ability of the system to reduce the resonance amplitude. For design storm conditions it should be checked whether resonance might occur and if so the basin length should be adapted.

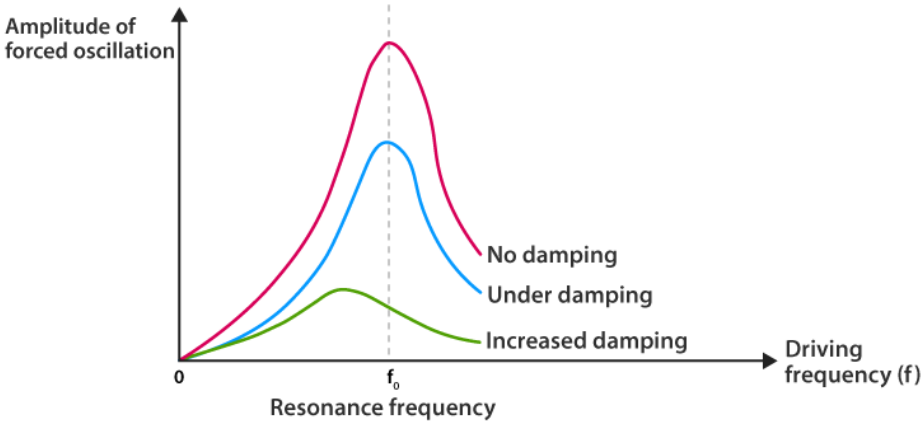

Figure A.3: The effect of resonance on the system behaviour, adopted from: https://byjus.com/physics/sharpness-of-resonance/

A.4. Water waves

A.4.1. Wave theories

A wave is a propagating perturbation of the free surface in arbitrary water depth. A wave has a wave height, wave length and wave period. The interaction between the wave and the bottom is important for the propagation behaviour of the wave. Once the wave interacts with the bottom the particle motion becomes more elliptical, the wave steepens and the wave length decreases. In order to describe a propagating wave field several wave theories are applicable for various ranges of water depth and wave characteristics. Figure A.4 presents the various wave theories and ranges of applicability. In this figure the two important wave breaking limits can be observed for depth induced breaking and steepness induced breaking. Generally a steepness of 0.01 indicates a typical swell sea and a steepness of 0.04 to 0.06 a typical wind sea Van der Meer et al. (2018).

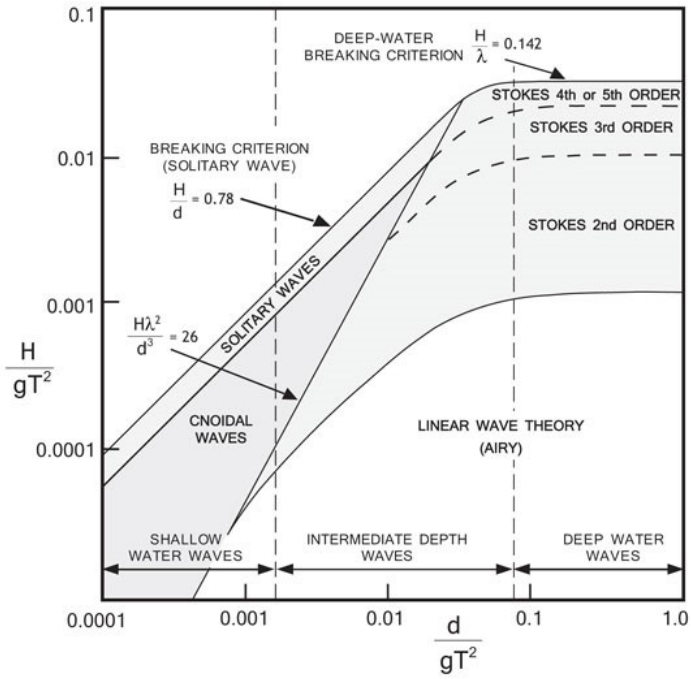

Figure A.4: Ranges of application of different wave theories

Airy wave theory

Airy wave theory describes the propagation of free surface waves for regular small amplitude gravity waves. It is described by a continuity mass balance equation and a momentum balance equation. The flow field in the domain can be described by a velocity potential equation which satisfies the Laplace equation. The Laplace equation is given as:

$$\frac{\partial^2 \phi}{\partial x^2} + \frac{\partial^2 \phi}{\partial y^2} + \frac{\partial^2 \phi}{\partial z^2} = 0 \tag{A.23}$$

One of the solutions to the Laplace equation is a long-crested harmonic wave for which the surface elevation, the dispersion relation, and the wave speed are given by:

$$\eta(x,t) = a \cdot \sin(\omega t - kx) \quad \text{or} \quad \eta(x,t) = \frac{1}{2} H \cdot \sin\left(\frac{2\pi}{T} t - \frac{2\pi}{L} x\right) \tag{A.24}$$

$$\omega^2 = gk \tanh(kd) \quad \text{or} \quad L = \frac{gT^2}{2\pi} \tanh\left(\frac{2\pi d}{L}\right) \tag{A.25}$$

$$c = \frac{\omega}{k} = \frac{g}{\omega} \tanh(kd) \tag{A.26}$$

Airy wave theory is only valid under the following assumptions: in-compressible fluid, constant density, no viscosity, continuous, no surface tension, the motions are only forced by the gravitation of the earth and water cannot penetrate the bottom nor leave the surface.

Non-linear wave theories

Non linear wave theories account for a finite wave height. When waves become too steep in deep water or enter shallow water and start to shoal, the linear sinusoidal profile of a wave no longer holds. These waves deviate from the assumptions used by linear wave theory and non linear wave theories are used to describe the surface elevation and the propagation of the wave. Non linear waves have higher crests than troughs and include both frequency and amplitude dispersion. There are several non-linear wave theories available which are given in figure A.4.

A.4.2. Wave momentum

Waves transport momentum which is equivalent to a stress. Variations in this stress cause forces on the water which can cause water level set-up or currents. The time averaged wave momentum stress is also called the radiation stress. This radiation stress has 4 components, 2 normal stresses and 2 shear stresses. By integrating these stresses over the depth and averaging in time, the following radiation stress components can be derived for a propagating wave in x direction according to linear wave theory (Holthuijsen, 2007):

$$\begin{aligned} S_{xx} &= \left(2n - \tfrac{1}{2}\right) E_{\text{total}} \\ S_{yy} &= \left(n - \tfrac{1}{2}\right) E_{\text{total}} \\ S_{xy} &= S_{yx} = 0 \\ n &= \tfrac{1}{2}\left(1 + \tfrac{2kh}{\sinh(2kh)}\right) \end{aligned} \tag{A.27}$$

The sub-indices xx and yy represent the normal stresses and the xy and yx represent the shear stresses which for a wave in in the direction of the positive x axis are zero. It has to be noted that the radiation stresses depend on the energy of the wave field and are therefore related to the wave height squared. From these radiation stresses the forces acting on the body of water can be calculated as:

$$\begin{aligned} F_x &= -\frac{\partial S_{xx}}{\partial x} \\ F_y &= -\frac{\partial S_{yy}}{\partial y} \end{aligned} \tag{A.28}$$

For a propagating wave in positive x-direction on a alongshore parallel beach the stationary water level set-up can be calculated using the radiation stress gradient driven body forces on the water. It assumes a balance between the time averaged radiation stress gradients and the water level set-up. For the assumption that the water level set-up is relatively small compared to the water depth the following balance holds:

$$\frac{d\bar{\eta}}{dx} = -\frac{1}{\rho g d}\frac{dS_{xx}}{dx} \tag{A.29}$$

From this equation the relation of the water level set-up and the wave height can be observed. For breaking waves there is an abrupt change in wave height which causes large negative gradients in radiation stresses and therefore a positive water level set-up.

Wave group pulsation

The set-up depends on the incoming wave height, which for stationary waves results in a stationary water level set-up. However for irregular sea states waves tend to arrive in groups which results in periodic behaviour of incoming wave heights. This results in a periodic fluctuation in water level set-up depending on the incoming wave groups. This beating of the SWL on lower frequencies compared to the incoming waves is called surf beat (Holthuijsen, 2007). Surf beat is one of the forms of infra-gravity waves. In order to understand infra gravity waves, first the origin of wave groups should be analysed. The next section (section A.4.3) treats wave groups and the formation of infra gravity waves.

A.4.3. Wave groups

Wave groups are composed of multiple waves travelling in the same direction. Irregular waves more or less appear in groups of waves with different frequencies. The groupiness of the wave field is caused by interference between waves of different frequencies Bosboom & Stive (2015). The phenomena that arises from the interference of waves with different frequencies can be explained by analysing two different harmonic waves with slightly different frequencies.

The two harmonic waves are described by their surface level elevation (η_1 and η_2) and will reinforce each other at one moment but cancel each other at another moment. This process repeats itself over and over, creating a series of wave groups (Holthuijsen, 2007). This formation process of wave groups using two harmonic waves with slightly different frequencies is presented in figure A.5.

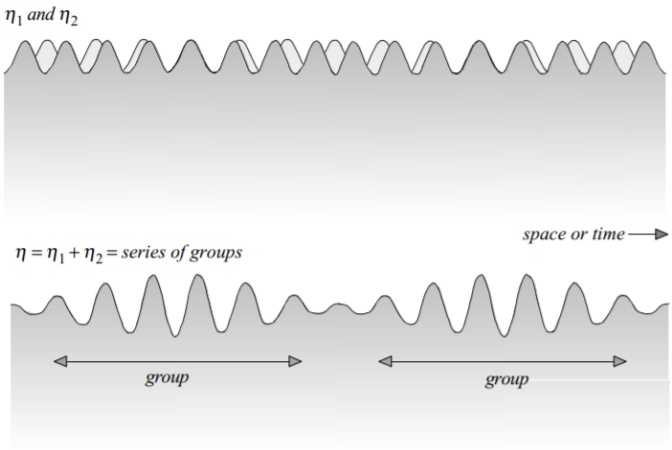

Figure A.5: Two harmonic waves with slightly different frequencies add up to a series of wave groups. Adopted from (Holthuijsen, 2007)

This process can be described using mathematical relationships of both harmonic waves respectively (Holthuijsen, 2007).

$$\eta(x,t) = \eta_1 + \eta_2 = a\sin(\omega_1 t - k_1 x) + a\sin(\omega_2 t - k_2 x) \tag{A.30}$$

This group has its maximum surface elevation if η_1 and η_2 are in phase. Using trigonometric relation ships equation A.30 can be rewritten as (Holthuijsen, 2007):

$$\eta(x,t) = 2a \cdot \cos\left(\frac{\omega_1 - \omega_2}{2}t - \frac{k_1 - k_2}{2}x\right) \cdot \sin\left(\frac{\omega_1 + \omega_2}{2}t - \frac{k_1 + k_2}{2}x\right) \tag{A.31}$$

in which the sine wave is the carrier wave and the cosine wave is the envelope wave which modulates the amplitude of the carrier wave. The wave group travels at the speed of the envelope wave, which is given as $\frac{\Delta\omega}{\Delta k} = n \cdot c$ with $n = \frac{1}{2}(1 + \frac{2kh}{\sinh(2kh)})$ according to the dispersion relation based on airy wave theory (equation A.25). The length and period of the wave groups can be computed using the difference in wave numbers and frequencies as described in Bosboom & Stive (2015):

$$L_{group} = \frac{2\pi}{\Delta k} \tag{A.32}$$

$$T_{group} = \frac{2\pi}{\Delta\omega} \tag{A.33}$$

An irregular wave field naturally consists of multiple wave groups with frequencies very close to each other, especially for narrow banded wave spectra. This results in numerous interactions between these series of irregular groups which results in a lot of groupiness. This groupiness results in wave motion on lower frequencies compared to the wind waves themselves. This wave motion on lower frequencies are also referred to as infra-gravity wave motion.

A.4.4. Wave breaking

There are two types of wave breaking, depth limited wave breaking and steepness limited wave breaking. The breaking limits are also presented in figure A.4 as limit values for applicability ranges of wave theories. For waves in shallow water the wave breaking criteria is based on the depth and given by $H/d = 0.78$. For deep water waves the wave breaking criteria is based on the steepness of the waves

which is given by $H/L = 0.142$.

For depth limited wave breaking also the type of breaker can be predicted using the surf similarity parameter (Iribarren number), which is given as (Holthuijsen, 2007):

$$\xi = \tan(\alpha)/\sqrt{H/L} \tag{A.34}$$

This relation will give the relative steepness of the wave to the steepness of the structure slope as it is defined as the steepness of the slope divided by the steepness of the wave. For these types of equation the input parameters (wave height and wave length) vary per application. Practical used values are the deep water values (in which: $L = L_{m-1,0} = gT_{m-1,0}{}^2/2\pi$ and $H = H_{m0}$). But also other values are found in literature.

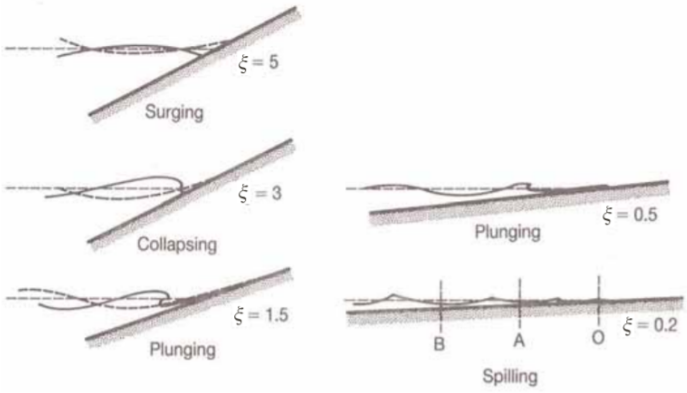

Figure A.6: Types of wave breaking on a slope (Ciria et al., 2007)

The surf similarity parameter does not only give insight in the type of breaker but can also characterise the amount of wave reflection, wave dissipation, wave run-up, overtopping and the stability of the armour of a breakwater (Holthuijsen, 2007).

Wave breaking on LCS

Wave breaking processes on the crest of LCS are important for the performance of the structures to reduce the transmitted wave energy and therefore prevent energetic wave conditions at the lee side of the structure. The shallow crest of LCS in combination with the seaward slope forces initiation of wave breaking. Wave breaking processes are characterised as large dissipation processes resulting in wave energy reduction. With more energy dissipation on the crest of the structure less energy is left to be transmitted to the lee side of the structure (i.e. wave transmission).

Hattori & Sakai (1994) investigated the behaviour of breaking waves over submerged permeable breakwaters using two parameters breaker height (H_b) and breaker depth (h_b). The breaker height is given as the wave height at the moment of breaking and the corresponding depth to the location of initiation of breaking is the breaker depth, see also figure 2.7a for a description of these parameters ($h_b = d_b$). In the study performed in Hattori & Sakai (1994) 6 physical model tests were performed on submerged breakwaters similar to prototype structures constructed in Japan for coastal protection. Breakwater material was changed from various sizes of gravel to artificial concrete elements to account for different porosity of the structure.

Hattori & Sakai (1994) concluded in his work that the breaker height exponentially reduces with distance from the top of the seaward crest towards the lee side of the structure. Moreover, the porosity plays and important role in the shore ward limit of the breaking position. The effect of porosity on wave breaking processes is especially important for HLCS which generally have higher porosity values compared to conventional rubble mound LCS. For an increase in porosity of the structure it was observed that the return flow over the structure reduced which resulted in less collapsing wave breaking of the lower part of the waves (i.e. hydraulic jump behaviour under rapid flows). Additionally, Hattori & Sakai

(1994) concluded that for the wave breaking process the porosity of the structure is more important than the roughness of the armour layer.

A.4.5. Wave energy

Waves will move water particles from their position at rest to some other position. Water particles will move in both vertical and horizontal direction. This change in location requires work to overcome gravitational forces which is represented by energy. The total wave energy has a potential energy component and a kinetic energy component:

$$E_{\text{total}} = E_{\text{potential}} + E_{\text{kinetic}} \tag{A.35}$$

The contributions and total wave energy can be estimated with linear wave theory by integrating the energy components over the depth. The total time-averaged wave-induced energy per unit of horizontal area is then given by (Holthuijsen, 2007):

$$E_{\text{total}} = \frac{1}{2}\rho g a^2 \tag{A.36}$$

From this equation it can be observed that the wave amplitude has the largest contribution to the wave energy of the wave field. As the wave height is twice the amplitude of the wave according to linear wave theory, the wave energy can also be expressed is terms of the wave height:

$$E_{\text{total}} = \frac{1}{8}\rho g H^2 \tag{A.37}$$

(This page is intentionally left blank)

B

Numerical model set-up

B.1. Numerical wave flume layout

The numerical flume that is used for the numerical experiments is based on the flume that has been used for the physical model experiments described in chapter 3. The exact recreation of the physical model flume in the numerical experiment is important for comparing wave field characteristics (i.e. the amount of observed non linearity and wave statistics). By reconstructing the exact physical model flume direct comparison between the extracted data from both models is possible without additional adaptions.

The numerical wave flume makes use of two numerical models, Oceanwave3D and OpenFOAM. If waves2Foam is used over the full domain of the numerical flume the computation will be computationally very expensive. To reduce computational time and therefore increase numerical efficiency OceanWave3D is introduced and coupled to OpenFOAM. OceanWave3D is a potential flow solver which is computationally less expensive but cannot model overturning waves, breaking waves and porous flow. If OceanWave3D is applied in a region where waves show overturning or breaking, OceanWave3D is not able to present physically sound surface elevation levels. In the part of the domain where the potential flow assumption is valid however it is more computationally efficient to use OceanWave3D. The coupling of both numerical models should be initiated at a location where the potential wave theory is still valid in order to generate realistic input data for the nested OpenFOAM model.

The coupling between both numerical models makes use of a relaxation zone, details of the use of a relaxation zone can be found in chapter 4.6. The quality of the coupling between both numerical models depends on the spatial and temporal resolution of both models. The grid resolution and the aspect ratio near the free surface are important for the diffusive behaviour of the numerical solution and therefore the correct representation of the surface elevation. A finer grid will increase the computation time as more cells should be resolved in both horizontal and vertical direction. The grid resolution should be based on a consideration between the required CPU time and accuracy of the solution. The accuracy of the numerical solution is determined using the concept of grid convergence (i.e. the solution should converge towards a constant value for increasing resolution). From grid convergence a grid independent solution can be obtained (i.e. the solution does not depend on the used grid resolution). For this research a difference in significant wave height between both numerical models of 1% is accepted for a grid independent solution. An analysis into the grid in-dependency is conducted to obtain an optimum between computation time and accuracy.

Relaxation zones are used to generate and absorb waves and couple both numerical models. The location of the relaxation zones depends on the adaptation distances. The solution in the vicinity of the structure should be independent on the distance from the structure to the relaxation zone. Especially for strong diffraction and reflection this is the leading criteria for the geometry of the inner domain according to Paulsen et al. (2014). As soon as the interaction between the incoming waves and the reflected waves can be neglected the inner domain can be truncated. For a cylindrical mono pile Paulsen

et al. (2014) found that the length should be 5 times the diameter of the mono pile to ensure that the interaction between the incoming and reflected wave field can be neglected. In order to recreate correct nonlinear behaviour of the waves after the coupling and to neglect the influence of interaction between the incoming and reflected waves a minimum distance of one wave length should be used as rule of thumb. Other rules of thumb for the relaxation zone lengths (minimum one wavelength) combined with the distance from the relaxation zone to the structure result in the numerical flume layout as presented in figure B.1.

The length of the relaxation zones is determined using the largest expected wave length during this research. The largest expected wave length can be obtained form a combination of the largest tested wave period and the largest water depth. During this research wave overtopping is one of the most important output variables. Wave overtopping is characterized by overtopping discharges. Recent studies have shown that low frequency waves caused by wave breaking may become very important for wave overtopping prediction (Van der Meer et al., 2018). In order to take the effect of low frequency waves into account in the numerical simulation the low frequency waves should be adequately modelled. For this reason $T_{m-1,0}$ is used to calculate the wave length to determine the length of the wave generation zone as this period gives more weight to the lower frequencies. Based on recommendations from Van der Meer et al. (2018), $T_{m-1,0}$ is calculated using the following relationship $T_{m-1,0} = T_p/1.1$. Using a T_p of 1.91 s, a $Lm-1,0 = 4.7m$ is calculated. However no fully deep water is present in the flume therefore also the wave length corresponding to the maximum water depth (0.33 m) is calculated which is $L_{m-1,0} = 2.9m$. For convenience a relaxation zone length of 4.0 m is used for both the OceanWave3D inlet relaxation zone and outlet pressure damping zone as well as for the OpenFOAM inlet and outlet relaxation zone.

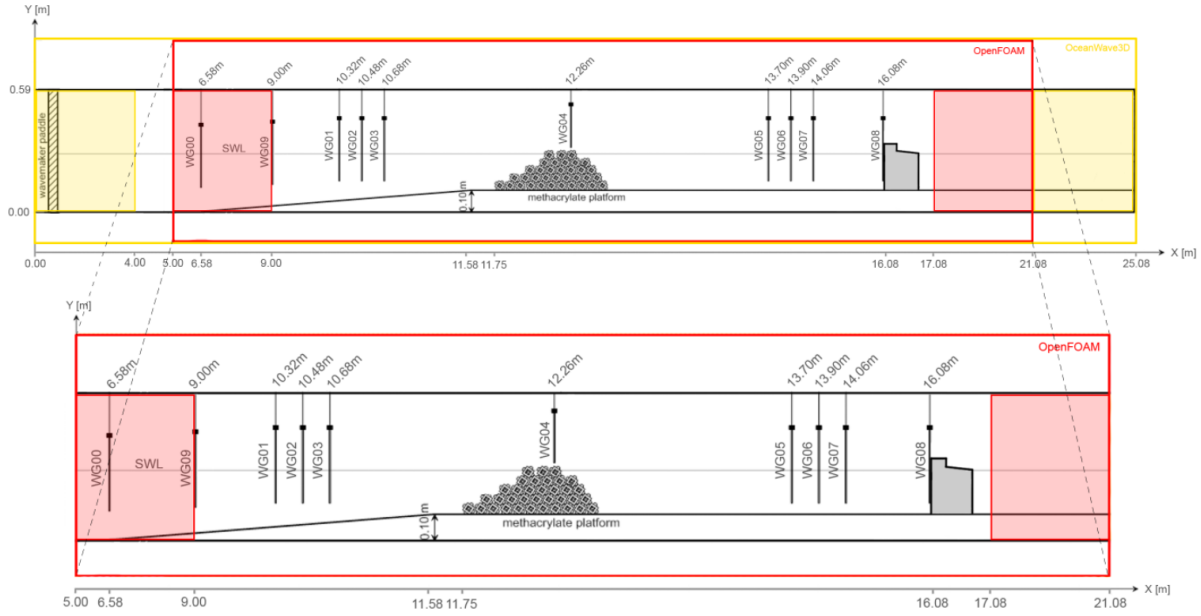

Figure B.1: Numerical flume layout including the OceanWave3D domain and the OpenFOAM domain (not to scale)

B.2. Numerical grid OceanWave3D

The design of the grid in OceanWave3D is much more simplistic compared to the grid design in OpenFOAM. The user only needs to describe the grid resolution in both horizontal and vertical direction. OceanWave3D uses a structured Cartesian finite difference grid in horizontal direction, determined by a grid size Δx. In vertical direction also a finite differences grid is used prescribed by a user selected number of layers. These layers are usually stretched towards the free surface to increase accuracy in regions of interest following recommendations of Paulsen et al. (2014). In order to determine the resolution of the OceanWave3D grid, several recommendations from various literature sources are analysed.

B.2.1. Vertical resolution

(Paulsen et al., 2014) prescribes 9 or 10 layers for the vertical discretization of the OceanWave3D grid using vertical stretching. Based on a sensitivity analysis conducted in preliminary OceanWave3D analysis prescribed in appendix D, is is concluded that the number of layers in vertical direction did not show adequate differences in the range that has been analysed (7-20 layers). Therefore the default number of 10 layers was chosen for this research as recommended by Paulsen et al. (2014).

B.2.2. Horizontal resolution

From the preliminary sensitivity analysis (see appendix D) the resolution in horizontal direction was found to be normative. The resolution in horizontal direction is especially important in the modelling of the steeper nonlinear peaks of the waves. During this research waves will behave up to the fifth order nonlinear waves which have very steep peaks and should be accurately modelled.

For the horizontal resolution the JIP programm recommends to use more than 10 cells per wave length. They use 15 grid cells per wave length based on a reference case of wave propagation in intermediate water depth with limited non linear behaviour. According to another literature source, ITTC (2011) prescribes to use 40 grid cells per wave length for a 4th order numerical scheme, which Oceanwave3D uses. In both recommendations the definition of wave length is not defined. Both these recommendations show large differences. Based on the conducted preliminary sensitivity analysis 40 grid cells per normative wave length based on the peak period are recommended for this research. This recommendation is mostly based on the expected high nonlinear waves within the numerical wave flume. For steeper peaks (more non linearity) higher horizontal resolution is recommended and it is concluded that the recommendation by the JIP program is not sufficient.

Because the wave length used for the determination of the resolution is not well described, this research uses a conservative approach in which the normative wavelength is based on the smallest near shore wave length which is expected during the numerical model runs conducted in this research. The shortest wave length is obtained from the hydraulic conditions with the smallest water depth and the smallest peak period resulting in the shortest waves. The smallest peak period examined during this research is 1.27 s. With a maximum freeboard of -0.03 m this results in a water depth of 0.16 m. These values results in a near shore wave length L_p of 1.5 m and a resulting grid resolution of $\Delta x = 1.5/40 = 0.0375m$. The numerical model domain of OceanWave3D has a total length of 25.08 m resulting in $25.08/0.0375 = 669$ grid cells in horizontal direction. For simplicity, 700 grid cells are selected for the numerical grid of OceanWave3D. This resolution is quite conservative because it is based on the smallest expected waves in the flume which results in higher level of detail for the larger waves. The OceanWave3D grid adopted in this research is presented in figure B.2.

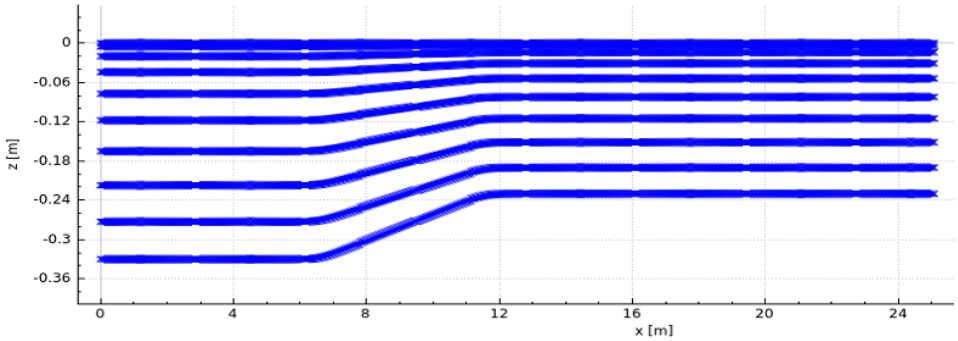

Figure B.2: The numerical grid used in OceanWave3D which covers fully covers the numerical flume (25.08 m). The blue dots represent grid points which are resolved by the OceanWave3D model. Note the stretching of the grid in vertical direction to obtain computational efficient accurate results.

B.3. Numerical grid OpenFOAM

In order to generate and refine the numerical grid in OpenFOAM the blockMesh and snappyHexMesh utility are used in this research. However also other meshing tools are available (e.g. cfMesh or independent meshing tools like gmsh and Salome). Several literature sources related to grid design and OpenFOAM grid resolutions have been analysed and based on these recommendations the grid is designed which will be scaled to the required grid resolution also following literature recommendations.

B.3.1. Grid design

The resolution around the SWL was found to be normative combined with the use of orthogonal grid cells with an aspect ratio of 1 ($\Delta x = \Delta y$) where the free surface is expected. This is found to have significant effect on the performance of OpenFOAM to model wave propagation (ITTC, 2011; Jacobsen et al., 2012; Roenby et al., 2017). (Roenby et al., 2017) investigated the effect of different aspect ratios around the SWL more in depth and found that while using the MULES VOF algorithm wiggles are found for tall cells ($\Delta y > \Delta x$) near the free surface. For flat cells ($\Delta y < \Delta x$) near the free surface the wiggles completely disappear but a phase error is introduced.

Taking these recommendations into account for this research a mesh structure of rectangular grid cells has been designed over the complete numerical domain. Moreover, refinements were applied to regions of interest and regions where larger gradients were expected in order to have achieve affordable computational costs without losing accuracy in the regions of interest. The regions of interest that were selected were those near the free surface elevation, near the HLCS and near the sea wall. Near the free surface elevation large gradients are expected as well as near the HLCS and sea wall. Refinements were applied near the sea wall in order to accurately capture the forces on the sea wall and the overtopping over the sea wall which increases for increasing grid resolution. Near regions of interest grid cells were resized up to 1/4 of the original size. While applying mesh refinements near solid boundaries like the sea wall highly skewed elements might be obtained from the meshing procedure. This problem has also been observed for the meshing around the slope of the platform and the edges of the sea wall where the slope introduces highly skewed meshes. Following Molines et al. (2019) this problem for is resolved by aligning the solid boundaries with the mesh axis for as far as possible.

Sea wall implementation

The sea wall has been implemented using snappyHexMesh. The initial location of the sea wall is at a distance of 4 m from the HLCS. This range is determined based on the bandwidth of the parametric study which follow from typical ranges for the construction of a HLCS. These type of detached structures mostly are constructed in a range from 0-150 m (prototype scale) from the coast. For larger distances between the sea wall and HLCS the material costs of a HLCS with certain freeboard will be unfeasible.

Generally overtopping using a physical model is measured by the use of a box behind the structure which collects the overtopped water. Numerical models like OpenFOAM instead use a overtopping face which calculates the amount of water that passes through the computational cells within this face. For details on measuring overtopping the reader is referred to chapter 4.7.1. The overtopping face used in this research is presented in figure B.3. For impulsive overtopping conditions large amounts of splashing water is expected. The dynamic behavior of these splashes might affect the predicted overtopping. In order to increase the accuracy of the measurements the overtopping face is not directly placed in line with the front face of the sea wall but slightly more on top of the sea wall.

Wave forces are measured using a separate cell face which is applied at the front face of the sea wall, see figure B.3. The ventilated boundary condition, following Jacobsen et al. (2018), is implemented on this face to correctly measure the impact forces. (Jacobsen et al., 2018) found that air entrapment can increase the force predictions to a high extent compared to the observed ones. Default values as described in (Jacobsen et al., 2018) are adopted for the boundary condition. More details on the ventilated boundary condition are described in chapter 4.7.2.

The grid design that has been designed for this research is presented in figure X and is examined in the grid resolution study for 4 different values of Δx (0.55, 1, 1,1 and 2 cm) according to literature

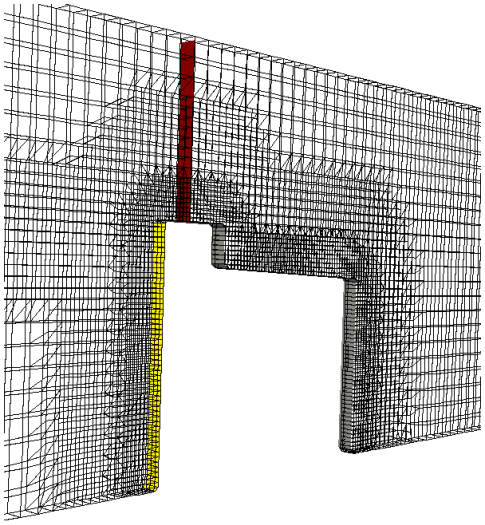

Figure B.3: Three dimensional view of the faces to measure overtopping (in red) and wave forces (in yellow). The sea wall which is extruded from the mesh using snappyHexMesh is presented combined for grid resolution 502.

recommendations which are elaborated hereafter.

B.3.2. Grid resolution

In order to perform a calibration based on numerical efficiency (i.e. computation time vs level of detail) several literature sources are analysed to set-up different grid resolutions which will be analysed in the calibration of the numerical model.

The JIP CoastalFOAM program recommends 100-150 cells per wave length based on the peak period for the horizontal resolution and a minimum of 5-10 cells over the wave height for the vertical resolution. However no description of the wave height and wave length are presented for random waves (i.e. an irregular wave field). Moreover, a specialist team on CFD computations in marine hydrodynamics ((ITTC, 2011)) recommends to use at least 20 cells in the vertical direction where the free surface is expected. This is interpreted by the author as using at least 20 cells per wave height for vertical resolution. However, also no description of which wave height is presented. Additionally other literature sources provide recommendations on the grid resolution in OpenFOAM, which are all presented in table B.1. From analysis of these recommendations it is found that for this research the vertical resolution around the free water surface is normative for the resolution compared to the wave length. This is however case specific due to the relatively shallow water in this research with corresponding non-linear waves which are steeper compared to less non-linear waves. Therefore is is recommended to check both criteria (i.e. wave height and wave length to determine the grid resolution) for different model set-up.

In order to determine which wave height or wave length should be used it is necessary to look at the intentions of the numerical model. For this research the physical phenomena of wave transmission, water level set-up and overtopping are important which show a high influence of the longer and larger waves. The numerical model therefore should should perform best for these conditions which can be set-up specific depending on the intended uses. Less effect is expected on the various wave structure interactions for the smaller and shorter waves and the criteria can be stretched a bit to increase computational efficiency. Considering all the above, the representative wave height used to calculate the grid resolution is taken as the significant wave height. By doing so the smaller wave heights are slightly less well described but on the other hand the most important larger waves are well described by the numerical model.

This research is consists of multiple phases. For the different phases different structure types (i.e.

Table B.1: Grid resolutions used and recommendations found in literature

Source	# of cells per wave length	# of cells per wave height
JIP CoastalFOAM	100-150	5-10
ITTC	-	20
Jacobsen, 2015	-	11
Jacobsen, 2018	-	10-20
Zaalberg, 2019	135	6
Moretto, 2020	635	20

sea wall, HLCS) are implemented resulting in slightly different grid resolutions and refinement. However the corresponding grid resolutions, number of cells, etc. indicated in table B.2 result from a numerical model setup with only the sea wall implemented. The reason for this is that after the calibration and validation of overtopping the grid resolution is determined and no more changes to the resolution are made.

Table B.2: Investigated grid resolutions and dimensionless characteristics

Grid ID	N_x	N_y	HLCS	Sea wall	$\#ofcells[-]$	$\Delta_{x,swl} = \Delta_{y,swl}[m]$	$\frac{H_s}{\Delta_{y,swl}}$	$\frac{L_p}{\Delta_{x,swl}}$
501	1462	54	No	Yes	111771	0.0055	20	418
502	731	27	No	Yes	27982	0.011	10	209
504	512	19	No	Yes	13721	0.016	7	148
503	366	14	No	Yes	7290	0.022	5	105

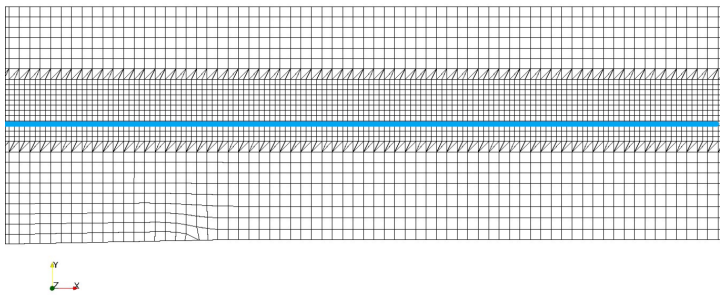

Figure B.4: Grid design BC502 including refinement near the free surface

B.4. Temporal resolution

Numerical models can use explicit or implicit time integration methods to calculate the state of system in time for a given grid design and resolution. Explicit time integration schemes can directly calculate the state of the system at following time steps using the previous time step. Implicit time integration schemes on the other hand find solutions by solving equations that include both the current and the later state(s) of the system. These type of time integration schemes do not have stability requirements but can become computationally very expensive. Explicit time integration methods are in general faster than implicit time integration methods but require stability requirements to prevent the solution to become unstable. Both OceanWave3D and OpenFOAM use an explicit time integration method. In order to obtain a stable solution for an explicit time integration numerical scheme the CFL condition can be used. First the CFL condition is explained after which the temporal resolution for both the OceanWave3D model and OpenFOAM are elaborated.

B.4.1. CFL condition

The CFL (Courant, Friedrichs and Lewy) condition is a necessary condition for the convergence of a finite difference scheme to a (non)linear hyperbolic partial differential equation (Zijlema, 2015). This means that in order for the numerical scheme to approach the exact solution of the physical equations the CFL condition should be met which limits the timestep that can be used to solve the system. If the CFL condition is not met the solution of the numerical model can become unstable and eventually blow up to infinity. The CFL condition can be explained using the concept of domain of dependence. The numerical domain of dependence must contain the analytical domain of dependence (Zijlema, 2015). This means that information must not travel faster than one computational cell per time step. For a one dimensional numerical model the CFL condition takes the following form:

$$\mid \sigma \mid \equiv \frac{\mid u \mid \cdot \Delta t}{\Delta x} \leq C \tag{B.1}$$

For a propagating wave the speed at which information travels can be approached using the concept of particle velocity. For this research the maximum expected particle velocity is adopted for the CFL condition. The maximum particle velocity can be approximated using linear wave theory and is equal to the amplitude of the wave multiplied with the period of the wave. The limiting time step can then be calculated using:

$$\Delta t = \sigma \cdot \frac{\Delta x}{\sqrt{g/h} \cdot 1.86 H_s} \tag{B.2}$$

B.4.2. Oceanwave3D

Oceanwave3D uses an explicit 4th order Runge-Kutta numerical Method therefore the CFL condition should be met. According to recommendatios by JIP CoastalFOAM, the maximum courant number for OceanWave3D is 0.8. Using the CFL condition, equation B.2, and a maximum courant number of 0.8 a limiting time step of 0.0187s is calculated. However this limiting time step is valid for linear waves. However the slope induces shoaling which results in higher flow velocities within the wave profile and therefore suppresses the limiting time step. For this reasons the limiting time step is reduced to 0.01 s to assure numerical stability. Please note that once OceanWave3D is coupled to OpenFOAM, OpenFOAM will adjust the time step of Oceanwave3D as well. However, due to the higher courant restriction of OpenFOAM this will not jeopardize the numerical stability of OceanWave3D. This will also be explained in more detail in the next section (i.e. section B.4.3).

B.4.3. OpenFOAM

OpenFOAM also uses an explicit time integration method and therefore also the CFL condition is normative for determining the limiting time step (i.e. temporal resolution). The temporal resolution in OpenFOAM is based on the limiting max courant number (C_{max}) which is prescribed by the user of the model. OpenFOAM, in contrary to OceanWave3D aims to increase the time step up to the limiting time step for every time step of the simulation. This adjustment method is based on computational efficiency while maintaining numerical stability. This method aims at adjusting the time step in such a way that the time step corresponds to the maximum prescribed courant number. OpenFOAM will adjust the next time step based on the maximum predicted flow velocity inside the numerical model, as described in chapter B.4.1. The initial time step and max courant number have to be prescribed to the model by the user. The CFL condition is used to calculate this initial time step which corresponds to a time step of 0.001s using the normative wave height with normative water depth and maximum particle velocity based on linear wave theory (using B.2). The max courant number has a large influence on the total computational time (i.e. numerical efficiency) and is therefore analysed in more depth without settling for the default courant number used in OpenFOAM of 0.35.

Maximum courant number (C_{max})

Various literature is reviewed to determine the max courant number (C_{max}) in relation to the grid resolution and the numerical schemes that are used by the OpenFOAM solvers. Larsen et al. (2019) studied the performance of interFoam (also the prescribed solver in this research) for propagating waves and found that from a computational point of view the decreasing of the maximum courant number is more

efficient to increase the accuracy of the solution than increasing the grid resolution. An increase in grid resolution namely also decreases the time step to maintain a given maximum courant number which therefore is less computationally efficient. Therefore the default courant number is reduced following recommendations by Larsen et al. (2019). In (Roenby et al., 2017) the effect on 2D wave propagation for the interFoam solver based on MULES limited interface compression is studied and compared the results with a newly developed isoAdvector method. From this analysis they concluded that an adaptive time stepping based on a maximum allowed courant number (C_{max}) of 0.1-0.2 gave good results regarding wave propagation for longer simulation times, however a slight phase lag error is observed for a maximum courant number of 0.2 when using the MULES method. The simulations conducted in this research are quite long (e.g. 680 seconds). Moreover for larger courant numbers, smearing of the interface can be observed. Additionally to only calibrating the grid resolution different combinations of grid resolution and courant numbers are analysed in this research to obtain the most computationally efficient grid and temporal resolution.

Numerical trick

OpenFOAM is a two phase model and also solves not only the fluid phase but also the air phase in the numerical model. It is observed during the simulations that the velocities of the air phase can become normative around the interface. These large interface air velocities therefore determine the limiting time step which reduces the computational efficiency of the model. If grid sizes become very small, interface iteration can relax the time step which otherwise results in large time step reduction. A method (i.e. numerical trick) is investigated which uses additional iterations around the interface of water and air in order to allow for a larger limiting time step without compromising the numerical stability. Because the pressure solver is the most computationally demanding and the alpha solver is relatively cheap, computational efficiency can be obtained by solving the alpha equation multiple times with smaller time steps for one pressure solve. This can be implemented by adjusting the nAlphaSubCycles in the fvsolutions file of OpenFOAM. The effect of this adjustment on the computational efficiency and the accuracy is also described in section 6.3.2.

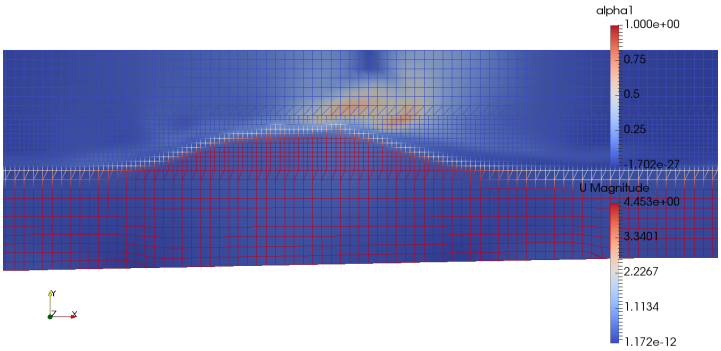

Figure B.5: Large air phase velocities observed during wave propagation

C

Model set-up and band width initial parametric study

This appendix is related to the choices regarding the bandwidth of the interesting parameters for the initial parametric study performed in this research. The effect of the geometrical layout is assessed on water level set-up, wave transmission and overtopping of the sea wall. The interesting geometrical parameters that have been defined are the crest width (B), freeboard (R_c) and distance between the HLCS and sea wall (L_{pool}), these parameters are presented in figure C.1. For each parameter the choices regarding the procedure that has been adopted for the different geometrical parameters that have been analysed in this research and the bandwidth of the corresponding geometrical parameters are explained in the following sections after which the test matrix is presented.

One set of hydraulic boundary conditions is used corresponding to severe overtopping (+- 300 l/s/m) for the base overtopping prediction. These conditions are characterised by $H_{s,i} = 11.24cm$, $T_{p,i} = 1.63s$, $L_p = 230cm$ and result in large overtopping events. Moreover the mesh is calibrated on these hydraulic boundary conditions which results in the most accurate numerical prediction.

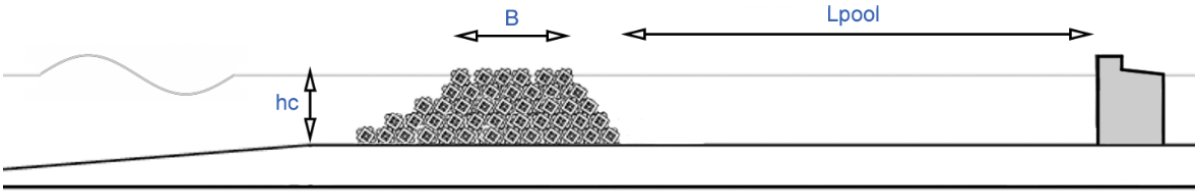

Figure C.1: Outline of the parametric study, indicated in the figure are the parameters that have been investigated

C.1. Crest height (h_c)

In order to increase and decrease the relative crest height the HLCS is increased and decreased in height by addition or removal of 1 layer of cubipods. The water level is kept constant instead of a constant structure height in order to keep the same wave characteristics at the HLCS and isolate only the effect of crest height. 1 layer of cubipods corresponds to a layer thickness of $1D_{n50}$. Only removing one layer results in a wider crest due to the shape of the cubipod HLCS. Therefore also 1 D_{n50} is added or removed at the rear side of the structure. Figure C.2 presents this procedure. Moreover, the pool length should remain constant therefore also the sea wall is moved with 1 D_{n50} depending on the increase or decrease of the crest height.

Bandwidth : $-0.4 \leq R_c/H_{s,i} \leq 0.4$

Considerations:

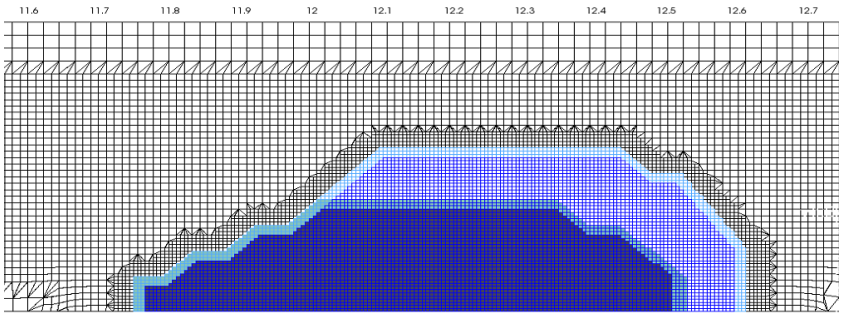

Figure C.2: Resulting mesh by increasing or reducing the crest height of the HLCS. In dark blue a relative crest height of $R_c/H_{s,i} = -0.4$ and in light blue a relative crest height corresponding to $R_c/H_{s,i} = 0.4$.

- Upper limit: 1 additional cubipod layer (6 layers total)
- Lower limit: 1 cubipod layer removed (4 layers total)

C.2. Crest width (B)

Crest width is analyzed by increasing the width of the structure in landward position, while keeping the distance from the HLCS to the sea wall constant (also shifting the sea wall landwards with the same magnitude as the additional crest width) in order to isolate only the effect of crest width with constant pool length. Figure C.3 presents the procedure of crest width increase.

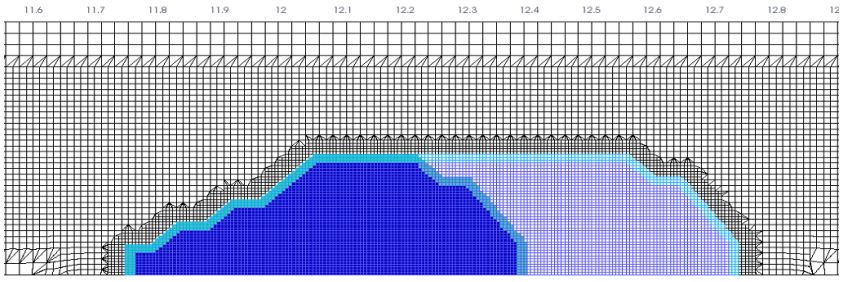

Figure C.3: Resulting mesh by increasing or reducing the crest width of the HLCS. In dark blue a relative crest width of $B/H_{s,i} = 1.5$ and in light blue a relative crest height corresponding to $B/H_{s,i} = 4.5$.

Bandwidth: $1.5 \leq B/H_{s,i} \leq 4.5$

Considerations:

- Upperlimit: Restricted by construction costs to obtain a cost effective solution –> max 4.5 B/H_i (10 units on crest) moreover far from the calibration case and therefore introduces a lot of uncertainty in the results for larger width. However, interesting to go to extreme values ($B/H_{s,i} = 20$), or for the transition range ($B/H_{s,i} = 10$) based on van der Meer et al. (2005) formula. For these low transmission coefficients almost no overtopping is expected but also transmission coefficients are presented.
- Lowerlimit: Little higher than the calibration case (4 units on crest) to cover the most interesting range while keeping close to the calibration case.

C.3. Basin length (L_{pool})

The relative basin length is increased or decreased by moving the sea wall shore ward or sea ward with a constant value while keeping the same location of the HLCS. This is in order to keep the same wave characteristics at the HLCS and only isolate the distance from the sea wall as parameter. The

HLCS remains at the same crest height and crest width. Figure C.4 presents the procedure that has been used to increase or reduce the pool length.

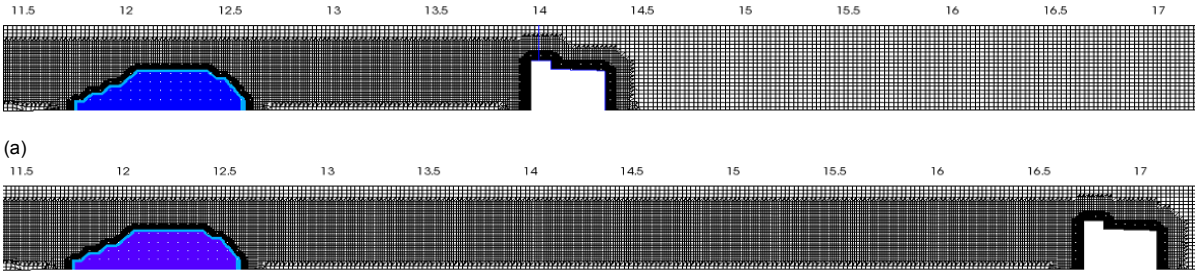

(a)

(b)

Figure C.4: Resulting mesh by increasing or reducing the pool length. a. Relative pool length = 0.6. b. Relative pool length = 1.8

Bandwidth: $0.6 \leq L_{pool}/L_p \leq 1.8$

Considerations:

- Upperlimit: Lpool = 415cm. This corresponds to a distance of 150m on prototype scale which is costs/realistic outer limit, due to depth constraints which would result in a very bulky construction with too high construction costs, other solutions would be more fit in this situation.
- Lowerlimit: Lpool = 139cm. This corresponds to a distance of 50m on prototype scale for which there is otherwise no room lef for a beach and therefore no need for a detached structure. Moreover a structure at this distance is located is well in the morphodynamic active zone therefore a tombolo/salient is likely to form quickly which has large influence on the hydrodynamic behaviour.

C.4. Test matrix

This section describes the complete test matrix that has been used to derive data for this research using the validated OpenFOAM model. The wave characteristics presented in table C.1 are extracted at wave gauge 2.

Table C.1: Test matrix. $H_{s,i}$ and $T_{p,i}$ measured at wave gauge 2.

Run ID	$H_{s,i}$ [cm]	$T_{p,i}$ [s]	h [cm]	h_c [cm]	B [cm]	L_{pool}[cm]	$R_c/H_{s,i}$ [-]	$B/H_{s,i}$ [-]	L_{pool}/L_p[-]
Base	11.24	1.63	33.0	23.0	33.0	277	0.0	3.0	1.2
Rch -0.4	11.24	1.63	33.0	18.7	33.0	277	-0.4	3.0	1.2
Rch 0.4	11.24	1.63	33.0	27.4	33.0	277	0.4	3.0	1.2
Rcw 1.5	11.24	1.63	33.0	23.0	16.0	277	0.0	1.5	1.2
Rcw 4.5	11.24	1.63	33.0	23.0	50.0	277	0.0	4.5	1.2
Rpl 0.33	11.24	1.63	33.0	23.0	33.0	139	0.0	3.0	0.6
Rpl 1.00	11.24	1.63	33.0	23.0	33.0	415	0.0	3.0	1.8
Rcw 7.0	11.24	1.63	33.0	23.0	77.0	277	0.0	7.0	1.2
Rcw 10.0	11.24	1.63	33.0	23.0	110.0	277	0.0	10.0	1.2
Rcw 15.0	11.24	1.63	33.0	23.0	166.0	277	0.0	15.0	1.2
Seichn1	11.24	1.63	33.0	23.0	33.0	115	0.0	3.0	0.5
Seichn2	11.24	1.63	33.0	23.0	33.0	230	0.0	3.0	1.0
Seichn2Rc-0.4	11.24	1.63	33.0	18.7	33.0	230	-0.4	3.0	1.0
Seichn2Rc+0.4	11.24	1.63	33.0	27.4	33.0	230	0.4	3.0	1.0

C.5. Test characteristics

This section describes the test characteristics that are obtained from running the simulations in table C.1 including the extracted hydrodynamic characteristics.

Table C.2: Table with parametric test runs and corresponding hydrodynamic characteristics extracted from OpenFOAM. Incoming and transmitted wave characteristics are extracted at wave gauge 2 and 6 respectively. Transmitted wave characteristics and water level set-up are extracted using a wave reflection procedure using wave gauges 5,6 and 7 with output at wave gauge 6. The incoming significant wave height is 11.24 cm with a basin water depth of 23 cm.

Test ID	$H_{s,i}$ [cm]	$R_c/H_{s,i}$ [-]	$B/H_{s,i}$ [-]	L_{pool}/L_p [-]	K_t [-]	$\overline{\eta}_{seawall}[cm]$	$i_{\overline{\eta},HLCS} \cdot 10^{-3}$[-]	$i_{\overline{\eta},basin} \cdot 10^{-3}$[-]	$q[l/s/m]$	$q/q_{initial}[-]$
BC502A	11.24	-	-	-	-	-	-	-	-	-
SW502B	11.24	-	-	-	-	-		-	1.2806	1.0
Rcw1.5	11.24	0.0	1.5	1.2	0.47	0.51	0.63	3.32	0.2799	0.22
Base	11.24	0.0	3.0	1.2	0.37	0.47	1.39	3.23	0.1508	0.12
Rcw4.5	11.24	0.0	4.5	1.2	0.30	0.56	2.56	3.08	0.0555	0.04
Rcw10.0	11.24	0.0	10.0	1.2	0.18	0.55	2.66	2.17	0.0098	0.01
Rcw15.0	11.24	0.0	15.0	1.2	0.13	0.56	3.52	0.77	0.0033	0.00
Rch-0.4	11.24	-0.4	3.0	1.2	0.53	0.42	-0.66	3.19	0.4495	0.35
Seichn2Rc-0.4	11.24	-0.4	3.0	1.0	0.50	0.46	-0.03	3.26	0.4484	0.35
Base	11.24	0.0	3.0	1.2	0.37	0.47	1.39	3.23	0.1508	0.12
Rch+0.4	11.24	0.4	3.0	1.2	0.40	0.47	2.48	2.54	0.0808	0.06
Seichn2Rc+0.4	11.24	0.4	3.0	1.0	0.44	0.34	2.50	2.26	0.1754	0.14
Rch+0.8	11.24	0.8	3.0	1.2	0.44	0.34	1.84	2.49	0.0993	0.08
Seichn1	11.24	0.0	3.0	0.5	0.41	0.38	2.97	10.32	0.5271	0.41
Rpl0.33	11.24	0.0	3.0	0.6	0.37	0.48	1.72	6.86	0.3043	0.24
Seichn2	11.24	0.0	3.0	1.0	0.41	0.50	1.61	4.31	0.2129	0.17
Base	11.24	0.0	3.0	1.2	0.37	0.47	1.39	3.23	0.1508	0.12
Rpl1.00	11.24	0.0	3.0	1.8	0.37	0.65	1.75	2.40	0.0766	0.06

D

Preliminary Oceanwave3D grid resolution study

In this appendix a preliminary grid resolution study is presented for the OceanWave3D numerical model based on regular waves. First, the model set-up is briefly explained. Then vertical, horizontal and temporal resolution sensitivity have been assessed based on initial recommendations from the JIP CoastalFOAM program. Based on this sensitivity analysis critical knowledge is obtained for the set-up of OceanWave3D for the final grid.

D.1. Model set-up

A numerical model should be designed to reproduce the correct physical processes. The most important physical process that should be accurately captured by the Oceanwave3D model is the shoaling over the slope and the corresponding surface elevation levels. The numerical grid of the OceanWave3D model is designed to give the best ratio of accurate representation of surface elevation in relation to the required CPU time at the coupling zone to the OpenFOAM domain. The waves are generated at the offshore OceanWave3D boundary condition and propagate through the domain until the coupling zone to OpenFOAM is reached. At the coupling zone the waves have started shoaling depending on the hydraulic boundary conditions input. This process of shoaling should be accurately captured by the numerical model as this model provides the input for the OpenFOAM model.

The preliminary numerical grid of Oceanwave3D is designed based on recommendations for horizontal and vertical resolution. The grid has 7 smoothed layers overt the vertical and a a horizontal resolution of $\Delta x = 0.067m$. This results in an aspect ratio of 0.3 at the offshore boundary and an aspect ratio of 1.9 at the location of the sea wall ($x = 77m$).

D.2. Vertical grid resolution

In order to better capture the vertical velocity profile, vertical stretching has been used for the grid. Due to the vertical stretching and the slope in the profile the vertical resolution is higher near the location of interest compared to the inlet boundary. Preferably a minimum number of layers is used as this reduces the computation time of the simulation. However, the number of layers cannot be reduced without a sacrifice as the resolution decreases and therefore also the accuracy. Moreover, for more reduction in vertical resolution also stability requirements start to play a role which limits the minimum number of layers that can be used. A number of 7 layers was found to be stable for this numerical model set-up. In figure D.2 the free surface elevation at $x = 63.5m$ is presented for 7,10 and 15 layers and the relative CPU time is also given. No difference is found for different vertical resolution from which it can be concluded that 7 layers is the optimal vertical resolution for Oceanwave3D for this numerical model set-up. If the effect of vertical resolution is checked at a location on the platform $x = 77m$ no differences are observed for 7,10 or 15 layers.

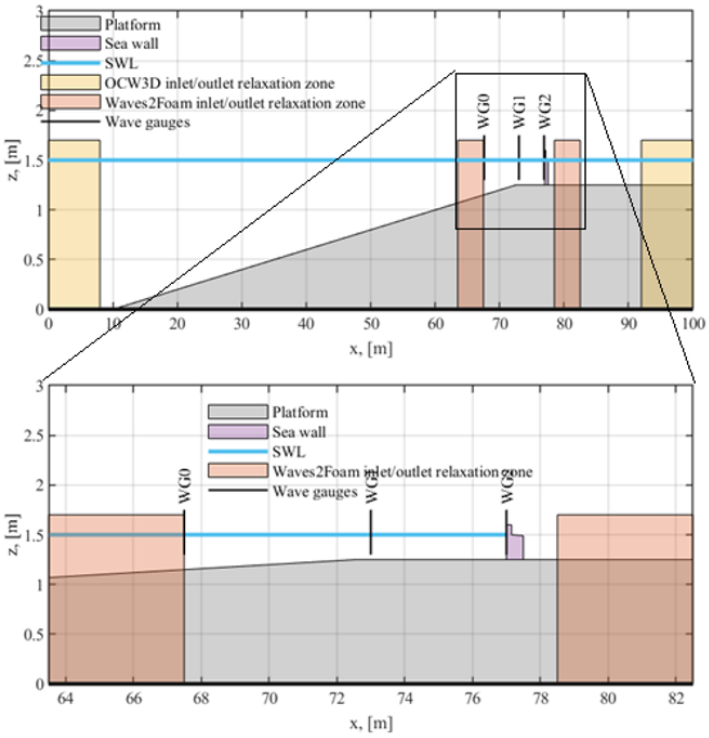

Figure D.1: Old numerical model set-up for which this preliminary grid resolution analysis has been performed.

D.3. Horizontal grid resolution

Horizontal discretization is found to be the most important factor related to the correct representation of the Oceanwave3D surface level elevation. Due to the shoaling of the waves the waves become steeper and the grid should be finer compared to non shoaling waves. The horizontal resolution determines the ability of the model to correctly represent the crest of the wave. In figure D.3 the wave gauge signal at $x = 67.5$ is presented for a horizontal resolution of 0.05m, 0.067m, 0.1m and 0.25m with the relative CPU times. The wave gauge signal for a horizontal resolution of 0.05m, 0.067m and 0.1m show similar behaviour around the crest of the wave whereas the wave gauge signal for 0.25m is not able to give the correct surface level elevation. Therefore it is concluded that a horizontal resolution of 0.1m should be used based on the relative accuracy and CPU time for the given hydraulic boundary conditions.

However, during this research also other hydraulic boundary conditions will be examined, where waves will behave differently in the coupling zone. Longer waves are more affected by the slope at the moment of coupling which might result in more non linear behaviour. For these different boundary conditions the Oceanwave3D model should still give the correct free surface elevations. If the wave gauge signal at $x = 77m$ is analysed, see figure D.4, the surface level elevation for the various horizontal resolutions show considerable differences caused by the non-linearity of the waves. From figure D.4 it can be concluded that for steeper waves more horizontal resolution is needed. The CPU time will not increase significantly for more horizontal resolution from 0.1m to 0.067m. With this taken in consideration and the various hydraulic boundary conditions that will be examined it is decided to use a finer horizontal resolution of 0.067m which corresponds to approximately 33 grid cells per L_p.

D.4. Temporal resolution

The used temporal resolution depends on the adopted numerical grid resolution and the maximum expected flow velocity within the numerical domain. Based on the courant number limitation the temporal resolution can be calculated for which numerical stability is guaranteed. A higher temporal resolution moreover result in lower courant numbers. The temporal resolution is not only used to guarantee numerical stability but also shows to have an effect on the numerical outcome. However a higher temporal

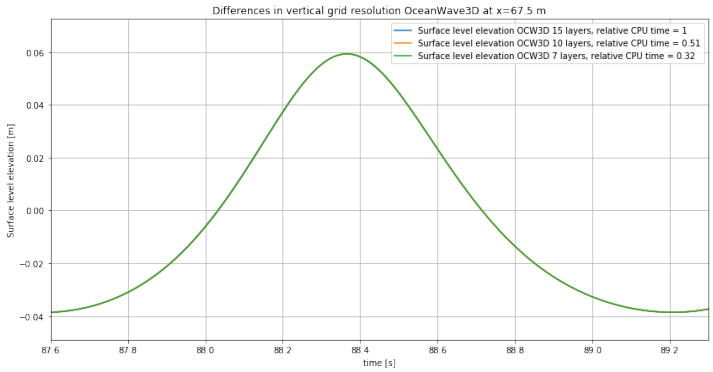

Figure D.2: Temporal resolution differences on surface level elevation OCW3D at x=67.5m

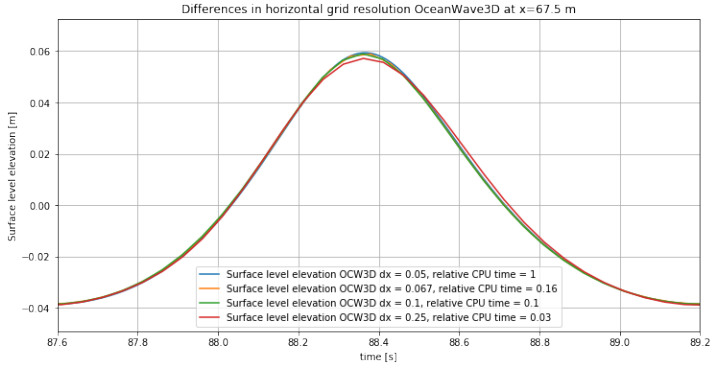

Figure D.3: Horizontal resolution differences on surface level elevation OCW3D at x=67.5m

resolution and thus a lower courant number also increases computation time. Therefore a proper grid resolution analysis should include the effect of different courant numbers on the numerical outcome. In figure D.5 the wave gauge signal at $x = 67.5m$ is presented for a temporal resolution of 0.01, 0.025 and 0.05 with the relative CPU time. For the gauge signal with temporal resolution of 0.01 and 0.025 the solutions are almost identical whereas for a temporal resolution of 0.05 differences can be observed related to the temporal resolution. Therefore it is concluded that a temporal resolution of 0.025 should be used based on the relative accuracy and CPU time. Also if the signal at $x = 77m$ is analysed the free surface elevation for the various temporal resolutions the temporal resolution of 0.025 gives the best results.

D.5. Conclusion

The vertical resolution is found to have minor effect on the numerical outcome and the default value of 10 grid layers is found to be sufficient. However, the horizontal resolution is found to be the most important factor related to the correct representation of the Oceanwave3D surface level elevation. Depending on the steepness of the waves in the flume large difference of the horizontal resolution are found. It is advised to use at least 40 grid cells per wave length (based on the peak period for irregular waves). Moreover it is recommended to do a proper grid resolution analysis with grid resolutions determined based on recommendations while taking into account the large dependency of the expected wave characteristics in the flume. Moreover the temporal resolution should be based on the courant number because OceanWave3D uses an explicit time integration method and numerical stability has to be guaranteed.

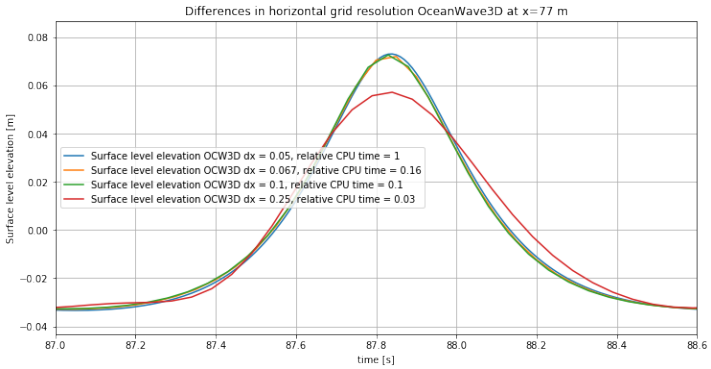

Figure D.4: Horizontal resolution differences on surface level elevation OCW3D at x=77m

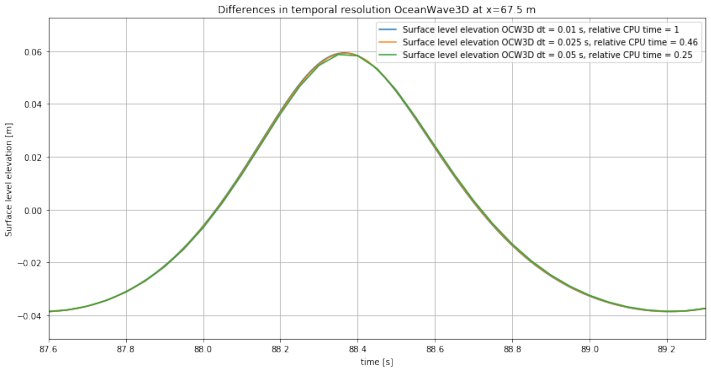

Figure D.5: Vertical resolution differences on surface level elevation OCW3D at x=67.5m